MICROCOPY RESOLUTION TEST CHART
NATIONAL BUREAU OF STANDARDS-1963-A

AD-A161 271

AFOSR-TR- 85-0900

DTIC FILE COPY

85 11 12 118

"A Program of Research on Microfabrication
Techniques for VLSI Magnetic Devices"

Mark H. Kryder
Magnetics Technology Center
Carnegie-Mellon University

DTIC
ELECTE
NOV 1 8 1985
S   D

B

AIR FORCE OFFICE   COTENTIFIC RESEARCH (AFSC)
I

REPORT DOCUMENTATION PAGE	READ INSTRUCTIONS BEFORE COMPLETING FORM	
1. REPORT NUMBER AFOSR FINAL REPORT 9 0	2. GOVT ACCESSION NO. AD-A161	3. RECIPIENT'S CATALOG NUMBER
4. TITLE (and Subtitle) "A Program of Research on Microfabrication Techniques for VLSI Magnetic Devices"	5. TYPE OF REPORT & PERIOD COVERED Final 01 Oct. 83 to 30 Sept. 84	
	6. PERFORMING ORG. REPORT NUMBER	
7. AUTHOR(s) M. H. Kryder, M. Alex, J. Artman, L. Bauer, R. Campbell, A. Guzman, S. Jo, C. Krafft, D. Saunders, R. Smith, T. Yoshiie	8. CONTRACT OR GRANT NUMBER(s) AFOSR-80-0284	
9. PERFORMING ORGANIZATION NAME AND ADDRESS Carnegie-Mellon University Pittsburgh, PA 15213	10. PROGRAM ELEMENT, PROJECT, TASK AREA & WORK UNIT NUMBERS 61102F 2305/C1	
11. CONTROLLING OFFICE NAME AND ADDRESS Air Force Office of Scientific Research/NE Bolling Air Force Base Washington, D.C. 20332	12. REPORT DATE Nov. 1984	
	13. NUMBER OF PAGES 296	
14. MONITORING AGENCY NAME & ADDRESS(if different from Controlling Office)	15. SECURITY CLASS. (of this report) Unclassified	
	15a. DECLASSIFICATION/DOWNGRADING SCHEDULE	

16. DISTRIBUTION STATEMENT (of this Report)

Unlimited

17. DISTRIBUTION STATEMENT (of the abstract entered in Block 20, if different from Report)

Unlimited

18. SUPPLEMENTARY NOTES

19. KEY WORDS (Continue on reverse side if necessary and identify by block number)

Magnetic Bubble, Memory, Logic, Garnet, VLSI, Magneto-Optic, Charged Walls, Ion Implantation, Transmission, Electron Microscopy

20. ABSTRACT (Continue on reverse side if necessary and identify by block number)

New materials, new fabrication techniques and new device structures for high density magnetic bubble devices were developed. The main focus of the work has been to develop ion implanted contiguous disk devices offering sixteen times the bit density of presently manufactured bubble devices and chip capacities of 64 Mbit.

Under this contract we developed a computer program for modeling magnetic bubble garnet materials and have applied it to the design of bubble materials

DD FORM 1473 EDITION OF 1 NOV 65 IS OBSOLETE
1 JAN 73

20. (cont'd.)

having isotropic magnetostriction. We have previously shown that such
materials would provide better device operating characteristics.
During this past year we also modeled the anisotropic stresses around
ion implanted propagation patterns and showed how they produce non-
uniform anisotropies due to magnetostrictive effects. --

An extensive investigation of the effects of ion implantation
on garnet materials we also completed. This study pertained partic-
ularly to the implantation of hydrogen, deuterium and oxygen. Means
of obtaining uniform implant damage profiles were developed. The
effects annealing on the magnetic properties of implanted garnets
were also studied. It was found that ion implantation not only
affected the anisotropy through magnetostriction, but in fact
caused a reduction in the growth-induced magnetic anisotropy.
Mechanisms for these other affects were identified.

Transition electron microscopy was used to study the microstructure
introduced by implantation in garnets. At high doses amorphization
was observed and with high temperature annealing recrystallization
occurred.

Progress was also made on high density bubble devices. Propagation
of 0.5μm bubbles in 2.5μm period devices was achieved and current-
access bubble logic gates were demonstrated. The dynamic gyrotropic
deflection of bubbles from the gradient field direction was observed
to strongly affect the performance of the gates.

Dist

A-1

i

Table of Contents

1. Introduction

Magnetic bubble technology is continuing to find new applications, and manufacturers (Intel, Motorola, Hitachi and Fujitsu) report increasing sales. In Japan Hitachi, Fujitsu, and NEC and several universities also have substantial research efforts on new advanced bubble domain technologies. On the other hand, research efforts in the U.S. on bubble technology were reduced during the past year when Bell Laboratories terminated its research on bubble devices. The only remaining large research effort on advanced bubble device technologies in the U.S. is now at Carnegie- Mellon University (CMU). This program at CMU has been receiving support from the Air Force Office of Scientific Research under grant AFOSR 84-0341 and lesser amounts from the National Science Foundation (Grants ECS-8319769 and ECS-8307261) and NASA (Grant NAG 1-395). This report describes work carried out under AFOSR Grant 84-0341. Where it was felt that research supported by NSF or NASA was particularly relevant to this report, a description of that work is also included. It is made clear in the text which work was carried out under which grant.

Highlights of the work carried out this past year include the development of new submicrometer garnet materials, extensive studies of the effects of ion implantation on the magnetic parameters of garnet, microfabrication of 0.5μm bubble-size ion-implanted devices and microfabrication of current-access bubble-logic devices. During the past year an extensive Ph.D. dissertation and five publications resulted from this work. We believe that the work we are carrying out will provide U.S. manufacturers with the knowledge to make future generations of bubble technology which they must have soon if they are to compete with the Japanese who are rapidly developing more advanced bubble technologies.

2. Magnetic Garnet Materials

The main thrust of our work on epitaxial magnetic garnets is to develop materials which will support submicrometer bubbles for ion-implanted contiguous-disk devices. In addition we have been growing materials for work on current-access bubble logic devices.

During this past year $Sm_{1.2}Lu_{1.7}Tm_{0.1}Fe_{4.7}Ga_{0.3}O_{12}$ films were developed for 0.5μm bubble size devices. Typical properties are: thickness from 0.7 to 1.1μm; stripe-width of 0.59μm; $4\pi M_s$ of approximately 1200 Oe; and a lattice mismatch to the gadolinium-gallium garnet substrate of less than 0.015A. These films have been successfully demonstrated to provide good propagation margins in devices with bit cells as small as 2.0μm.

A computer program was written this past year which facilitates the design of melts for desired film properties. The user of this program must input desired film properties such as magnetization, anisotropy, and magnetostriction and the program will calculate the melt composition necessary to achieve these properties. This program has been used extensively in the design of the melts used for the

films grown in our laboratory.

A major area of research on magnetic garnets under this program is now the development of materials having isotropic magnetostriction. Films with isotropic magnetostriction will provide more isotropic bubble propagation in ion-implanted contiguous disk devices and are expected to lead to improved operating margins. We have designed both deuterium and bismuth containing films to achieve these properties. The bismuth containing films are somewhat more difficult to grow than most other garnets because large supercooling of the melt must be used which in turn leads to problems with nucleation in the melt and difficulties in getting flux droplets off the grown film after it is removed from the melt (because of the high melt viscosity). During the past year we grew several bismuth containing films. Early films had severe problems of lattice mismatch and we were not successful in removing flux from the wafer. These problems have now been solved by the addition Vanadium Oxide to the flux and slight adjustments in the melt composition; however, the films do not yet provide the desired magnetic properties. We are working to solve the remaining difficulties.

For a detailed description of this work see the report entitled "Liquid Phase Epitaxial Growth of Garnets" by R. O. Campbell and M. H. Kryder.

3. Effects of Ion Implantation on Magnetic Garnets

We have placed a major emphasis on the study of the effects of ion implantation on garnet, because we believe that ion implanted contiguous disk devices, which offer four to sixteen times the bit density of permalloy bubble technology, are the most likely successor to permalloy bubble devices. This view if shared by a majority of workers on bubble technology.

Our studies of the effects of ion implantation on garnet during the past year were concentrated into two areas: (1) an experimental study of the effects of deuterium, oxygen, and hydrogen implants on the magnetic anisotropy, magnetization, and gyromagnetic ratio of garnets and (2) a theoretical study of the effects of stress introduced by implantation on the magnetization near boundaries between implanted and unimplanted regions of a film.

3.1. An Experimental Study of The Effects of Ion Implantation on the Magnetic Parameters of Garnet

During the past four years, with support from AFOSR Grant 84-0341, we have conducted a study of the effects of ion-implantation with deuterium, hydrogen and oxygen on the magnetic properties of garnet. Attached to this report is a copy of a Ph.D. thesis by C. S. Krafft which describes this work.

A unique set of experimental equipment was established to carry out this work. Ferromagnetic

resonance measurements were done using a wideband microwave spectrometer, to determine the magnetic anisotropy and gyromagnetic ratio. A vacuum attachment was used to measure the magnetostriction in the virgin and implanted layers. The anisotropy fields and the magnetostriction were measured from $0^{\circ}C$ to $200^{\circ}C$. The implant-induced strain was determined from double crystal X-ray diffraction rocking curves.

While the results obtained in this study are in agreement with some of the results of previous investigations, including the large anisotropy field change and the annealing behavior of hydrogen (deuterium) implants, the explanation for the hydrogen implant mechanisms which was previously given does not satisfactorily explain our results. The notable differences are that we find a significant contribution from a non-magnetostrictive anisotropy effect to the total implantation-induced anisotropy field change, even after the deuterium (hydrogen) has been annealed out of the film. Changes in the gyromagnetic ratio in the implanted layer, and the magnetostriction which we found have also not been previously reported.

Previous investigators have suggested that the excess anisotropy field change observed in hydrogen implanted films, which cannot be attributed to magnetostrictive effects is only found in films in which the hydrogen has not been annealed out [Y. Sugita, T. Takeuchi, and N. Ohta, Paper CA-5, Magnetism and Magnetic Materials Conference, Atlanta, 1981; V.S. Speriosu and C. H. Wilts, J. Appl. Phys.. 54, 3325 (1983)]. Our results indicate that there is a substantial non-magnetostrictive effect, even in films which were annealed at temperatures which are substantially higher than the hydrogen (deuterium) desorption threshold. It was shown that the magnetostrictive field ΔH_{σ} only accounts for between 1/3 to 1/2 of the total implantation induced uniaxial anisotropy field change ΔH_E in deuterium (and hydrogen) implanted films. The ratio $\Delta H_{\sigma}/\Delta H_E$ is approximately 1/2 for low to medium doses (up to 1×10^{16} D_2^+/cm^2), but decreases for high implant doses, due to a reduction in the ratio of magnetostriction to magnetization, λ_{111}/M_s in the ion implanted layer.

The deuterium implants exhibit a substantial "non-magnetostrictive" effect which is attributed to at least two sources. The first mechanism is related to the presence of the implanted ions. This is most clearly detected by measuring the change in the anisotropy field as a function of annealing. A rapid decrease in the anisotropy field in the uncoated films near $250^{\circ}C$, and an increase in the anisotropy field near the film surface in the coated films after the $450^{\circ}C$ anneal are attributed to this effect which has been termed a chemical effect. In contrast to reports of previous investigators, who stated that there was only a magnetostrictive effect and a chemical effect, we have clearly shown that there is at least one and probably two other mechanisms. There is some permanent damage to the lattice which suppresses some of the growth-induced anisotropy by displacing some of the rare-earths from their original sites. The contribution of the suppression of the growth-induced anisotropy can be estimated from a plot of ΔH_E

versus maximum implant strain, obtained by annealing the film. At zero strain, by definition, there is no magnetostrictive effect so a positive intercept at zero strain indicates a contribution from non-magnetostrictive effects. However, there is still a portion of the anisotropy field change which is unaccounted for and is presumed to be attributed to yet another mechanism which exhibits a linear dependence with strain. While this mechanism appears to be unique to deuterium and hydrogen implanted films, its source has not been identified.

The temperature dependence of ΔH_E was found to depend on the deuterium implant dose. In films with a sufficient dose to create a negative anisotropy energy in the surface layer, ΔH_E decreased nearly linearly with temperature. No saturation in ΔH_E was observed for the highest implant strain measured, up to 2.2% although degradation of the resonance signal, the Curie temperature, and an increase in the linewidth were observed in the heavily implanted films. The ΔH_σ was found to decrease smoothly with temperature. The relative change in the temperature dependence of ΔH_σ compared to ΔH_E was dependent on the implant conditions. High temperature measurements of ΔH_σ in films where the anisotropy decreases uniformly with temperature through the implanted layer thickness indicates that ΔH_σ and ΔH_E both decrease smoothly to zero at the Curie temperature.

In heavily implanted films, the non-magnetostrictive portion of the anisotropy field decreases more rapidly with temperature than the magnetostrictive portion. As a result, the value of ΔH_σ at high temperatures, calculated from the vacuum-induced shift in the principal surface mode and the maximum implant strain, overestimated the magnetostrictive contribution, as evidenced by the fact that the calculated value of ΔH_σ was larger than ΔH_E. However, this is an artifact and does not represent the actual situation, since the maximum ΔH_E shifts away from the region of maximum strain at high temperatures.

The annealing results from SiO_2 coated films indicate that the threshold temperatures for desorption of the deuterium correspond with those for hydrogen. In the uncoated films, a significant amount of the deuterium has desorbed after a 250°C anneal. In the coated films, the desorption is moderated by the SiO_2 overlayer. The trapped deuterium increases the anisotropy field near the film surface after a 450°C anneal. At higher annealing temperatures, the deuterium diffuses out of the film.

In addition to the effects of the SiO_2 layer on the annealing behavior, there was a significant difference in the film properties of the as-implanted films which were coated before implantation, compared to uncoated films. In heavily implanted films with an SiO_2 overlayer, there was a significantly stronger resonance signal in the implanted layer than in films with identical implants which were not coated with SiO_2. In addition, the gyromagnetic ratio was drastically reduced and the resonance linewidth was considerably broader in the uncoated, as-implanted films. The nature of the mechanism is not

understood, but the difference in the properties of the SiO_2 coated film may be attributed to a thermal effect or to a surface effect. The annealing studies indicate that the γ is restored after a relatively low temperature anneal (250°C). The change in γ suggests that there is a fundamental difference in the properties of the garnet, such as a change in the valence of the iron atoms, or formation of metastable compounds of hydrogen (deuterium) and the garnet atoms. We should also note that the change in the iron valency, from Fe^{3+} to Fe^{2+}, increases λ_{111} (less negative) [P. Hansen, J. Appl. Phys. 48, 801 (1977)]. This may be the mechanism for the reduction in γ as well as the observed decrease in λ_{111}/M_s, since M_s is also decreased.

The temperature dependence of λ_{111}/M_s in the bulk [$\lambda_{111}/M_s(B)$] and in the ion implanted layer [$\lambda_{111}/M_s(I)$] were measured. At low doses, $4\pi M_s(I)$ is decreased more than $\lambda_{111}(I)$, so $\lambda_{111}/M_s(I)$ is increased slightly compared to $\lambda_{111}/M_s(B)$. However, $\lambda_{111}/M_s(I)$ decreases more rapidly with temperature. At higher doses, $\lambda_{111}/M_s(I)$ is less than $\lambda_{111}/M_s(B)$ at room temperature, indicating that λ_{111} is decreased more than $4\pi M_s$ by the implant. In these films, the temperature dependence of $\lambda_{111}/M_s(I)$ is less than $\lambda_{111}/M_s(B)$, so that $\lambda_{111}M_s(I)$ is larger than $\lambda_{111}/M_s(B)$ above a certain temperature which depends on the implant dose.

Results from hydrogen implanted films are in agreement with those published by other investigators, with regard to the large non-magnetostrictive portion of ΔH_E, and the observed annealing behavior. We found that the annealing behavior was similar to that for the deuterium implanted films. However, in both hydrogen and deuterium implanted films, we found that even after annealing the non-magnetostrictive change in the anisotropy field played an important role. Thus, the conclusions of previous investigators [Y. Sugita, T. Takeuchi, and N. Ohta, Paper CA-5, Magnetism and Magnetic Materials Conference, Atlanta, 1981; V.S. Speriosu and C. H. Wilts, J. Appl. Phys. 54, 3325 (1983)] who attributed the non-magnetostrictive portion of ΔH_E to the presence of the hydrogen ions, are called into question. We propose here that the non-magnetostrictive effects of the hydrogen (deuterium) implants are not solely attributed to the presence of the implanted ions. The results from oxygen implants indicate that above 1.0% strain the film properties are degraded. This includes a significant reduction in the Curie temperature in the region of maximum implant damage, and the formation of a bimodal anisotropy profile due to overdamage in the region of maximum strain. In films which were implanted with both oxygen and deuterium, to achieve a uniform strain profile, the maximum ΔH_E was attributed to the deuterium implant. The anisotropy profile and strain profiles cannot be made uniform simultaneously, due to the difference in the implant mechanisms of deuterium and oxygen implants. To obtain uniform strain and anisotropy profiles, multiple energy implants, with the same ion species, are recommended over combined implant species.

For a more extensive discussion of this work the reader is referred to the Ph.D. thesis of C. S. Krafft

entitled "Deuterium Implantation in Magnetic Garnets," Carnegie-Mellon University, September 5, 1984.

3.2. Investigations of the Effects of Ion-Implantation on the Microstructure of Garnet

Studies were continued on the effects which ion implantation has on the microstructure of garnet. Using special thinning and cross-sectioning techniques, ion implanted garnets were thinned both from the bottom and in cross-section to prepare samples for transmission electron microscopy. The garnet thin films were grown by liquid phase epitaxy of $\{111\}$ gadolinium gallium garnet substrates and subsequently implanted with ions of deuterium at 60keV and doses ranging from 0.50 to $4.5 \times 10^{16} D_2^+/cm^2$ and ions of oxygen at 110 keV and doses ranging from 0.95 to $8.6 \times 10^{14} 0^+/cm^2$. It was found that higher doses caused the garnet thin films to change from perfect single crystals to amorphous films. The amorphization process was found to evolve in four separate stages: (1) an implanted (crystalline) band, delineated by the implantation strain profile, forms at doses of about $0.5 \times 10^{16} D_2^+/cm^2$ and $0.95 \times 10^{14} 0^+/cm^2$, (2) isolated amorphous regions of about 10nm in diameter form at doses of about $1.0 \times 10^{16} D_2^+/cm^2$ and $1.9 \times 10^{14} 0^+/cm^2$, (3) the amorphous regions merge to form a continuous band below the implanted surface at doses of about $3.0 \times 10^{16} D_2^+/cm^2$ and $5.7 \times 10^{14} 0^+/cm^2$, and (4) this band expands to the implanted surface at larger doses. Amorphization is caused by implantation with oxygen, but prior implantation with deuterium sensitizes the lattice by increasing the strain.

If the samples were annealed subsequent to amorphization, they were observed to recrystallize. The crystallization process was found to evolve in three separate stages: (1) small crystallites, about 10 nm in size, form throughout the entire amorphous band after annealing for 30 min at $350^\circ C$, (2) larger crystallites nucleate and grow from the implanted surface and amorphous/crystalline interface after annealing for one hour at $450^\circ C$, and (3) these crystallites grow in size until they merge to form a continuous polycrystalline layer. Some epitaxial regrowth of the monocrystalline into the amorphous region is also observed.

For a more detailed report of these findings and a discussion of their relationship to the magnetic characteristics of these films, the reader is referred to the papers entitled "Investigation of Amorphization and Crystallization Processes in Ion-Implanted Garnet by Transmission Electron Mircroscopy," by T. Yoshiie, C. L. Bauer and M. H. Kryder (to be published in J. Appl. Phys., 1985) and "Amorphization of Garnet by Ion Implantation," by A. M. Guzman, T. Yoshiie, C. L. Bauer and M. H. Kryder, Mat. Res. Soc. Symp. Proc., Vol. 27, 139(1984).

3.3. A Theoretical Study of the Magnetization Configuration Near Boundaries Between Implanted and Unimplanted Regions of Magnetic Garnets

In ion implanted contiguous disk magnetic bubble devices, the bubbles are propagated by highly polarized domain walls known as "charged walls," which move along the edges of ion-implanted patterns in response to a rotating in-plane field. These walls form as a result of magnetostrictive anisotropies caused by implantation induced stress [M. H. Kryder and D. A. Saunders, IEEE Trans. Magnet. MAG-15, 1817 (1981)]. During this past year a model has been developed to describe these magnetostrictive anisotropies and their effects on charged wall formation and propagation.

The model shows that stress relaxation in the vicinity of an implantation edge decreases with distance from the edge with an exponential decay length of approximately 4t, where t is the implanted layer thickness. Stress perpendicular to the film surface and shear stresses are significant near the implantation boundary, but decrease quickly with decay lengths of approximately 0.8t and 0.6t, respectively. The perpendicular and shearing stresses cause an anisotropy under the edge of the implantation mask which favors planar magnetization. This previously unreported effect was found to be larger in materials having large anisotropic magnetostriction. Also, due to the large perpendicular and shear stresses, the anisotropy in the implanted region near the mask edge is found to favor perpendicular magnetization, causing an effective outward shift of the mask edge. The shift is on the order of 2.5t for a material with $\lambda_{111} = -\lambda_{100}$. The anisotropy distribution near a beveled mask edge indicates that the beveling causes a poorly defined edge to the region of in-plane anisotropy.

For a more detailed report of this work see the report entitled "Charged Wall Formation in Ion Implanted Garnets" by D. A. Saunders and M. H. Kryder or the paper entitled "Stress Gradients and Magnetoelastic Anisotropies at Implantation Edges in Ion-Implanted Garnet Films" by D. A. Saunders and M. H. Kryder presented at the Magnetism and Magnetic Materials Conference, San Diego, Nov. 27-30 (1984), which is to be published in the Journal of Applied Physics (1985).

4. Microfabrication of High Density Magnetic Bubble Devices

Although the major emphasis of our research has been on ion-implanted contiguous disk technology, we have placed modest resources on the development of current access technology because of its capabilities for high data rate and for performing logic in addition to memory functions. The work on current-access bubble logic is supported under NSF Grant ECS-8319769, but reported here because it complements the work under AFOSR Grant 84-0341. A hybrid technology combining the performance features of current-access with the high density of ion-implanted contiguous-disk devices was developed under AFOSR Grant 84-0341 and progress on it is also reported in this section.

4.1. Microfabrication of Ion-Implanted Contiguous Disk Devices

Ion implanted contiguous disk devices are considered to be the most likely successor to the permalloy technology now in production. They offer order of magnitude higher bit densities and significantly lower rotating drive fields than permalloy devices with equivalent photo lithographic resolution. Under this research program we have been pursuing the microfabrication of devices using 1.0μm and 0.5μm diameter bubbles. Our main emphasis during this past year has been on obtaining reliable propagation of 0.5μm diameter bubbles in 2.0 to 2.5μm device cells, although full chip designs with generation, transfer and detection have also been evolved for 1μm diameter bubbles.

To optimize the propagation of 0.5μm diameter bubbles, a large variety of propagation patterns were designed and tested with a variety of ion implantation dosages and energies. Using knowledge gained from our studies of the effects of ion implantation on garnet (section 3.1), and empirical optimization of margins, we demonstrated 11% and 9% bias margins and a 50 Oe minimum drive field for quasistatic 2.5μm period and 2.0μm period propagation patterns, respectively. These margins are thus comparable to the margins of the 8μm period permalloy devices presently being manufactured.

For a more detailed description of our work on ion implanted contiguous disk devices see the report entitled "Contiguous Disk Magnetic Bubble Memory Devices" by S.C.Jo and M. H. Kryder.

4.2. Microfabrication and Operation of Current-Access Bubble-Logic Devices

As noted above current-access technology offers order of magnitude higher data rates than either field-access permalloy technology or ion-implanted contiguous-disk devices. High on-chip power dissipation limits its utility for large chips [M. H. Kryder, IEEE Trans. Magnet. MAG-17, 2392 (1981)]; however, we believe that small amounts of current-access bubble logic circuits can be used on field access memory chips to provide substantial improvements in chip performance and functionality [R. L. Smith, et al., IEEE Trans. Magnet., MAG-19, (1983); M. H. Kryder and D. E. Thomas, "Magnetic Bubble Technology: Status and Future," Proc. of Int. Conf. on Comp. Design, Port Chester, NY, p. 328, Oct. 31-Nov. 3, 1983; J. P. Hwang et al., IEEE Trans. Magnet., MAG-20, 1096 (1984)]. Perforated-sheet current-access technology is well suited for bubble logic because there is no magnetic overlayer, as in permalloy or ion-implanted devices, to interfere with bubble interactions.

During this past year bubble logic gates based on bubble-bubble interactions were fabricated and demonstrated. A computer model previously developed [D. Shenton et al., IEEE Trans. Magnet., MAG-17, 2677(1981)], was refined and shown to provide qualitative agreement with the experimental data on the margins of operation for these gates. An important finding was that dynamic gyrotropic deflection of the bubbles from the gradient field direction significantly affects the performance of the gates. This gyrotropic deflection must be taken into account in the model to provide agreement with the experimental

data and also must be taken into account in the design of gates to obtain large operating margins.

For a more extensive description of this work the reader is referred to the attached report entitled "Current-Access Perforated Sheet Magnetic Bubble Logic Devices" by R. L. Smith and M. H. Kryder. A paper describing this work is being submi ʒd to the 1985 Intermag conference.

4.3. Microfabrication of Current-Access Ion-Implanted Magnetic Bubble Devices

The current-access ion-implanted bubble device structure is a novel structure developed under AFOSR Grant 84-0341 which combines the high bit density of ion-implanted contiguous-disk devices with the high performance of current-access devices. During this past year a reliable process for the microfabrication of these devices was developed. This included, but was not limited to: conductor deposition and etching, very high resolution photolithography and a pad build-up procedure that required the development of a lift-off process.

Testing of the devices was delayed by difficulties in obtaining good magneto-optic images of the 1μm domains and by requirements for a high current driver for the low impedance conductor sheets used in the device. The difficulties in observing the 1μm domains was solved by using an improved polarized light microscope, and a high current driver has been designed and is now under construction.

For a detailed description of this work see the report entitled "Current-Access Ion-Implanted Magnetic Bubble Devices" by M. Alex and M. H. Kryder.

5. Attachments

1. R. O. Campbell and M. H. Kryder, "Liquid Phase Epitaxial Growth of Garnets"

2. C. S. Krafft, "Deuterium Implantation in Magnetic Garnets," Ph.D. Thesis, Carnegie-Mellon University, September 5, 1984.

3. C. S. Krafft, M. H. Kryder and J. O. Artman, "Annealing Behavior of Deuterium Implanted Garnet Films," IEEE Trans. Magnet., MAG-20, 1111 (1984).

4. C. S. Krafft and M. H. Kryder, "Temperature Dependence of Anisotropy Fields in Deuterium Implanted Garnet Films," J. Appl Phys. 55, 2557 (1984).

5. A. M. Guzman, T. Yoshiie, C. L. Bauer and M. H. Kryder, "Amorphization of Garnet by Ion Implantation," Mat. Res. Soc. Symp. Proc., vol. 27, 139 (1984).

6. T. Yoshiie, C. L. Bauer and M. H. Kryder, Investigation of Amorphization and Crystallization Processes in Ion-Implanted Garnet by Transmission Electron Microscopy," to be published in J. Appl. Phys. (1985).

7. D. A. Saunders and M. H. Kryder, "Charged Wall Formation in Ion-Implanted Garnets"

8. D. A. Saunders and M. H. Kryder, "Stresses and Magnetoelastic Anisotropies at Implantation Edges in Ion-Implanted Garnets," paper AD-07, Magnetism and Magnetic Materials Conference, San Diego, Nov. 27-30, 1984; to be published in J. Appl. Phys., April 1985.

9. S. C. Jo and M. H. Kryder, "Contiguous Disk Magnetic Bubble Memory Devices"

10. R. L. Smith and M. H. Kryder, "Current-Access Perforated Sheet Magnetic Bubble Logic Devices"

11. M. Alex and M. H. Kryder, "Current-Access Ion-Implanted Magnetic Bubble Devices"

Deuterium Implantation in Magnetic Garnets

Charles Stuart Krafft

5 September 1984

Table of Contents

List of Figures

List of Tables

Deuterium Implantation in Magnetic Garnets

ABSTRACT

The effects of deuterium ion implantation in magnetic garnet epitaxial films were studied using ferromagnetic resonance (FMR) and X-ray diffraction characterization techniques. A range of deuterium implant doses, including those which could be used in submicron-diameter contiguous disk bubble devices, were investigated. The magnetostrictive portion of the total uniaxial anisotropy field change and its temperature dependence, from $0°C$ to $200°C$, were determined using FMR and X-ray diffraction techniques. The FMR measurements were done at different frequencies in the 2 to 8 GHz range, thus minimizing the uncertainty in determining parameters. The magnetostriction was determined in both the bulk and implanted layers of the epitaxial film. The deuterium results are compared to those for hydrogen and oxygen implants.

The magnetic properties of deuterium implanted films became increasingly degraded for doses which were above approximately 1×10^{16} D_2^+/cm^2 at a nominal energy of 40 keV. However, films which were coated with SiO_2 prior to implantation exhibited remarkably better properties, as evidenced by the lack of degradation in the FMR signal, than the films which were left uncoated. The use of multiple species implants to achieve a uniform strain profile was found to result in a non-uniform anisotropy profile due to the difference in the implant mechanisms for deuterium and oxygen.

The magnetostrictive field in deuterium and hydrogen implanted films was found to account for only 1/3 to 1/2 of the total implantation-induced change in the uniaxial anisotropy field ΔH_E, even after the films have been annealed up to $800°C$. A sudden change in the ΔH_E, and a change in the FMR spectra which is related to the desorption of the deuterium (hydrogen), was observed after a $250°C$ anneal in uncoated films. In SiO_2 coated films, the desorption threshold was approximately $450°C$. The gyromagnetic ratio was reduced in films with high dose deuterium implants, but was restored upon annealing at relatively low temperatures ($250°C$). A reduction in λ_{111}/M_s was also observed. The temperature dependence of ΔH_E and ΔH_σ were

measured from 0 to 200°C. There was a significant reduction in the Curie temperature in the most heavily damaged region of the deuterium and oxygen implanted films at higher temperatures. In oxygen implanted films, ΔH_{σ} was greater than 70% of ΔH_E, indicating that magnetostriction accounts for most of ΔH_E.

ACKNOWLEDGEMENTS

List of Symbols

A	Exchange constant
(B) and (I)	Note that the (B) and (I) suffixes on any symbol refer to the bulk or nonimplanted and implanted layers respectively.
D_2	Molecular deuterium
E	Young modulus
F	Stress averaging factor
H_1	Cubic crystalline anisotropy field
H_k	Uniaxial anisotropy field = $2K_U/M_s$
$H_E(B)$	Effective anisotropy field in the bulk (= $H_k - 4\pi M_s - (2/3)H_1$)
$H_E(I)$	Effective anisotropy field in the implanted layer
H_{un}	Field for uniform resonance
K_U	Uniaxial anisotropy energy density
M_s	Magnetization
Q	Quality factor = $H_k/4\pi M_s$
R_r	Projected ion range
T	Wafer thickness
T_G	Growth temperature
U	Strain uniformity = $(\epsilon_{max} - \epsilon_{min})/\langle \epsilon \rangle$
a	O-ring radius
f	Microwave frequency = $\omega/2\pi$

l	Characteristic length
p	Vacuum suction
t	Epitaxial film thickness
w	Wafer deflection induced by vacuum suction
α	Gilbert damping parameter
a	Thermal expansion coefficient
γ	Gyromagnetic ratio
ΔH	FMR peak-to-peak absorption derivative linewidth
ΔH_{fwhm}	FMR absorption full-width at half maximum linewidth
ΔH_E	Implant-induced change in the effective anisotropy field (= $H_E(B)$ − $H_E(I)$)
ΔK	Implant-induced change in the uniaxial anisotropy energy density (=$\Delta H_E \cdot 4\pi M_s / 8\pi$)
$\Delta K_{as\ ii}$	ΔK for as-implanted sample
ΔK_{ann}	ΔK for 200°C annealed film
δ_W	Wall width
ΔH_σ	Magnetostrictive field (= $3\ \sigma\lambda_{111}/M_s(I)$)
δH_{111}	Vacuum-stress induced resonant field shift
Δa	Lattice mismatch = $a_{substrate}$ − a_{film}
ϵ_{max}	Maximum implant-induced strain
ϵ_{min}	Minimum implant-induced strain (Surface strain)
$\langle\epsilon\rangle$	Average implant-induced strain
ν	Poisson ratio
θ_B	Bragg angle for x-ray diffraction
λ_{111}	Magnetostriction coefficient

$\lambda_{111}/M_s(B)$	Magnetostriction coefficient divided by magnetization in the bulk layer
$\lambda_{111}/M_s(I)$	Magnetostriction coefficient divided by magnetization in the implanted layer
σ_W	Wall energy
σ	Maximum implant-induced stress
σ_v	Vacuum-induced stress
σ_{max}	Maximum stress induced by wafer deflection
ω	Microwave angular frequency
$4\pi M_s$	Saturation magnetization
$2\pi M_s^2$	Demagnetization energy density

Chapter 1
INTRODUCTION

Ion implantation has been widely used to modify the magnetic anisotropy in the surface layers of magnetic garnet films. While the mechanisms of the anisotropy field change are moderately well described by magnetostrictive effects in films implanted with ions such as neon and oxygen, the results from hydrogen implanted films indicate that other mechanisms play an equally important role. In this thesis, the effects of deuterium implantation in magnetic garnet films were investigated. The goal of this research was to increase the understanding of the mechanisms responsible for the anisotropy field change in deuterium (hydrogen) implanted magnetic garnet films.

1.1. BACKGROUND

Magnetic bubbles are cylindrical domains in an appropriate thin film which have a magnetization direction perpendicular to the plane of the film, and reversed from that in the surrounding area. In a bubble material, with no external fields applied, the film will be in a demagnetized state, as indicated by the maze pattern shown in Fig. 1-1. The light and dark areas in Fig. 1-1 represent magnetic domains with oppositely directed magnetization. In Fig. 1-2 a field has been applied such that the domains with magnetization oriented in the direction of the applied field expand at the expense of those which are oriented anti-parallel. In Fig. 1-3, a bubble domain is shown. The bubble domain will exist over a range of bias fields, as determined by the bubble stability criteria [2]. The bubble is surrounded by a domain wall, which is the region between the areas of oppositely directed magnetization. The wall width δ_w, is given by $\pi(A/K_U)^{\frac{1}{2}}$ where A is the exchange constant and K_U is the anisotropy energy density. The exchange energy will be minimized as the wall expands, while the anisotropy energy will be minimized as the wall shrinks. For the magnetization to orient perpendicular to the plane of the film, it is necessary to induce a uniaxial anisotropy energy density K_U, which is sufficient to overcome the demagnetization energy density $2\pi M_s^2$. The wall energy σ_w, is given by $4(A K_U)^{\frac{1}{2}}$. The ratio of the wall energy to the demagnetizing energy is used to define a characteristic length l which is given by
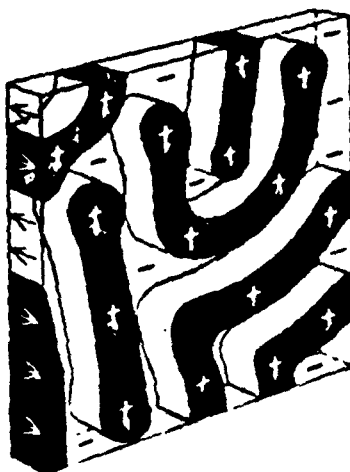
Fig. 1-1: Demagnetized State of Garnet Material with no Field Applied [1]
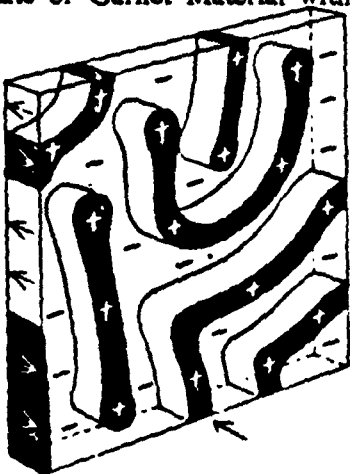
Fig. 1-2: Magnetic Bubble Material with External Field Applied
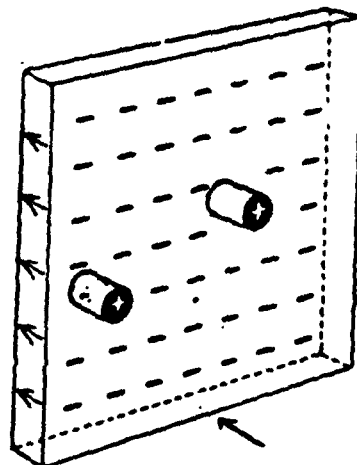
Fig. 1-3: Magnetic Bubble Domain

$$l = \frac{\sigma_w}{4\pi M_s^2} = \frac{(A\ K_U)^{\frac{1}{2}}}{\pi M_s^2} \qquad (1.1)$$

. In the presence of an external field which is antiparallel to the direction of the magnetization in the bubble, the bubble domain will collapse at high field and stripeout from a circular to an elliptical domain at low field. The range of applied field is determined from the minimization of the wall, demagnetization, and applied field energies [2].

Magnetic garnets were found to be an appropriate material for bubbles, since there is a growth-induced K_U as a result of the liquid phase epitaxial growth process [3]. The general structural formula for an oxide garnet is $\{C_3^{3+}\}\ [A_2^{3+}]\ (D_3^{3+})\ O_{12}$, where $\{C\}$ stands for the three dodecahedral lattice sites, [A] stands for the two octahedral sites, and (D) stands for the three tetrahedral sites. The garnet film parameters are tailored by adjusting the rare-earth ions in the dodecahedral sites to get the desired uniaxial anisotropy, and magnetostriction, as well as other parameters. The magnetization is controlled primarily by diluting the iron in the tetrahedral sites with Ga, Al, Ge, etc. The melt compositions and material parameters for the films used in this thesis are given in the appendices.

1.2. BUBBLE MEMORY DEVICES

In a magnetic bubble memory device, the presence or absence of a bubble is used as the basis for the binary encoding of data. In the design of a bubble memory device, it is necessary to control movement of the bubbles. This is done in today's manufactured devices by using the fields created by permalloy patterns. The permalloy patterns are photolithographically defined on top of the bubble layer. An early permalloy pattern design which was used to propagate the bubbles is shown in Fig. 1-4. With an appropriate bias field, indicated as H_B in Fig. 1-4, bubbles will exist in the bubble film. An in-plane field H_{ip} is used to create a potential well at one end of the permalloy pattern which will attract the bubble. As the in-plane field is rotated, the bubble will be attracted to the alternate ends of the permalloy patterns and be propagated from one pattern to the next, as indicated in the sequence shown in Fig. 1-5.

The architecture for a typical bubble memory chip, shown in Fig. 1-6, consists of a series of propagation elements which are organized into minor loops. The minor loops are connected to a major loop using current activated transfer gates. The bubble
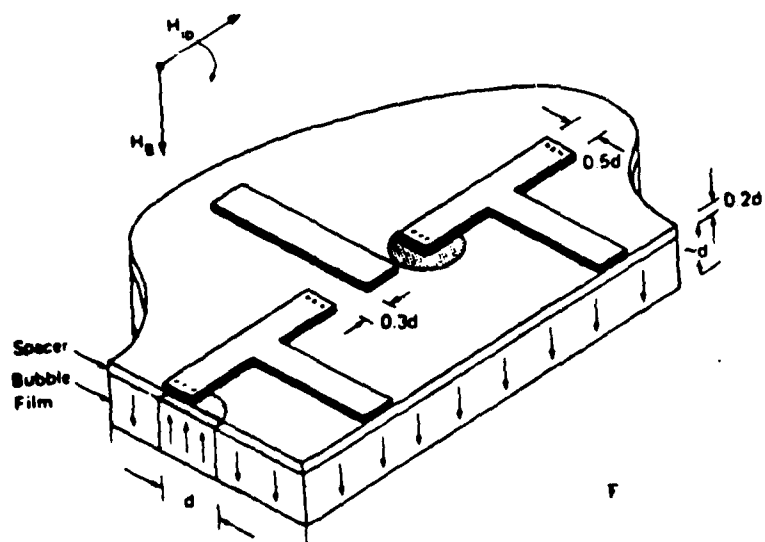
Fig. 1-4: Permalloy Propagation Patterns
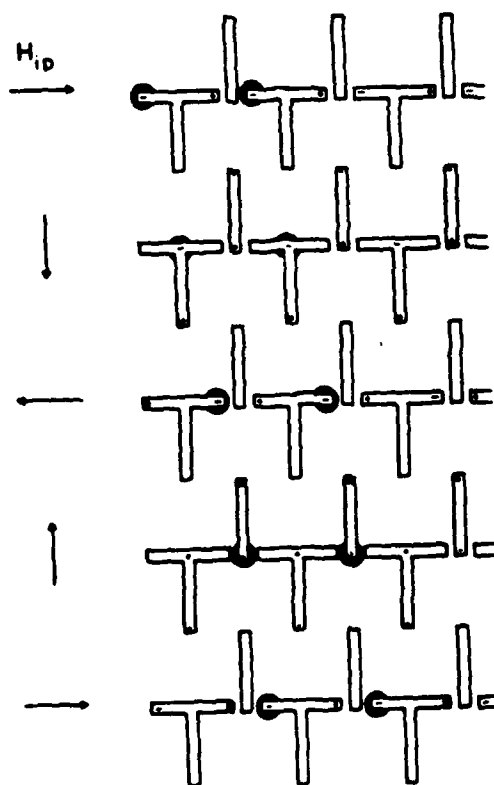
Fig. 1-5: Bubble Propagation Using TI Patterns

transfer into and out of the minor loops is achieved by applying a field with an external current in an overlying conductor. With the major and minor loops, the transfer functions, and generation and detection elements, the basic bubble memory device is realized.
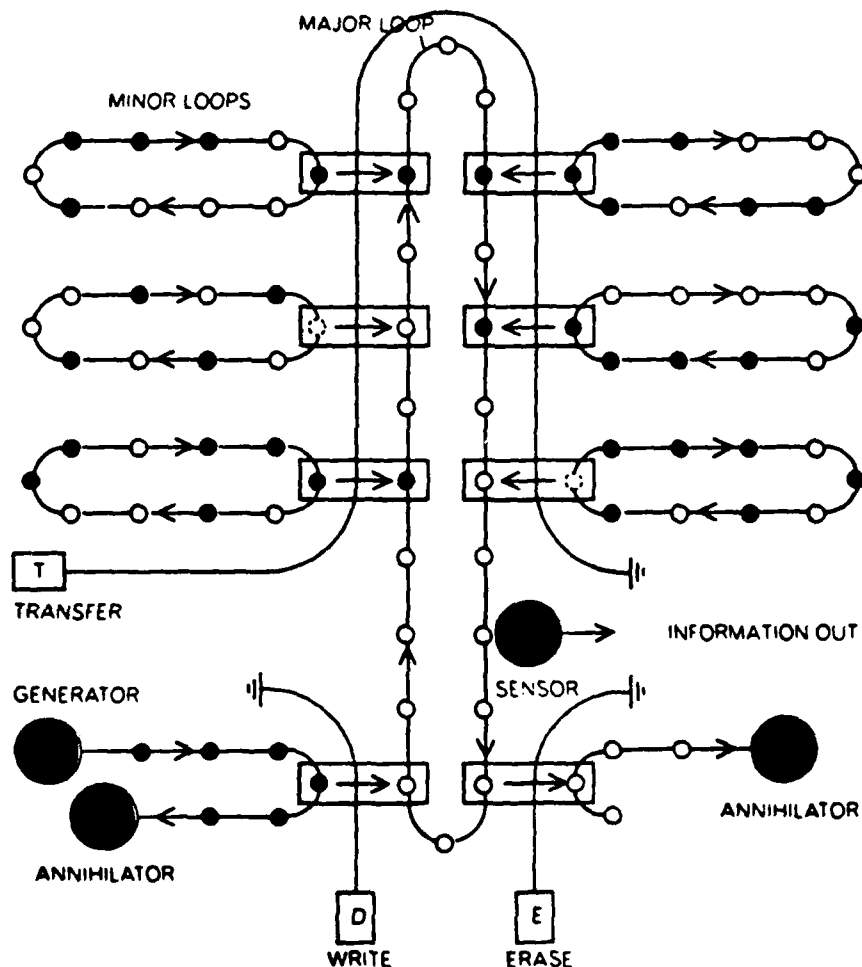
Fig. 1-6:   Bubble Memory Device with Major-Minor Loops [1]

Contiguous disk bubble devices are designed with the same major-minor loop layout as the permalloy devices, however the bubble propagation mechanism is different. In a contiguous disk device the propagation patterns are photolithographically defined on top of the bubble film, as shown in Fig. 1-7. A layer with in-plane magnetization is created in the surface of the bubble film which will support magnetically charged walls. Details of the mechanism for creating the in-plane magnetization using ion implantation will be discussed later. It is energetically more favorable for the bubbles to exist under

the implanted region, due to the flux closure provided by the layer with in-plane magnetization. Charged walls will form at the pattern boundaries, due to the uniaxial anisotropy produced by stress relaxation [4]. The bubbles in the underlying layer will be attracted to the edge of the propagation patterns by the charged wall with polarity opposite to the top of the bubble. The charged wall will move around an implanted pattern in response to a rotating in-plane field, and thus propagate the underlying bubble. In a contiguous disk bubble memory, disks are placed adjacent to one another to form a contiguous pattern. With appropriate transfer gates from the minor to the major loop, and bubble generation and detection capability, a contiguous disk bubble memory device is achieved.
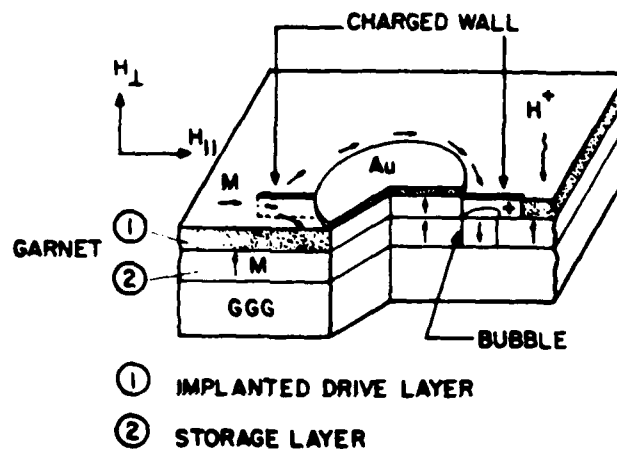
Fig. 1-7: Contiguous Disk Pattern [5]

The contiguous disk technology offers a sixteen fold increase in device density over conventional permalloy bubble devices made with the same lithographic techniques [5], and requires a lower drive field, making it a viable choice as a possible successor to present day permalloy devices.

Ion implantation was originally used in garnet films to suppress hard bubbles [6]. Hard bubbles result from multiple Bloch lines in the domain wall . Bloch lines are a transition region of tight, in-plane rotation of magnetization in a domain wall [5]. The layer with in-plane magnetization provides a means for the Bloch lines in the wall to unwind. Hard bubbles·typically have a significantly higher collapse field, due to the contribution of the Bloch lines to the wall energy, which includes a magnetostatic energy due to the divergence of the magnetization, which is not present in the Bloch wall. As hard bubbles move erratically under the influence of an applied field, they are undesirable in a device.

Submicrometer diameter bubbles are currently being investigated for the next generation of bubble devices. Since the density of permalloy devices is expected to be limited to 4 Megabits/chip, considerable effort has been put into the development of ion-implanted bubble devices in order to achieve a 16 Mbit/chip memory. In materials with smaller diameter bubbles, $4\pi M_s$ is larger, as is the uniaxial anisotropy energy density K_U. In a contiguous disk device, the change in the anisotropy energy required to orient the magnetization in the plane of the film increases as K_U increases. The change in the uniaxial anisotropy energy density ΔK is given by

$$\Delta K = \Delta H_E \times 4\pi M_s / (8\pi) \tag{1.2}$$

where ΔH_E is the change in the effective anisotropy field which is given by

$$\Delta H_E = H_E(B) - H_E(I) \tag{1.3}$$

where $H_E(B)$ and $H_E(I)$ are the effective anisotropy fields in the nonimplanted or bulk, and implanted layer respectively, and

$$H_E = H_K - 4\pi M_s - (2/3)H_1 \tag{1.4}$$

where $H_K = 2K_U/M_s$ is the uniaxial anisotropy field, and H_1 is the cubic crystalline anisotropy field. Thus for submicron diameter bubble devices, materials with higher K_U are required as are implants which produce a large ΔK.

1.3. IMPLANT MECHANISMS

Initially, investigators attributed the implant-induced change in the anisotropy energy ΔK to magnetostrictive effects. The damage caused by the implanted ions strains the lattice. As the expansion of the lattice in the in-plane direction is prevented by the gadolinium gallium garnet (GGG) substrate, which is approximately three orders of magnitude thicker than the implanted layer, the lattice expands perpendicular to the film plane and the implanted surface layer is in a state of lateral compression. The films which were typically used have a negative magnetostriction λ_{111}, which means that they will contract in the presence of an applied field, along the direction of the field. The compressive implant stress will, through the inverse magnetostrictive effect, create a magnetostrictive energy which is given by [7]

$$K_\sigma = -(3/2)\lambda_{111}\sigma\cos^2\phi \tag{1.5}$$

where σ is the stress and ϕ is the direction between the stress and the [111] direction perpendicular to the film plane. When the implant dose is sufficient, so that the sum of the implant induced change in anisotropy energy, which is negative, and K_U, which is positive, are less than the demagnetization energy density $2\pi M_s^2$, the magnetization, which was initially perpendicular to the film plane, will be oriented in the film plane.

In a device, the implant is designed to make the magnitude of the implant-induced anisotropy energy change sufficiently larger than $K_u - 2\pi M_s^2$. Here we have assumed that the cubic crystalline anisotropy is small compared to K_u and can be neglected.

The implantations with ions such as neon and oxygen are used to strain the lattice and create magnetostrictive energy. Provided the implant dose is kept below the level where extensive lattice damage occurs and the garnet is turned paramagnetic or amorphous, the change in the anisotropy energy is well described by the magnetostrictive energy given by Eq. (1.5). In films which have strains above approximately 1.5%, the anisotropy change saturates. This saturation has been attributed to extensive damage in the lattice [8]. The damage is the displacement of the host oxygen atoms from their regular positions in the lattice [9]. The rare-earth ions and iron atoms are also displaced, but to a lesser extent. The displacements of the oxygen ions will break the super-exchange interaction, resulting in a reduction of the magnetization and the exchange interaction. Displacement of the rare-earth ions will destroy the growth-induced anisotropy.

In contrast to the heavier ions such as neon and oxygen, the effects of hydrogen implantation are remarkably different. The ΔK in films implanted with hydrogen (or its isotope deuterium) does not saturate with increasing implant strain [10], and is at least twice as large as ΔK in films with the same strain which were implanted with any other ion. The difference in the mechanism of the hydrogen implant is presumably related to a combination of three factors. First, the hydrogen doses used are typically one to two orders of magnitude higher than those of the heavier ions, even though the implant strains are comparable. Second, hydrogen is both chemically active and extremely mobile. Third, the damage produced by the hydrogen ion collisions produces a more homogenous strain. Matsutera et al. [9] calculated that 90% of the hydrogen collisions bring about an energy transfer of less than 10 eV, which is significantly less than the binding energy of the garnet atoms. Thus, only 10% of the hydrogen collisions generate damage. By comparison, more than 80% of the neon collisons with the garnet nuclei generate damage, with more than 40% of these involving energy transfers greater than 100 eV. Matsutera considered not only stopped ion distribution from the theory of Lindhard, Sharf, and Schiott (LSS) [11], but also took account of the scattering process in order to account for observed differences in the properties of neon and hydrogen implanted films. Whereas most of the energy of the neon ion goes into displacing the host oxygen nuclei, thus creating damage, the energy transferred from the hydrogen ion causes a much smaller displacement of the host nuclei. Most of

the energy of the hydrogen ions is absorbed by lattice vibrations. Therefore, a difference in the scattering cross-sections for neon and hydrogen implants apparently explains the significantly lower damage in hydrogen implanted films.

In hydrogen implanted films, the change in ΔK is not described by magnetostrictive effects alone. Some researchers have suggested that the non-magnetostrictive change in anisotropy is dependent upon the presence of the implanted hydrogen ions and that a sudden reduction in anisotropy is observed when the hydrogen escapes as a result of annealing at elevated temperatures [12]. It was observed that SiO_2 overcoated films did not suffer a sudden change in anisotropy when thermally annealed at moderate temperatures (250°C), and it was suggested that the overcoat inhibited the escape of hydrogen [13]. In both coated and uncoated films, previous investigators have found that the non-magnetostrictive portion of the anisotropy field disappeared when the hydrogen was annealed out of the sample [13, 14]. Results presented here indicate that the non-magnetostrictive effect is still important, even after the films have been annealed above the hydrogen desorption threshold.

Some investigators have suggested that the hydrogen forms metastable compounds [15, 16]. The proposed mechanism for the formation of a hydrogen compound in the garnet with the host iron nuclei is related to the change of the valence of iron from Fe^{3+} to Fe^{2+} during a low temperature (50°C) anneal of the hydrogen implanted film [17]. Chemical effects have not been observed with heavier ions, ostensibly because doses comparable to those used in hydrogen implants would make the garnet amorphous [18, 19].

The annealing behavior of hydrogen implanted films has been studied by several investigators. In films which were not coated with SiO_2, a rapid decrease in the anisotropy field change and the strain were observed after annealing between 200°C and 250°C [12, 15]. This was ascribed to desorption of the hydrogen. In the annealing temperature range from 350–600°C, short range re-ordering of the Fe–O–Fe bond geometry occurs. This is also the origin of strain relief. Above 600°C, long range order is restored. The rare-earth ions which were decoupled from the lattice can migrate back to their initial positions, restoring the growth-induced anisotropy. However, if the garnet is severely damaged during the implantation, the rare-earth ions may not return to their original sites. The preferential decoupling of the rare-earth ions is expected to decrease the as-grown anisotropy and the magnetostriction, but not the magnetization and g factor. In films with a large percentage of FMR relaxer ions,

such as Sm, which broaden the FMR linewidth, the linewidth is expected to decrease when the bonds to the relaxer ions are broken as a result of high dose implantation. However, the damage, which induces general disorder to the garnet structure is expected to increase the linewidth.

Deuterium is especially interesting as an implant species as it, like hydrogen, does not cause ΔK to saturate [20]. However, we will show that at high deuterium doses, the film properties become degraded. Since the ion mass of deuterium is twice that of hydrogen, the damage is twice as great. The nuclear energy loss for deuterium (which is proportional to the damage) is twice that of hydrogen, at the same implant energy. However, since the electronic energy loss is lower for deuterium, the projected range of the implanted ions is greater than that for hydrogen at the same energy. Thus, at an implant energy which will yield the same implanted layer thickness, the nuclear energy loss for deuterium is about 2.4 times that of hydrogen [21]. Since the nuclear energy loss is higher for the same dose and range of deuterium, the relative contribution of the magnetostrictive field is expected to be slightly larger than that in hydrogen implanted films.

While much work has been done to explain the mechanisms of hydrogen implantation, there is still considerable uncertainty with regards to the nature of the additional, non-magnetostrictive contribution to ΔK. In this thesis, ΔK and the magnetostrictive portion of ΔK (ΔK_σ) were measured for a wide range of deuterium implanted films. A comparison to hydrogen implants indicates that behavior reported here for the deuterium implanted films is similar to that observed in hydrogen implanted films.

Recently, investigators reported that treatment of neon implanted films with an argon plasma in a planar reactor can cause ΔK to increase beyond the saturation level [22]. This phenomenon has been attributed to incorporation of hydrogen into the implant damaged layer during the plasma treatment. The hydrogen is present as a residual species in the argon gas. This effect has substantial importance for those involved in device fabrication, as it provides an alternative to using hydrogen or deuterium implants and has the advantage of significantly reducing the implant time. However, since the phenomenon is presumably related to the incorporation of hydrogen into the surface layer, it is important to understand the mechanisms of hydrogen implantation.

In the remainder of this thesis, the characterization techniques which were used are described in Chapter 2. The investigations of the deuterium implanted films, which

constitutes the major portion of this thesis, are reported and discussed in Chapter 3. The effects of hydrogen and oxygen implants are reported in Chapter 4. Chapter 5 contains a summary, conclusions, and suggestions for future research.

Chapter 2
CHARACTERIZATION TECHNIQUES

2.1. INTRODUCTION

In this thesis the mechanisms of ion implantation in magnetic garnet films were investigated using ferromagnetic resonance (FMR) and X-ray diffraction. FMR is used to determine the implant-induced change in the uniaxial anisotropy field and X-ray diffraction is used to measure the implant-induced strain. The magnetostriction may also be determined using FMR techniques [23, 24]. The FMR results were obtained using a wideband resonance spectrometer with a minibox which used a microwave stripline structure. The FMR measurements were made over the temperature range from 0°C to 200°C. From these measurements, the effective anisotropy fields and the magnetostriction in both the bulk and implanted layers of the garnet film were deduced. The X-ray diffraction measurements were obtained using a double crystal X-ray diffractometer.

Previous investigators have used a wide range of techniques to characterize ion-implanted films. The characterizations may be divided into three areas: (1) magnetic, (2) lattice disorder, and (3) impurity profile measurements. The most commonly employed technique for magnetic measurements is FMR. Other techniques include bubble collapse field [25, 26], a.c. susceptibility [27], vibrating-sample magnetometry (VSM) [28, 29], conversion electron Mossbauer spectroscopy (CEMS) [30], and magneto-optics [31]. For lattice disorder, the most commonly employed technique is X-ray diffraction [8, 32, 33]. Other techniques include relative etching rates [26], stress [34], Rutherford backscattering and channelling [35], transmission electron microscopy (TEM), electron diffraction [36], and optical absorption [37]. To measure the impurity profiles, secondary ion mass spectrometry (SIMS) [38] and nuclear reaction [39] have been used.

In both the FMR and X-ray techniques, the analysis of the results from the ion-

implanted films is complicated by the fact that the magnetic anisotropy and strain profiles are not uniform through the thickness of the implanted layer. This results in complicated multiple resonance FMR spectra. In addition, the X-ray rocking curves have multiple diffraction peaks. The anisotropy profile can be determined by matching the experimental spectra to spectra which are calculated from a numerical solution for the spin waves for an assumed anisotropy profile [40]. In a similar fashion, the strain and damage profiles can be determined by matching the experimental rocking curve to that calculated based on an assumed strain and damage profile using X-ray diffraction theory [41, 42]. While both procedures require a significant amount of time and expertise to obtain precise fits, the essential information can be extracted without doing a rigorous analysis. As a verification of this, a rigorous FMR spin wave analysis was done on one of the films. Other FMR results were compared to published results and found to be in good agreement. Several of the X-ray rocking curves obtained here were evaluated by V. Speriosu, who has had extensive experience analyzing rocking curves from ion-implanted garnet films. Other rocking curves were compared to published curves for films with comparable implants and found to be in good agreement. Thus, with confidence, we can relate the FMR spectra and X-ray rocking curves to the anisotropy and strain profiles.

The material parameters of the liquid phase epitaxial (LPE) garnet films were measured prior to implantation using the characterization techniques which are described in the author's Masters thesis [43]. Characterization of the as-grown films included film thickness t, with a scanning wavelength spectrophotometer, and zero-field stripwidth and bubble collapse field, with a polarized light microscope equipped with bias field coils, to determine the magnetization and characteristic length l [44]. The lattice mismatch $\Delta a = a_{substrate} - a_{film}$, where $a_{substrate}$ and a_{film} are the lattice constants of the GGG substrate and LPE film respectively, were determined by double crystal X-ray diffraction. The temperature coefficient of bubble collapse field was measured on selected samples to determine the temperature dependence of $4\pi M_s$ [44].

2.1.1. Ferromagnetic Resonance

For a (111) oriented garnet film, with a magnetic field H, applied perpendicular to the film plane, the ferromagnetic resonance condition is given by [45]

$$\omega/\gamma = H + H_E \tag{2.1}$$

where ω is the microwave frequency, γ is the gyromagnetic ratio, and the effective field H_E is given

$$H_E = H_K - 4\pi M_s - (2/3)H_1 \qquad (2.2)$$

where H_K is the uniaxial anisotropy field, $4\pi M_s$ is the magnetization, and H_1 is the cubic crystalline anisotropy field. Using Eq. (2.1), the resonance field at several frequencies is fit using linear regression, where the slope of the resonance frequency versus resonance field is γ, and the zero-frequency intercept is $(-H_E)$. Typically, the resonance field is measured at three or more frequencies. If the field is applied at an arbitrary angle, the resonance condition will in general be more complicated since the magnetization in the sample may not be aligned with the applied field. The resonance condition can be obtained from the solution of the free energy equation for the garnet film, taking into account the difference in the direction of magnetization and the applied field [46]. This solution will be given later. The H_1 is calculated from the angular dependence of the resonance field [47], using the method developed by Makino et al. [48]. A program was written by X. Wang, and modified by the author, to compute H_1. A description of the solution, a listing of the program, and a trial run are given in the appendices.

2.1.2. Ferromagnetic Resonance Apparatus

·The FMR measurements were done using a wideband microwave spectrometer with a serpentine-shaped microstrip transmission line [49]. The microwave propagation mode is quasi-TEM. The FMR system, shown schematically in Fig. 2-1, consists of the standard apparatus for phase lock detection of the resonance signal. The operational details, and an equipment list of the spectrometer system are given in the appendices. The microwave frequency range which was typically used was from 4.5 to 7 GHz, although frequencies as low as 2 GHz were used occasionally.

The sample is placed in a minibox, which is shown in Fig. 2-2. The stripline is terminated in a short. The reflected signal is directed by the circulator to a diode detector. The serpentine-shaped conductor pattern was used instead of a straight conductor to increase the signal-to-noise ratio so that weak surface modes in thin ion-implanted layers could be detected. Measurements made with both structures yielded the same results. Use of the minibox with the stripline had several advantages over a resonant cavity and other non-transmission resonance structures. These include operation over a wide frequency range, and compatibility with full-wafer garnets. In addition, there are no problems associated with cavity detuning or coupled resonances. In a wideband system, H_E and γ can be determined from the frequency dependence of the resonance field using only perpendicular resonance, which improves the accuracy since results of measurements at several frequencies can be averaged.
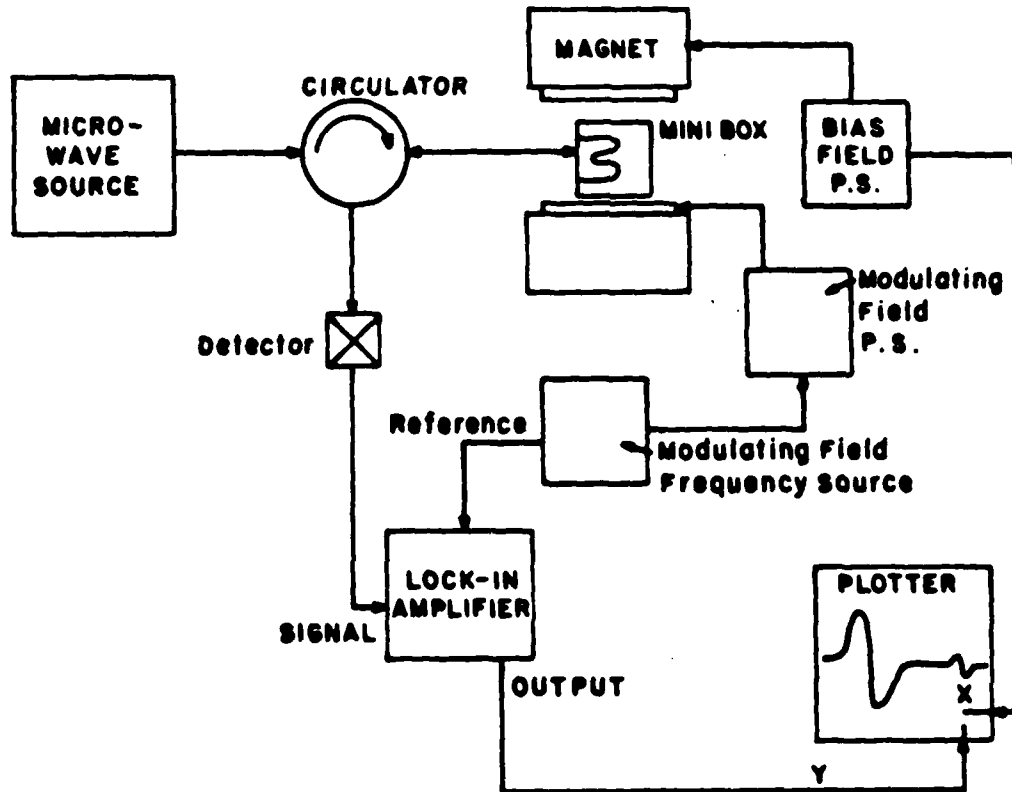
Fig. 2-1:   FMR Apparatus
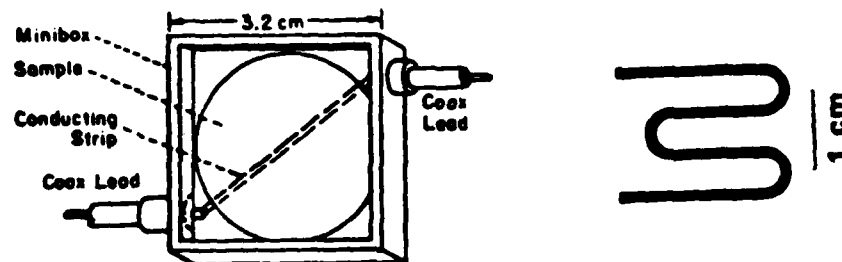
Fig. 2-2:   Minibox used in FMR Measurements

To establish the validity of measurements which were obtained using the wideband spectrometer, a film was measured in the minibox, and then diced into 7 × 8 mm chips, one of which was measured in the cavity. The H_E and γ were calculated using linear regression analysis from the frequency dependence of perpendicular resonance from 4 to 7.5 GHz. From the linear regression fit, the resonance field at the cavity frequency (9.36 GHz) was calculated to be 2836 Oe. The measured resonance field was

2826 Oe. Thus the agreement between the cavity and the minibox is quite good. As the cavity was not set up for high temperature or magnetostriction measurements, all of the results reported here were obtained with the minibox.

The ion-implanted layer will typically support several spin wave modes. The spin wave modes may either extend through the entire thickness of the implanted region or be localized in separate layers. The total width of the spin wave spectra for modes which extend through the entire implanted region is given by

$$H_{un} - \omega/\gamma \qquad (2.3)$$

where H_{un} is the field for uniform resonance of the layer with in-plane anisotropy. For applied fields less than $H_{un} - \omega/\gamma$, the resonance modes may not be observed since the applied field is not sufficient to align the magnetization in the region with the maximum anisotropy field change [50]. An example of this is shown in Fig. 2-3. Thus there is an inherent limitation with the use of lower frequencies to measure films with a large in-plane anisotropy.
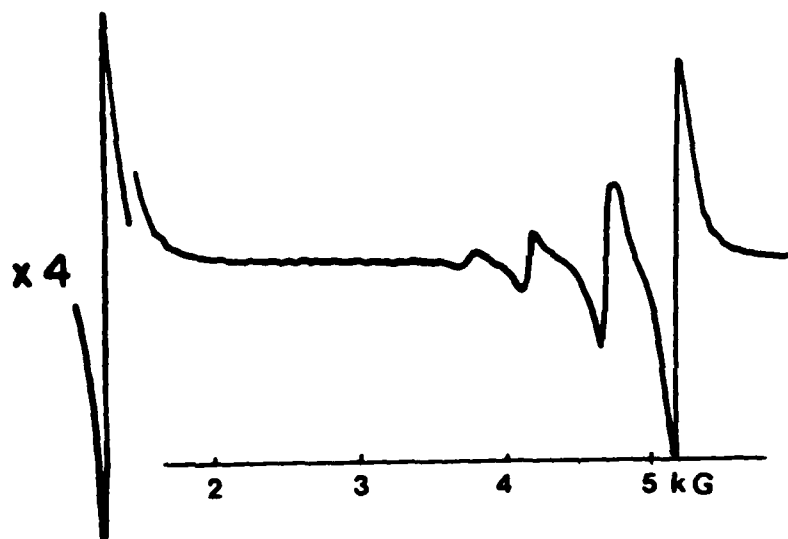
Fig. 2-3: Resonance Spectra for an Implanted Film, f = 4.5 GHz

The spectra shown in Fig. 2-3 are for Film 84 and were measured after the film had been annealed at 200°C. The properties and the implant conditions for film 84 will be discussed in Chapter 3. Here, the ω/γ is 1823 Oe (f = 4.5 GHz) and the H_{un} is 5361 Oe. The surface spin wave modes extend from 5361 to 3885 Oe, which is 1476 Oe below H_{un}. As will be shown later, modes with amplitudes comparable to the fourth surface mode are expected at fields less than 3885 Oe, based on the numerical spin wave analysis; however, they are not observed experimentally since the magnetization in

the region of the maximum anisotropy field change is not aligned with the applied field. The width of the envelope of the surface modes will increase with frequency, however H_{un} will also increase, which may pose a practical problem for measurement in films with a large in-plane anisotropy, due to the field limitation of the magnet which is used. As a consequence, the numerical spin wave analysis will be complicated by the fact that not all of the calculated modes are observed experimentally, which increases the uncertainty in determining the anisotropy profile.

A nichrome wire heater, attached to the minibox, was used to heat the sample up to 200°C. Sample temperature during a series of measurements was typically held to within ± 1°C, as determined by measuring the temperature inside the minibox with a type S (Pt-Pt10%Rh) thermocouple. Nitrogen gas, cooled by passing it through copper coils immersed in liquid nitrogen, could be blown into the minibox to cool the sample to approximately -10°C. Nitrogen or compressed air were also used to cool the minibox after high temperature measurements, which decreased the total time required to complete a series of measurements over the entire temperature range.

2.2. MAGNETOSTRICTION MEASUREMENT

The technique for measuring the magnetostriction using the wideband spectrometer and the minibox was developed as part of this project [49]. We were the first investigators to report on the use of a wideband spectrometer to measure the magnetostriction in garnet films. Magnetostriction measurements on LPE garnet films using a milliscoop cavity have been reported by previous investigators [51]. The milliscoop cavity consists of a rectangular TE_{102} cavity with a hole in the wall of the cavity. The sample is placed outside the cavity. The resonance is excited in that portion of the sample which is facing the hole. Hoekstra et al. [51] stressed the film using a screw to displace the middle of a rectangular sample which was supported at two of the ends. Vella-Coleiro reported on the use of a shorted wave guide, with the sample placed in front of the short [52]. The film was placed under compressive stress with vacuum suction.

Here, the magnetostriction divided by the magnetization λ_{111}/M_s, was determined from the resonant field shift δH_{111} in a film which was placed in compression by bowing it over an O-ring with vacuum suction [52, 49]. To avoid the problem of the resonant field shift from the backside film interfering with the film on the front side of the GGG substrate, the backside film was etched off prior to the magnetostriction measurement. A cross section of the apparatus used to measure the magnetostriction is

shown in Fig. 2-4. The vacuum attachment used to flex the wafer was an integral part of the minibox, as it served as the ground plane. The alumina substrate was supported at its edges so that there was an air gap between the alumina and the back of the minibox. A polytetrofluoroethylene (teflon) O-ring supported the wafer. Vacuum grease was used to prevent the wafer from slipping off the O-ring and to improve the vacuum seal. The stress calibration and the techniques used in determining the magnetostriction up to 200°C will be discussed later.
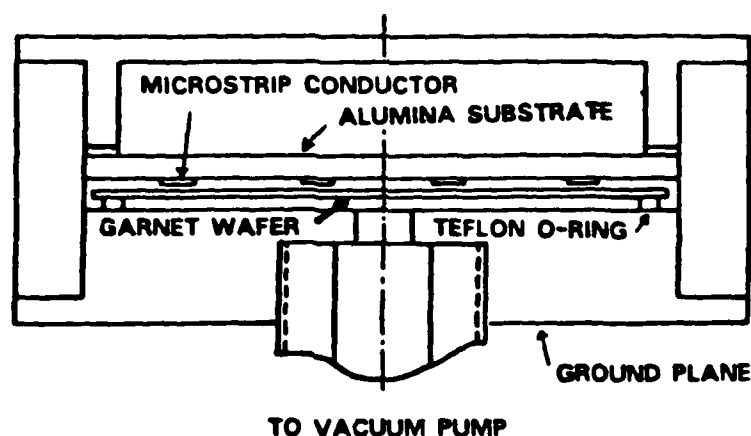
Fig. 2-4: Cross Sectional View of Minibox used for Magnetostriction Measurement

The method employed here had advantages over previously used techniques which included ability to make repeated measurements quickly, so that slight temperature variations could be accounted for by measuring the resonance field in the unstressed film both before the vacuum suction was applied and after it was released without moving the sample from the magnet. This is important since the temperature dependence of the resonance field was as large as 40 Oe/°C in the implanted layer in some of the films which were measured.

The magnetostrictive effect is calculated by considering the contribution it makes to the total free energy. The free energy is given by:

$$(2.4)$$

$$E = - M_s \cdot H + (K_U - 2\pi M_s^2)\sin^2\theta + K_1(\alpha_x^2\alpha_y^2 + \alpha_y^2\alpha_z^2 + \alpha_z^2\alpha_x^2)$$

$$+ (3/2)\ \sigma\ \lambda_{100}(\alpha_x^2\gamma_x^2 + \alpha_y^2\gamma_y^2 + \alpha_z^2\gamma_z^2)$$

$$+ 3\sigma\ \lambda_{111}(\alpha_x\alpha_y\gamma_x\gamma_y + \alpha_y\alpha_z\gamma_y\gamma_z + \alpha_z\alpha_x\gamma_z\gamma_x)$$

where $M_s \cdot H$ is the Zeeman energy, (H is the applied field and M_s is the magnetization), K_1 is the cubic magnetocrystalline anisotropy energy density (the α 's

are the direction cosines of the magnetization), and the terms with λ_{100} and λ_{111} are the stress-induced magnetostrictive energy densities (the γ 's are the direction cosines of the uniaxial compressive stress). The K_1 crystalline anisotropy terms, in spherical polar coordinates will be given in the appendix in the discussion of the H_1 calculation, but will be neglected here for clarity, since they do not have a significant effect on the magnetostriction calculation. The resonance condition is determined by finding the minimum energy conditions, using the following equation

(2.5)

$$(\omega/\gamma)^2 = \frac{1}{M_s^2 \sin^2\theta} \left[\frac{\partial^2 E}{\partial\theta^2} \frac{\partial^2 E}{\partial\phi^2} - \left(\frac{\partial^2 E}{\partial\theta\partial\phi}\right)^2 \right]$$

While the general solution to Eq. (2.5) is rather complicated, it can be simplified by choosing the applied field along the (110) plane. Under this condition, the magnetization and applied field will both lie in this plane. In the solution, for E without the stress energy terms, $\partial E/\partial\phi = 0$ will hold for $\phi = 0$. The magnetostrictive energy terms in spherical polar coordinates are given by [4]

(2.6)

$$E = [\sigma_x \tfrac{1}{4}(5\lambda_{111} + \lambda_{100}) + \sigma_y\tfrac{1}{4}(\lambda_{111}-\lambda_{100}) - \sigma_z(\tfrac{3}{2}\lambda_{111})]\cos^2\theta$$

$$+ \tfrac{1}{2}(2\lambda_{111}+\lambda_{100})(\sigma_x-\sigma_y)\sin^2\theta\cos^2(\phi-\psi)$$

$$+ (2)^{1/2}/4 \ (\lambda_{111}-\lambda_{100})(\sigma_x-\sigma_y)\sin2\theta\cos[(\phi-\psi)+3\psi]$$

$$+ (2)^{1/2}/2 \ (\lambda_{111}-\lambda_{100})(\sigma_{xz}\sin^2\theta\sin[2(\phi-\psi)+3\psi]$$

$$+ \tfrac{1}{2}(\lambda_{111}+2\lambda_{100})\sigma_{xz}\sin2\theta\sin(\phi-\psi)$$

where θ and ϕ are the polar and azimuthal angles of the magnetization, as indicated in Fig. 2-5, and ψ is the angle of the boundary from the [112] direction. σ_x, σ_y, and σ_z are the stress components along the x, y, and z directions respectively, as defined in Fig. 2-5, and σ_{xz} is a shearing stress.

In the experiment here, the vacuum suction creates in-plane stress components, but $\sigma_z = 0$. To evaluate the shift in the minimum energy condition, note that the terms in Eq. (2.6) which have a $\cos\psi$ or $\sin\psi$ dependence will integrate to zero, so that Eq. (2.6) can be simplified to

(2.7)

$$E = [\sigma_x \tfrac{1}{4}(5\lambda_{111} - \lambda_{100}) + \sigma_y\tfrac{1}{4}(\lambda_{111}-\lambda_{100}) - \sigma_z(\tfrac{3}{2}\lambda_{111})]\cos^2\theta$$

$$+ \tfrac{1}{2}(2\lambda_{111}+\lambda_{100})(\sigma_x-\sigma_y)\sin^2\theta\cos^2(\phi-\psi)$$
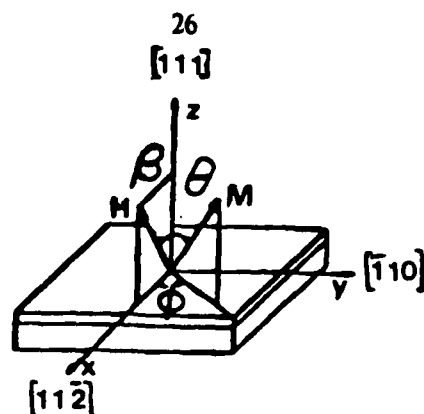
Fig. 2-5: Coordinate System for Eq. (2.6)

which can be further simplified to

$$E = \tfrac{3}{2} [\lambda_{111}[\tfrac{1}{2}(\sigma_x+\sigma_y) - \sigma_z] \cos^2\theta \tag{2.8}$$

Using the expression in Eq. (2.8), the resonance equation can be solved for the stressed film. The relationship between the vacuum-induced shift in the resonance field δH_{111} and the magnetostriction is given by [23, 24]

$$\lambda_{111}/M_s \approx 2/3 \;\; \delta H_{111}/\sigma_v \tag{2.9}$$

where δH_{111} is the shift in the resonant field, and σ_v is the vacuum-suction induced stress. The quantities $\lambda_{111}/M_s(B)$ and $\lambda_{111}/M_s(I)$, where (B) and (I) refer to the bulk and implanted layers respectively, are calculated from the $\delta H_{111}(B)$ of the bulk mode and $\delta H_{111}(I)$ of the principal surface mode.

The serpentine-shaped conductor provided a significant improvement in the signal-to-noise ratio compared to a straight conductor since a larger portion of the sample was coupled to the microwave field. However it had one drawback. The average value of the vacuum stress σ_v over the area of the sample which couples to the microwave magnetic field could not be easily calculated. As σ_v is needed to calculate λ_{111}/M_s using Eq. (2.9), a calibration standard was needed. Since values of λ_{111} and $4\pi M_s$ for $Y_3Fe_5O_{12}$ (YIG) were available in the literature [53], and we were able to obtain a YIG LPE film [54], the stress was calibrated using the YIG film.

2.2.1. Stress Calculation

To relate the average stress determined using the YIG wafer to that on other films, the maximum stress in the film was calculated. The radial and tangential stress, σ_r and σ_t are given by [55]

$$\sigma_r = \frac{2ETw(3+v)(a^2-r^2)}{[(5+v)(1-v)a^4]} \qquad \sigma_t = \frac{2ETw\langle(3+v)a^2-(1+3v)r^2\rangle}{(5+v)(1-v)a^4} \tag{2.10}$$

where E is the Young modulus, 2.08×10^{12} dynes/cm^2 for GGG, and ν is the Poisson ratio, 0.29, w is the deflection at the center of the wafer, a is O–ring radius, and T is wafer thickness. Evaluation of Eq. (2.10) at the center of the wafer (r=0) gives the maximum stress in the film

$$\sigma_{max} = \frac{4ETw(3+\nu)}{(5+\nu)(1-\nu)a^2} = \frac{3\ [3+\nu]\ qa^2}{4T^2} \tag{2.11}$$

where q is vacuum suction in dynes/cm^2. The deflection at the center of the wafer is given by [55]:

$$w = \frac{3(5+\nu)(1-\nu)qa^4}{16ET^3} \tag{2.12}$$

The O–ring radius was calculated using Eq. (2.12) and compared to the value which was measured with a set of calipers. Results for the O–ring radius measurement, determined from the wafer deflection, are summarized in Table 2–1. For a=1.08 cm, the calculated radius is in reasonable agreement with the measured radius. For larger a, the calculated radius was larger than the measured radius. This may be attributed to slight dilation of the O–rings when the vacuum suction is applied. The larger radii O–rings have the potential advantage of improving the accuracy by increasing the magnitude of δH_{111}. However, variations in δH_{111} which exceeded 20% were observed with the largest radii O–ring under presumably identical conditions. Problems with reproducibility of δH_{111} eventually led to the standardization of the O–ring radius at 1.08 cm. Other investigators who have used the vacuum suction technique calculate the stress by measuring the deflection at the center of the wafer before each measurement [56]. Here, results on the a=1.08 cm O–ring were reproducible within uncertainty of δH_{111}, so the wafer deflection did not need to be measured before each δH_{111} measurement. For all the O–rings, the maximum wafer deflection was less than 1/10 of the wafer thickness, which validates the assumption that the deflection is proportional to q/T^3, as indicated in Eq. (2.12). For larger deflections, the stress calculation is significantly more complex [55].

The resonant field shift was measured as a function of vacuum suction and found to increase linearly. Results for three films, including the YIG film, are plotted in Fig. 2–6. Film 172 was measured in compression, and then in tension after the wafer was

Table 2-1:   Calibration Of O-ring Radius from Wafer Deflection

Vacuum Suction 9.33×10^5 dyn/cm^2 = 70 cm Hg

Wafer Thickness 0.0523 cm

Measured Deflection	O-ring Inner Radius	Calculated
.0031 (cm)	1.08 (cm)	1.09 (cm)
.0037	1.11	1.14
.0041	1.15	1.19

O-rings were 0.0508 cm thick with 1.25 cm outer radius.
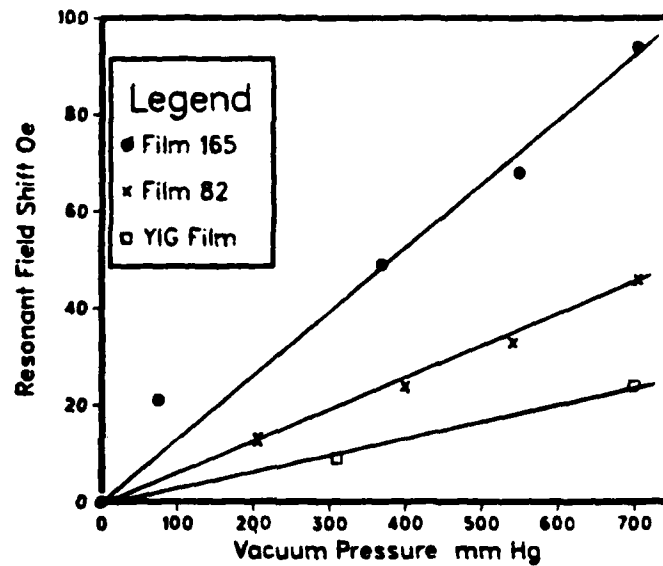
Fig. 2-6:   Resonant Field Shift versus Vacuum Suction for Films 82, 165, and the YIG film

flipped over.   The results are summarized in Table 2-2.   The back film was etched away prior to measurement.   Averaging the results from measurements at several frequencies, the δH_{111} for the compressive stress is 82 Oe, whereas that for the tensile stress is 87 Oe.   The uncertainty in each is approximately $\pm 10\%$.   Although there is a significant amount of scatter in the data, we can conclude that there is no significant difference in the δH_{111} measured in compression, compared to that measured in tension. The $\pm 10\%$ uncertainty is presumably related to the frequency response of the system which will be discussed later.

Table 2-2: Resonant Field Shift Measurements on Film 172

Freq	Compression δH_{111}	Tension δH_{111}
5.0 GHz	88 Oe	-87 Oe
5.5	79	-79
6.0	79	-91
6.5	-	-92
6.8	71	-

O-ring radius 1.15 cm. Suction 700 mm Hg

2.2.2. Vacuum Stress Determination

One of the significant problems in determining the magnetostriction as a function of temperature was the calibration of the vacuum-induced stress σ_v. Whereas previous investigators measured the wafer deflection before each resonance measurement to calculate the stress, this method was not practical for the high temperature measurements which were made here. To calibrate the stress, a series of δH_{111} measurements were made using the YIG film. The δH_{111} was measured using three different O-rings, over the temperature range from 24° to 200°C. The results are summarized in Table 2-3. The resonance spectrum from the YIG film, shown in Fig. 2-7, was radically different from those of all the other films. The two curves shown correspond to the film with no stress (lower curve), and 700 mm Hg vacuum suction applied (upper curve). The peculiar spectra are attributed to the large absorption of microwave power at resonance. There may also be a combination of magnetostatic and spin wave modes. The δH_{111} was determined from the shift in the location of the highest field peak of the spectra, since the spectra had unusual mode shapes and no clear zero-crossing point could be identified. The shape of the spectra changed when the sample was stressed, as shown in Fig. 2-7. While the shape of the resonance spectra was slightly different at different frequencies. the resonant field shift measured at several frequencies was reproducible within 2 Oe. The linewidth of the highest field mode was less than 3 Oe so that any error introduced by incorrectly identifying the resonance field was small.

The ratios of the experimentally determined stress calculated from Eq. (2.9), to the maximum stress, at the center of the film as determined from Eq. (2.11), are given in Table 2-3. The ratio $F = \sigma_v/\sigma_{max}$ is 0.93 at 24°C, for all three O-rings. As the
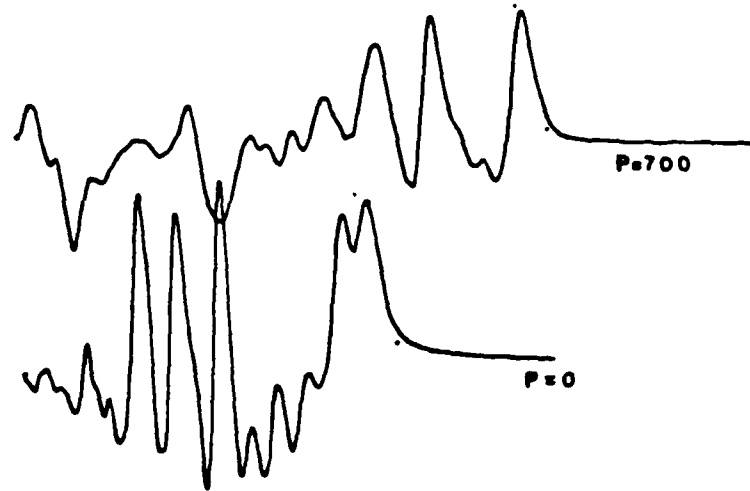
Fig. 2-7:   Resonance Spectra for YIG film:

Vacuum suction = 0, 700 mm Hg, O-ring radius a = 1.08 cm,

δH_{111} = 23 Oe, Temperature = 24°C, Frequency = 5.0 Ghz

Table 2-3:   Experimental Results for YIG Film

a=1.08 cm	σ_{max}= 9.71 × 10^8 dynes/cm^2		
Temperature	δH_{111}	λ/M (10^{-8}G^{-1})	F = σ_v/σ_{max}
24 °C	24 Oe	-1.89	0.93
123	16	-1.42	0.78
188	10	-1.20	0.63
a=1.12 cm			
27°C	26 Oe	-1.89	0.94
123	18	-1.47	0.82
166	12	-1.28	0.65
204	9	-1.1	0.53
a=1.19 cm			
24°C	29 Oe	-1.89	0.93
84	23	-1.64	0.96
117	23	-1.50	0.93
158	18	-1.32	0.81

temperature was increased, F decreased.   To determine the source of this decrease, the deflection at the center of the wafer was measured as a funtion of temperature.   The deflection measured using a 1.08 cm O-ring increased linearly from 33 μm at 25 °C to

42 μm at 150 °C. This increase may be due either to an increase in the O-ring radius or a decrease in the elastic constants of the garnet. Assuming it is caused by an increase in the O-ring radius, since w is proportional to the fourth power of a in Eq. (2.12), then a would increase from 1.08 cm at 25°C to 1.175 cm at 200°C. The change in O-ring radius, calculated from the wafer deflection, is plotted in Fig. 2-8.
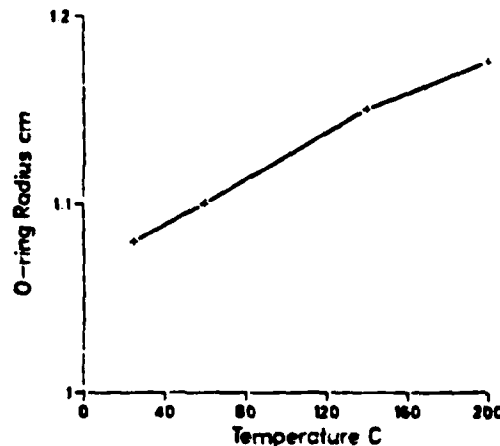
Fig. 2-8: Temperature Dependence of O-ring Radius

The teflon O-ring has a thermal expansion coefficient of $10^{-4}/°C$. Therefore the expansion at 150°C cannot account for the calculated increase in the O-ring radius. However, it is possible that the O-ring dilates slightly at high temperatures when it is stressed. This would explain the observed increase in the deflection.

While results from wafer deflection measurement suggest that an increase in the radius a is the probable cause of the increased deflection, this would cause σ_{max} to increase. However, results for the YIG film at high temperatures indicate that σ_{max} decreases, as evidenced by the decrease in σ_v/σ_{max}. The YIG film properties which were used in the calculation of σ_v were taken from the literature [53], and not determined on the film measured here. However, the temperature dependence of H_E was measured. In YIG, since the uniaxial and crystalline anisotropy fields are relatively small compared to $4\pi M_s$, H_E is approximately equal to $-4\pi M_s$. The $-H_E$ and $4\pi M_s$, which are plotted versus temperature in Fig. 2-9, agree within 60 Oe over the entire temperature range. The λ_{111} data were taken on YIG spheres, although the room temperature values are in reasonable agreement with published data for LPE YIG, -2.8×10^{-6} [52]. Thus a discrepancy in the ratio of σ_v/σ_{max} due to erroneous values of $4\pi M_s$ at high temperatures is improbable. No results for the temperature dependence of λ_{111} for LPE YIG were found in the literature, but there is not expected to be a significant
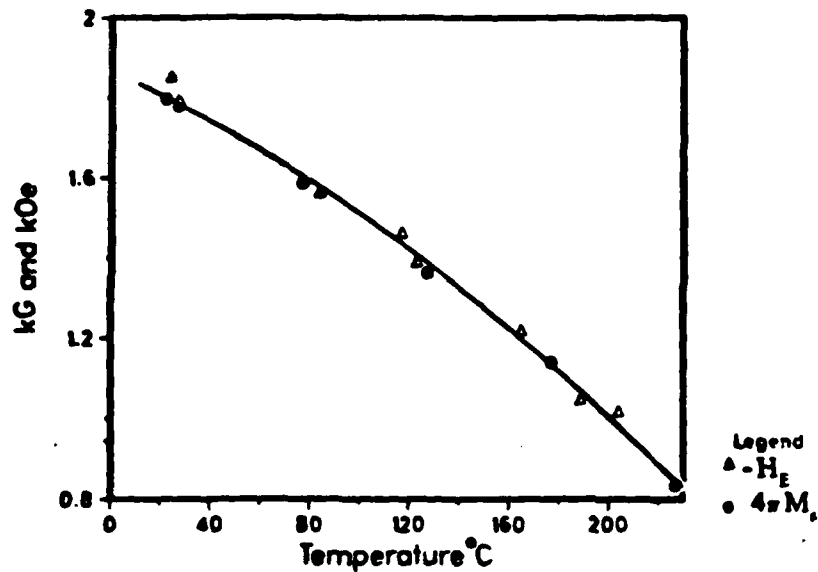
Fig. 2-9: Minus Effective Field and Magnetization for YIG film

discrepancy here either. The temperature dependence of λ_{111}/M_s for YIG is plotted in Fig. 2-10. Note that there is a near linear decrease in λ_{111}/M_s over the temperature range from 0 to 200°C.
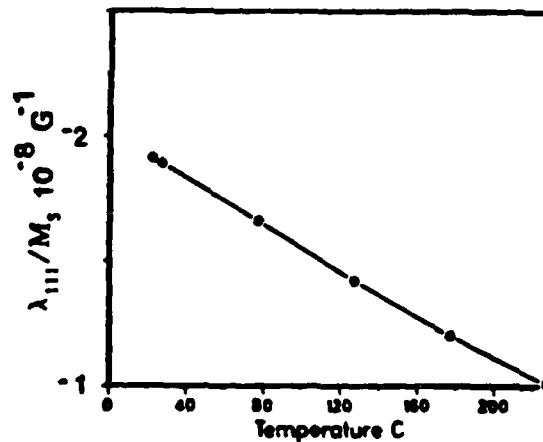
Fig. 2-10: Temperature Dependence of λ_{111}/M_s for YIG, After Hansen [53]

If the O-ring radius remained constant and the elastic constants decreased at higher temperatures, then the stress in the film would not change, since the product (w • E) in Eq. (2.12) would remain constant. This would correspond to a 25% decrease in E from 26°C to 200°C. Previously, we suggested that the increase in wafer deflection was due to an decrease in the Young modulus [57]. While this cannot be completely ruled out as a possibility, this assumption is now believed to be incorrect. However, discrepancies in the high temperature measurements on the YIG films indicate that this issue has not been completely resolved.

One source of error in the high temperature measurements of the YIG film is the uncertainty of δH_{111}. Since δH_{111} at 200°C was only 10 Oe, a ±2 Oe uncertainty results in a ±20% uncertainty in the calculated stress σ_v. The accuracy of δH_{111} can be improved by increasing the magnitude of δH_{111}. A larger δH_{111} can be achieved by increasing the stress, or by measuring the resonance in a region of the film which has a higher average stress. The stress can be increased by thinning the wafer, increasing the O-ring radius, or increasing the vacuum suction. Thinning the wafer by mechanical lapping resulted in wafer breaking during measurement when it was stressed, as the scratches which were created during the lapping nucleated cracks. Increasing the O-ring radius was not practical, as the reproducibility of δH_{111} was very poor, and the wafer tended to slip off the larger O-rings at high temperatures. Use of a higher vacuum suction was not pursued, as the stress would only be increased by approximately 10% if a perfect vacuum were achieved. There are other techniques for stressing the film which include deflecting it with a screw [51], or pushing on it with a rod [24, 23]. Those techniques were not tried here, as they do not have the versatility of the vacuum suction method. Measurement of the resonance in a region of the film with a higher average stress could be achieved either by redesigning the microstrip structure, or etching away all of the film except a small region at the center of the film as other investigators have done [58]. In summary, the best solution for increasing the magnitude of δH_{111} is to thin the substrate. However, a thinning technique which does not create scratches, such as chemical etching or ion milling is required. These were not used here.

The measurements on the YIG film indicate that the stress applied to the wafer decreases with increasing temperature, as evidenced by a decrease in the ratio σ_v/σ_{max}. However, measurement of the wafer deflection indicate that σ_{max} increases with temperature. To take account of the apparent increase in the radius as well as the effects of the nonuniform stress distribution over the serpentine conductor, an averaging factor F, for the vacuum stress was determined from the measurements on the YIG film at room temperature, and the temperature dependence of the wafer deflection. The averaging factor F, is plotted versus temperature in Fig. 2-11. Based on the increase in O-ring radius in Fig. 2-8, the vacuum-induced stress will increase nearly linearly with temperature. The average stress σ_v, which is used in the calculation of λ_{111}/M_s, is given by

$$\sigma_v = \sigma_{max} \times F \qquad (2.13)$$
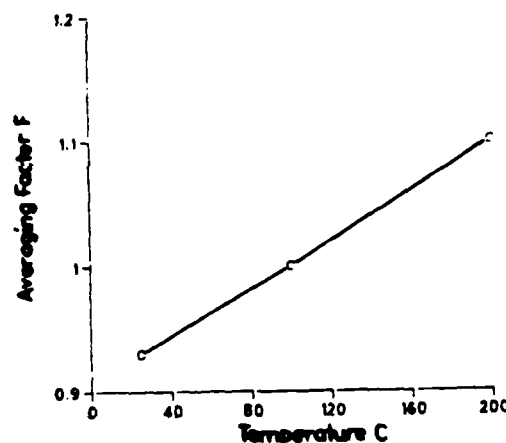
Fig. 2-11:   Temperature Dependence of Stress Averaging Factor F

While an averaging factor is required to account for the discrepancy in the measurements on the YIG film, its effect is relatively small. At room temperature, the average stress is 90% of the maximum stress in the film. If the averaging factor was lower than calculated using the YIG film, than the calculated λ_{111}/M_s would increase proportionately. This in turn would increase the calculated magnetostrictive contribution to the total implantation-induced ansitropy field change. The magnetostrictive field calculation will be discussed later. Analysis shows that the λ_{111}/M_s measurements at temperatures above 150°C are subject to a potential uncertainty of 10% to 20%, based on the increase of the averaging factor with temperature.

2.2.3. Uncertainty in Vacuum-Stress Induced Resonant Field Shift

To determine the reproducibility and uncertainty of the δH_{111} measurements, the potential error sources were evaluated. Experimental results indicated that δH_{111} was reproducible within ±10%. The main source of the uncertainty in δH_{111} is attributed to the frequency response of the microwave network. A typical trace of the frequency response from 4 to 8 GHz is shown in Fig. 2-12. The response is characterized by relatively rapid oscillations which are superimposed on more slowly varying oscillations. The rapid oscillations are attributed to an impedance mismatch which creates reflections in the coaxial cable connecting the microwave source to the minibox. The period of the oscillations is proportional to the length of the cable. The shape of this particular spectrum is not unique. Slight perturbations of the cable or the connections of the cable to the minibox resulted in spectral shifts. To determine the effects of the peculiar frequency response, the resonant field shift was measured at selected points in
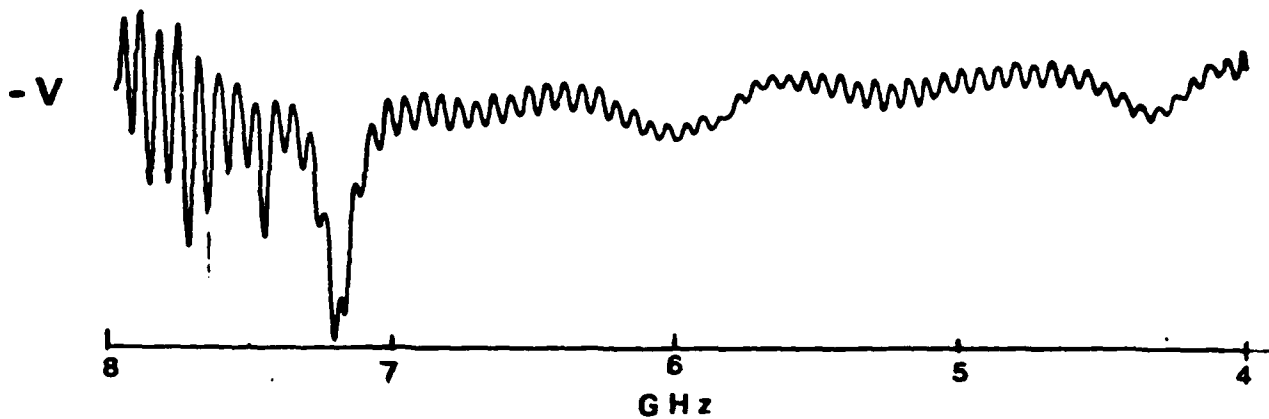
Fig. 2-12: Frequency Response of the Microwave Signal Using Serpentine Conductor

the frequency spectrum, corresponding to maxima and minima in the detector output voltage. Results for the resonance field and the field shift measured on the bulk layer of an LPE film are summarized in Table 2-4.

Table 2-4: Frequency Dependence of δH_{111} Measurements

F (GHz)		H_{res}	δH_{111}	F (GHz)		H_{res}	δH_{111}
4.207	max	368 Oe	76 Oe	4.240	min	386 Oe	76 Oe
5.034	max	725	64	5.064	min	739	66
5.950	max	1121	62	5.981	min	1138	67
7.609	min	1824	78	7.673	min	1860	90
7.713	max	1860	58	7.741	min	1813	97
7.739	min	1863	140				

The data in Table 2-4 include the frequency F, the resonance field H_{res}, and the resonant field shift δH_{111}. Note that the first three sets of data correspond to adjacent extrema, corresponding to the spectra in Fig. 2-12. In the regions of the spectrum where the amplitude of the oscillations are small, such as over most of the region from 4.5 to 6.5 GHz, the δH_{111} measurements were within ± 4 Oe. However, in the region where the amplitude of the oscillations are large, such as at the low and high ends of the frequency range, δH_{111} was dramatically different. Over the relatively narrow frequency range, from 7.61 to 7.74 GHz, δH_{111} varies by more than 100%. The explanation for the unusually large variation in δH_{111} is that due to a change in the impedance mismatch when the vacuum suction is applied, the location of the extrema in the frequency response shifts slightly (0.003 GHz). In the region where the oscillations

are large, this results in a significant shift in the detected signal level. In this same region, the location of the resonance field H_{res} was inconsistent with the usual frequency dependence. The H_{res} is expected to increase linearly with frequency, which it does over the entire frequency range. However H_{res} measured where the oscillations are very large decreased by as much as 50 Oe for an increase in frequency of 0.002 GHz, between 7.739 and 7.741 GHz. This discrepancy coincided with an anomalously large shift in δH_{111}. The discrepancy in the resonance field will also affect the γ calculation.

In spite of the $\pm 10\%$ uncertainty in δH_{111} in the frequency range from 4.5 to 6.5 GHz, the relative uncertainty between $\delta H_{111}(B)$ of the bulk mode and $\delta H_{111}(I)$ of the main implanted was considerably smaller. Results are summarized in Table 2-5.

Table 2-5: Comparison of $\delta H_{111}(B)$ to $\delta H_{111}(I)$

Freq.	$\delta H_{111}(B)$	$\delta H_{111}(I)$
4.5 GHz	94 Oe	98 Oe
6.0	87	92
7.0	80	83

There is a ± 7 Oe uncertainty in the δH_{111} in either layer, however the relative difference at a given frequency is within ± 1 Oe. Thus the relative change in the magnetostriction of the implanted layer compared to the bulk can be accurately determined.

In summary, the values of δH_{111} which are reported in this thesis represent the average of measurements at three or more frequencies, typically between 4.5 and 7.0 GHz. While the reproducibility of δH_{111} at any given frequency is typically within ± 2 Oe, the results averaged over several frequencies is typically $\pm 10\%$ of δH_{111}, but generally not larger than ± 7 Oe. If the measurement frequencies are chosen in regions where the oscillations in the frequency response are small, the uncertainty in δH_{111} can be reduced to approximately $\pm 5\%$. This is a relative uncertainty and is separate from the uncertainty in the calibration of the stress using the YIG film. The estimated uncertainty in λ_{111}/M_s and ΔH_σ considering both the relative and calibration uncertainties is approximately $\pm 10\%$.

2.2.4. Measurement of Resonant Field Shift

The δH_{111} measurements were made from the absorption derivative resonance curve, by measuring the shift in the zero crossing point. A typical resonance curve is shown in Fig. 2-13. Note that the resonance linewidth and amplitude for the stressed film (right curve) is quite similar to that for the unstressed film (left curve). Note that the shift in the resonance mode is a significant portion of the total linewidth of the mode. For films in which δH_{111} is considerably smaller than the linewidth, the accuracy is not as high. If the resonance curve of the stressed film is symmetric with respect to that of the unstressed film, as it was for most of the films studied here, then the technique of measuring the difference in the zero-crossing provides reasonably consistent results. However asymmetric resonance curves for the stressed film were observed in some of the films. An example is shown in Fig. 2-14. The resonance field in the stressed film determined from the Zero-crossing is different from that obtained by measuring the midpoint of the curve. No correlation was found between the film properties, FMR system frequency response, or the phase of the resonance signal, which could explain the asymmetric resonance curves. Thus, the use of asymmetric resonance curves was avoided. One source for the asymmetric curves obtained in the initial stages of this research was the proximity of a thermistor to the microwave field. The thermistor was placed inside the minibox to measure the temperature. The asymmetric resonance was attributed to the magnetic material in the thermistor. This necessitated the use of a thermocouple to measure the sample temperature.

The non-uniform stress distribution in the garnet film does not significantly increase the resonance linewidth, in spite of the fact that regions of the film with different amounts of stress have different effective fields. The effect of non-uniform stress has been equated to that of a non-uniform magnetic field distribution across the sample [51]. The resonance linewidth in a sample which was in a non-uniform field was found to be comparable to that for a film in a uniform field [59]. This was attributed to the long range of the dipolar forces which tend to force the spins to precess together as a single system. This assumption is valid as long as the perturbing field is smaller than the magnetization. The Geschwind and Clogston experiment was done on truncated spheres of YIG and manganese ferrite $Mn\,Fe_2\,O_4$. The lack of substantial linewidth broadening in the stressed film, compared to the unstressed film, suggests that despite the non-uniform stress distribution, the resonance is predominantly localized in the central portion of the film which has the maximum stress.

50 Oe

P=0   700
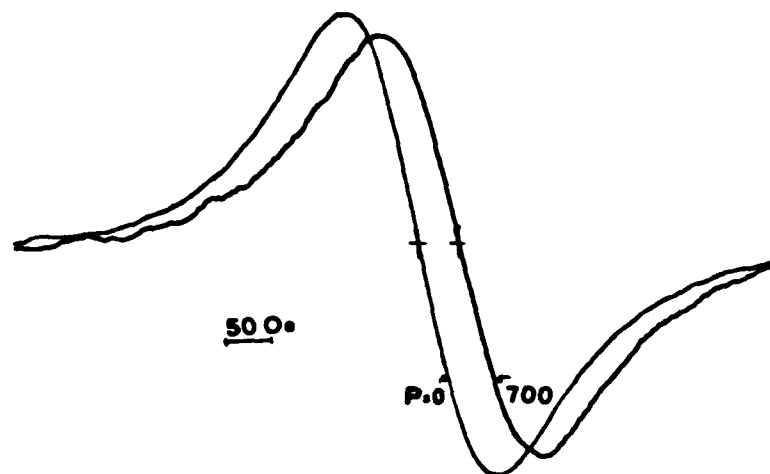
Fig. 2-13: Typical Resonance Curves for Stressed and Unstressed Film

Stressed
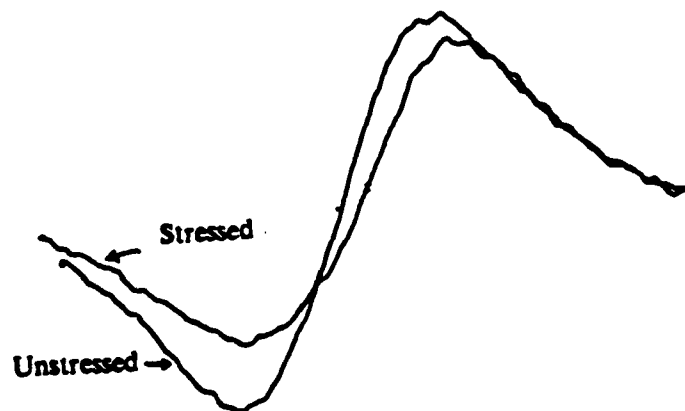
Unstressed →

Fig. 2-14: Absorption Derivative Resonance Curve for Film 159,
Unstressed and Stressed

2.2.5. Comparison of Vacuum-Induced Resonant Field Shift Using Straight and Serpentine-Shaped Conductors

To determine if the serpentine-shaped conductor had an anomalous effect on the stress averaging factor $F = \sigma_v / \sigma_{max}$, results were compared to those obtained using a straight conductor. The results are summarized in Table 2-6. Comparing results for each film using the straight and serpentine conductors gives an indication of the difference in the average stress in that part of the film which couples to the microwave field, since the λ_{111}/M_s and the applied stress were the same. The stress averaging factor F for the straight conductor is 3/5 to 3/4 of that for the serpentine-

Table 2-6: Comparison of Serpentine to Straight Conductor

Film	δH_{111} Serpentine	δH_{111} Straight
106	60 Oe	37 Oe
117	84 Oe	62 Oe

Suction 57 cm Hg, O-ring inner radius 1.17 cm

shaped conductor which indicates that the serpentine conductor is more effective in coupling into the central region of the wafer which has a higher average stress.

The consistency of the measurement results were checked by measuring δH_{111} as a function of O-ring radius. Results are summarized in Table 2-7.

Table 2-7: Results for δH_{111} Measurement With Different O-ring Radii

Film	Pattern					
39	Serpentine	radius a	1.08 cm	1.15 cm	1.20 cm	
		δH_{111}	66 Oe	90 Oe	104 Oe	
		F	0.86	0.91	0.95	
151	Serpentine	a	1.08 cm	1.15 cm	1.17	1.20 cm
		δH_{111}	48 Oe	57 Oe	68 Oe	68 Oe
		F	1.0	0.96	0.83	0.88
117	Straight	a	1.08 cm	1.15 cm	1.17 cm	
		δH_{111}	40 Oe	50 Oe	62 Oe	
		F	0.52	0.57	0.68	

The values of the stress averaging factor F, given in Table 2-7, were calculated using the λ_{111}/M_s values given in Table 2-8, which in turn were calculated assuming that F = 0.93 for the serpentine conductor. Thus the results show the self consistency of the λ_{111}/M_s calculation, using different radii O-rings. The increase in F with O-ring radius, which was observed with both structures, may be indicative of a systematic measurement error such as an incorrect value for the O-ring radius. However the discrepancy in F cannot be separated from the 10% uncertainty in the δH_{111} measurement. Thus no trend relating the change in F to a single factor was established.

The compositions, based on unity segregation coefficients for the rare-earths in the melt, for several films are given in Table 2-8. The λ_{111} values can be compared to the compositions to determine if the observed trends are consistent with the film

properties. The λ_{111} is expected to be higher in film 117 than in film 106, due to the increased samarium content in the film. The λ_{111} of film 39 is expected to be lower than that for the other films, due to the larger amount of iron dilutant (Ga) in the film. The observed trends in the magnetostriction agree with the differences in the film compositions.

Table 2-8:   Magnetostriction Measurement Results

Film	λ_{111}/M_s	λ_{111}
39	$-4.2 \times 10^{-8}G^{-1}$	-2.1×10^{-6}
106	-2.9	-3.1
117	-3.6	-3.9
151	-3.0	-3.3

Compositions (inferred from melt constituents)

Film	Y	Sm	Tm	Gd	Lu	Fe	Ga	Al	O
39	0.9	0.2	1.3	0.6	0	4.64	0.36	0	12
106	1.05	0.35	1.3	0.3	0	4.8	0	0.2	12
117	0.97	0.54	1.21	0.28	0	4.8	0	0.2	12
151	0.80	0.63	1.0	0.24	0.33	4.8	0	0.2	12

In summary, the calibration of the stress in the film deflected by the vacuum suction is based on the results for the YIG film at room temperature, and measurement of the wafer deflection at high temperatures. Since the exact compositions of the films studied here are not known, it is not possible to accurately predict the magnetostriction coefficients using White's method [60]. However, it has been shown that the techniques employed here are self-consistent, provided that the measurements are made at frequencies which are in the region with a relatively flat frequency response. Furthermore, on a relative basis, the magnetostriction results are in agreement with expected trend based on the differences in the film composition.

2.3. IMPLANTED FILM CHARACTERIZATION

The implanted films were studied using FMR and X-ray diffraction characterization techniques. The FMR spectra from an ion implanted film typically have multiple surface modes which are related to the anisotropy profile through the depth of the implanted layer. Since the effective anisotropy field in the implanted layer $H_E(I)$, varies through the film thickness, the value which most investigators cite is the difference between the bulk mode and the principal surface mode. Furthermore, since most investigators made measurements in resonant cavities which are limited to a narrow frequency range, they have assumed that $\gamma(I)$ in the implanted layer is equal to $\gamma(B)$ in the bulk. Here, H_E and γ in the bulk and implanted layers were determined from the frequency dependence of the bulk and principal surface modes. The change in uniaxial anisotropy energy is given by

$$\Delta H_E = H_E(B) - H_E(I) \tag{2.14}$$

where $H_E(B)$ and $H_E(I)$ are the effective uniaxial anisotropy fields in the bulk and implanted layer. The $H_E(I)$ is determined from the highest field mode in perpendicular resonance. Depending on the anisotropy profile this may not necessarily represent the average anisotropy through the thickness of the implanted layer. A detailed description of the procedure for obtaining the anisotropy field profile will be discussed. This involves fitting all of the experimental modes to a spectra calculated for an assumed anisotropy profile. This is done by finding a numerical solution to the eigenvalue equation for spin waves using the program developed by Wilts [40].

2.3.1. Magnetostrictive Field

The magnetostrictive contribution to ΔH_E was determined from direct measurements of the strain and the magnetostriction in the implanted layer. Previous investigators have usually assumed that the implant did not affect the magnetostriction, and used the bulk magnetostriction to determine the magnetostrictive field. The magnetostrictive field ΔH_σ is given by

$$\Delta H_\sigma = 3 \ \sigma \ \lambda_{111}/M_s(I) \tag{2.15}$$

where the implant-induced stress σ is given by

$$\sigma = \frac{E}{(1+v)} \frac{\delta d}{d} \tag{2.16}$$

where $\delta d/d = \epsilon_{max}$ is the lattice strain perpendicular to the film plane. The $\delta d/d$ is determined from x-ray diffraction and is given by

$$\frac{\delta d}{d} = \frac{\delta \theta}{\tan \theta} \qquad (2.17)$$

where $\delta \theta$ is the angular separation between the LPE film peak and the low angle maximum of the implanted layer X-ray diffraction peaks, and θ is the Bragg angle. The $\lambda_{111}/M_s(I)$ is determined from Eq. (2.9), using the δH_{111} of the highest field (uniform) surface mode. Note that the calculation of ΔH_σ does not require that the magnetization in the implanted layer be determined.

A double crystal X-ray diffractometer was used to measure the lattice mismatch and the strain in the implanted layer. The double crystal diffractometer effectively eliminates the Cu $K_{\alpha 2}$ radiation from the X-ray beam which reaches the detector. The double crystal diffractometer, is shown schematically in Fig. 2-15. Here, the sample crystal is placed in the usual sample position for single crystal diffraction, on the θ rotation circle. The second crystal, which is a $Gd_3Ga_5O_{12}$ (GGG) substrate with no epitaxial film, is placed at the normal detector position, on the 2θ rotation circle. The detector is fixed with respect to the second crystal, such that when the Bragg condition for the incident X-rays are satisfied, the diffracted X-rays will reach the detector. The Bragg angle for a particular reflection (hkl) in a cubic crystal is determined from

$$\sin^2 \theta_B = \frac{\lambda^2}{4a^2} \ (h^2 + k^2 + l^2) \qquad (2.18)$$

where h, k, and l are the indices for the reflection, and a is the lattice parameter (a = 12.383 Å for GGG). The angle of the second crystal is set, such that when the Bragg condition for the first crystal is satisfied for the Cu $K_{\alpha 1}$ reflection, it is simultaneously satisfied for the second crystal. Since the Bragg condition for the $K_{\alpha 2}$ reflection will occur at a different angle, it will not be simultaneously satisfied for both crystals. Thus the second crystal effectively eliminates the $K_{\alpha 2}$ diffraction peak. The double crystal diffractometer design which was implemented here is reversed from the conventional design. In the conventional set-up, the first crystal (GGG) is set so that the Bragg condition is satisfied only by the $K_{\alpha 1}$ radiation. The diffracted X-rays from this crystal are used as a monochromatic source for the second (sample) crystal. The second crystal is rotated through the appropriate angles and the diffracted intensity is measured. While the rocking curves obtained from the two methods contain the same information, the peaks are slightly broader in the conventional method. The drawbacks with the method used here is that it precludes determination of the absolute reflection from the sample, since the intensity of the incident beam is not measured, and it prohibits measurement of diffraction from planes not parallel to the film surface,

although this could be done if the sample holder were redesigned. The absolute reflectance is used in determining the damage profile and the asymmetric reflections are used to measure the lateral strain [41].
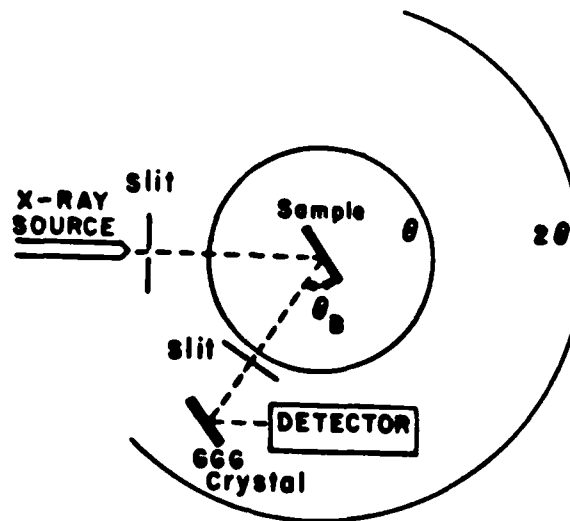
Fig. 2-15: Double Crystal X-ray Diffractometer

X-ray results using both the (888) and (444) reflections were obtained. While both contain the same basic information, there are several differences, notably the angular spread of the interference peaks and their amplitudes. In the (888) reflection, the total angular spread of the interference peaks is three times larger, the reflecting power is an order of magnitude less, and the number of oscillations is almost twice that of the (444) reflection. However, the envelope of the X-ray peaks has the same shape. Thus, while the (444) reflection may be more desirable because of the stronger signal, the (888) reflection has higher accuracy for measurements of films with low implant strains, and for measurement of the lattice mismatch. Most of the measurements here were made using the (888) reflection.

The X-ray rocking curves from the implanted garnet have multiple interference peaks which are caused by the interference of the X-ray wave fields inside the crystal [61]. The interference peaks in X-ray rocking curves are related to the strain and damage distribution through the thickness of the implanted layer. To determine the strain and damage profiles from the X-ray rocking curves, it is necessary to analyze the diffracted wave intensity [41, 42]. While a detailed analysis is necessary to accurately determine the strain and damage profiles, certain features of the strain profile can be determined

without doing the complete analysis. The maximum angular width of the spectrum is related to the maximum strain, the spacing of the peaks is related to the thickness of the implanted layer, and the height of the envelope of the lower peaks is related to the strain gradient with respect to the depth [42].

An X-ray rocking curve which was used to calculate the bulk and implanted layer thickness is shown in Fig. 2-16. The implanted layer thickness can be determined from the period of oscillation of the diffraction peaks which are on the high θ wing of highest amplitude surface layer peaks. The thickness is calculated from [41]

$$T = \frac{\lambda |\gamma_H|}{P_{min} \sin 2\theta_B}$$
(2.19)

where λ is the X-ray wavelength, 1.5405 $\overset{o}{A}$ for Cu K_{a1}, γ_H is the direction cosine of the diffracted wavevector, θ_B is the Bragg angle, and P_{min} is the minimum period of oscillation. For commonly used reflections, Eq. (2.19) simplifies to

$$T = \frac{1.518}{P_{min}} \quad \text{(888) reflection} \quad T = \frac{0.854}{P_{min}} \quad \text{(444) reflection}$$
(2.20)

T is in $\overset{o}{A}$, and P_{min} is the period of oscillation in angle θ (not 2θ), measured in radians.
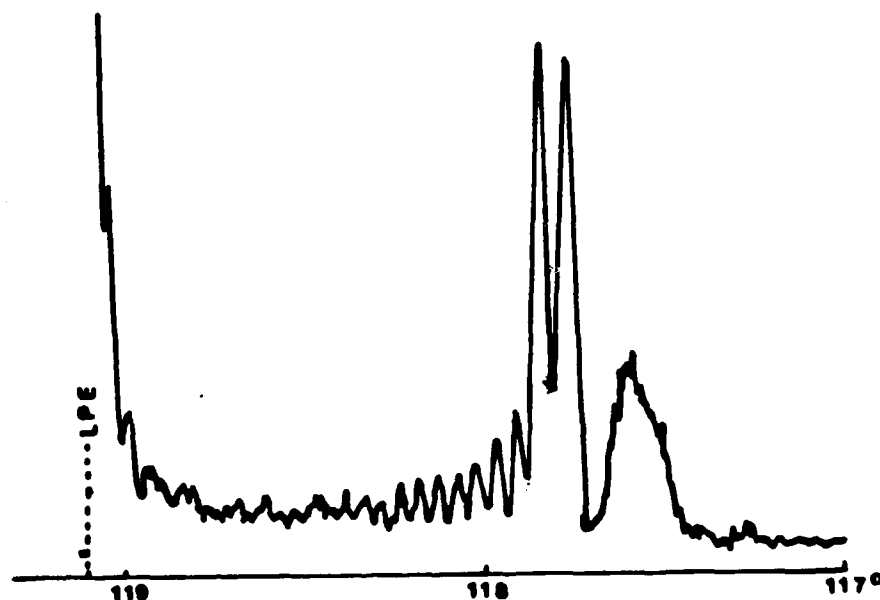
Fig. 2-16: X-ray Rocking Curve for film 112

In Fig. 2-16 the LPE peak at 119.1° is off the plot. The period of the oscillations

45

just below this peak are related to the thickness of the unimplanted LPE layer. The period of the oscillations near 118.2° are proportional to the implanted layer thickness (0.35 μm). The peak at 117.6° is related to the maximum strain in the film, which in this case is due to an oxygen implant. The large peaks near 117.8° are related to the implant strain created by a deuterium implant. The results for this film will be discussed in Chapter 4. The implant conditions are 5×10^{15} D_2^+/cm^2 at 60 keV and 0.95×10^{15} O^+/cm^2 at 110 keV.

The X-ray rocking curve for a high energy, single dose implant (3×10^{16} D_2^+/cm^2 at 88 keV) is shown in Fig. 2-17. The location of the LPE film peak is indicated by the dashed line near 50.8°. The strain in the implanted layer was measured from the angular separation between the LPE film peak and the low angle maximum in diffracted intensity, which is near 49.6°. Strain uniformity was judged from the angular spread of the implanted layer diffraction spectra, between 49.6° and 50.2°. The peak at 50.2° is related to the surface strain. This same film also received additional implants at lower energies (1.25×10^{16} D_2^+/cm^2 at 55 keV and 8×10^{15} D_2^+/cm^2 at 25 keV) which were designed to improve the strain uniformity. The rocking curve is shown in Fig. 2-18. Although the rocking curves in Figs. 2-17 and 2-18 cannot be compared directly, since one is a (444) reflection and the other is an (888) reflection, calculation of the maximum and minimum implant strain indicates that the strain uniformity was improved by the multiple implant. These results will be presented later.

While the spectra for the singly implanted films had interference peaks on the high angle side of the surface spectra with well defined periods of oscillation, which are proportional to the thickness of the implanted layer, the rocking curves from multiply implanted films did not. Thus the implanted layer thickness could not be accurately determined from the spectra for the multiply implanted films.

2.3.2. High Temperature X-ray Results

To determine if the implant strain changes significantly at higher measurement temperatures, the implant strain was measured as a function of temperature using the hot stage attachment on a single crystal X-ray diffractometer. Measurements were made on film 96-1, which was implanted with 8×10^{15} D_2^+/cm^2 at 60 keV and 1.2×10^{14} O^+/cm^2 at 80 keV. Diffraction measurements were made after a pre-anneal, so that no annealing-induced changes in the implant strain occurred. Results indicate that the implant strain does not change by a significant amount over the temperature range from 25° to 300°C.
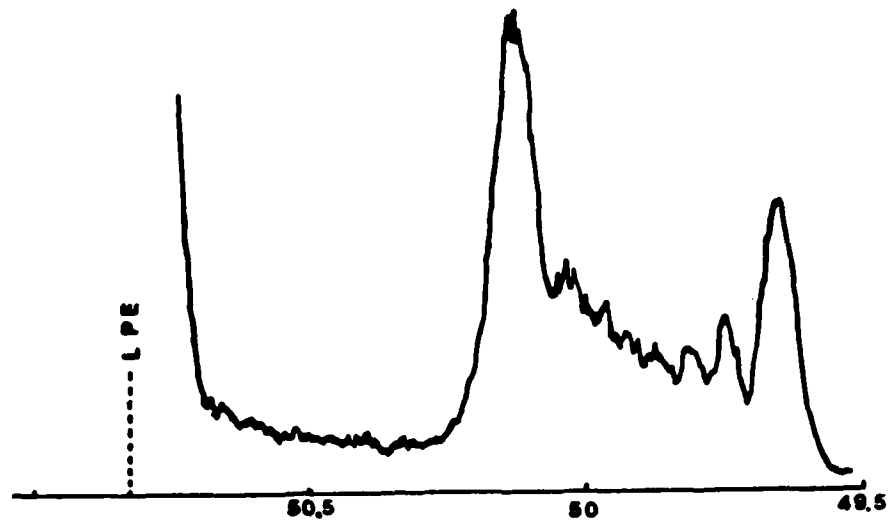
Fig. 2-17: X-ray Diffraction Rocking Curve for a High Energy Deuterium Implant: Film 150
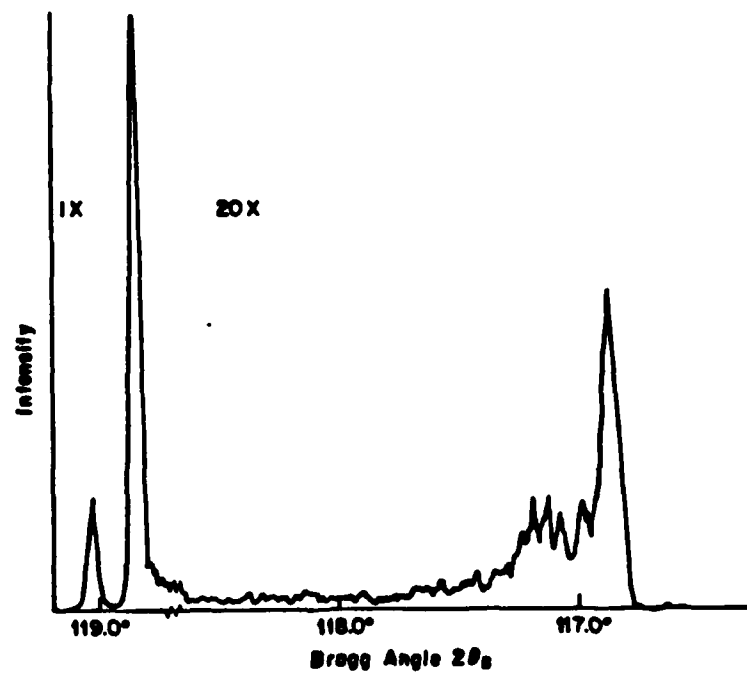
Fig. 2-18: X-ray Diffraction Rocking Curve for Multiple Energy Deuterium Implant: Film 150

While any change in the implant strain was smaller than the measurement uncertainty, there was a detectable change in lattice mismatch, due to the difference in the thermal

expansion coefficients of the substrate and the LPE film. The thermal expansion in the LPE film was estimated using the lattice mismatch measured at room temperature on the double crystal X-ray diffraction curve, as the LPE film peak in the single crystal X-ray diffraction curve could not be resolved from the GGG peak. The linear coefficient of expansion a, was determined to be 3.0×10^{-6}/K in the GGG, which is in good agreement with the published a of 3.25×10^{-6}/K for GGG [62]. In the LPE film, the a was found to be 7.8×10^{-6}/K, which is reasonably close to the published value for YIG, 8.13×10^{-6}/K from 293 K to 500 K [62].

2.4. FERROMAGNETIC RESONANCE SPIN WAVE ANALYSIS

The FMR spectra from ion-implanted garnet films can be used to determine the depth profiles of the anisotropy field H_K, magnetization $4\pi M_s$, and exchange constant A. In the case of a uniform profile, the amplitudes and spacings of the spin wave modes are given by the simple algebraic expression [63]

$$(\omega/\gamma) = H + H_E + (2A/M)k^2 \tag{2.21}$$

where $k = n\pi/t$ is the wave vector, t is the film thickness and n is the mode number. However since the depth profiles of the anisotropy are not usually uniform, the spectra cannot be fit using Eq. (2.21) and a numerical technique must be used. The magnetic anisotropy profile is obtained by fitting the experimental spectra to the spin wave modes which are calculated numerically for an assumed profile of film parameters, using the program developed by Wilts and Prasad [40], and implemented here by DeCesaris [64].

In Wilts' program, the Schroedinger-type wave equation is solved numerically for assumed profiles of H_K, $4\pi M_s$, and A. The location and amplitudes of the experimental resonance modes are compared, by the program user, with those of the calculated modes. The profile is adjusted until the calculated spectra matches the experimental spectra. The resonance spectra are taken with the field applied perpendicular and parallel to the plane of the film.

The FMR spin wave modes for the applied field H, perpendicular to the plane of the film are obtained by solving the second order differential equation [63]

$$(2A/M)d^2m/dz^2 + \left((\omega/\gamma) - H - H_E(z) - (2A/M^2)\frac{d^2M}{dz^2}\right) m = 0 \tag{2.22}$$

where M is the saturation magnetization. m is the amplitude of the spin wave mode which is equivalent to the rf magnetization in the sample, and $H_E(z)$ is the z-axis dependent effective uniaxial anisotropy field, where the z direction is perpendicular to the film plane.

The parallel resonance condition is described by two coupled second-order differential equations:

$$d^2m_\theta/dz^2 = M_s/2A \{(H + 4\pi M_s - H_K - \tfrac{1}{2}H_1)m_\theta - (\omega/\gamma)m_\phi\}$$ (2.23)

$$d^2m_\phi/dz^2 = M_s/2A \{Hm_\phi - (\omega/\gamma)m_\theta\}$$

Wilts' program solves the equations for perpendicular and parallel resonance, based on an assumed profile of H_K, $4\pi M_s$, crystalline anisotropy H_1, and A. These parameters are constant in each layer but can be different in the different layers. The implanted region is divided into a number of layers and the perpendicular and parallel resonance equations are solved in each layer, such that the following boundary conditions are met:

$$m_h/M_h = m_{h+1}/M_{h+1}$$ (2.24)

$$(A_h/M_h)dm_h/dz = (A_{h+1}/M_{h+1})dm_{h+1}/dz$$ (2.25)

where the subscript h refers to the layer number. The final solution is arrived at by solving the wave equation iteratively until the slope of the solution to the wavefunction is zero at the bulk interface in perpendicular resonance, and zero at the air interface in parallel resonance [64].

The mode intensity is obtained by evaluating

$$\left[\int_0^\bullet m(z)dz\right]^2 \left[\frac{a}{\gamma M}\int_0^\bullet |m(z)|^2dz\right]^{-1}$$ (2.26)

where a is the Gilbert damping parameter which is given by

$$a = \frac{\Delta H_{1whm}\gamma}{2\omega}$$ (2.27)

where ΔH_{1whm} is the full width at half maximum linewidth of the resonance absorption curve. · Since all of the measurements here were done using derivative absorption, ΔH_{1whm} is related to the peak-to-peak linewidth ΔH by [65] $\Delta H_{1whm} = \Delta H \times (3)^{1/2}/2$. The mode amplitudes in Wilts' program are calculated based on absorption resonance spectra. To calculate the mode intensity for the derivative absorption spectra, the peak-to-peak absorption derivative linewidth is multiplied by the mode amplitude [50].

The linewidth-corrected highest field mode, in both perpendicular and parallel resonance, is assigned an amplitude of 100%, and all the higher order modes, at lower fields are normalized to it.

Additional details of the solution to the FMR spin wave problem, and its implementation in the program developed by Wilts and Prasad appear elsewhere and will not be repeated here [40, 63].

2.4.1. Program Implementation

Operational details of the FMR program, which was implemented here on an HP-9826, as well as an HP-9836 computer, are given in a report prepared by Decesaris [64]. In the FMR program, the user selects the number and thickness of each of the surface layers, and specifies the values of the film parameters in each layer. The profiled parameters include H_K, $4\pi M_s$, A, and H_1. The program does not profile the gyromagnetic ratio γ, and damping parameter α, but different values of each can be specified in the bulk and surface layers.

The ratio $A/(M_s t^2)$ specifies the number of spin wave modes. The thickness t is usually determined independently, either from the X-ray rocking curve or by an etching experiment. It is not convenient to use the implanted layer thickness as a fitting parameter, as only the relative value can be determined. While it is usually necessary to profile $4\pi M_s$, A, and H_1 to achieve a reasonable fit, it is more expedient to keep them constant initially, while the general features of the H_K profile, and an approximate value of $A/(M_s t^2)$ are determined. Other investigators have profiled $4\pi M_s$ and A in proportion to the strain profile [14]. The accuracy with which $4\pi M_s$ and A can be determined independently is approximately $\pm 10\%$ [40, 14]. The H_1 has a significantly smaller effect on the mode spectra compared to A and $4\pi M_s$, and is not usually profiled.

The FMR program computes the perpendicular and parallel resonance mode locations and amplitudes, and plots the H_K profile and the solution to the spin wave equation through the depth of the film for each mode at a given frequency. The resonance modes are numbered, starting at the highest field. In perpendicular resonance, the first mode corresponds to the maximum uniaxial anisotropy field in the implanted layer $H_K(I)$, whereas in parallel resonance the first mode corresponds to $H_K(B)$. In perpendicular resonance, the higher order modes represent solutions to the spin wave

equation in the implanted or surface layer, whereas in parallel resonance the intermediate modes are mixed solutions for modes in both the surface and the body. However, in parallel resonance, the surface mode which is localized at the film surface can be identified from the plot of the solution to the spin wave equation through the depth of the film. These plots are useful in adjusting the profile as they provide information about the localization of particular modes.

2.4.2. Determination of the Magnetization from FMR

The magnetization in the implanted layer was not measured directly, however the ratio of the surface to the bulk magnetization can be determined from the FMR measurements. The linewidth is assumed to have a Lorentzian form, which is based on the principle that the linewidth broadening is attributable to the different magnetic fields experienced by the different atoms [45]. The derivation here assumes that the FMR is done in a disk-like specimen. With the DC field perpendicular to the plane of the specimen, there is a linearly polarized microwave drive field, and the small signal approximation is valid [65]. Assuming the Lorentzian form for the resonance, the mode amplitude and the linewidth can be related to the magnetization. A reasonable approximation for the microwave absorption, normalized with respect to the incident power is given by [65]

$$\chi''\Delta V = \frac{\frac{1}{2}4\pi M\ (\Delta H_{fwhm}/2)}{(H - H_{res})^2 + (\Delta H_{fwhm}/2)^2}\Delta V \tag{2.28}$$

where ΔH_{fwhm} is the full width of the absorption resonance at half the maximum power, H_{res} is the field for resonance, and ΔV is a volume element. At resonance $H = H_{res}$.

$$\chi''\Delta V \sim \frac{4\pi M}{\Delta H_{fwhm}}\Delta V \tag{2.29}$$

Evaluating the derivative of Eq. (2.28) to relate the absorption derivative linewidth to the absorption linewidth, we find that

$$4(H - H_{res})^2 = (\Delta H_{fwhm})^2/3 \tag{2.30}$$

where $(H - H_{res})$ is half the derivative absorption peak-to-peak linewidth. From the maximum of the derivative of Eq. (2.28), we find that the magnetization is proportional to the product of the absorption derivative peak amplitude and the square of the linewidth. To evaluate the magnetization in the implanted and bulk layers of a film, we can define an intensity ratio I which is given by

$$I = \frac{I_1(\Delta H_1)^2}{I_B(\Delta H_B)^2} = \frac{M_1 L_1}{M_B L_B} \qquad (2.31)$$

where I_1 and I_B are the mode intensities. ΔH_1 and ΔH_B are the absorption derivative mode linewidths. M_1 and M_B are the magnetizations, and L_1 and L_B are the layer thicknesses for the implanted and bulk layers, respectively. While Eq. (2.31) is useful in determining the relative changes in M_1 and M_B, for instance as a function of temperature, or annealing treatments, it is not an accurate method for determining either M_1 or M_B independently. This is partially attributed to the uncertainty in the FMR linewidth measurement, as well as the effects of spin pinning at the boundary between the bulk and implanted layer, which may shift the resonance field and distort the lineshape. We should point out that Suran et al. [15] used a factor $f(K_s)$, to account for the effect of the spin pinning. The $f(K_s)$ is 1 if there was no exchange coupling between the two layers, and $4/\pi^2$ when there is complete spin pinning at the interface of the bulk and implanted layers. That factor was not considered here, as the complete spin wave analysis has to be done to determine the spin pinning boundary condition.

Chapter 3
DEUTERIUM IMPLANT RESULTS

3.1. OVERVIEW '

The motivation for studying deuterium implants was twofold. First, they have a practical application in the fabrication of contiguous disk (CD) bubble memory devices. Second, although the the sources of the large anisotropy field change in hydrogen implanted films have been investigated by several workers [12, 42], it is still not well understood. We will show in this and the next chapter that the anisotropy field change in hydrogen and deuterium implants are attributable to the same mechanisms. Here, we report on a systematic study of the properties of deuterium implanted films, with emphasis on establishing the range of implant conditions which are suitable for use in CD bubble devices. The effects of implant dose on the film properties, multiple implants on the uniformity of the strain and anisotropy through the implanted layer, and annealing-induced changes in the film parameters were all studied. These are related to the design of an implanted layer which has good characteristics for device use. The mechanisms responsible for the implant-induced change in the uniaxial anisotropy field were also investigated.

Using the unique set of characterization techniques which were developed as part of this project, and described in Chapter 2, significant insight into the mechanisms which contribute to ΔH_E was gained. This included calculation of the magnetostriction, and the magnetostrictive field contribution to the total implantation-induced change in the uniaxial anisotropy field. Measurements of the temperature dependence of the anisotropy fields and magnetostriction provided information about the effects of different implant doses, and the degradation in the film properties attributed to deuterium overdoses. There are three principle reasons for analyzing the temperature dependence of the anisotropy fields. First, the analysis provides insight into the implant mechanisms. Second, the uniformity of the anisotropy and magnetization through the film thickness can be evaluated. Finally, good temperature dependent

behavior of magnetic properties in the implanted layer are desired in magnetic bubble devices. There has been considerable effort to extend the operating range of a bubble memory chip to -54°C to 155°C [66]. Thus, the analysis of the results from the implanted films at high temperatures are of substantial interest.

One of the unique characterization techniques involved implementing a wideband stripline structure which had sufficient sensitivity to measure the weak spin wave modes in the thin, ion implanted layers. As the implanted film thicknesses were typically in the range from 0.2 μm to 0.4 μm, it was necessary to boost the signal to noise ratio so that all of the detectable spin wave modes could be accurately measured. This was achieved with the serpentine-shaped microstrip conductor, DC block to reduce modulating field pick-up, and placement of the sample between the conductor and the ground plane, so the microwave magnetic field in the sample was stronger. The improvements to the FMR apparatus made the measurements reported here possible, as the existing apparatus [67] did not have sufficient sensitivity. The technique for measuring the magnetostriction, and its temperature dependence, is unique to this project.

3.2. ANALYZING RESULTS FOR DEUTERIUM IMPLANTED FILMS

The principle objective in selecting implant conditions for a CD device is to create a sufficient change in the anisotropy field so that the implanted layer will support magnetically charged walls. The implant-induced change in the anisotropy field must be larger than the uniaxial anisotropy field minus the magnetization, assuming that the effects of the cubic crystalline anisotropy field are small compared to $H_K - 4\pi M_s$. With single energy implant doses, the strain and anisotropy profiles are not uniform, but are peaked at or near the end of the projected range for the implanted ions [14]. Previous investigators have reported that films with uniform anisotropy and strain profiles have better bubble device operating margins [13]. To achieve uniform properties through the implanted layer multiple implants are used. While some investigators have used multiple species implants [68], we will show here that a combined deuterium and oxygen implant can produce a uniform strain, but due to the difference in the implant mechanisms for deuterium and oxygen, will not necessarily yield a uniform anisotropy profile. In this chapter, the use of multiple deuterium implants to create uniform strain and anisotropy profiles through the implanted layer thickness is discussed.

The FMR spectra of an implanted film typically consist of a series of spin wave modes, which are related to the magnetic anisotropy profile through the implanted layer. To evaluate the effects of the various implants, it is important to establish the relationship between the spectra and the anisotropy profile. While the spectra for singly implanted films have been adequately described [14], those for multiple energy implants have not been. In this thesis, a numerical spin wave analysis for a film with a multiple energy implant is done. The analyses of the spectra provided significant insight into the relationship between characteristic spectra and the anisotropy profiles and were of great utility in analyzing the results from the other films which were investigated.

3.2.1. Analysis of Ferromagnetic Resonance Spectra

To relate the FMR spectra to the anisotropy profile, the spectra from a multiply implanted film were analyzed. The FMR spectra for film 84, measured after a $250°C$ and a $700°C$ anneal, were analyzed using the program developed by Wilts and Prasad [40]. The implant conditions for film 84, given in Table 3-1, were selected to create a uniform strain and anisotropy profile through the implanted layer. The criteria for selecting these implants were based on the ion range statistics [11, 21] for deuterium in garnet. The procedure used in selecting the implant conditions will be discussed later.

Table 3-1:   Deuterium Implant Conditions for Film 84

Dose	Energy
1.2×10^{16} D_2^+/cm^2	80 keV
5×10^{15} D_2^+/cm^2	50 keV
3×10^{15} D_2^+/cm^2	25 keV

To compare the experimental results with those for a film with a uniform anisotropy profile through the implanted layer, the spectra for a uniformly implanted film were calculated using Wilts' program. The film parameters which were used in this calculation are similar to those for film 84. They are given in Table 3-2. The perpendicular resonance mode locations and amplitudes for the uniform anisotropy profile are given in the second and third columns of Table 3-3. The locations and amplitudes for the experimental modes in film 84 after the $700°C$ anneal, and those calculated using the spin wave analysis are also given. In a surface layer with uniform properties the amplitudes of the higher order modes decrease quadratically, and the spacing between higher order modes increases quadratically.

Table 3-2: Parameters for a Uniform Anisotropy Profile in Film 84

Bulk Data

$4\pi M_s$	$\gamma \times 10^{-7}$ (Oe-sec)$^{-1}$	$A \times 10^{7}$ ergs/cm	H_J	H_K	α	t
1160 G	1.551	3.5	-200 Oe	1620 Oe	.043	6000 Å

Surface Data

| 1100 | 1.54 | 3.4 | -200 | -550 | .04 | 4000 |

Table 3-3: Perpendicular Modes for Uniform Profile, Experimental Spectra and Calculated Fit using Numerical Spin Wave Analysis for Film 84 after a 700°C Anneal

1	2	3	4	5	6	7
Mode	Uniform		Experimental		Spin Wave Analysis	
	Field	Ampl.	Field	Ampl.	Field	Ampl.
1	3457 Oe	100%	3473 Oe	100%	3473 Oe	100%
2	3369	12	3317	20	3332	17
3	3196	5	3109	17	3119	14
4	2934	3	2853	4	2853	6
5	2588	2	2530	9	2512	5
6	2162	2	2157	7	2100	4
7	1662	4	1665	16	1621	8
Body	1339	143	1341	170	1339	184

The FMR spectra from film 84 after the 700°C anneal are shown in Figs. 3-1 and 3-2. In perpendicular resonance, seven surface modes are observed, whereas in parallel resonance, there is a significant amount of mode overlap so that the intermediate mode locations and amplitudes cannot be accurately identified. The perpendicular resonance spectrum is characterized by the spin waves which extend from the uniform mode to the bulk mode, and the closer spacing between modes 1 and 2 than between any of the higher order modes. The perpendicular mode locations and amplitudes for the best fit using the spin wave analysis are also given in Table 3-3. The calculated mode locations are within 20 Oe of the experimental values for the first 5 perpendicular modes. The calculated mode amplitudes are all within 4% of the experimental values, except for modes 7 and 8. However mode 7 can be adjusted independently from the other surface modes by changing H_K in the surface layer adjacent to the bulk, so this discrepancy is not considered to be significant. Mode 8 is the bulk mode. Its amplitude is very

Fig. 3-1: Perpendicular Resonance Spectra for Film 84
after 700°C anneal f = 4.78 GHz
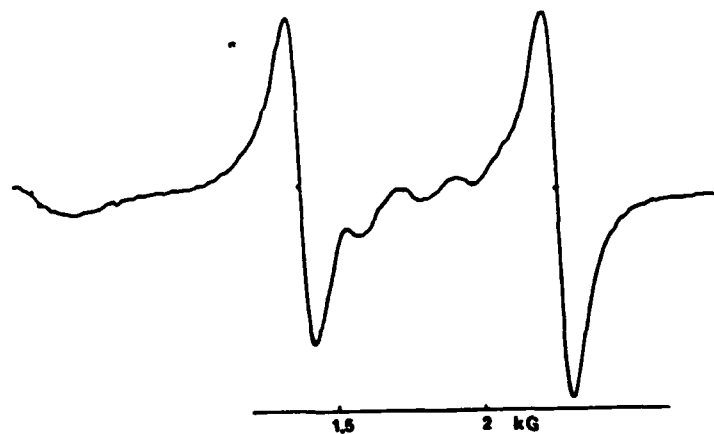
Fig. 3-2: Parallel resonance Spectra for Film 84
after 700°C anneal f = 4.78 GHz

sensitive to the bulk layer thickness and the other bulk parameters, and can be adjusted accordingly. Comparing the spectra for the uniform anisotropy profile with the experimental spectra, we note that there is a 50 to 100 Oe discrepancy in the mode locations for the modes 2 through 5, and the amplitudes for the experimental modes 2, 3, and 7 are significantly greater than those for the uniform profile. Thus the spin

Table 3-4: Parallel FMR Modes for Film 84 after 700°C Anneal
Experimental Modes Correspond to Spectra in Fig. 3-2

	Experimental		Calculated Fit	
1 Body	2124 Oe	100%	2120	100%
2			2080	12%
3			2000	5%
4	1813	4%	1880	4%
5			1725	4%
6	1626	9%	1541	5%
7	1432	22%	1343	17%
8 Surface	1245	80%	1248	98%

wave modes for the anisotropy profile which is shown in Fig. 3-3 gives a better fit to the experimental spectra than those for the uniform profile.

The most prominent features of the parallel resonance spectrum are predicted in the calculated spectrum. Both spectra are listed in Table 3-4. These include the location of the main surface mode (8) and a relatively large amplitude for the adjacent mode (7). Experimentally, the presence of the mode next to the body mode could be detected as an asymmetric line shape of the first mode, as can be seen in Fig. 3-2, but its location and amplitude could not be accurately determined. As most of the intermediate parallel modes, between the body and principal surface modes, are localized in the unimplanted layer, they are not affected by slight variations in the anisotropy field in the implanted layer.

For precise fitting of all of the modes, profiles of A and $4\pi M_s$ may be required. Since the film was annealed to 700°C, the variations in A and $4\pi M_s$ are expected to be small, as most of the implant-induced damage is reportedly restored upon annealing at that temperature [14]. Experimental evidence for the annealing-induced restoration of $4\pi M_s$ will be given later. The value of $4\pi M_s$ in the ion implanted layer was chosen to match the first resonance mode location in the calculated spectrum with the experimentally determined location after the best fit was obtained. The spin wave mode spacing is proportional to $A/M_s t^2$, so it is only possible to obtain relative values of A and M_s for a given implanted film thickness t. The uncertainty in the $4\pi M_s$ in the implanted layer is estimated to be less than 100 G. The H_1 was not varied in the fitting procedure. Although the H_1 value is significant, it is small compared to H_K and

$4\pi M_s$. Thus a variation in H_1 has a much smaller effect on the spectra than variations in H_K, $4\pi M_s$, or A.

The H_K profiles for film 84, after a 700°C anneal is plotted in Fig. 3-3. The film parameters used in the fit are listed in Table 3-5.
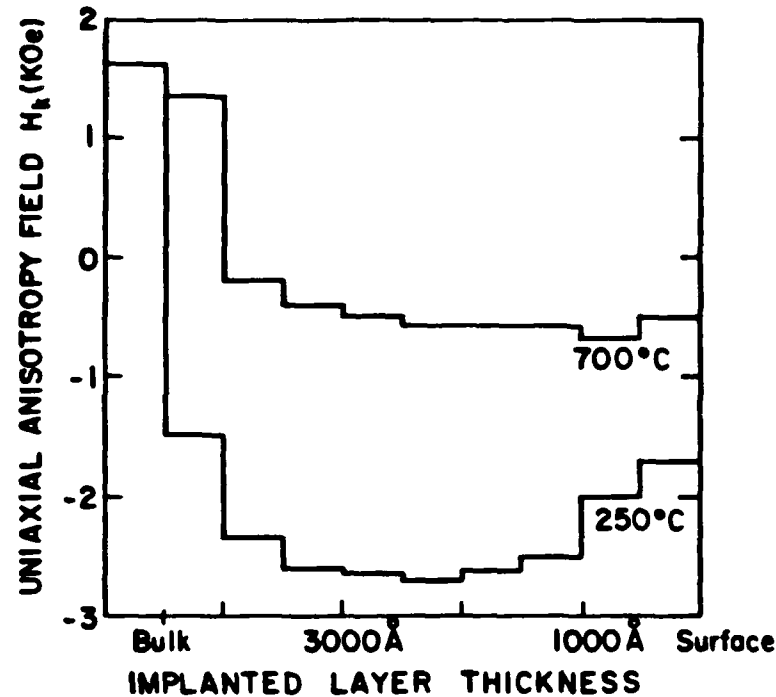
Fig. 3-3: H_K Profile For Film 84

Table 3-5:   Parameters for Film 84 Used in Spin Wave Analysis

Layer	H_K	$4\pi M_s$	A	H_1	α	γ
250°C Anneal			ergs/cm			(Oe-sec)$^{-1}$
Bulk	1595 Oe	1257 G	3.5×10^{-7}	−146 Oe	.05	1.58×10^7
Implant	•	900	2.2	−100	.06	1.60
700°C Anneal						
Bulk	1620	1160	3.5	−200	.043	1.55
Implant	•	1100	3.4	−200	.04	1.54

• Profiled through thickness

Some of the significant features of the magnetic anisotropy profile for film 84, after a 700°C anneal, shown in Fig. 3-3, include the gradual transition from the bulk to the surface layer, an increase in ΔH_K towards the surface-air interface, and a maximum ΔH_K near, but not at the air interface. The uncertainty in H_K in the region from 1000

$\overset{\circ}{A}$ to 4500 $\overset{\circ}{A}$ from the bulk–surface interface is less than 100 Oe. The relative H_K values are accurate to within 50 Oe in this region, as determined by varying the H_K surface values by this amount and noting the change in the calculated mode spectra. To obtain this fit, no profiles of $4\pi M_s$, A, or H_1 were used. While certain changes in the profile can be related to changes in specific mode locations and amplitudes, in general the entire spectrum is extremely sensitive to minor variations in the anisotropy profile. An analysis of the sensitivity of the calculated spectra to variations in the anisotropy profile are given in the appendices.

The fitting procedure was also performed using the spectra for film 84, measured after the 250°C anneal. The experimental and calculated resonance mode positions and amplitudes are listed in Tables 3–6 and 3–7, and the anisotropy profile is plotted in Fig. 3–3. The most notable features of the profile include the lower change in the anisotropy field at the film surface and the maximum change in the anisotropy field near the center of the implanted region. In contrast to the 700°C annealed film, there is a relatively sharp transition in H_K from the implanted to the bulk layer.

Table 3-6: Perpendicular FMR Modes for Film 84 after 250°C Anneal

	Experimental*		Calculated Fit*	
Mode	Field	Amp.	Field	Amp.
1	5186 Oe	100%	5188 Oe	100%
2			4978	0%
3	4737	40%	4733	35%
4			4456	3%
5	4176	16%	4230	24%
6			3969	0%
7	3793	4%	3614	6%
8			3215	3%
9			2797	3%
10			2326	6%
11			1779	6%
12 Body	1337	400%	1337	294%

* f = 4.5 GHz

The perpendicular and parallel spectra for film 84, measured after a 250°C anneal, are shown in Figs. 3-4 and 3-5. In the perpendicular spectra, four surface modes were

Table 3-7:   Parallel FMR Modes for Film 84 after 250°C Anneal

		Experimental		Calculated	
1	Body	1940 Oe	100%	1941 Oe	100%
2				1889	12%
3		1770		1787	4%
4		1616		1632	2%
5		1416		1424	2%
6				1164	2%
7				861	5%
8		788	50%	816	47%
9				695	57%
10				616	0%

observed, which had progressively decreasing amplitudes for the higher order modes. The main surface mode and the bulk mode had comparable linewidths. In the parallel spectra, there is a mode overlapped with the bulk mode. The principal surface mode, which is at the low field end of the spectrum, appears to be comprised of two adjacent, overlapping modes. In the calculated spectra, there is an alternating sequence of strong-weak mode amplitudes. The first and third calculated mode locations match the first two experimental modes, and the second and fourth calculated modes have amplitudes which are too small to be detected. Although the measured modes do not overlap, the spacing and linewidth prevent detection of any weak modes which may lie between the observed modes. The calculated locations of the fifth and seventh surface modes are 54 Oe higher and 179 Oe lower than the experimental mode locations, respectively. The discrepancy in the calculated and experimental mode locations for the higher order modes may be related to the fact that the magnetization in the region with the maximum ΔH_E is not aligned with the applied field at the fields where the higher order modes are expected to be found. This will either shift the location of the experimental modes, or cause them to not be observed experimentally, even though they are predicted in the calculated spectrum. This effect will be discussed later. The mode amplitudes are within 3% on all but the fifth and the body mode. The discrepancy in the body mode may be related to a shift in the bulk film properties caused by annealing, and will be discussed later. This discrepancy can be removed by appropriate choice of the bulk film parameters.

In these measurements, the parallel resonance was measured with the field along the

in-plane [110] direction, instead of the [112] direction which is normally used. The resonance spectra here will be shifted by less than 30 Oe, due to the effects of the crystalline anisotropy field. In parallel resonance, there are two surface modes with nearly equal amplitudes which straddle the location of the experimentally measured mode at 788 Oe. The distorted lineshape of the experimental mode leads us to conclude that it is comprised of two overlapping modes, as predicted in the calculated spectra. The experimental mode amplitudes for the intermediate modes are typically less than 4%. Their values are not given in Table 3-7, as they could not be accurately determined due to overlap of the adjacent modes.

The fit for the 250°C annealed film is not as good as that for the 700°C annealed film. This is attributed in part to the problem with exciting all of the spin wave modes, but may also be caused by minor variations in $4\pi M_s$ and A through the film thickness which were not taken into consideration. However from the fit which was obtained it is clear that the anisotropy field change at the film surface is considerably lower than that in the central part of the film, which indicates that either a lower energy implant or a higher dose for the 25 keV implant are required to improve the uniformity of the anisotropy profile.

To relate the anisotropy profiles to the FMR spectra for the films which were investigated, we will compare the results for film 84. The separation between the highest and lowest field modes in the FMR spectra is related to the maximum change in the anisotropy field in the film. For film 84, the ΔH_E after the 700°C anneal is 2257 Oe. In the anisotropy profile shown in Fig. 3-3, the H_K in the bulk is 1620 Oe, compared to a minimum (negative maximum) of −650 Oe, which corresponds to a total change of 2270 Oe. The ΔH_E after the 250°C is 4148 Oe, compared to a difference of 4320 Oe from the bulk to the negative maximum in the surface layer. Thus the agreement between the H_K profile and the ΔH_E calculated from the frequency dependence of the bulk and main surface mode is better for the more uniform profile.

In summary, the numerical spin wave analysis was used to analyze the ion implanted garnet films. Once the anisotropy profiles for a particular implant is determined, the implant conditions can be modified to improve the uniformity. The major drawbacks of the spin wave analysis are that the fitting procedure requires considerable time to achieve a good fit, so that it is not convenient to use as a routine analytical tool. Furthermore, due to the large number of parameters which affect the spin wave
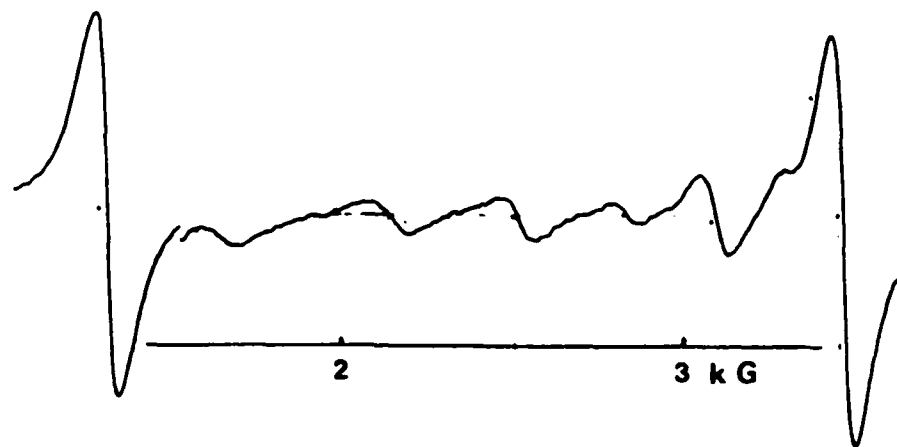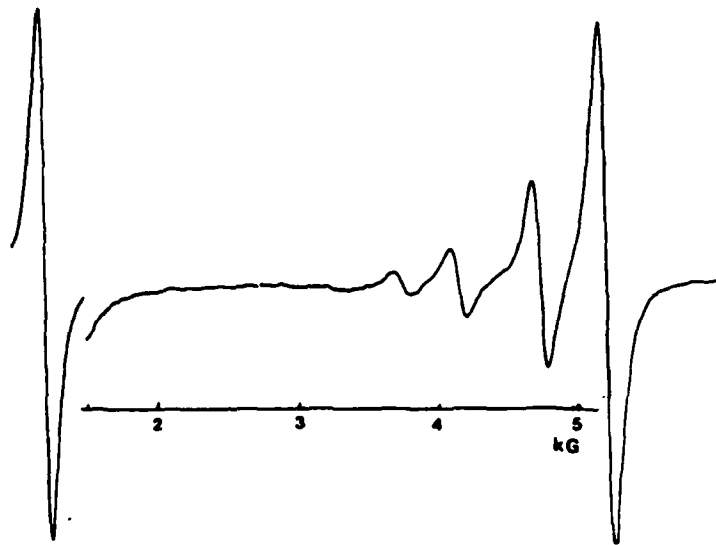
Fig. 3-4: Perpendicular resonance spectra for Film 84
After 250°C Anneal, f = 4.5 GHz
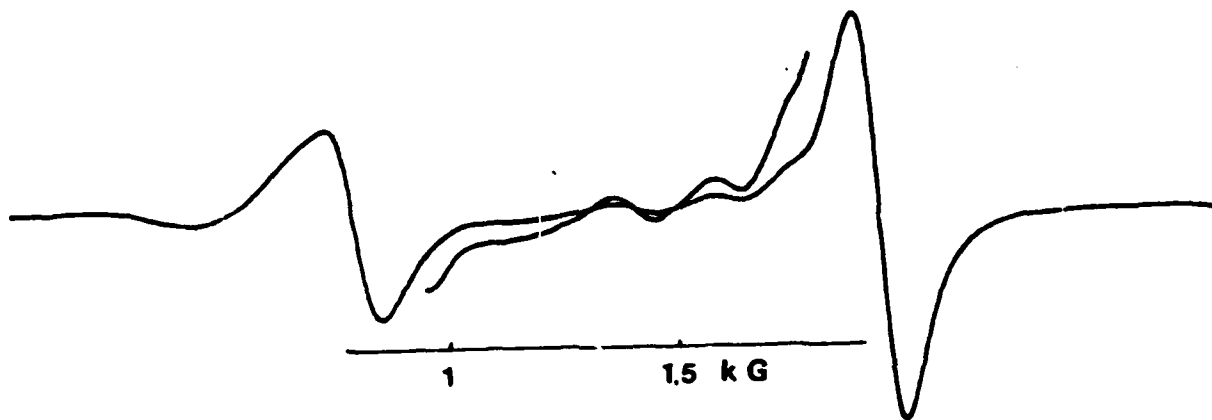
Fig. 3-5: Parallel resonance spectra for Film 84
After 250°C Anneal, f = 4.5 GHz

spectra, it is difficult to establish a unique set of conditions which match any given set of experimental spectra. If only a few surface modes are observed, then accurate fitting is more difficult. In films which have a multiply peaked (bi- or polymodal) anisotropy profiles, due either to multiple energy implants or excessive damage created

by a single or multiple energy implant, the spin waves may not extend throughout the entire implanted layer. In these films, analysis of the spin wave spectra can only be done by etching the film and reconstructing the profile in reverse order of the etching steps. No etching experiments were done here. Calculated spectra for hypothetical bimodal anisotropy profiles are given in the appendices. We will only note here that they are characterized by irregular mode spacings, although there are an infinite number of anisotropy profile configurations which will result in an infinite combination of surface modes. On the positive side, certain features of the experimental spectra can be related to particular anisotropy profiles. This is a great aid in the comparison of the spectra for films after various implants and annealing treatments. Examples of the relationships between the spectra and the implant conditions will be discussed in the following sections.

3.3. TOWARDS A UNIFORM IMPLANTED LAYER

The purpose of the investigation here was to find the optimal implant conditions for bubble devices. This includes characterizing the effects of multiple deuterium implants on the film properties, and establishing the implant conditions where the magnetic properties in the film and their temperature dependences become seriously degraded. The multiple implants are intended to improve the uniformity of the anisotropy and strain through the implanted layer. The effectiveness of the multiple implants is evaluated. Results are given for implants which produced reasonably uniform properties for both one micron and half micron diameter bubble devices.

3.3.1. Characteristic Features of Multiple Implants

Multiple energy implants are used to achieve uniform strain and anisotropy profiles. To characterize the effects of additional implants on the film properties, multiply implanted films 55, 82, and 150 were measured after each implant. Material parameters are given in Table 3-8 and the implant conditions are listed in Table 3-9.

Table 3-8: Garnet Film Parameters

Sample	t (μm)	l (μm)	$4\pi M_s$ (G)	H_E (Oe)	λ_{111}
55	0.96	0.10	704	577	-2.1 (10^{-6})
82	0.70	0.06	1212	601	-2.6
150	0.70	0.06	1292	810	-2.1

The FMR spectra for film 55 after the first implant, shown in Fig. 3-6, consists of

Table 3-9: Implant Conditions

Film	Implant #	Dose D_2^+/cm^2	Energy	Dose D_2^+/cm^2	Energy
55	1	1×10^{16}	88 keV		
	2	5×10^{15}	44		
	3	5×10^{15}	80	3×10^{15}	25 keV
82	1	2×10^{16}	88		
	2	1×10^{16}	44		
150	1	3×10^{16}	88		
	2	1.25×10^{16}	55	8×10^{15}	25

five surface modes with alternating strong and weak amplitudes. This difference is expected based on the spin wave analysis, as the anisotropy profile is peaked deeper in the implanted layer of film 55 due to the higher implant energy. The odd, higher order mode amplitudes increase as the thickness of the surface layer increases, as it does when the implant energy is increased.
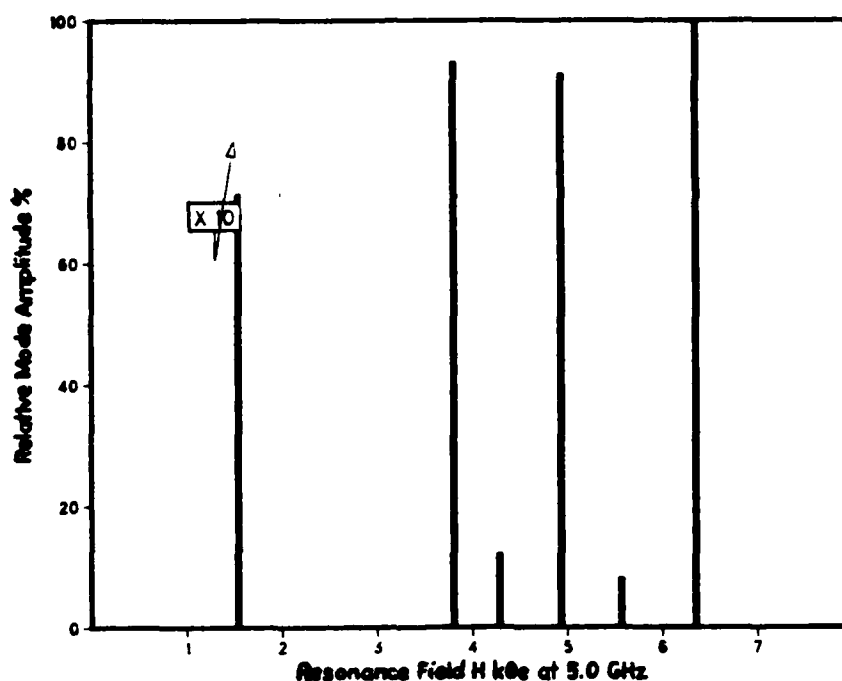
Fig. 3-6: FMR spectra for Film 55 After First Implant

The FMR spectra for film 55 after the second implant, and 200°C anneal are shown in Fig. 3-7. The three strong surface modes which were observed in the spectra measured after first implant, shown in Fig. 3-6, were observed, although the third and

fifth mode amplitudes are smaller. The spectra are compressed, with the largest change in the highest order modes. The 200°C anneal decreased the positions of the lower order surface modes. There was a weak second mode which disappeared after the anneal.
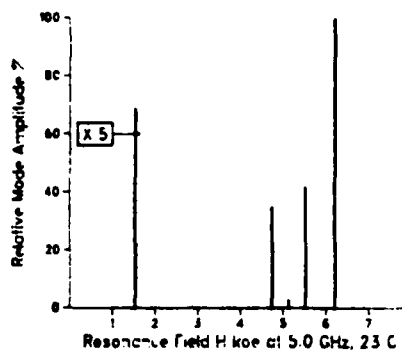
Fig. 3-7: FMR Spectra for Film 55 after the Second Implant and Anneal: at 23°C

The rocking curve for film 55 after the first, second, and third implants are shown in Fig. 3-8. After the first implant, there are strong peaks at the low and high angle side of the rocking curve. This implies that there is a relatively large region of constant strain, between the film surface and the location of the maximum implant strain deep in the film. The X-ray rocking curves for film 55, After the second implant, the strong peak on the high angle side of the envelope of the surface peaks, which is related to the strain at the film surface, was weaker and broader. The maximum strain ϵ_{max}, and surface strain ϵ_{surf} at room temperature in the as-implanted and annealed films are given in Table 3-10. The anneal improved the strain uniformity, as indicated by the reduced width of the envelope of X-ray rocking curve peaks.

Since the first two implants on film 55 did not result in a particularly uniform anisotropy and strain profile, a third implant was used. The third implant was designed to improve the uniformity of the anisotropy profile by increasing ΔH_E both deep in the film and at the film surface. The implant energy for the high energy implant was slightly less than that for the first implant to accomodate the needs of other workers whose samples were implanted at the same time, although this was not expected to have a significant effect on the results. The FMR spectra for film 55 after the third implant are shown in Fig. 3-9. The relative bulk mode amplitude is nearly twice what
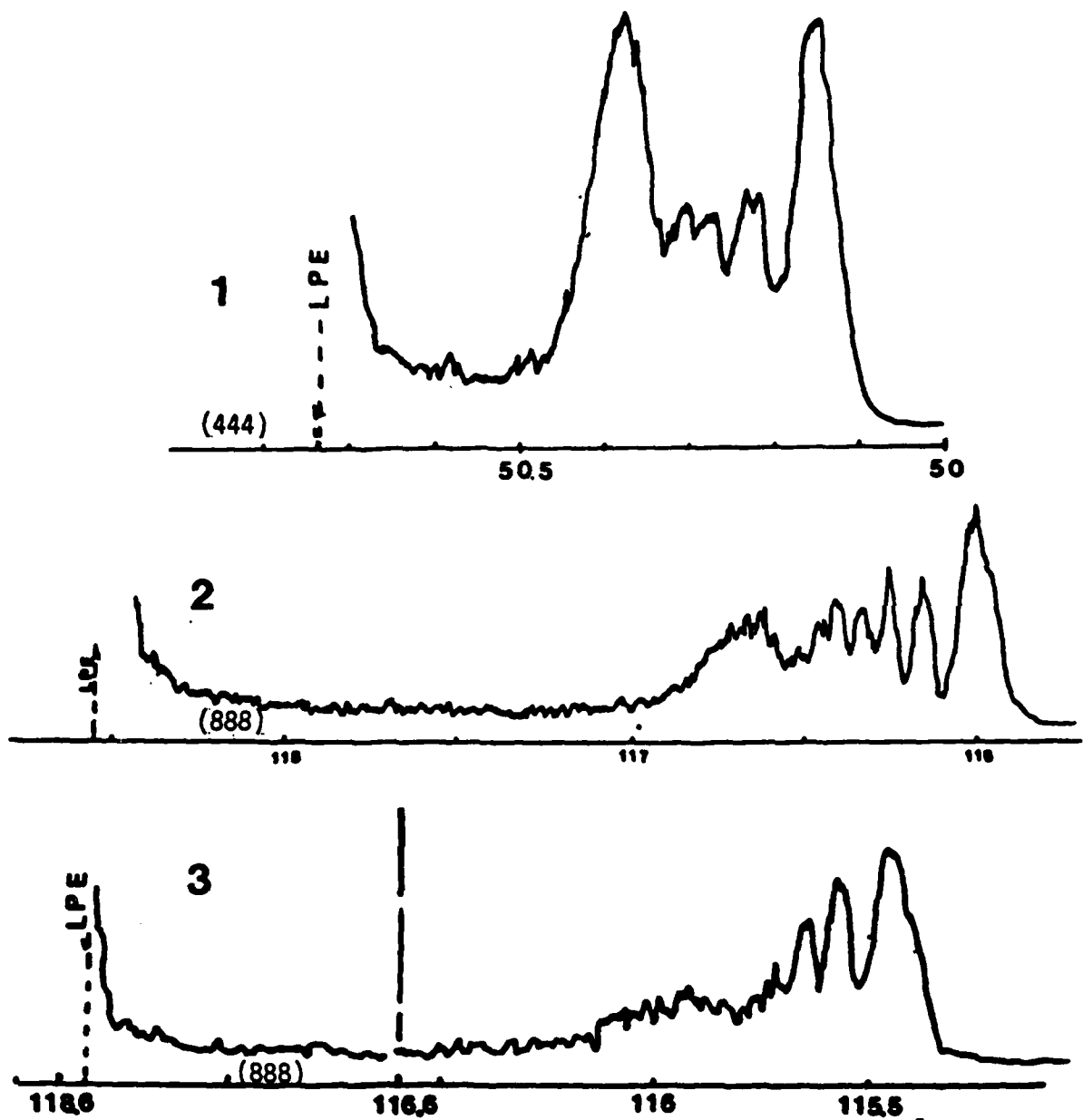
Fig. 3-8:   X-ray Rocking Curves for Film 55 after First, Second, and
Third Implants

it was after the second implant and anneal. This indicates that the third implant caused a considerable reduction in the magnetization in the implanted layer. The proximity of the first and second surface modes, and the relatively strong amplitude of the second mode, indicates that the anisotropy profile is not uniform, presumably due to the overdamage caused by the 80 keV implant. To produce a more uniform anisotropy profile, the high energy implant dose should be reduced. The rocking curve after the third implant is shown in Fig.3-8. The third implant did improve the strain uniformity, as evidenced by the narrower envelope of the diffraction peaks in the rocking curve. Thus, the third implant did improve the strain uniformity even though the magnetic properties were degraded due to overdamage in the film.
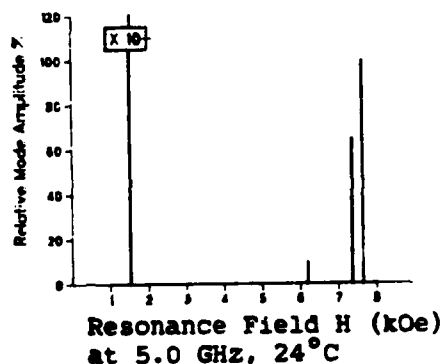
Fig. 3-9: FMR Spectra for Film 55: After Third Implant

The first dose for film 82 was twice that for film 55. We will show here that this dose resulted in the formation of a bimodal anisotropy profile, presumably because of the overdamage caused by the implant. The envelope of the X-ray rocking curve peaks was quite similar to that for film 55, although the envelope was shifted to lower angles, since there was more strain in the film, as indicated in Table 3-10.

The FMR spectra for film 82 are shown in Fig. 3-10. The spectra for film 82 has the same alternating sequence of mode amplitudes as that for film 55, which was shown in Fig. 3-6. However there is a significant difference in the spectra which is attributed to overdamage which resulted in the formation of a bimodal anisotropy profile. For the magnetization in the region of the maximum ΔH_E to align with the applied field H_A, H_A must be greater than $(H_{UN} - \omega/\gamma)$, where H_{UN} is the field for uniform resonance in the implanted layer at frequency ω [50]. If this condition is not met, then the higher order modes will either not be excited, or their location will be shifted from that predicted in the spin wave analysis. Results for films 55 and 82 are listed in Table 3-11.

Table 3-10: Strain in Films 55, 82 and 150

Film 55	Implant 1	Implant 2	1 hr 200°C	Implant 3
ϵ_{surf}	0.65%	0.96%	0.74%	1.24%
ϵ_{max}	1.07%	1.32%	1.10%	1.57%

Film 82	Implant 1	Implant 2
ϵ_{surf}	0.82%	1.22%
ϵ_{max}	1.51%	1.79%

Film 150	Implant 1	2:20 hr 200°C	Implant 2 and Anneal
ϵ_{surf}	1.29%	1.07%	–
ϵ_{max}	2.17%	1.70%	1.87%
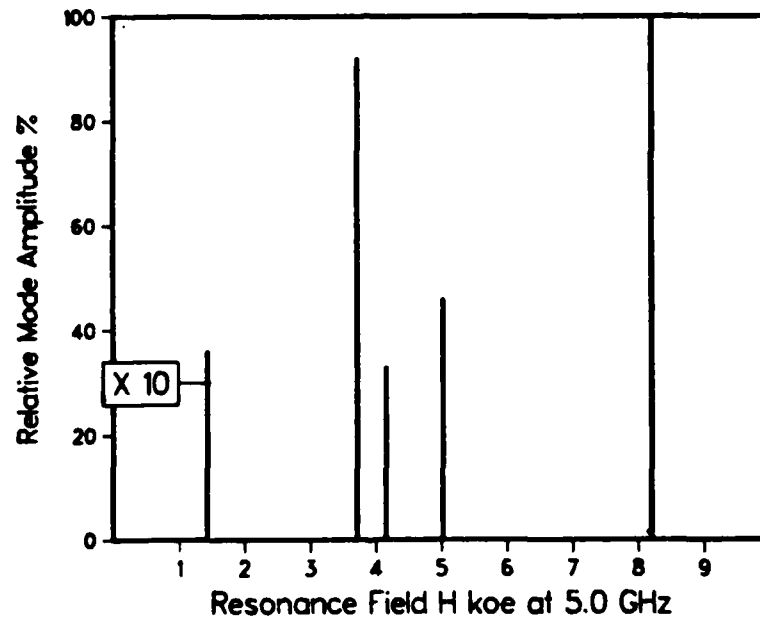
Fig. 3-10: FMR Spectra for Film 82: As-Implanted, 25°C

Table 3-11: Evidence for Bimodal Anisotropy Profiles

	Film 55	Film 82
$H_{UN}-\omega/\gamma$	4218 Oe	6083 Oe
Lowest Field Mode	3805 Oe	3723 Oe

For film 55, the lowest field surface mode, at 3805 Oe, is approximately 400 Oe below the lower limit given by the ($H_{UN}-\omega/\gamma$) criterion. However in film 82, there

is a 2.3 kOe discrepancy. This indicates that the spin wave modes are localized in different regions of the film, and do not extend through the entire surface layer. Thus the implant in film 82 apparently created a bimodal anisotropy profile, which is presumably due to overdamage in a portion of the film.

Film 82 also received a second implant, at half the dose and energy of the first, as indicated in Table 3-9. The FMR spectra for film 82 after the second implant are shown in Fig. 3-11. The surface modes appear to be localized in the same regions as those measured after the first implant, however more spin waves, which are apparently localized in the region of the maximum ΔH_E were observed and the large amplitude surface mode at the lowest field disappeared. The peculiar mode distribution indicates that the second implant did not improve the uniformity of the anisotropy profile.
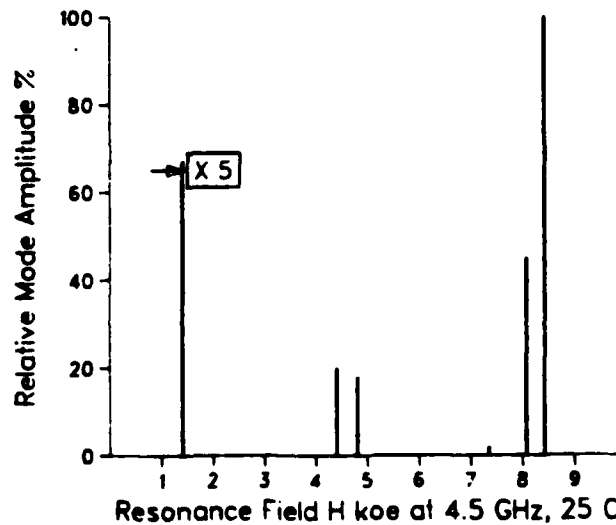
Fig. 3-11: FMR Spectra for Film 82 after the Second Implant

The results from films 55 and 82 indicate that a second implant at half the dose and energy of the first does not produce a particularly uniform implanted layer, presumably because the lower energy implant dose is too high, as evidenced by the increase in ϵ_{max}, which is given in Table 3-10. Ideally the lower energy implant should increase the surface strain without significantly increasing the maximum implant strain attributed to the high energy implant. To achieve a more uniform strain profile in film 150, a slightly different strategy than using half the dose at half the energy of the first implant was employed.

The initial implant on film 150 was three times larger than that for film 55, as

indicated in Table 3-9. The spectra for film 150 which were measured after a 200°C anneal at 25°C are shown Fig. 3-12.
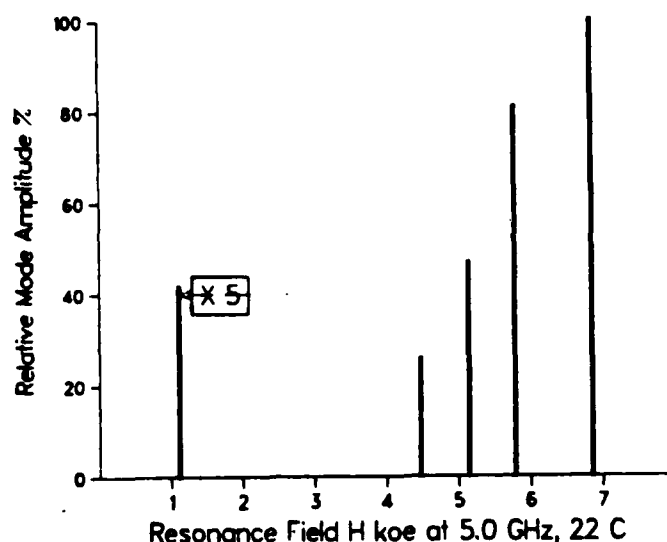
Fig. 3-12: FMR Spectra for Film 150 after First Implant and 200°C Anneal: 22°C at 5.0 GHz

The ΔH_E in the as-implanted film was estimated to be 9575 Oe, as determined from extrapolation of high temperature measurements to room temperature. After a 200°C anneal ΔH_E was reduced to 5706 Oe. The anneal also caused the maximum implant strain to decrease from 2.18% to 1.70%. Although the principle surface mode was not detected in the as-implanted film at room temperature due to the field limit of the magnet, the higher order surface modes which were detected were weak and had considerably broader linewidths than the bulk mode, indicating that the magnetic properties of the implanted film were degraded by the implant. The surface modes in film 150 in Fig. 3-12, measured after the 200°C anneal have progressively decreasing amplitudes for the higher order modes. However, this is not analogous to the situation where the anisotropy profile is uniform. The high temperature measurements indicate that the anisotropy profile does not decrease uniformly with temperature through the film thickness. These results will be presented in the next section. In an attempt to create a more uniform strain profile, the additional implants for film 150 were done under slightly different conditions then those for films 55 and 82. The implant conditions for the second implant are given in Table 3-9. The FMR spectra for film 150 in Fig. 3-13 were measured after a 200°C anneal.

The second implant did increase the maximum strain in film 150, as indicated in

Resonance Field H (kOe)
at 4.5 GHz
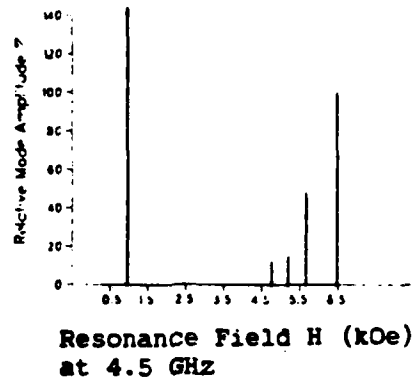
Fig. 3-13: FMR Spectra for Film 150: After 2nd Implant and 200°C Anneal
at 25°C

Table 3-10, from 1.70 to 1.87% (after 200°C anneal), however the strain profile became
more uniform, as evidenced by the single, strong implanted layer diffraction peak in
the double crystal X-ray diffraction rocking curve, which is shown in Fig. 3-14.
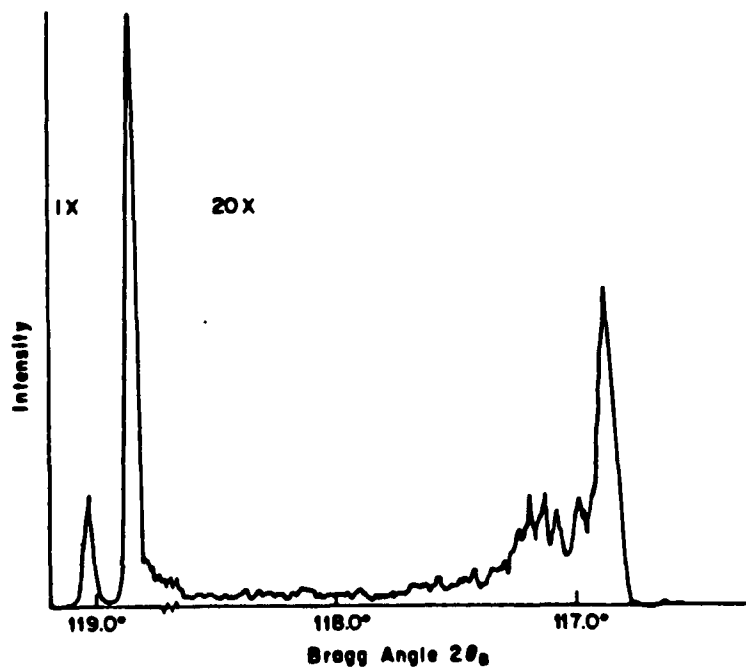
Fig. 3-14: X-Ray Rocking Curve for Film 150 After Second Implant and Anneal

Here, we have shown that the multiple implants which were chosen did improve the
strain uniformity, but due to overdamage in the central part of the film, did not create

the desired uniform anisotropy profile.   More evidence for the degradation of the film properties will be given later.   The implant conditions which resulted in relatively uniform anisotropy profiles will also be given.

3.3.2. Temperature Dependence of Anisotropy Fields in Singly Implanted Films

The temperature dependence of the anisotropy fields were determined in films which received a single energy and dose implant.   The bulk film properties measured before implantation including t, l, and $4\pi M_s$, and the change in the uniaxial anisotropy energy density in the as-implanted film $\Delta K_{as,\,u}$, and the 200°C annealed film ΔK_{ann}, are given in Table 3-12.

Table 3-12:   Bulk Parameters and Implant Results for Films 94, 140, and 172

Film	t	l	$4\pi M_s$	$\lambda_{111}/M_s(B)$ G^{-1}
94	0.85 μm	0.11 μm	770 G	-3.9 (10^{-8})
140	1.2	0.11	790	-3.9
172	3.5	0.19	504	-5.0

Implant Conditions 5×10^{15} D_2^{+}/cm^2 at 44 keV

The X-ray rocking curve for film 172 taken before and after a 200°C are shown in Fig. 3-15.   Annealing decreased the maximum implant strain slightly, as evidenced by the shift in the lowest angle peak to a higher angle, but did not significantly affect the shape of the rocking curve.   The FMR spectra for film 140, measured after the annealing are shown in Fig. 3-16.   The FMR spectra in Fig. 3-16 are characterized by the alternating strong-weak mode amplitude sequence, and are similar to spectra from films which received single energy hydrogen implants reported by previous investigators [14].   Stick diagrams representing the FMR spectra for film 140, both as-implanted and after the 200°C anneal, the latter of which corresponds to the spectra in Fig. 3-16, are given in Fig. 3-17.   In Fig. 3-17, as in most of the figures where the FMR spectra are shown in stick diagram form the principal surface mode is assigned an amplitude of 100%.   The bulk mode amplitude, relative to the principal surface mode is indicated by the scale factor when it would otherwise be offscale.   The annealing sharpened up the surface modes and the mode intervals decreased, with the larger decrease in the higher order modes.

The FMR spectra were measured as a function of temperature on film 140.   Material
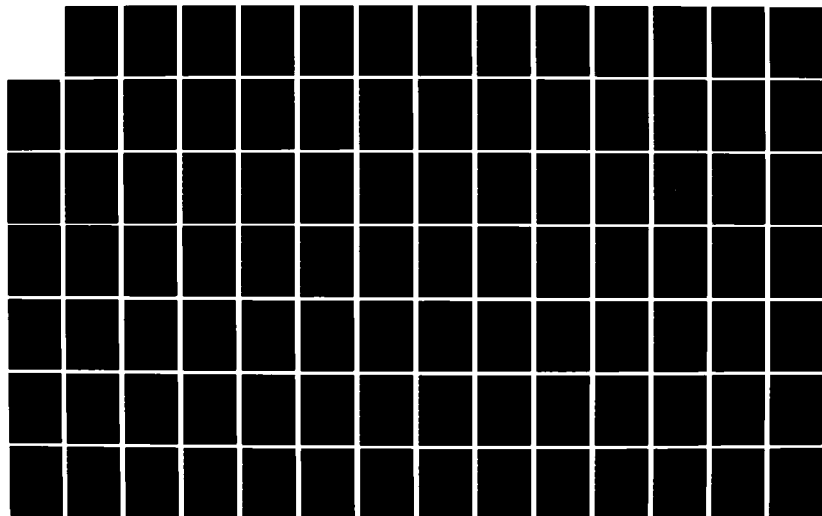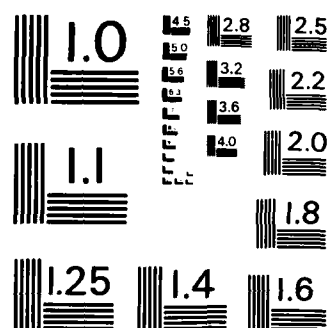
MICROCOPY RESOLUTION TEST CHART

NATIONAL BUREAU OF STANDARDS-1963-A
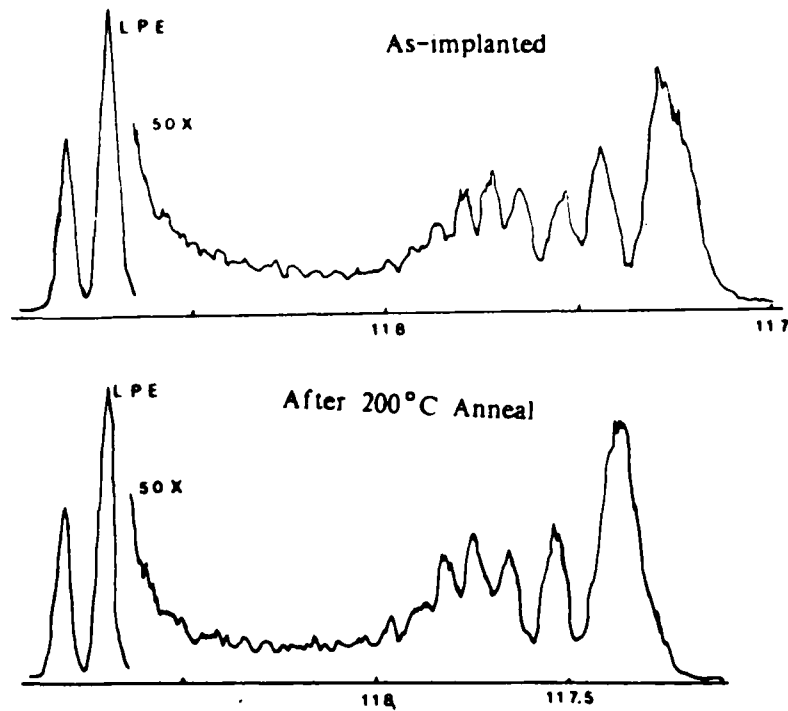
Fig. 3-15: X-Ray Rocking Curve for Film 172:
As-implanted and After 200°C Anneal
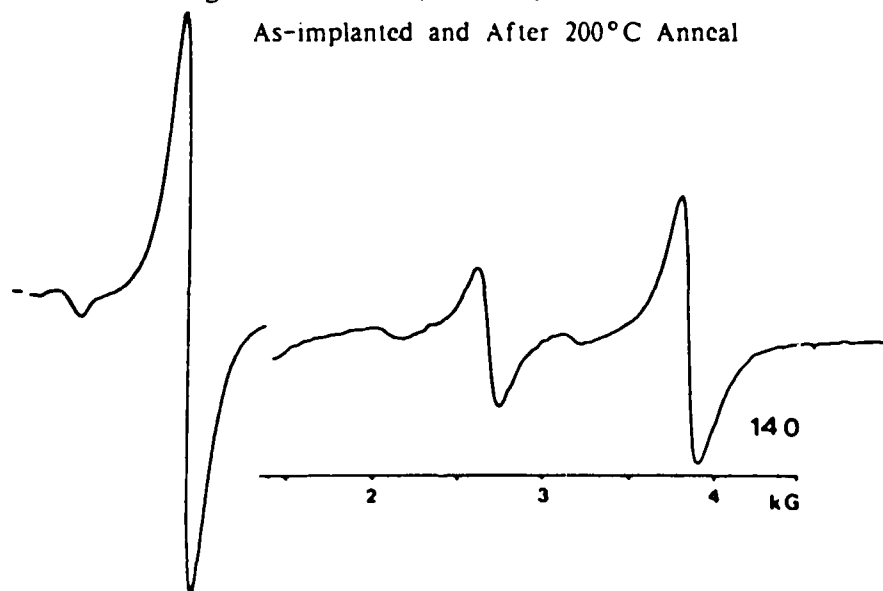
Fig. 3-16: FMR Spectra for Film 140 : After 200°C Anneal

parameters and implant conditions are given in Tables 3-8 and 3-9. The perpendicular
FMR spectra of the annealed film (2½ hrs. at 200°C) are shown in Fig. 3-18. As the
temperature was increased, the mode positions decreased, although the relative amplitude
of the modes was nearly constant. The amplitude of the bulk mode relative to that of
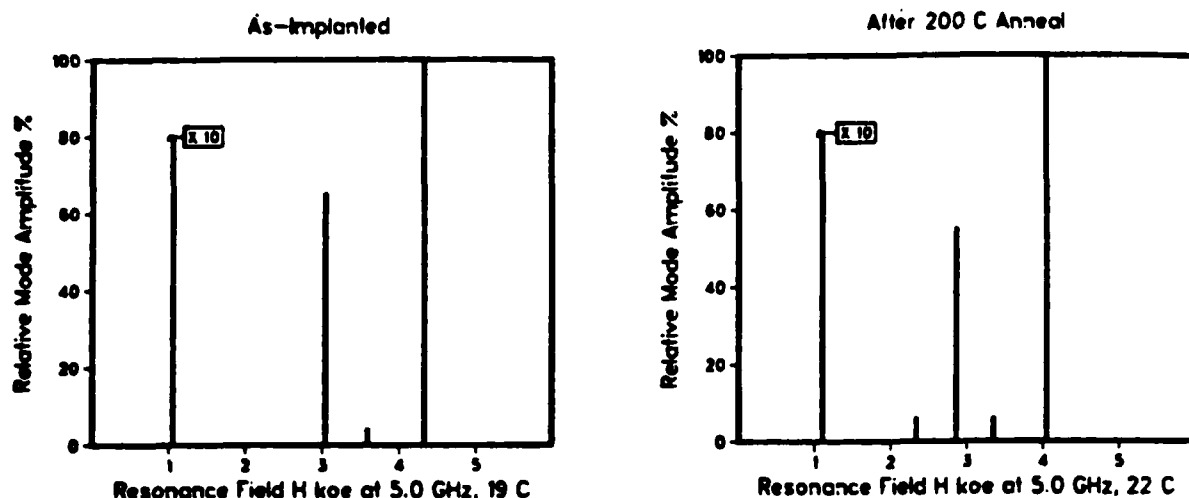
Fig. 3-17: Stick Diagrams of FMR Spectra for Film 140 As-Implanted and after a 200°C Anneal

the first surface mode was the same at all three measurement temperatures. This indicates that the magnetization in the bulk and implanted layer decrease proportionately with temperature. The similarity of the spectra at high temperatures suggests that the anisotropy decreases uniformly through the film thickness with increasing temperature, and not more rapidly in the region with the maximum damage as will be shown later for overdamaged films. Thus, the implant dose for film 140 did not cause a significant degradation in the temperature dependences of the magnetic properties of the implanted layer.

The $H_E(B)$ and $H_E(I)$ for film 140, measured after a 150 min. anneal at 200°C are plotted in Fig. 3-19. Both $H_E(B)$ and $H_E(I)$ decrease smoothly with increasing temperature. The Curie temperature $T_C(I)$ in the implanted layer is given by their intersection at 195°C. Above this temperature there is only one mode, which corresponds to the bulk layer. The $T_C(B)$ in the bulk was not measured, but is estimated to be significantly higher than 200°C based on the strong bulk mode that was observed at the highest measurement temperature. The ΔH_E and ΔH_σ versus temperature in the as-implanted sample and annealed film are plotted in Fig. 3-20. The ΔH_E in film 140 decreased by approximately 10% at 25°C after the 200°C anneal. The ΔH_σ was approximately 60% of ΔH_E over the entire measurement temperature range from 19°C to 123°C, in the as-implanted sample. The relative contribution of ΔH_σ to ΔH_E was nearly the same in the as-implanted and annealed film.
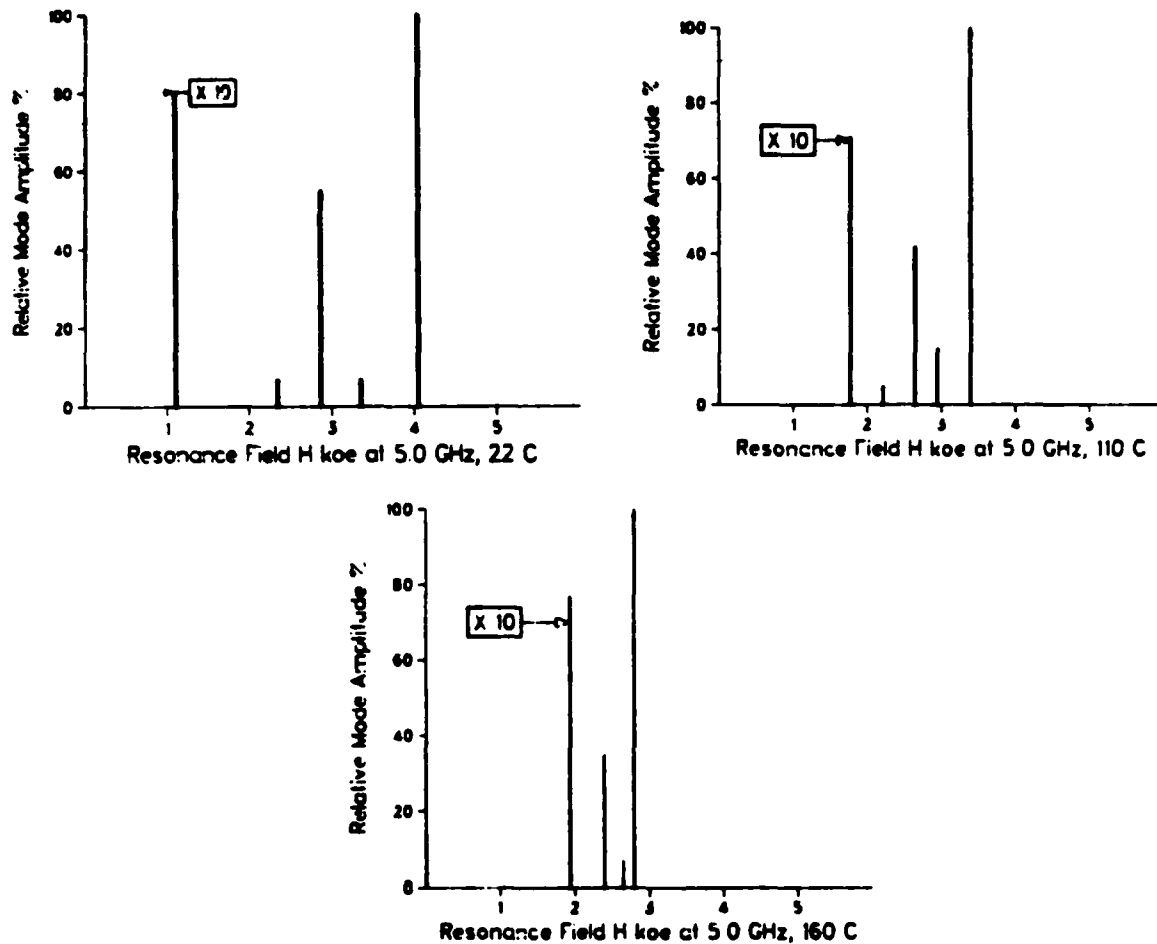
Fig. 3-18: Perpendicular FMR Spectra for Film 140 after 200°C Anneal
at 22°C, 110°C and 160°C

3.3.3. Temperature Dependence of Anisotropy Fields in Multiply Implanted Films

The high temperature FMR measurements were used to determine if the anisotropy decreased uniformly through the film thickness with temperature. It will be shown that the implanted layer of films with high deuterium doses does not have good temperature characteristics due to overdamage which results in a reduction of the Curie temperature in the overdamaged region.

The spectra for higher temperature measurements on film 55 are shown in Fig. 3-21. At 121°C, there are two strong surface modes and three modes with near equal amplitudes which are presumably spin wave modes. These modes span the range
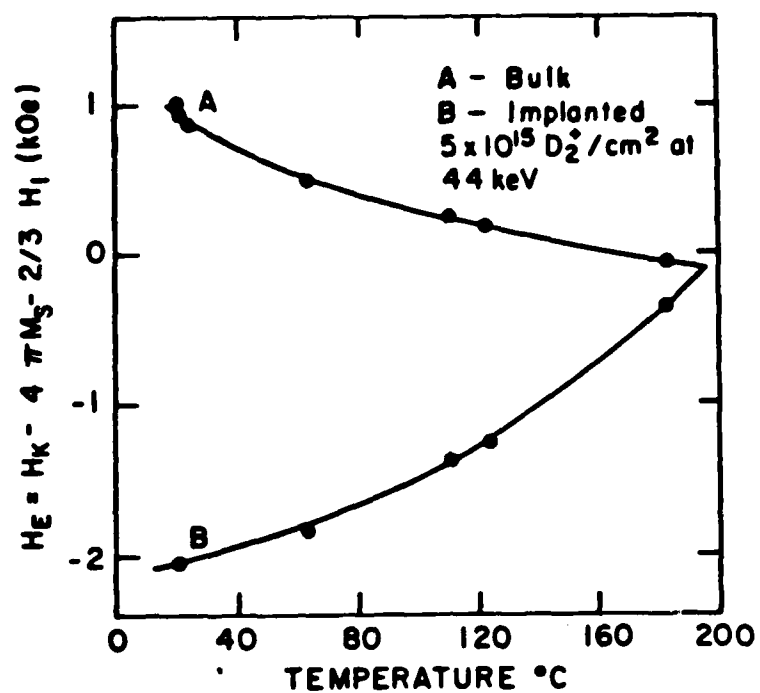
Fig. 3-19: Temperature Dependence of $H_E(B)$ and $H_E(I)$ for Film 140
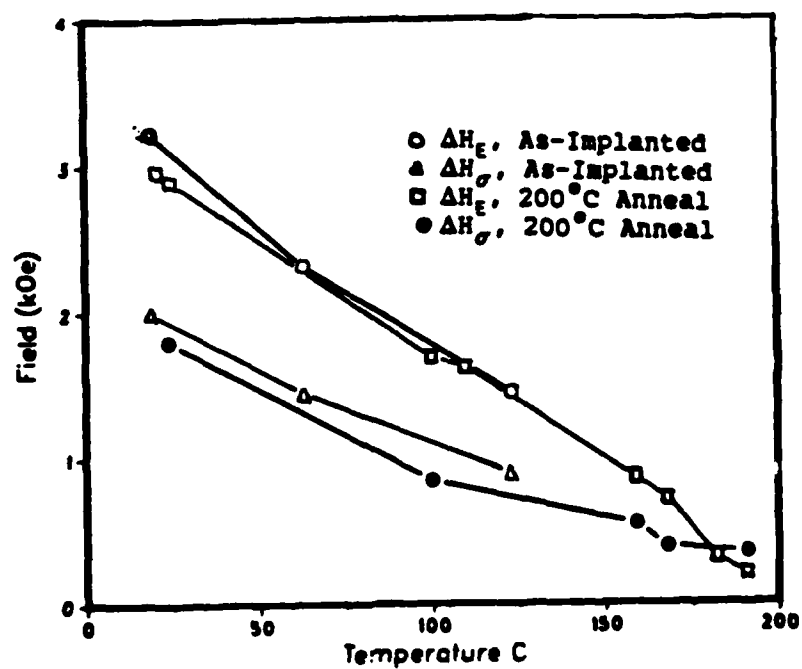
Fig. 3-20: Temperature Dependence of ΔH_E and ΔH_σ for Film 140

between the two strong surface modes and the bulk modes. At 154°C, the two strong surface modes are still observed, but two of the three weak amplitude modes have disappeared, presumably because of the small difference in field between the bulk and strong surface modes.
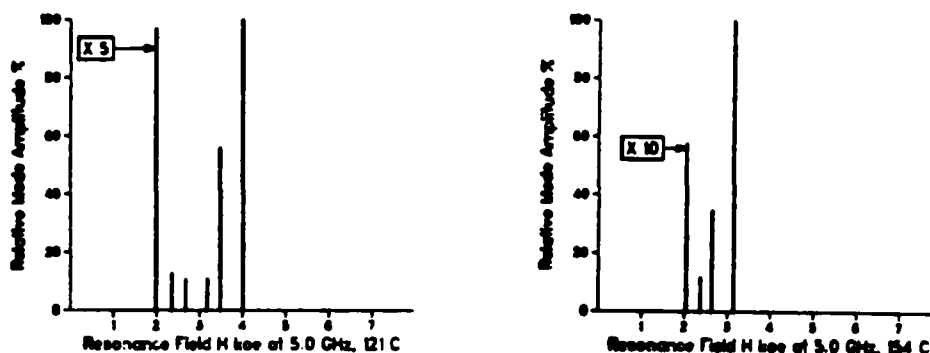
Fig. 3-21:   FMR Spectra for Film 55 after the Second Implant and Anneal:
at 121°C and 154°C

The temperature dependence of ΔH_E in film 55, measured after the first and second implants, is plotted in Fig. 3-22.   The ΔH_E, measured after each implant, decreases linearly with temperature.   The ΔH_E, measured after the second implant (curve B) increased slightly, although the increase was not as large as the percentage increase in the maximum implant strain.   Annealing the film after the second implant caused ΔH_E to decrease below its value after the first implant.

The second implant in film 55 did not have a significant effect on ΔH_E or its temperature dependence, but did improve the strain uniformity.   Thus the uniformity was improved without degrading the film properties.

In contrast to film 140, the relative mode amplitudes in the FMR spectra for films 82 and 150 changed with temperature.   The spectra for film 150 after the first implant and anneal, at 100°C, are shown in Fig. 3-23.   The amplitude of the second mode nearly doubled, compared to the 25°C spectra which were shown in Fig. 3-12, and is considerably larger than the first mode.   The intermediate modes are overlapped and have irregular spacings, which is characteristic of bimodal anisotropy profiles.

In Fig. 3-24 stick diagrams of the FMR spectra for film 150 after the second implant, which were measured at 71°C, and 139°C, are shown.   At 71°C, four surface
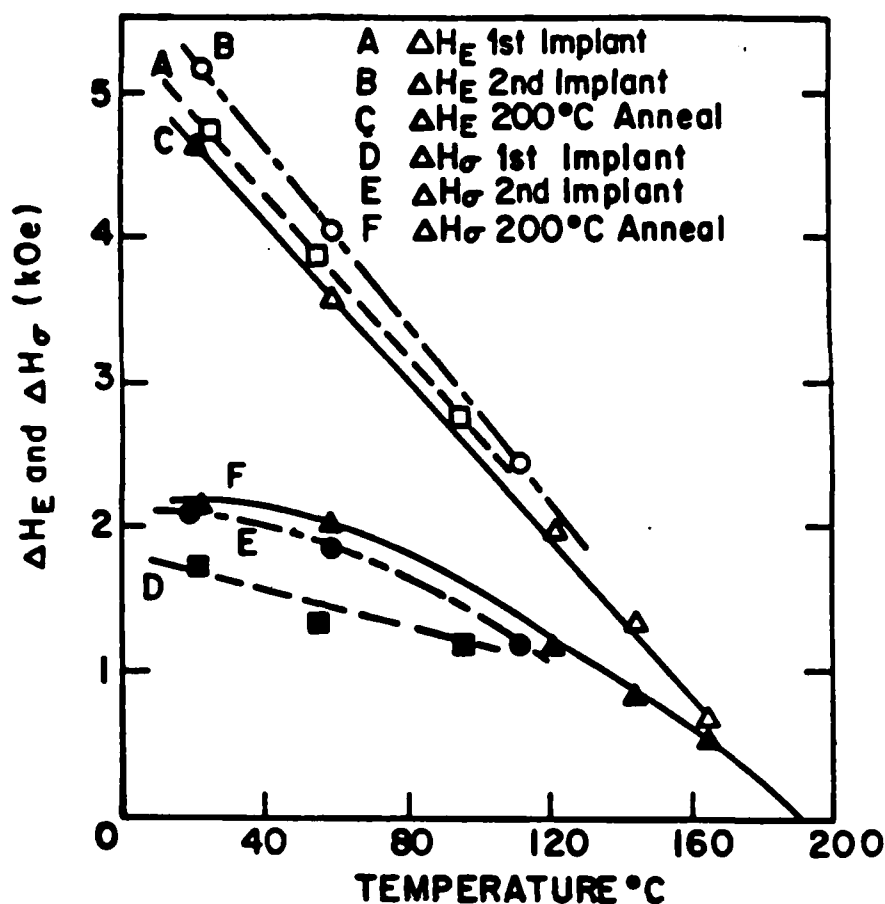
Fig. 3-22: Temperature Dependence of Anisotropy Fields in Film 55

modes were observed. The intermediate surface modes, between the highest and lowest surface modes were not observed at 139°C. The disappearance of the intermediate modes indicates that the anisotropy profile is varying with temperature.

The spectra for film 82 at 95°C are shown in Fig. 3-25. The surface modes are shifted uniformly to lower fields and the amplitude of the second strong mode nearly doubled compared to the spectra at 25°C, which are shown in Fig. 3-10. The relative amplitude of the bulk mode at 95°C was approximately half its value at 25°C.

The change in the relative amplitudes of the surface modes in films 82 and 150, at high temperatures indicates that the Curie temperature is not uniform throughout the implanted layer, but is reduced in the region of maximum implant damage. This is ascertained from the reduction in the first mode amplitude, relative to the second strong mode at higher temperatures. Thus the anisotropy profile shifts with temperature. We should point out that the room temperature FMR spectra for film
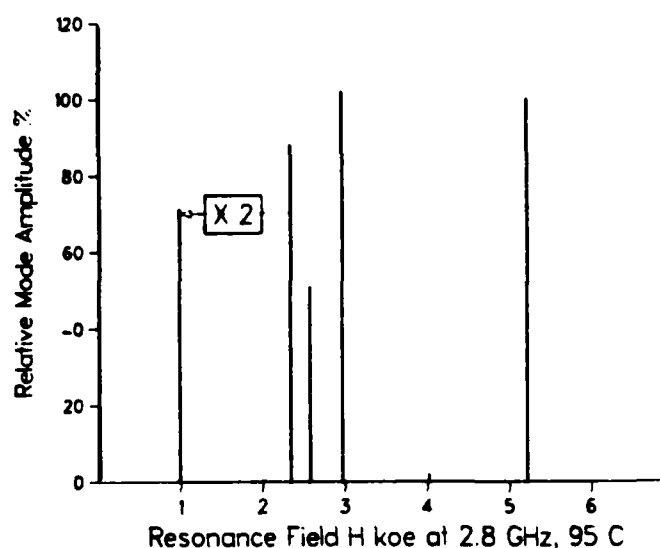
Fig. 3-25:   FMR Spectra for Film 82 After First Implant, 95°C 2.8 GHz

operation for a bubble device that can be achieved with these films for the given implant conditions. The $H_E(B)$ and $H_E(I)$ in film 150 are plotted versus temperature in Fig. 3-26. The $H_E(B)$ decreases smoothly with temperature. The $H_E(I)$, calculated from the highest field mode, is given by mode 1, and the second surface mode is given by mode 2. Whereas previous investigators have ascribed the multiple modes in heavily implanted films to sublayers resulting from multiple implants [15], the results here indicate that mode 2 is not specifically related to a particular implant in a multiple energy dose, since a single energy was used. However the disappearance of mode 2 at a relatively low temperature indicates that it is localized in a region with greater implant damage.

The FMR measurement results for film 150, after the second implant and a 2 hour, 200°C anneal are also plotted in Fig. 3-26. The $H_E(B)$ was the same over the entire measurement temperature range as that measured after the first implant. The $H_E(I)$ calculated from the first surface mode was virtually identical to that measured after the first implant. Thus any increase in ΔH_E caused by the second implant was annealed out.

While the temperature dependence of the anisotropy field in the implanted layer in film 150, after the second implant and anneal, is suitable for device use, that in the bulk is the limiting factor for high temperature operation of a device on film 150. However if a film which has better bulk film temperature characteristics, the temperature dependence of the anisotropy field in the implanted layer will be sufficient for device operation up to relatively high temperatures (greater than 150°C).
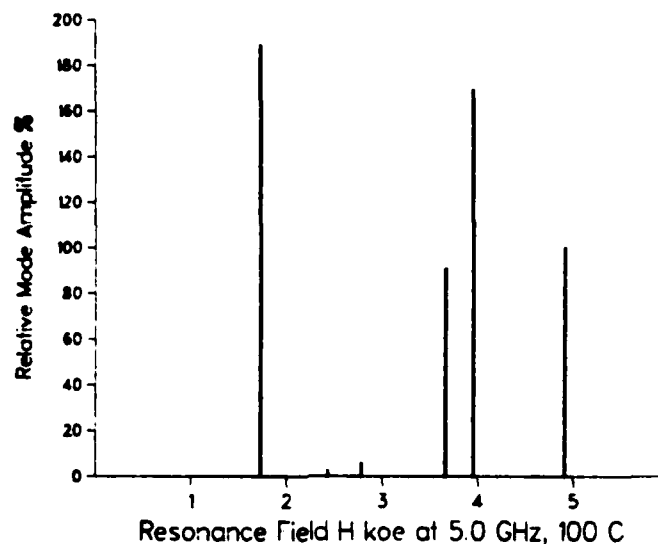
Fig. 3-23:   FMR Spectra for Film 150 after First Implant and 200°C Anneal: 100°C at 5.0 GHz
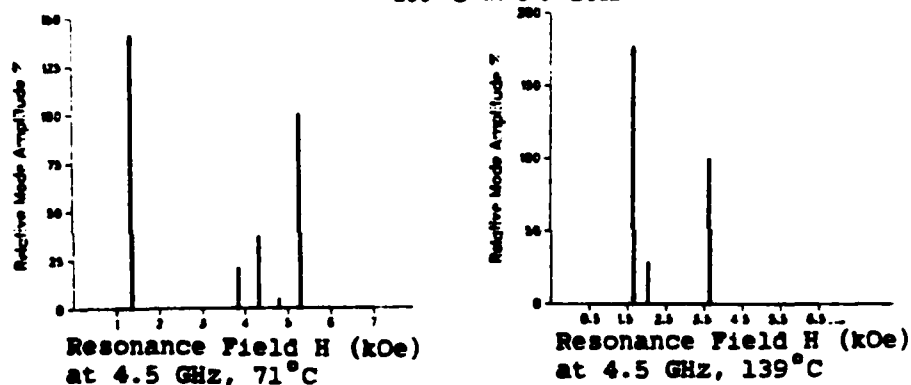
Fig. 3-24:   FMR Spectra for Film 150: After 2nd Implant and 200°C Anneal: 71°C, and 139°C

150 give no indication of the reduction of the Curie temperature in the heavily damaged region, as they appear to indicate that the anisotropy profile is relatively uniform, as evidenced by progressively decreasing mode amplitudes.

The effects of high dose deuterium implants are similar in some respects to moderate to high dose implants with heavier ions, where severe degradation of the magnetic properties was observed in the region of maximum implant damage.   Results for implants with other species, besides deuterium, will be discussed in the next chapter.

The temperature dependence of the anisotropy field change was measured on each of the films studied here.   This information is useful in determining the range of
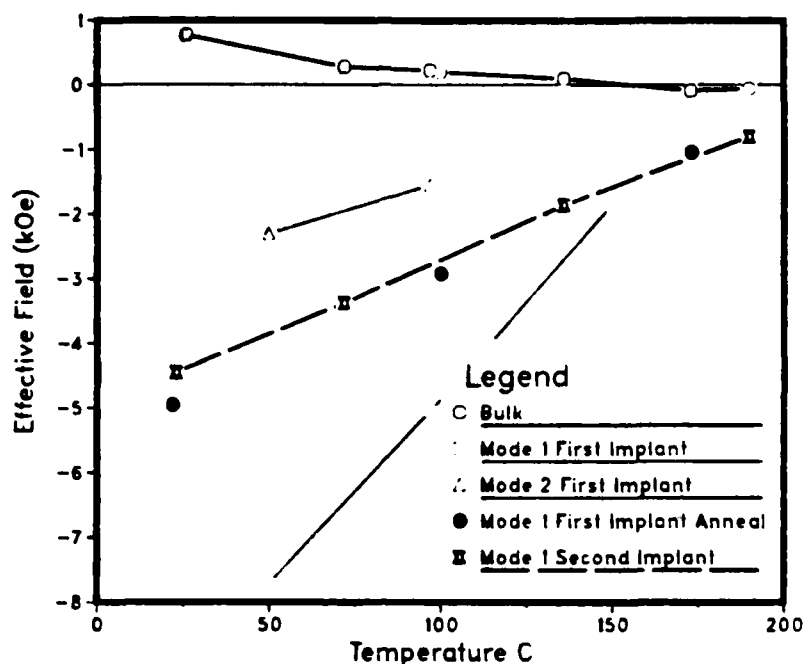
Fig. 3-26:   Temperature Dependence of the Effective Anisotropy Field
in the Bulk and Implanted Layers of Film 150

In summary, the high temperature FMR spectra for films with low to moderate implant damage are similar to those at room temperature, with respect to the relative mode amplitudes and locations, whereas those for high dose implants are different. The high dose results indicate that there is significant degradation in the magnetic properties in the region of maximum implant damage. Determining the dose levels where the film properties become degraded is addressed in the next section.

3.3.4. Effects of Implant Energy and Dose on Film Properties

In the previous section, it was shown that the magnetic properties of heavily implanted films were degraded. Here results for two other films which received the same implant doses as films 55 and 82, but at a considerably lower energy, are evaluated to determine the threshold dose – energy combination where degradation of the film properties occurs.

Film parameters and implant conditions for films 121 and 126 are given in Table 3-13. The implant depth was estimated from the projected range of the deuterium ions to be 0.27 μm for films 121 and 126 (40 keV) compared to 0.48 μm for films 55 and 82 (88 keV) [21, 69]. The X-ray rocking curve for film 121 is shown in Fig. 3-27.

Table 3-13:   Bulk Film Parameters and Implant Conditions for Films 121 and 126

Film	t	l	$4\pi M$	H_E	λ_{111}
121	0.75 μm	0.06 μm	1362 G	595 Oe	$-3.0*(10^{-6})$
126	0.73	0.06	1389	526	-3.8

Film	Dose	Energy
121	1×10^{16} D_2^+/cm^2	40 keV
126	2×10^{16} D_2^+/cm^2	40 keV

In contrast to the the rocking curve for film 55 after the first implant which was shown in Fig. 3-8, the strong peak on the high angle side of the envelope of surface peaks is not well-defined for film 121, as there is a large gradient in the strain near the film surface.
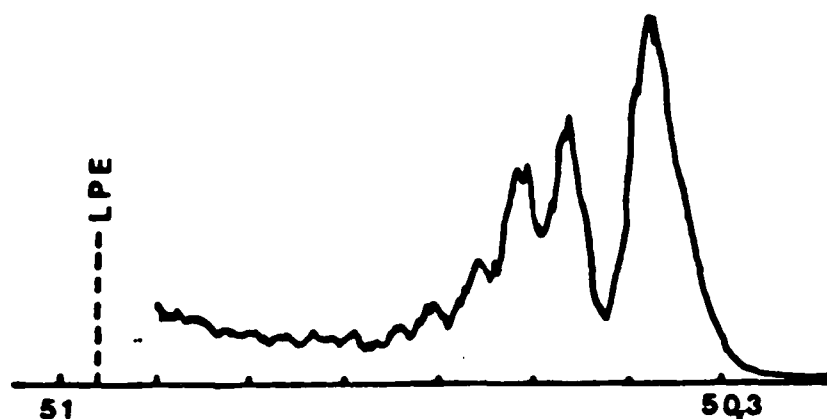
Fig. 3-27:   X-ray Rocking Curve for Film 121

The FMR spectra for film 121, which are shown in Fig. 3-28, are quite different than those for film 55 after the first implant which were shown in Fig. 3-6. There are two strong modes with spacing similar to that between the first and third modes in film 55. However the lowest field mode corresponds with the fourth mode observed in film 55, but has a substantially larger amplitude.

In film 126, the principle surface mode in the as-implanted sample was not detected at room temperature. Subsequent measurements up to 129°C indicated that the surface modes were weak and broad. The amplitude of the bulk mode at 30°C was nearly 40 times greater than that of the main implanted mode, even though the bulk layer thickness was only twice that of the implanted layer. The linewidth of the main surface mode was estimated to be 4 to 5 times broader than that of the bulk mode at
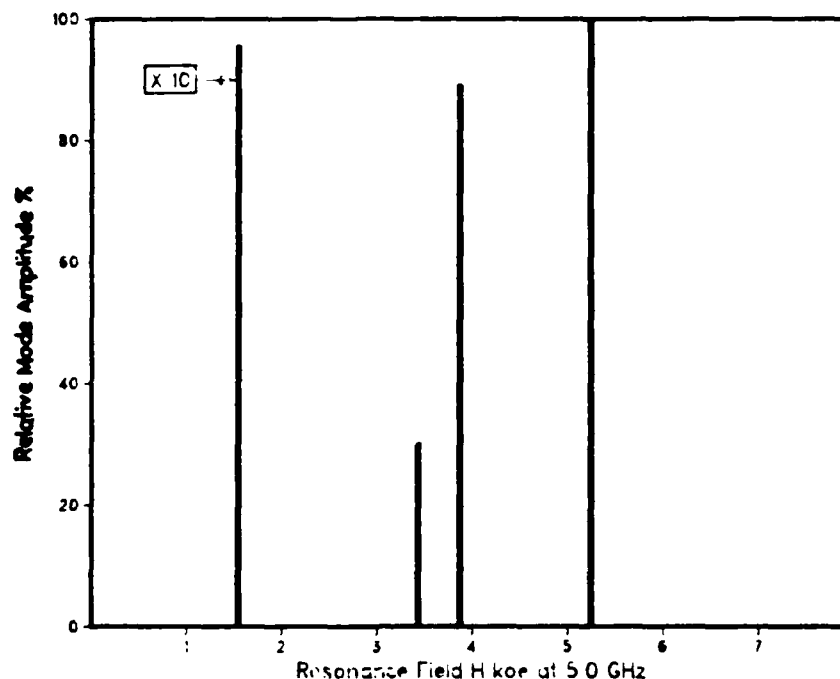
Fig. 3-28: FMR spectra for Film 121

25°C. This indicates that the properties of the implanted layer were severely degraded in the as-implanted sample, but were partially restored by low temperature annealing (during measurement at 129°C). Measurements of δH_{111} in the implanted layer, made after the film was annealed during the 129°C measurement, were subject to an unusually large uncertainty. The $\delta H_{111}(I)$ was 150 ± 50 Oe compared to a $\delta H_{111}(B)$ of 75 ± 7 Oe. The large variation in $\delta H_{111}(I)$ may be attributed, in part, to the high concentration of deuterium in the film. Due to the extremely large variation in $\delta(H)_{111}(I)$, ΔH_σ was not calculated.

The results from films 55, 82, 121, and 126, including ϵ_{max}, ΔK, $\Delta H_\sigma/\Delta H_E$, and $\lambda_{111}/M_s(B)$ and $\lambda_{111}/M_s(I)$ as determined from the δH_{111} measurements, are given in Table 3-14.

The ΔK for film 121 is approximately 50% larger than that for film 55. This is expected as the lower implant energy for film 121 concentrates the damage closer to the film surface. The $\lambda_{111}/M_s(I)$ is about 10% higher than $\lambda_{111}/M_s(B)$ in film 55, but 20% higher in film 121. This suggests that $4\pi M_k$ is reduced more than λ_{111} as the implant dose is increased.

The maximum implant strain for 40 keV deuterium (D_2), determined from films 121,

Table 3-14:   Implanted Film Results: Films 55, 121, 82, and 126

Film	ϵ_{max}	ΔK ergs/cm^3	$\Delta H_\sigma / \Delta H_E$	$\lambda_{111}/M_s(B)$ G^{-1}	$\lambda_{111}/M_s(I)$ G^{-1}
55	1.07%	132	0.39	$-3.4(10^{-8})$	$-3.7(10^{-8})$
121	1.06	197	0.48	-2.9	-3.6
82	1.56	322	0.27	-2.8	-2.6
126	1.9 - 2.1	442	-	-3.4	-

126, and two other films which received lower dose implants, and for 88 keV deuterium, determined from films 55, 82, and 150, is plotted versus implant dose in Fig. 3-29. The nonlinearity in the curves may be attributed to scatter in the data. However, at a given dose the strain is expected to be higher for a lower energy implant due to the higher concentration of damage near the film surface. Previous investigators have reported that the effect of increasing the implant dose in hydrogen implanted films is to increase the maximum strain and the surface strain without appreciably increasing the width of the damaged region [14]. The deuterium is expected to exhibit similar behavior.
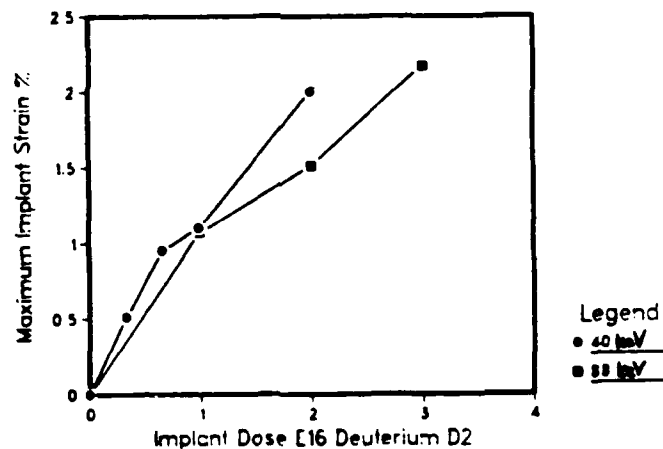
Fig. 3-29:   Maximum implant strain versus Dose for 40keV and 88 keV Deuterium

In summary, there was a significant degradation in the film properties for films with strain above approximately 1.0%. The high dose implant at high energy (88 keV) apparently created a bimodal anisotropy profile similar to that reported for neon implanted films.

3.3.5. Conditions for Uniform Implants

Up to this point, the implant conditions which were used did not produce particularly uniform implanted layers, with the exception of those for film 84. However, we have shown that overdamage occurs if the deuterium dose is too high. Here, the implant conditions which created relatively uniform properties through the implanted layer are given. The implants are suitable for a nominal one micron diameter bubble device (film 114) and a half micron diameter bubble device (film 83). The most significant difference between the results for the two films is the thickness of the implanted layer, 0.5 μm for film 83 and 0.35 μm for film 114, as estimated from the ion range statistics [11]. Implant conditions for film 83 are given in Table 3-15. Note that the implant doses for the highest energy implants on film 83 were identical to those for film 114. Bulk film parameters for film 83, 113, and 114 are listed in Table 3-16.

Table 3-15: Implant Conditions for Films Used to Evaluate Strain Uniformity

Film	Dose	Energy	Dose	Energy	Dose	Energy
83*	8×10^{15}	100 keV	4×10^{15}	50 keV	1×10^{15}	25 keV
113*	8×10^{15}	60	4×10^{15}	25		
114	8×10^{15}	60	4×10^{15}	25		
172	5×10^{15}	44				
55-1	1×10^{16}	88				
55-2	5×10^{15}	44				
55-3	5×10^{15}	80	3×10^{15}	25		
63	5×10^{15}	80	5×10^{15}	40		
165-1	8×10^{15}	48				
165-2	1.25×10^{16}	55	3×10^{15}	25		

*SiO_2 coated before implant; all doses in D_2^+/cm^2

Stick diagrams for the perpendicular and parallel FMR spectra are given in Fig. 3-30. The higher order modes in the perpendicular FMR spectra are spin wave modes with progressively decreasing amplitudes. Note that the bulk amplitude is only 14% of the first surface mode. The parallel resonance spectra are also shown in Fig. 3-30. Here, the bulk mode is significantly stronger than the surface modes. There are two strong surface modes, indicating that the anisotropy profile is not uniform, although their proximity suggests that the film has two regions with slightly different values of ΔH_E. In the X-ray rocking curve in Fig. 3-31 there are two sharp diffraction peaks from the implanted layer, which presumably originate from two regions with slightly different

Table 3-16:   Results for Film 83: Evaluation of Strain Uniformity

Film	t	l	$H_E(B)$	$4\pi M_s$	$\Delta K \times 10^{-3}$
83	0.66 μm	.06 μm	545 Oe	1217 G	145.5 ergs/cm^3
113	0.85	0.06	620	1247	174
114	0.85	0.06	583	1234	167

Film	Implant	ϵ_{max}	ϵ_{min}	U
83	Triple	0.89%	0.77%	0.14
113	Double	1.11	0.96	0.14
114	Double	1.09	0.95	0.14
172	Single	0.74	0.44	0.51
55-1	First	1.07	0.65	0.48
55-2	Second	1.10	0.74	0.39
55-3	Third	1.57	1.24	0.21
63	Double	0.91	0.47	0.62
165-1	First	0.98	0.62	0.43
165-1	200°C Anneal	0.90	0.62	0.33
165-2	Second	1.43	1.16	0.19

values of strain. However, the proximity of the peaks, and the absence of any other distinguishable peaks indicates that the strain profile is reasonably uniform. The strain uniformity is evaluated using the following equation

$$U = \frac{\epsilon_{max} - \epsilon_{min}}{\langle \epsilon \rangle} \tag{3.1}$$

where the average strain $\langle \epsilon \rangle$, is assumed to be equivalent to the average of ϵ_{max} and ϵ_{min}, which is a reasonable estimate if the difference between them is small. The low U value for film 83, in Table 3-16, indicates that the triple implant produced a more uniform strain than most of the other implants which were measured. Since film 83 was not annealed prior to measurement, the profile may shift slightly as a result of annealing. In general, annealing improves strain uniformity.

While the FMR spectra are not equivalent to that for a uniform anisotropy profile, the spectra shown in Fig. 3-30 are significantly more well-behaved (i.e. no oscillating sequence of mode amplitudes or overlapped modes in perpendicular spectra) than those for most of the other films which were investigated here.
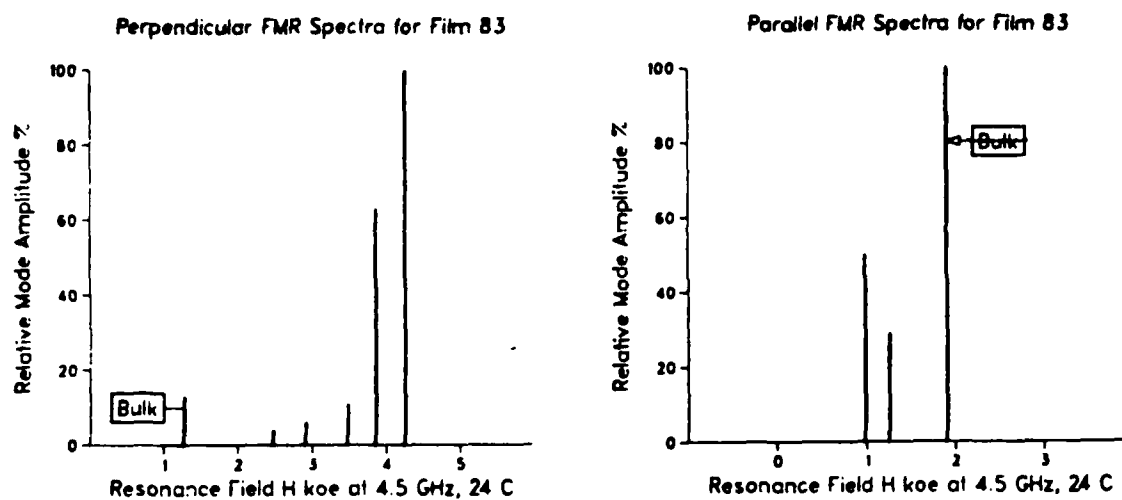
Fig. 3-30:   FMR Spectra for Film 83
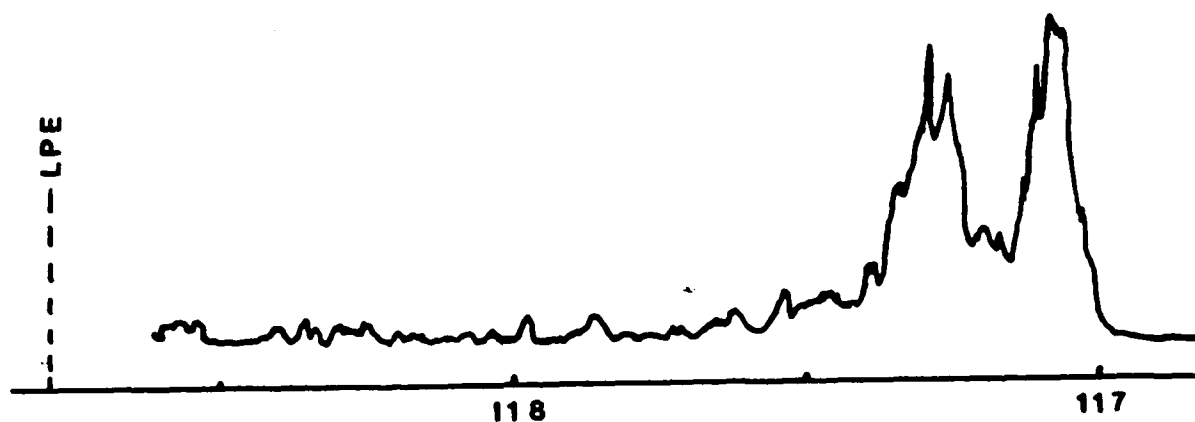
Fig. 3-31:   X-ray Rocking Curve for Film 83

The results for film 114, which received a double implant, similar to that reported for 1 μm diameter contiguous bubble devices [70], were also analyzed. The implant conditions are given in Table 3-15. Stick diagrams of the FMR spectra are shown in Fig. 3-32. Measurements were made at 4.5 GHz at 25°C. The parallel resonance (field along [112]) was also measured. The irregular spacing and sequence of alternating mode amplitudes indicates that the anisotropy is not uniform. The parallel spectra are similar to that for film 83, shown in Fig. 3-30. The uniformity of the strain was determined from the spread of the X-ray rocking curve peaks, which is shown in Fig. 3-33. The presence of two sharp, large amplitude peaks, and a third peak at the lowest angle, which had a smaller amplitude and was significantly broader, indicates that the strain was not uniform through the implanted layer thickness.

Perpendicular FMR Spectra for Film 114

Relative Mode Amplitude %

X 10

Resonance Field H koe at 4.5 GHz, 24 C

Parallel FMR Spectra for Film 114

Relative Mode Amplitude %

Resonance Field H koe at 4.5 GHz, 24 C
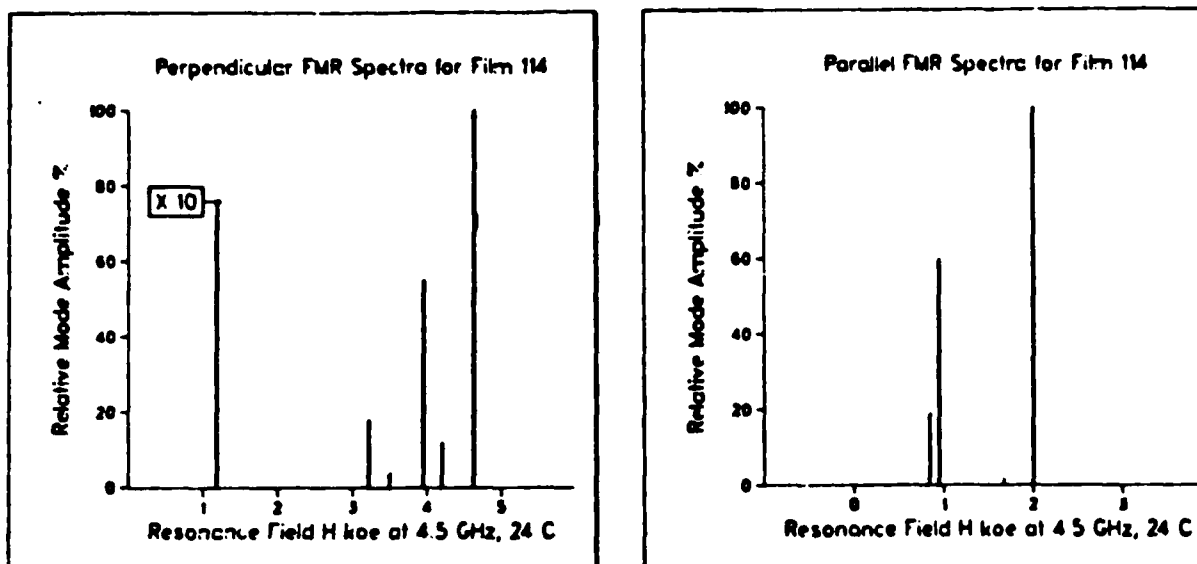
Fig. 3-32:   FMR Spectra for Film 114

LPE

112   117

Fig. 3-33:   X-ray rocking curve for film 114

However the U is small, which indicates that the strain profile is reasonably good.   The implant energies for film 114 were chosen such that the difference between the projected range R_p and standard deviation S.D. of R_p, (R_p-S.D.)   of the high energy implant is equal to R_p+S.D. of the low energy implant.   That condition was approximately satisfied here, as seen from implant range statistics in Table 3-17.   A similar procedure was used to select the implant conditions for film 83.   The dose is chosen so the high energy implant creates the desired ΔK.   The low energy dose is chosen so as not to significantly increase the maximum strain induced by the first implant.   Thus to achieve a uniform implant, it is necessary to select the principle (high energy) implant and then adjust the second implant until an acceptable uniformity is achieved.   For 1 μm films, the low energy dose of a double species implant between 1/4 to 1/2 of the high energy dose can be expected to produce a reasonably uniform implanted layer.

Table 3-17:   Projected Range and Standard Deviation For Deuterium [21, 69]

Energy	R_p	S.D.
25 keV	0.13 μm	0.05 μm
50	0.24	0.07
60	0.28	0.08
100	0.42	0.10

Based on Range of D^+ at 1/2 energy of D_2^+

The uniformity ratio U for a few typical implants is given in Table 3-16.   Note that a lower uniformity ratio corresponds to a more uniform strain profile.   Implant conditions corresponding to each are given in Table 3-15.   Although the implant sequence for film 165 produced a relatively uniform strain, those for the single energy implants, or the second implant on film 55 (55-2) did not produce particularly uniform strain profiles.   Comparison of results from films 55 and 63, which both received double dose implants at energies of 44 and 88 keV for film 55, and 40 and 80 keV for film 63, indicate that lowering the dose of the lower energy implant from the same as the high energy dose to half of it improves the strain uniformity.   However, this was not enough.   For these two films an additional low energy implant is needed to increase the minimum strain.

While the final criterion for evaluating an implant dose is the operating margins for the bubble device, if the strain and anisotropy profiles play an important role, as previous investigators have suggested, then the implants with the lower uniformity ratio represent better choices for use in bubble device fabrication.   An additional consideration in the selection of implant conditions to achieve a uniform strain and anisotropy profile is the expected migration of the implanted ions upon annealing.   The implant dose should be selected to create a uniform damage profile through the film thickness.   However, it has been shown [9] that the stopped ion distribution does not correspond to the damage profile, but must be calculated from both the nuclear collisions, which result in permanent damage, and the ion scattering.   In hydrogen implanted films, the stopped ions are located deeper in the film than the location of maximum damage.   With annealing, the ions reportedly migrate towards the region of maximum damage [14].   However, if the annealing temperature is too high, than the ions will migrate out of the film, or accumulate at the film surface if an SiO_2 overlayer is used.   Thus if the hydrogen effect, which is the large change in ansiotropy due to the presence of the hydrogen (deuterium) ions, is to be utilized, the implant and

annealing conditions have to be chosen such that the hydrogen stays uniformly dispersed through the implanted region.

3.4. ANNEALING BEHAVIOR OF DEUTERIUM IMPLANTED FILMS

The annealing behavior of the deuterium implanted films was studied. Since the implanted films are typically subjected to high temperature treatments during device fabrication it is important to characterize the annealing-induced changes in the properties of the implanted layer. Since there are different threshold temperatures for different annealing mechanisms, it is important to determine where they occur so the appropriate annealing conditions can be selected. In addition to the changes in the anisotropy field, the effects of implantation and annealing on some of the other film parameters, including the gyromagnetic ratio, the magnetization, and the bulk (unimplanted) region properties will be discussed.

3.4.1. Implant-Induced Changes in the Gyromagnetic Ratio

Previous investigators have assumed that γ in the implanted films is not significantly different from that in the bulk films. In contrast to results of other investigators, we found significant implant-induced changes in $\gamma(I)$. This may be partially attributed to the fact that most of the previous investigations have been made using resonant cavities, which are typically operated at a single frequency. The γ in the bulk is calculated from the perpendicular and parallel resonances, and γ in the implanted layer is assumed to be the same. Since the measurements here were made using the wideband spectrometer, we could calculate γ in both the bulk and implanted layers from the frequency dependence of the perpendicular resonance field.

The gyromagnetic ratio γ is the ratio of the orbital magnetic moment to the spin moment and is given by [71]

$$\gamma = ge/2mc \qquad (3.2)$$

where e is the electronic charge, m is the electron mass, c is the speed of light and the g factor is 1 for pure orbital motion and 2 for spin motion. In most of the garnet films, the g factor is approximately 2.

Films 84 and 129 received the same triple dose implant, which was listed for film 84 in Table 3-1. Film 84 was coated with SiO_2 prior to implantation while film 129 was left uncoated. Both films were annealed successively up to 800°C. The annealing

times, which ranged from ½ to 2 hrs. at each temperature, will be given later. In Figs. 3-34 and 3-35, γ(B) and γ(I) are plotted versus annealing temperature for films 84 and 129. The γ(B) for film 84 is 2.53 ± .01 MHz/Oe. The γ(I) does not have a well-defined value, but is scattered, mostly below γ(B). The average value and deviation of γ(I) is 2.49 ± .12 MHz/Oe. In film 129, γ(I) is only 70% of γ(B) after implantation, however γ(I) is approximately equal to γ(B) after the 250°C anneal.
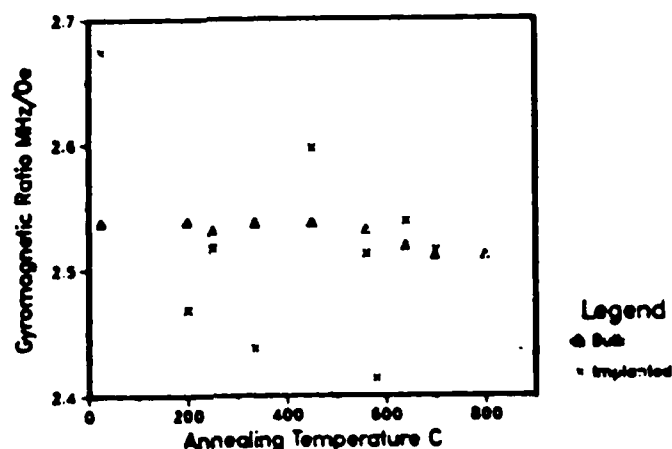
Fig. 3-34: Gyromagnetic Ratio Versus Annealing Temperature for Film 84
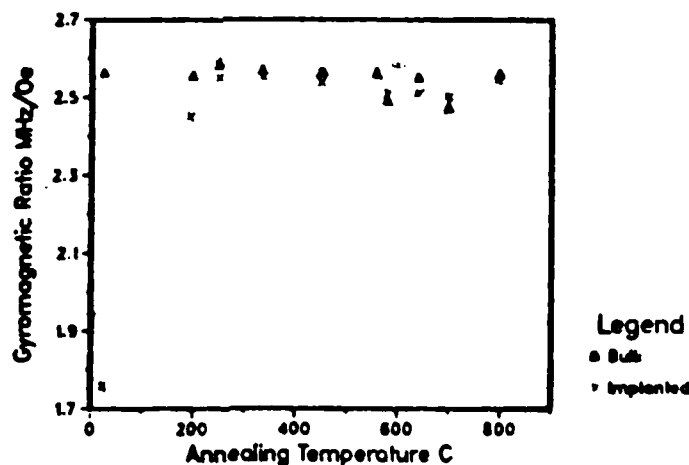
Fig. 3-35: Gyromagnetic Ratio Versus Annealing Temperature for Film 129

The gyromagnetic ratio was also measured as a function of temperature in each of the films which were studied. Results for film 150, measured after the first implant and a 200°C anneal are given in Table 3-18. There is no significant difference in γ over the temperature range from 22 to 173 °C.

Table 3-18: Temperature Dependence of the Gyromagnetic Ratio in Film 150

Temp.	$\gamma(B)$	$\gamma(I)$
22°C	2.61 MHz/Oe	2.53 MHz/Oe
100	2.59	2.51
173	2.60	2.63

Thus, the gyromagnetic ratio is reduced by implantation but restored after the films are annealed. The reduction in $\gamma(I)$ is dependent on the implant damage.

3.4.2. Effects of Annealing on Bulk Film Properties

There is evidence of a systematic variation in the bulk properties of deuterium implanted films which is presumably related to the presence of deuterium in the film. The ratio of $H_E(B)$ after each annealing to $H_E(B)$ measured before implantation for films 77, 84, and 129, is plotted in Fig. 3-36. Each of the films received the same implants. Film 84 was coated with SiO_2 prior to implantation, film 77 was coated afterwards, and film 129 was not coated. An increase in the ratio was observed above 450°C for films 84 and 77, and above 250°C for film 129, which corresponds with the threshold temperatures for deuterium desorption. Although results for hydrogen implants will be discussed in Chapter 4, we will note here that a similar annealing-induced variation in $H_E(B)$ was observed in hydrogen implanted films. The reason for the difference in the ratios in the different deuterium implanted films at high temperatures may be attributed to changes in the bulk parameters which are attributed to the annealing, but not specifically to the implant. However, since the films had different compositions it is difficult to make a comparison of the results.

Previous investigators have found that the strain profile in the bulk layer under a hydrogen implant is not uniform, whereas the profile for a similar film implanted with neon was [14]. The difference in the strain profiles is presumably caused by the diffusion of hydrogen into the bulk layer. Thus, it is plausible that some of the deuterium has diffused into the bulk layer.

In summary, the change in the bulk film properties caused by annealing appears to be related to the presence of the deuterium, although we can not rule out the effect of exchange shift. The magnitude of the exchange shift is related to the transition in the anisotropy field between the bulk and implanted layers. If there is an abrupt transition, the exchange shift will be negligible, but with a gradual transition the
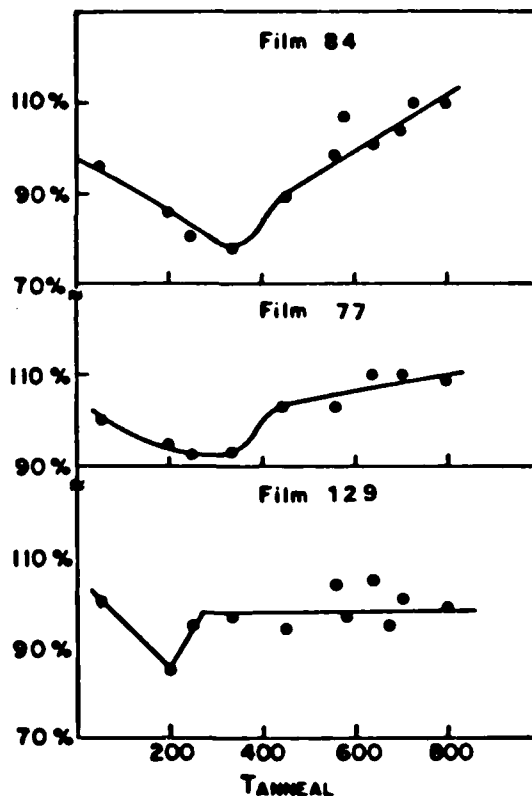
Fig. 3-36: Ratio of $H_E(B)(T_{ANNEAL})$ to $H_E(B)$ Measured Before Implantation
for Films 84, 77, and 129

exchange shift may be considerable, depending on the difference in the anisotropy between the layers. Based on the annealing behavior of $H_E(B)$ and its relation to the deuterium desorption threshold, we suggest that the effect is predominantly caused by the presence of deuterium in the bulk film. The variation in $H_E(B)$, which is approximately 10%, will affect the calculated value of ΔH_E. The change in ΔH_E depends on the magnitude of ΔH_E, but will typically be less than the percentage variation in $H_E(B)$ since $H_E(I)$ is usually significantly larger than $H_E(B)$.

3.5. IMPLANTED LAYER MAGNETIZATION

Ion implantation reportedly decreases the magnetization in the implanted layers [14, 42]: The change in the magnetization can be determined from vibrating sample magnetometer (VSM) measurements or from FMR.

3.5.1. Magnetization Measurements

Direct measurement of the magnetization in the implanted layer has been reported by several investigators using a VSM [29, 58]. Similar measurements were attempted here but were not successful due to the large signal from the paramagnetic GGG substrate which obscured the signal from the implanted layer. However the relative change in the magnetization in the bulk and surface layers can also be determined from the FMR measurements. The relative change in the magnetization in the bulk and the implanted layer were determined from the amplitude and linewidth of the FMR modes using Eq. (3.3) which was previously discussed in Chapter 2, section 2.4.3.

$$I = \frac{I_I(\Delta H_I)^2}{I_B(\Delta H_B)^2} = \frac{M_I L_I}{M_B L_B} \tag{3.3}$$

where I and ΔH are the absorption derivative mode amplitude and linewidth, M is the magnetization and L is the layer thickness of the bulk (B) and implanted (I) layers.

3.5.2. Magnetization Measurement Results

The magnetization in the implanted layer was compared to that in the bulk layer as a function of temperature for film 140. The relative change in the bulk to implanted layer magnetization was measured as a function of annealing for films 84 and 129.

The peak-to-peak linewidth ΔH of the first surface mode (I) and bulk mode (B) for film 140 are given in Table 3-19. Material parameters for film 140 were given in Table 3-8. The implant conditions were 5×10^{15} D_2^+/cm^2 at 44 keV. The measurements were made under identical experimental conditions, so that the temperature dependence of the magnetization in each layer could be compared. The values in the columns labelled (Bulk)* and (Implanted)* in Table 3-19 are the product of the mode amplitude and the square of the linewidth, which is proportional to the magnetization times the layer thickness. The ratio of the magnetization in the bulk and implanted layers is obtained assuming L_I is 0.28 μm and L_B is 0.92 μm. The implant thickness was estimated from the ion range statistics [11], and the total film thickness was measured using the scanning wavelength spectrophotometer. The magnetization in the implanted layer is half that in the bulk at 25°C, and 15% of the bulk at 165°C. The FMR measurement results, taking account of the layer thicknesses, indicate that the magnetization in the implanted layer decreases by 15% from 25°C to 100°C. The bubble collapse field measurements indicate that $4\pi M_s$ in the unimplanted film decreases by 11% over a similar temperature range. The FMR results from the bulk film

indicate that there is a slight increase in the magnetization at 103°C. This is attributed to the ± 10 Oe uncertainty in the linewidth measurement. The results at 191°C indicate that $4\pi M_s$ is half of its value at 25°C. It is worth noting that the mode amplitude A_p, increased with temperature, due to narrowing of the linewidth. However the total area under the resonance curve is expected to decrease. The increase in the mode amplitudes, which occurred for both the bulk and implanted layer modes, permitted the detection of weak modes which were not observed in the room temperature spectra.

Table 3-19:   Resonance Data for film 140 at 4.5 GHz

Temp.	Bulk Layer			Implanted Layer		
	ΔH	A_p	(Bulk)*	ΔH	A_p	(Implanted)*
25°C	132 Oe	28	49	155 Oe	3.0	7.2
103	103	47	50	99	6.3	6.1
165	75	57	32	92	1.7	1.4
191	73	47	25	**		

* Proportional to Magnetization in arbitrary units

** too close to bulk mode to accurately measure

Bulk Magnetization from Bubble Collapse Field

16°C	782 G
109°C	695 G

While the magnetization can be estimated from the FMR results, this is not a highly accurate technique. However results from comparative measurements do provide insight into changes in the magnetization in the implanted layer both with temperature, and after different sample treatments. The data from film 140 indicate that moderate dose implantation can lead to more temperature dependent magnetization.

3.5.3. Effects of Annealing on Magnetization

Annealing of the implanted films repairs some of the implant-induced damage. The relative change in the magnetization of the implanted layer compared to the bulk was determined for films 84 and 129 Results in Table 3-20 include the annealing temperature, the bulk and implanted mode absorption derivative linewidths ΔH_B and ΔH_I, and the ratio of the magnetization in the implanted to bulk layer M_I/M_B. The ratio M_I/M_B was calculated from Eq. (3.3) assuming that the ratio of the implanted to

Table 3-20: Implanted to Bulk Layer Magnetization Ratio

T°C	Film 84			Film 129		
	ΔH_B	ΔH_I	M_I/M_B	ΔH_B	ΔH_I	M_I/M_B
As I.I.	94 Oe	131 Oe	.20	150 Oe	300 Oe	.31
250°C	94	103	.37	150	161	.50
560	94	105	.55	156	138	.48
700	93	111	.70	156	137	.58
800	–	–	–	159	155	.66

unimplanted layer thickness L_I/L_B, was 1.22 for film 84 and 1.56 for film 129 as estimated from optical measurement of the film thickness and the ion range statistics for deuterium [21]. The ΔH_I of film 129 before annealing was difficult to accurately determine, since the peak was broad, and the signal-to-noise ratio was not favorable. As a result, the magnetization ratio in film 129, before annealing, is subject to a large uncertainty.

The results given in Table 3-20 for the magnetization ratio indicate that M_I was initially 20% to 30% of M_B, but was gradually restored upon annealing. After a 700°C anneal, the M_I is approximately 70% of the M_B. The trend agrees with results of some investigators, where a 60% reduction in the $M_s(I)$ was found in hydrogen implanted films, but $M_s(I)$ was restored upon annealing [14]. We should point out that recently reported magnetization measurements in hydrogen implanted films indicate that the magnetization in the implanted layer is only reduced by 17% in YIG and 31% in a bubble garnet at 1% strain [58]. The strain in films 84 and 129 is 1.5% in the as-implanted sample and decreases to 0.55% after a 700°C anneal. Furthermore, in contrast to earlier results, a larger reduction in the magnetization was observed in neon implanted films. The results here indicate that there is a large reduction in $M_s(I)$, although there is a relatively large uncertainty in this method which is estimated to be ±15%.

3.5.4. Annealing Dependence of FMR Linewidth

Previous investigators have stressed that the FMR linewidth is an important parameter that is often overlooked in the analysis of the effects ion implantation [15]. Here, the effects of high temperature annealing on the linewidth provide some insight into the annealing mechanisms for deuterium implanted films.

The ΔH_I after a 560°C and 700°C anneal was about 10% greater than ΔH_B in film 84, but was about 10% less than ΔH_B in film 129 as indicated in Table 3-20. The linewidth narrowing between 250°C and 700°C is believed to be attributed to the repair of broken oxygen bonds. After an 800°C anneal on film 129, ΔH_I was approximately equal to ΔH_B. Suran et al. proposed a model for linewidth broadening in which the implanted layer linewidth was attributed to the rare-earth contribution and a disorder-induced linewidth, specific to the implanted layer [15]. Thus the linewidth broadening is attributed to the implant-induced disorder, whereas the linewidth narrowing is attributed to the breaking up of the Sm-Fe bond geometry. When the Sm-Fe bonds break, the number of FMR relaxer ions decreases so the FMR linewidth decreases. Since film 129 contains significantly more Sm than film 84, as indicated in Table 3-21, and evidenced by the broader linewidth of the bulk mode, it is plausible that the implant breaks some of the Fe-Sm bonds. This claim is further supported by the increase in linewidth between 700°C and 800°C anneals. At these temperatures cation diffusion occurs [33], resulting in the reformation of the Fe-Sm bonds.

Table 3-21: Film Compositions Based on Unity Segregation Coefficients for
the Rare-Earths

Film	Sm	Tm	Gd	Y	Lu	Fe	Al
77	0.35	1.3	0.45	0.9	0	4.7	0.3
84	0.35	1.3	0.30	1.05	0	4.8	0.2
129	0.69	1.09	0.25	0.88	0.09	4.8	0.2

3.5.5. Annealing Behavior of Anisotropy Fields in Deuterium Implanted Films

The annealing-induced changes in the total uniaxial anisotropy field, magnetostrictive field, and implant strain were measured on films 77, 84, and 129, which received the same triple energy deuterium implant. Surface treatments and annealing conditions are listed in Table 3-22. All of the SiO_2 layers were sputter deposited at 500 W RF power. The films were successively annealed in air. The anneals on each of the films were done at the same time to avoid any discrepancies associated with differences in annealing times or temperatures.

The threshold temperatures for the desorption of deuterium from the garnet were deduced from the FMR spectra. Perpendicular FMR spectra after some of the annealing steps are shown in Fig. 3-37. All of these spectra were measured at 24°C and at 4.5 GHz. The position of the bulk mode and its amplitude relative to the

Table 3-22: Sample Treatment and Annealing Conditions for Films 77, 84, and 129

Film	Sample Treatment
77	500 Å SiO_2 After Implant
84	500 Å SiO_2 Before Implant
129	Uncoated

Annealing Conditions

200°C	90 (min)	640°C	40 (min)
250	80	700	50
335	30	670	120
450	60	800	70 (84 and 129 only)
560	30	800	120
580	50		

highest field surface mode are indicated in each spectrum. On film 84, there is an alternating strong-weak mode amplitude sequence up to 335°C, and the second mode amplitude increased dramatically after a 450°C anneal. A similar increase in the second mode amplitude was also observed on film 77, but not on film 129. The alternating strong-weak mode amplitude sequence is typical of films which have a maximum ΔH_E in the interior of the film; whereas, the strong second mode amplitude after the 450°C anneal is typical of films in which the maximum ΔH_E is located near the surface. Based on the anisotropy profiles in Fig. 3-3, and the FMR spectra, we conclude that in films 84 and 77, prior to annealing at 335°C, the anisotropy profile is peaked well within the film. However, after the 450°C anneal, the peak has shifted towards the film surface, due to the build-up of deuterium there. This correlates with reported annealing behavior of hydrogen implanted films, where hydrogen was found to accumulate at the film surface after a 450°C anneal, but was prevented from escaping by the SiO_2 layer [13]. By comparison, on film 129, the strong second mode is not observed after the 450°C anneal. Results for film 129 agree with previous studies on hydrogen implanted films, where desorption is found to occur between 200°C and 250°C [12, 15]; however the proportional change in ΔH_E on the deuterium implanted film is significantly smaller. We should note that in the previously reported measurements of hydrogen implanted films, no change in the gyromagnetic ratio in the implanted layer was observed. The spectra for film 77 at higher annealing temperatures are similar to those for film 84 although they are not identical. The differences may be related to the desorption of some of the deuterium during the SiO_2 deposition.
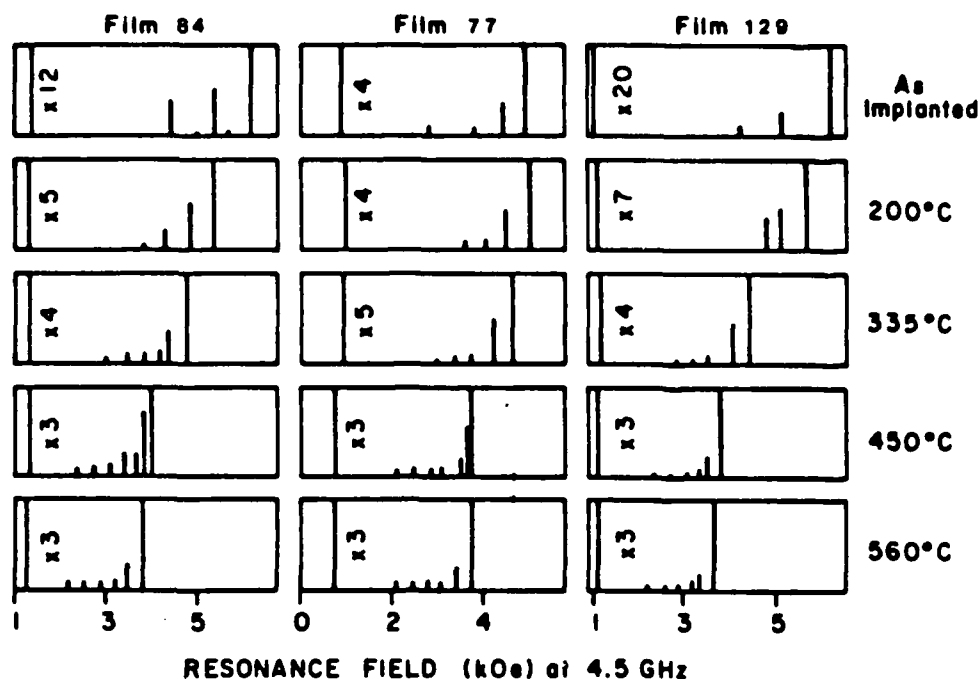
Fig. 3-37:   Stick Diagrams for Perpendicular FMR Spectra
for Films 84, 77, and 129

The ΔH_E, ΔH_σ, and ϵ_{max} in film 84 are plotted versus annealing temperature in Fig. 3-38.   There is a linear decrease in ΔH_E over the range from 25°C to 450°C, and then a linear decrease at a lower rate above 450°C.   The knee at 450°C is believed to be related to the threshold temperature for deuterium desorption through the SiO_2 layer.   The change in the slope of ΔH_E is accompanied by a change in the slope of ϵ_{max}.   The ΔH_E, ΔH_σ, and ϵ_{max} for film 129 are plotted versus annealing temperature in Fig. 3-39.   Above 250°C, ΔH_E decreases smoothly   The ϵ_{max} has a similar annealing temperature dependence as that in film 84.

The ΔH_E for film 77 increased slightly after the 200°C and 250°C anneals, due primarily to an increase in $\gamma(I)$.   Over this same temperature range ϵ_{max} was constant, as shown in Fig. 3-40.   Thus we conclude that the SiO_2 deposition which was done after the implantation, but before any measurements were made, partially annealed out some of the implant damage.   The as-implanted film properties were presumably similar to those for film 129, as evidenced by the decreased $\gamma(I)$ and the broader linewidth of the implanted modes.   At annealing temperatures above 250°C, the ΔH_E has a similar

behavior to that in film 84, with a knee at 450°C. However, between 450°C and 640°C. ΔH_E increased slightly after successive anneals. This increase is attributed to a shift in the location of the maximum anisotropy field change and the localization of the spin wave modes in the region of the maximum ΔH_E.
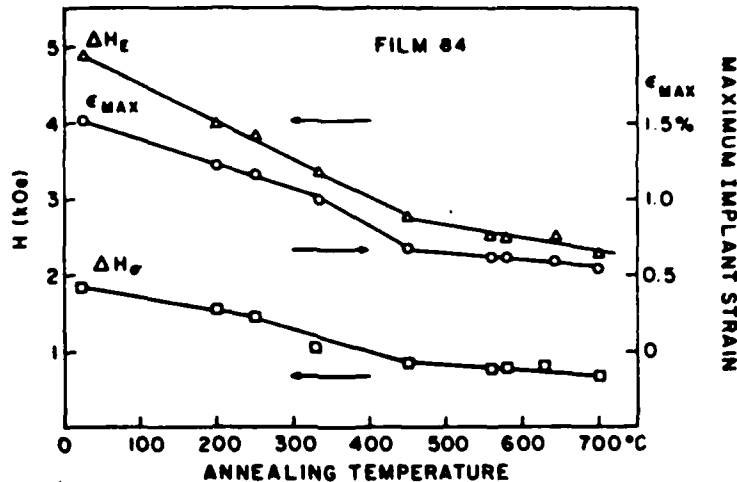
Fig. 3-38: Annealing Temperature Dependence of ΔH_E, ΔH_σ, and ϵ_{max} for Film 84
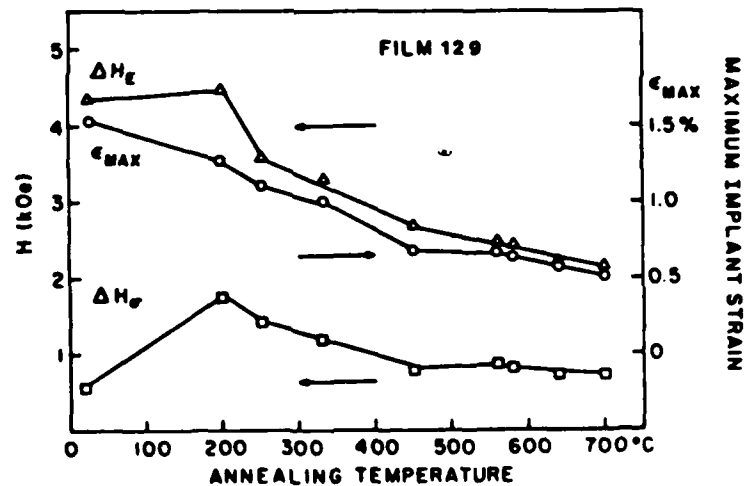
Fig. 3-39: Annealing Temperature Dependence of ΔH_E, ΔH_σ, and ϵ_{max} for Film 129

The relative change in ΔH_E is plotted versus annealing temperature for the coated and uncoated deuterium implanted films in Figs. 3-41 and 3-42. These plots are useful to those interested in device fabrication, as they show the relative change in the anisotropy field which can be expected for a given annealing treatment. While the choice of annealing conditions is somewhat dependent on the particular implant conditions,
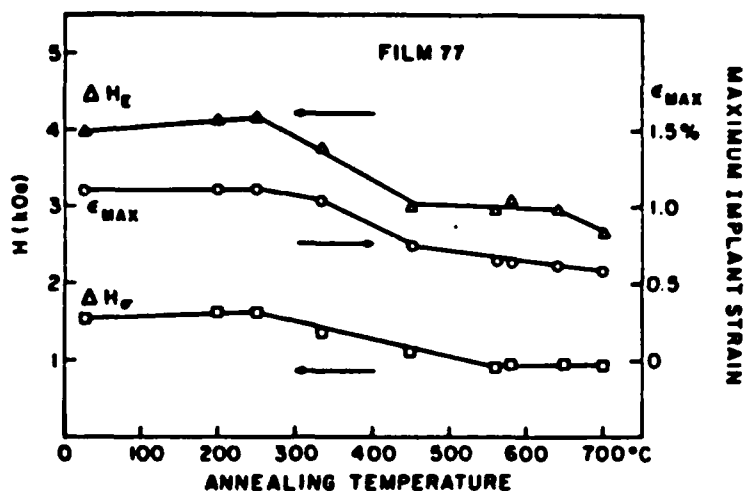
Fig. 3-40: Annealing Temperature Dependence of ΔH_E, ΔH_σ, and ϵ_{max} for Film 77

temperatures reached in subsequent processing steps, and desired operating temperature range for the device, the following points should be considered. The principle effects of annealing are to repair the implant-induced damage and to drive the deuterium out of the implanted region. There are threshold temparatures near 250°C for deuterium desorption in uncoated films and near 450°C in SiO_2 coated films. As shown in Figs. 3-41 and 3-42, the ΔH_E is continually reduced as the annealing temperature is increased. Previous investigators have generally reported better device operating margins for annealed films. Here, we have shown that in deuterium implanted films which are coated with SiO_2 prior to implantation, there is a significant difference in the film properties, compared to uncoated films. Thus, the annealing treatment necessary to obtain optimal operating margins for the films implanted through the SiO_2 overlayer are expected to be significantly different than those for the uncoated films. It remains to be shown what the annealing time and temperature required to stabilize the film properties are.

3.5.6. Mechanisms for the Implant-Induced Change in Uniaxial Anisotropy

The annealing studies were also used to investigate the mechanisms responsible for the anisotropy field change. Previous investigators have reported that the non-magnetostrictive contribution to ΔH_E disappears after the hydrogen is annealed out of the film [13, 14]. Here, we will show that the non-magnetostrictive effect plays an important role, even after the deuterium is annealed out of the films. It will be shown that the deuterium which desorbs from the garnet is not responsible for all of the non-

Deuterium Implanted Film, Silicon Dioxide Film 84
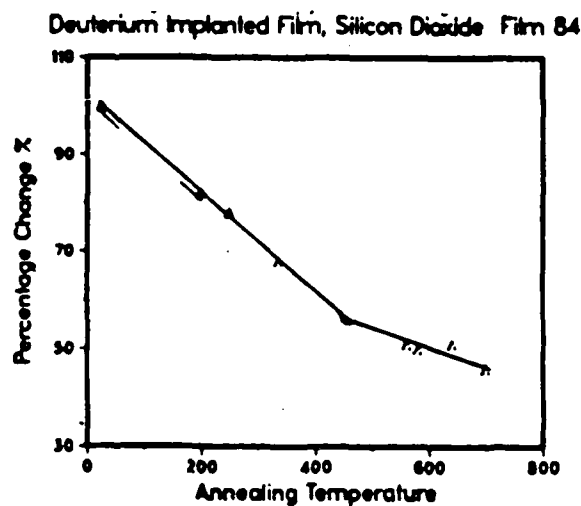
Fig. 3-41: Relative Change in ΔH_E Versus Annealing Temperature for SiO$_2$ Coated Films

Deuterium Implanted Film, No Silicon Dioxide Film 129
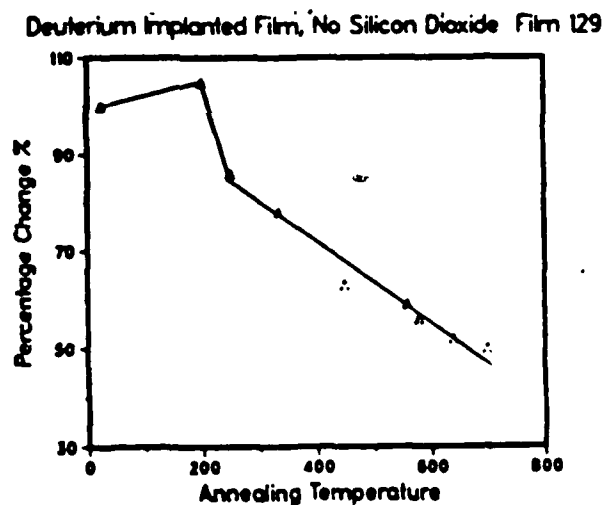
Fig. 3-42: Relative Change in ΔH_E Versus Annealing Temperature for Uncoated Films

magnetostrictive portion of ΔH_E. In these experiments, the magnetostriction/magnetization in the implanted layer is measured so the magnetostrictive contribution to ΔH_E can be accurately calculated. We should note that previous investigators have usually estimated the magnetostriction coefficient in the implanted layer from the slope of a plot of the anisotropy field change versus the implant strain.

The magnetostrictive contribution to the total implantation-induced anisotropy field change was measured after each annealing step. In Figs. 3-43, 3-44, and 3-45 the ΔH_E and ΔH_σ for films 84, 129, and 77 are plotted versus ϵ_{max}. The annealing temperatures, corresponding to those in Table 3-22, are indicated next to some of the data points. The ΔH_E for film 84 decreases linearly with implant strain and has a positive intercept. The zero-strain intercept of ΔH_E for film 129 is also positive, and is approximately 800 Oe. This indicates that if all of the strain were annealed out of the film there would be a non-zero implant-induced anisotropy field change. This has been observed previously in neon implanted films [72], but not in hydrogen or deuterium implanted films.

From the annealing study we conclude that there is a substantial non-magnetostrictive portion of ΔH_E as evidenced by the large difference between ΔH_E and ΔH_σ above the deuterium desorption threshold temperatures. This claim is further supported by the non-zero intercept of the ΔH_E versus implant strain, which was obtained by annealing the films. Thus we propose that there is at least one and possibly two mechanisms which contribute to ΔH_E besides the magnetostrictive effect and the hydrogen (deuterium) effect. One of these mechanisms appears not to depend on the implant strain, as evidenced by non-zero intercept of ΔH_E versus ϵ_{max}, while the other one decreases linearly with decreasing strain. Due to difficulties in establishing the absolute accuracy of ΔH_σ, it is not possible to investigate this mechanism from the results here. Additional experiments are suggested in Chapter 5 which may help to further identify the source of the non-magnetostrictive mechanisms.

3.6. MAGNETOSTRICTION MEASUREMENTS

The magnetostriction and magnetostrictive field were measured on several films. The ΔH_σ was found to saturate above a certain strain level due to a degradation in $\lambda_{111}/M_s(I)$. Analysis of the temperature dependence of ΔH_σ and ΔH_E indicates limitations in the use of the technique used here to determine ΔH_σ.

3.6.1. Effects of Dose on the Magnetostrictive Field

The effects of increasing the implant dose on ΔH_E and ΔH_σ were studied for film 94. Implant conditions for film 94, which was implanted three separate times, and room temperature results are given in Table 3-23. All of the anneals were done at 200°C.
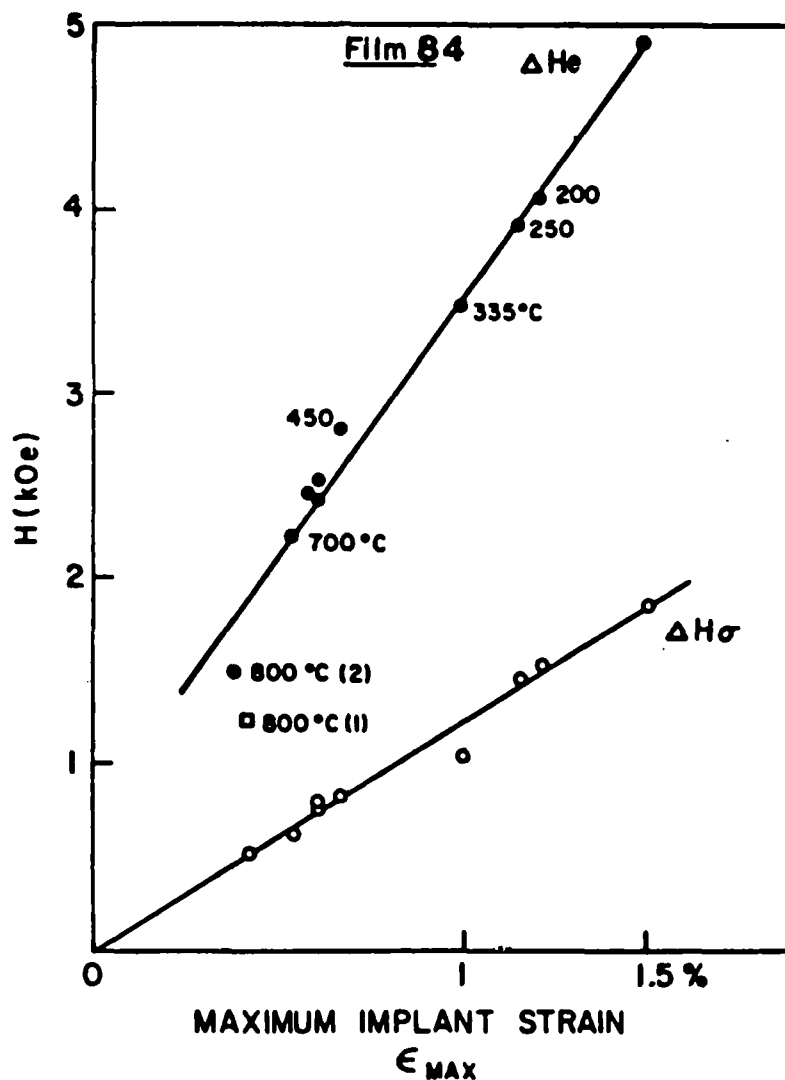
Fig. 3-43: Implant-Induced Change in Uniaxial Anisotropy Field ΔH_E and Magnetostrictive Field ΔH_σ Versus Implant Strain ϵ_{max} for Film 84

The room temperature $H_E(B)$ for film 94 varied by more than 200 Oe. As all of the measurements were made at 24 ± 2°C, the variation in $H_E(B)$ cannot be attributed to a difference in the temperature. Thus, it appears that some of the deuterium has diffused into the bulk film and affects the $H_E(B)$.

In Fig. 3-46, ΔH_E and ΔH_σ are plotted versus the maximum implant strain. The second implant increased ΔH_E, but the ratio of ΔH_E to the implant strain was nearly constant, as can be seen from the near linearity of ΔH_E versus strain in Fig. 3-46.
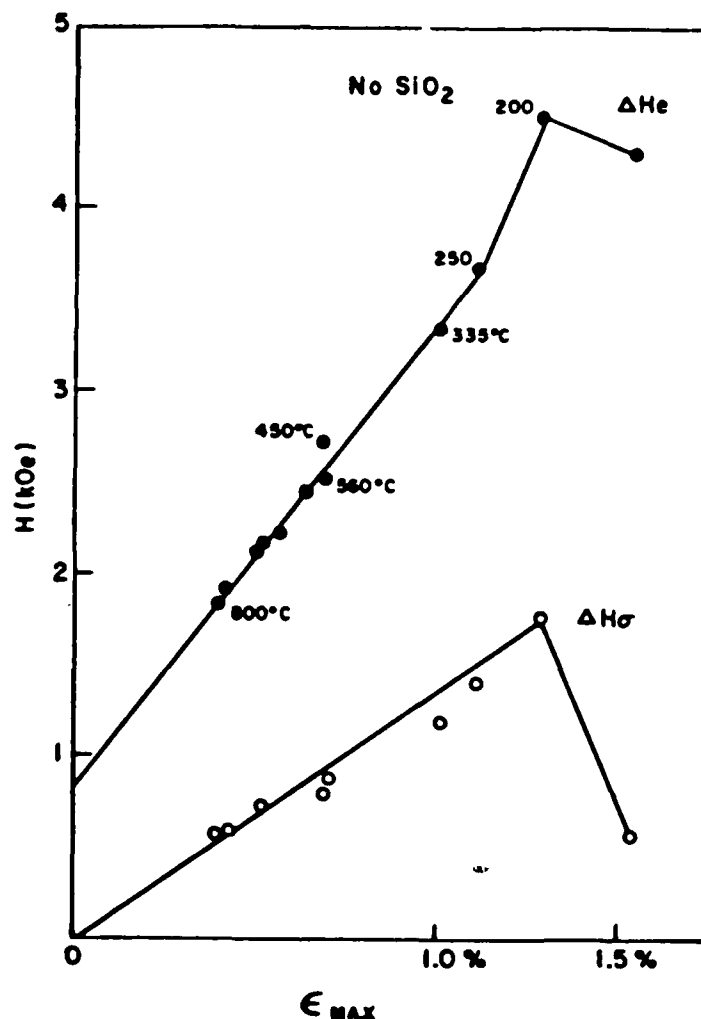
Fig. 3-44: Implant-Induced Change in Uniaxial Anisotropy Field ΔH_E

and Magnetostrictive Field ΔH_σ Versus Implant Strain ϵ_{max}

for Film 129

The ΔH_σ was approximately the same after the second implant and anneal as it was after the first implant. After the second implant, the resonance signal from the implanted layer was so severely degraded that $\delta H_{111}(I)$ could not be measured. The $\delta H_{111}(I)$ measurements, obtained after the anneal indicated that $\lambda_{111}/M_s(I)$ was reduced. The reduction in $\lambda_{111}/M_s(I)$ caused ΔH_σ to saturate. The saturation in ΔH_σ is attributed to the reduction in $\lambda_{111}/M_s(I)$ at higher strains. The ΔH_σ after the anneals for all three implants are given by points 1A, 2A, and 3A in Fig. 3-46. The two data points for ΔH_σ after the second implant were measured after two successive anneals.
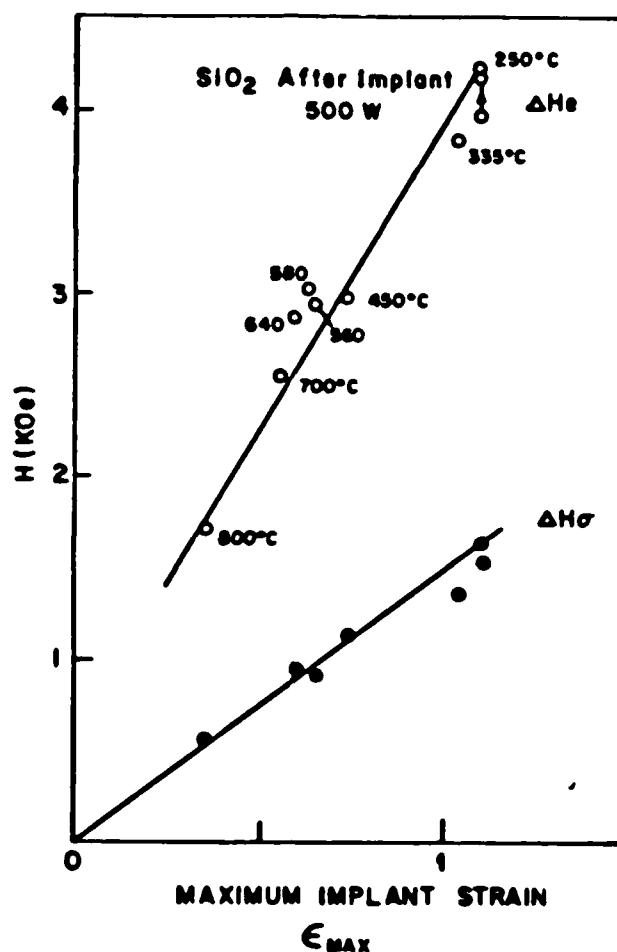
Fig. 3-45:   Implant-Induced Change in Uniaxial Anisotropy Field ΔH_E
and Magnetostrictive Field ΔH_σ Versus Implant Strain ϵ_{max}
for Film 77

The $\lambda_{111}/M_s(I)$ increased after the second anneal. This increase was accompanied by an increase in ΔH_E and $\gamma(I)$.

In summary, we found that the decrease in $\lambda_{111}/M_s(I)$ in heavily implanted films led to a saturation in ΔH_σ. This may explain why ΔH_E in Fig. 3-46 does not increase linearly with strain. Since ΔH_σ is only about 30% to 40% of ΔH_E, we still observe a significantly larger ΔH_E than we do with heavier ions at the same strain. Results for a heavier ion (oxygen), which are shown to be quite different, will be discussed in the next chapter.

Table 3-23:   Results for Film 94

Implant Conditions

Implant	Dose	Energy	Dose	Energy
1	5×10^{15} D_2^+/cm^2	44 keV		
2	5×10^{15} D_2^+/cm^2	55	5×10^{15} D_2^+/cm^2	25 keV
3	5×10^{15} D_2^+/cm^2	50		

Before	$H_E(B)$
	794 Oe

	$H_E(B)$	ΔH_E	ΔH_σ	$\Delta H_\sigma / \Delta H_E$	ϵ_{max}	ϵ_{min}
Implant 1	1036 Oe	3262 Oe	1380 Oe	0.42	0.74%	0.44%
Anneal	934 Oe	2915 Oe	1798	0.62	0.69	0.39
Implant 2*	934 Oe	5986 Oe				
Anneal	916 Oe	5095 Oe	1582 Oe	0.31	1.16%	0.69%
Implant 3	854 Oe	6230 Oe	1865 Oe	0.30	1.55%	1.24%
Anneal	811 Oe	5236 Oe	1968 Oe	0.38	1.32	1.06

All Anneals at 200°C   *weak implanted resonance signal

3.6.2. High Temperature Magnetostriction Measurements

The temperature dependence of ΔH_E and λ_{111}/M_s were measured on several films. The temperature dependence of the magnetostrictive portion of the total anisotropy field change was determined from the temperature dependence of $\lambda_{111}/M_s(I)$ and room temperature measurements of the implant strain. This information is of practical use for those interested in bubble devices, as it will provide information regarding the useful range of operation for an ion implanted bubble device. It is also useful for analyzing the mechanisms of implantation. Measurements were made over the temperature range from 0°C to 200°C or some fraction thereof on films with a variety of implant conditions. The effect of the implant conditions and the uniformity of the implanted layer properties on the ΔH_σ are evaluated. In films which have an anisotropy profile that decreases uniformly with temperature through the implanted layer thickness, it will be shown that the ΔH_σ decreases smoothly with temperature. Furthermore ΔH_σ goes to zero at the same temperature that ΔH_E does. However in films which are overdamaged, the ΔH_σ at high temperatures cannot be determined using the techniques employed here.
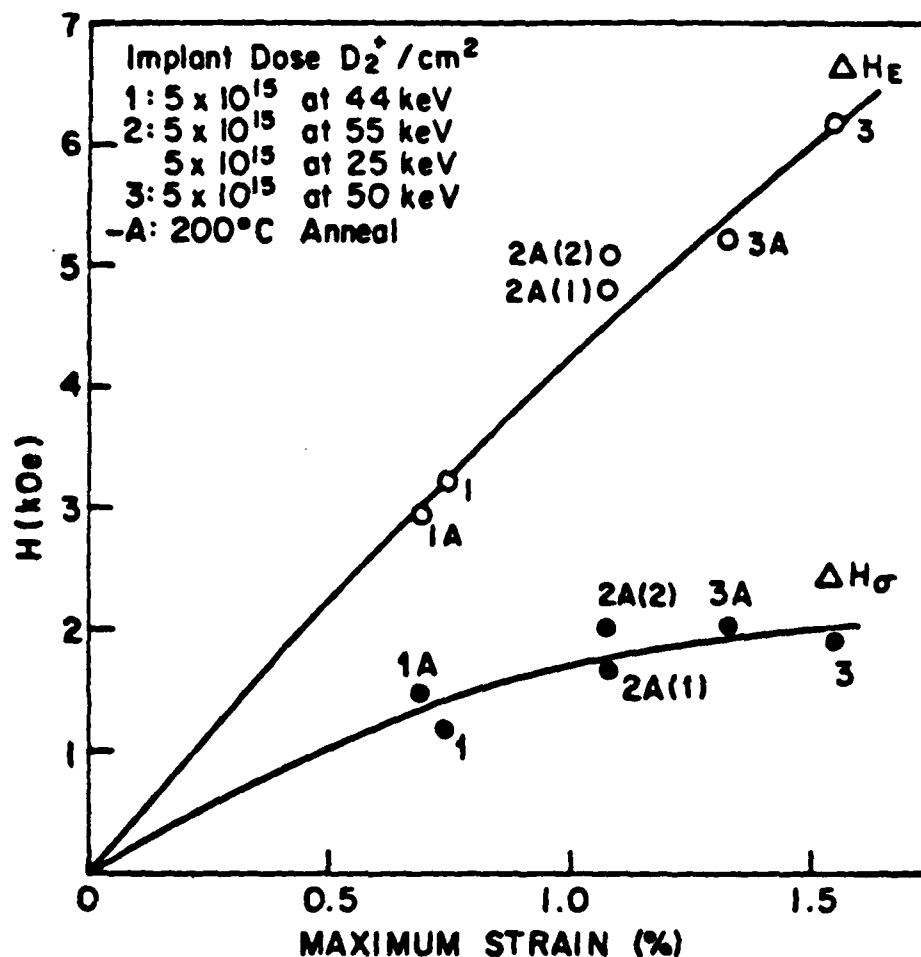
Fig. 3-46: ΔH_E and ΔH_σ versus Maximum Strain for Film 94

The calculation of the ΔH_σ at high temperatures (greater than $150°C$) is dependent on the temperature dependent variation of the strain and anisotropy profiles. The discussion here is motivated by the apparent discrepancy between ΔH_E and ΔH_σ which was observed at high temperatures in some of the films. An analysis of the ΔH_σ calculation for film 165 provides insight into the source of the discrepancy.

Film parameters and implant conditions for film 165 are given in Table 3-24.

The ΔH_E and ΔH_σ for film 165, measured after the first implant and the second implant and $200°C$ anneal, are plotted in Fig. 3-47. Above $120°C$ ΔH_E for the first and second implants are equal, which indicates that the additional change in the anisotropy field caused by the second implant has a different temperature dependence than ΔH_E caused by the first implant. After the second implant and anneal, the

Table 3-24:   Material Parameters and Implant Conditions for Film 165

t	l	$4\pi M_s$	H_E	λ_{111}
0.94 μm	0.14 μm	590 G	1273 Oe	-2.0×10^{-6}
Implant 1	8×10^{15} D_2^+/cm^2 at 48 keV			
Implant 2	1.25×10^{16} D_2^+/cm^2 at 55 keV	3×10^{15} D_2^+/cm^2 at 25 keV		

magnetostrictive field contribution to ΔH_E at 24°C was only 30%, compared to 40% after the first implant, and the ratio $\Delta H_\sigma/\Delta H_E$ increased with temperature. At 180°C, ΔH_σ is more than 3 times larger than ΔH_E.

The coincidence of ΔH_E at high temperatures after the first and second implants can be explained using the FMR spectra. In the spectrum measured after the first implant at 24°C, which is shown in Fig. 3-48, mode amplitudes have the typical alternating sequence which is characteristic of a single energy implant. At 103°C, all of the modes observed at 24°C are observed, as well as additional spin wave modes with smaller amplitudes. The ratio of the bulk to first surface mode amplitude did not change appreciably. At 167°C only one surface mode was observed. The resonance spectra for film 165 after the second implant, shown in Fig. 3-49, are significantly different than those measured after the first implant. Three strong surface modes were observed at 24°C. However, at 122°C only one strong surface mode was observed. This suggests that the T_c is not uniform through the implanted layer, but is reduced in the region of maximum implant damage. Thus we assume that the location of maximum ΔH_E shifts away from the region of maximum implant strain at high temperatures. This would explain why ΔH_E after the second implant is the same as that after the first implant at higher temperatures, and why ΔH_σ is larger than ΔH_E at high temperatures. Since the room temperature value of ΔH_E after the second implant is increased over that measured after the first implant, we assumed that the maximum strain corresponds to the maximum ΔH_E in the low temperature region. However, at higher temperatures, the anisotropy profile shifts, as evidenced by a change in the FMR spectra, so the calculation of ΔH_σ is no longer valid using the techniques employed here.

The $\lambda_{111}/M_s(l)$ which is calculated from $\delta H_{111}(l)$ corresponds to the magnetostriction in the region of maximum ΔH_E. In films which have uniform properties through the thickness of the implanted layer, there is no ambiguity between $\lambda_{111}/M_s(l)$ and the maximum implant strain, so the calculation of ΔH_σ is valid. However, if $\lambda_{111}/M_s(l)$ varies through the thickness of the film, or if the maximum ΔH_E shifts away from the

region with the maximum implant strain at high temperatures, due to a reduction in the Curie temperature, then the calculation of ΔH_σ will be incorrect. To accurately determine ΔH_σ at high temperatures, the temperature dependence of the depth profiles of the strain and anisotropy would have to be determined.
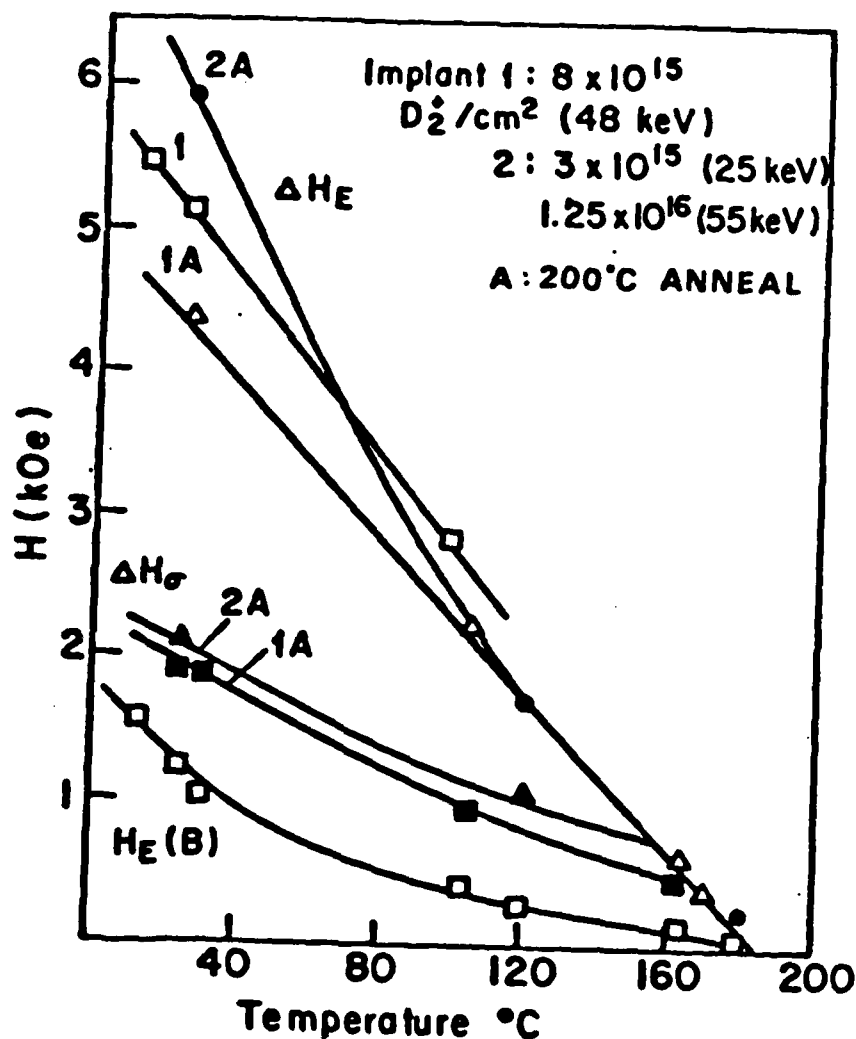
Fig. 3-47:   Temperature Dependence of ΔH_E and ΔH_σ for Film 165

3.6.3. Effects of Implant Dose on Temperature Dependence of Magnetostriction/Magnetization

The $\lambda_{111}/M_s(I)$ in the implanted layer had a different temperature dependence, compared to $\lambda_{111}/M_s(B)$, which depended on the implant dose. The temperature dependence of $\lambda_{111}/M_s(I)$ as a function of implant dose was determined for film 165
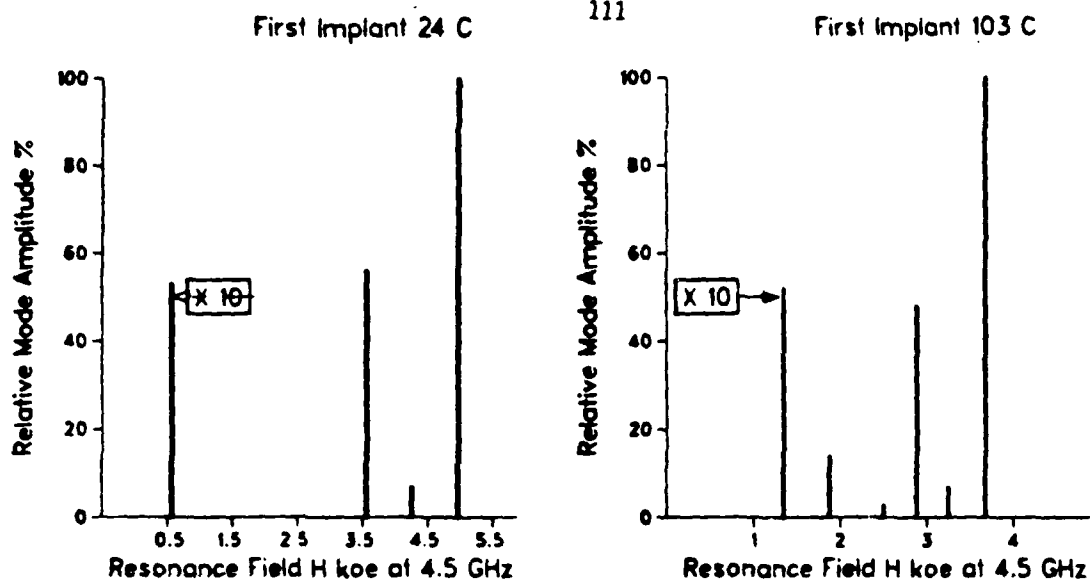
Fig. 3-48:   FMR Spectra for Film 165: First Implant 24°C and 103°C
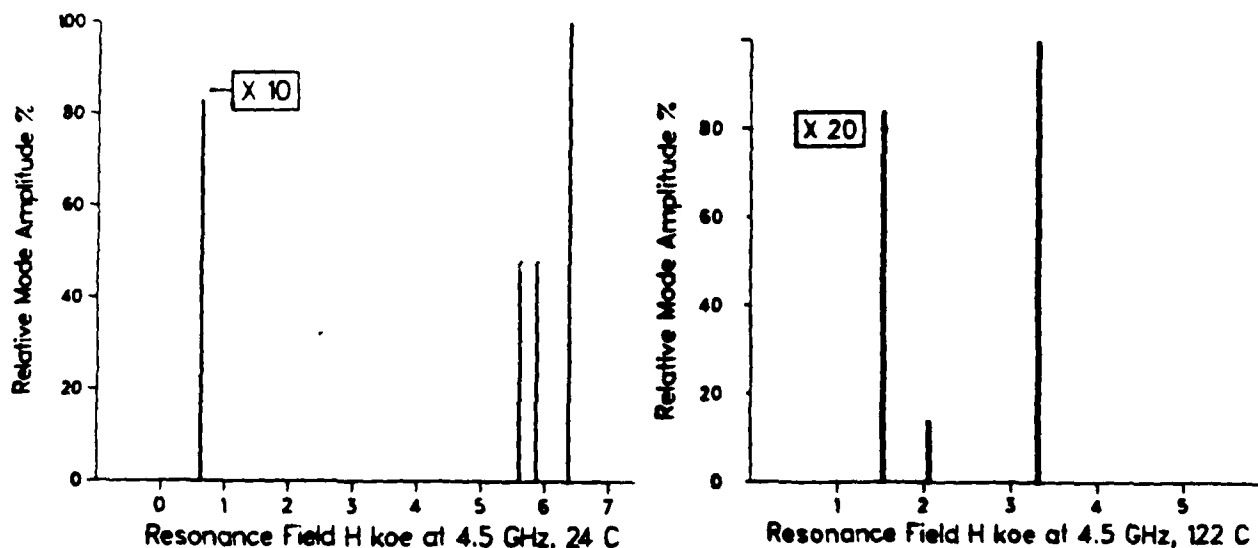
Fig. 3-49:   FMR Spectra for Film 165: Second Implant 24°C and 122°C

after the first and second implants. The $\lambda_{111}/M_s(B)$ and $\lambda_{111}/M_s(I)$ after the first and second implants are plotted versus temperature in Fig. 3-50. The $\lambda_{111}/M_s(I)$ after the first implant was approximately equal to $\lambda_{111}/M_s(B)$ at room temperature, although $\lambda_{111}/M_s(I)$ decreased more rapidly with temperature. The $\lambda_{111}/M_s(I)$ was reduced significantly by the second implant, but decreased more slowly with temperature than $\lambda_{111}/M_s(B)$. The significance of the difference in the temperature dependence of $\lambda_{111}/M_s(I)$ compared to $\lambda_{111}/M_s(B)$ is not well understood, since the effects of a variation in $\lambda_{111}/M_s(I)$ through the thickness are not known. The interpretation is further complicated by the uncertainties in the δH_{111} measurement.
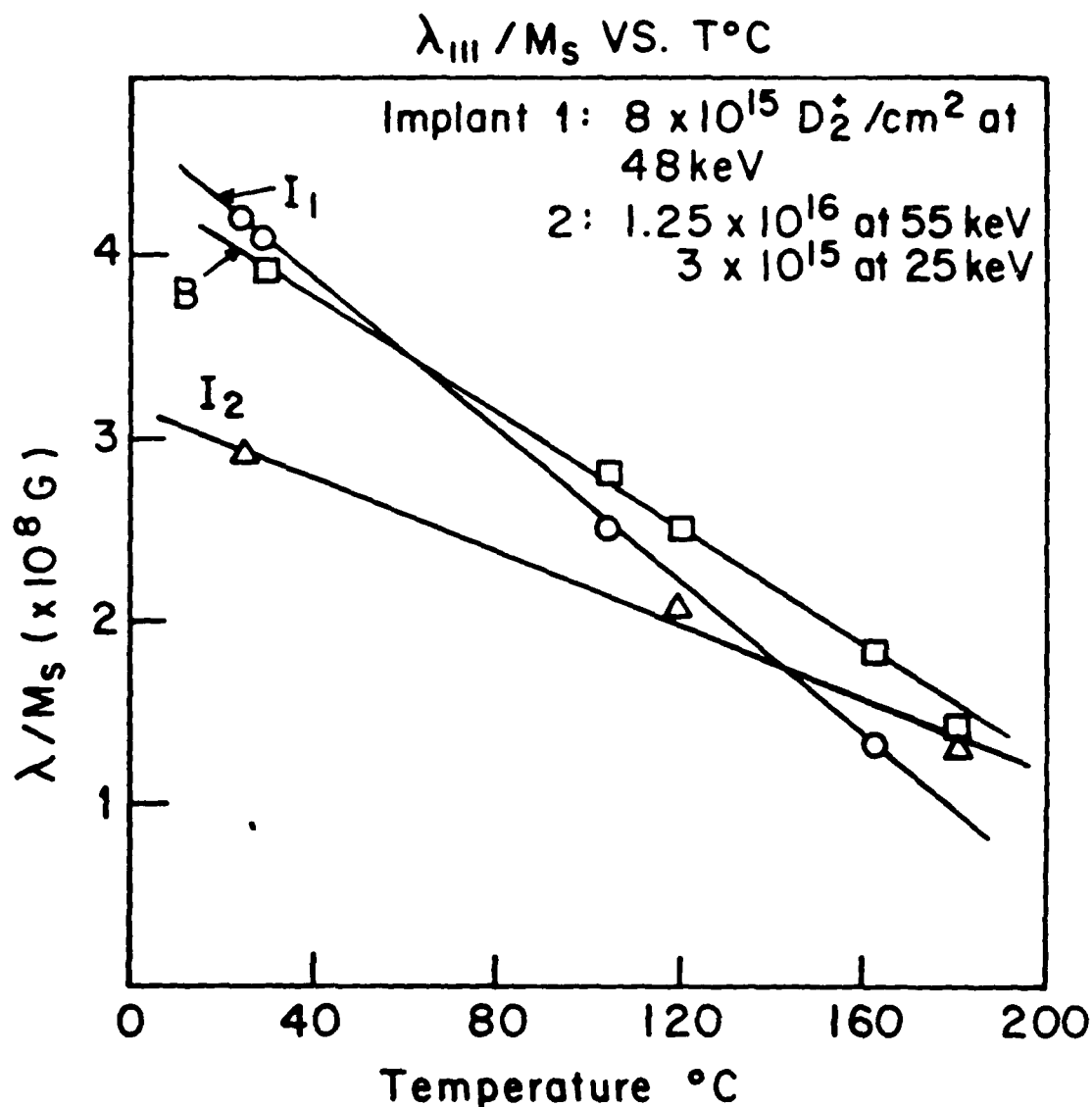
Fig. 3-50: Magnetostriction in Bulk and Implanted Layers of Film 165

For low to intermediate dose implants $\lambda_{111}/M_s(I)$ is either the same or slightly larger than $\lambda_{111}/M_s(B)$ at room temperature. For high implant doses the $\lambda_{111}/M_s(I)$ is significantly degraded at room temperature, but decreases more slowly with temperature. Thus the temperature dependence of $\lambda_{111}/M_s(I)$ is dependent on the implantation-induced damage. If we assume that $4\pi M_s$ decreases with deuterium implantation, as it reportedly does in hydrogen implanted films [14, 29, 42], then the low dose implants reduced $4\pi M_s$ more than λ_{111} but the temperature dependence of $\lambda_{111}(I)$ was higher than that for $4\pi M_s(I)$.

3.6.4. Magnetostrictive Field Contribution in Films with Low Dose Implants

The magnetostrictive contribution to ΔH_E was also measured on a film which received a relatively low implant dose. Film 151 was implanted with 2.8×10^{15} D_2^+/cm^2 at 48 keV. The gyromagnetic ratio and linewidths in bulk and surface layer were equal (ΔH = 145 Oe at 4 GHz), indicating that the implant did not degrade the film properties. The temperature dependence of the film properties are plotted in Fig. 3-51. The uppermost curve in Fig. 3-51 is the magnetization in the bulk layer, as determined from the temperature dependence of the bubble collapse field which was measured before the implantation. The temperature dependence of $H_E(B)$ and $H_E(I)$ are also plotted in Fig. 3-51. Since the implant-induced anisotropy was less than the as-grown uniaxial anisotropy, K_1 (= $(H_E(I) \times M_s)/2$) is positive. Thus the temperature dependence of $H_E(I)$ is not dominated by that of K_1, as it typically is when K_1 is large and negative, but is more equally affected by K_1 and $4\pi M_s$. The temperature dependence of ΔH_E and ΔH_σ are plotted in Fig. 3-51. The ΔH_σ has the same temperature dependence as ΔH_E from 4°C to 84°C. The ratio $\Delta H_\sigma/\Delta H_E$ is 0.48. The $\lambda_{111}/M_s(B)$ was approximately equal to $\lambda_{111}/M_s(I)$ over the temperature range which was measured. Magnetostriction measurements at higher temperatures could not be made since the sample broke during measurement.
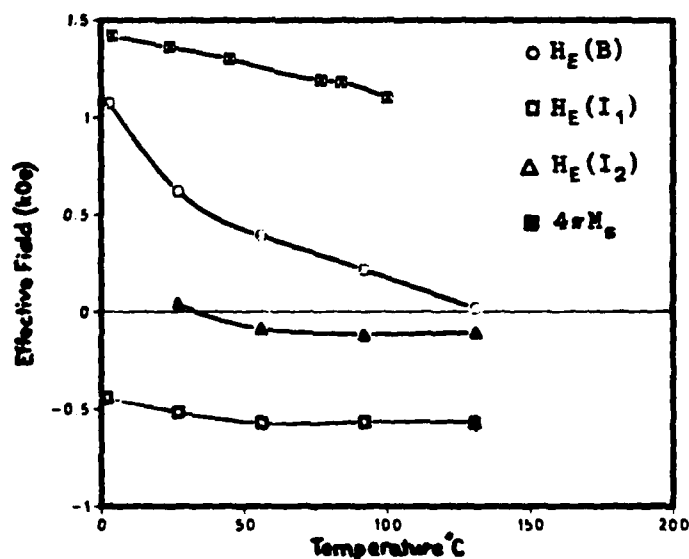
Fig. 3-51: Anisotropy Fields and Magnetization Versus Temperature for Film 151

Thus, the properties of the implanted layers in films with low implant doses, including λ_{111}/M_s, γ, and α, are not significantly different from those in the unimplanted film. Furthermore, an $H_E(I)$ which is nearly temperature independent can be achieved by balancing K_1 with the demagnetization energy.

3.7. EFFECTS OF SiO_2 LAYERS ON FILM PROPERTIES

In the fabrication of contiguous disk bubble memory devices, SiO_2 is often used as a spacer between different thin film layers. While the SiO_2 layers have been found to prevent the annealing-induced desorption of the hydrogen from the implanted layer [13], it was not made clear whether it made any difference whether the SiO_2 layers were deposited before or after the implantation. Here the magnetic properties of films with identical implants which were coated both before and after implantation are compared to uncoated films. We find dramatic differences in the film properties, which depended on when the SiO_2 layer was deposited.

Films 77, 84, and 129 each received an identical triple energy deuterium implant. The implant conditions are listed in Table 3-25. Film 84 was coated with 500 $\overset{o}{A}$ of SiO_2 prior to the implantation, film 77 was coated with 500 $\overset{o}{A}$ of SiO_2 afterwards, and film 129 was not coated. Analysis of the data indicates that film 77 was partially annealed during the SiO_2 deposition, so the results for it will be discussed later. The X-ray rocking curves for films 84 and 129 were similar, indicating that the strain and damage profiles were equivalent, as they were expected to be since the implants were identical. However, there was a remarkable difference in the FMR spectra, which are shown in Fig. 3-52. In spite of the differences in the spectra, the change in the uniaxial anisotropy energy density ΔK ($= \Delta H_E \times 4\pi M_s/8\pi$) was nearly the same in films 84 and 129 (2.44×10^5 ergs/cm^3). For film 129, since $\gamma(I)$ was only 70% of $\gamma(B)$, the value of ΔH_E, calculated from $(H_E(B) - H_E(I))$ is significantly different than the difference in the resonance field of the bulk and main implanted modes at a single frequency. In film 84, on the other hand $\gamma(I)$ was 5% greater than $\gamma(B)$.

Absence of the SiO_2 overcoat led to a significant degradation of the FMR signal from the implanted layer, as evidenced by an increase in the linewidth and a decrease in the amplitude of the surface modes relative to the bulk modes. The linewidth of the main implanted mode on film 129 was twice that of the bulk, compared to 1.4 times the bulk on film 84. Furthermore, the bulk mode amplitude on film 129 was 20 times the main surface mode, whereas on film 84 the bulk mode was 12 times the main surface mode, even though film 129 was slightly thinner. Despite the significantly broader and weaker resonance signal for film 129, the reduction in the magnetization in the implanted layer, calculated from the amplitude and the linewidth of the principal surface mode was similar to that in film 84. Thus the SiO_2 layer does not affect the strain profile, the change in the anisotropy energy density, or the magnetization of the

FILM 84

FILM 129

SiO₂ BEFORE IMPLANT
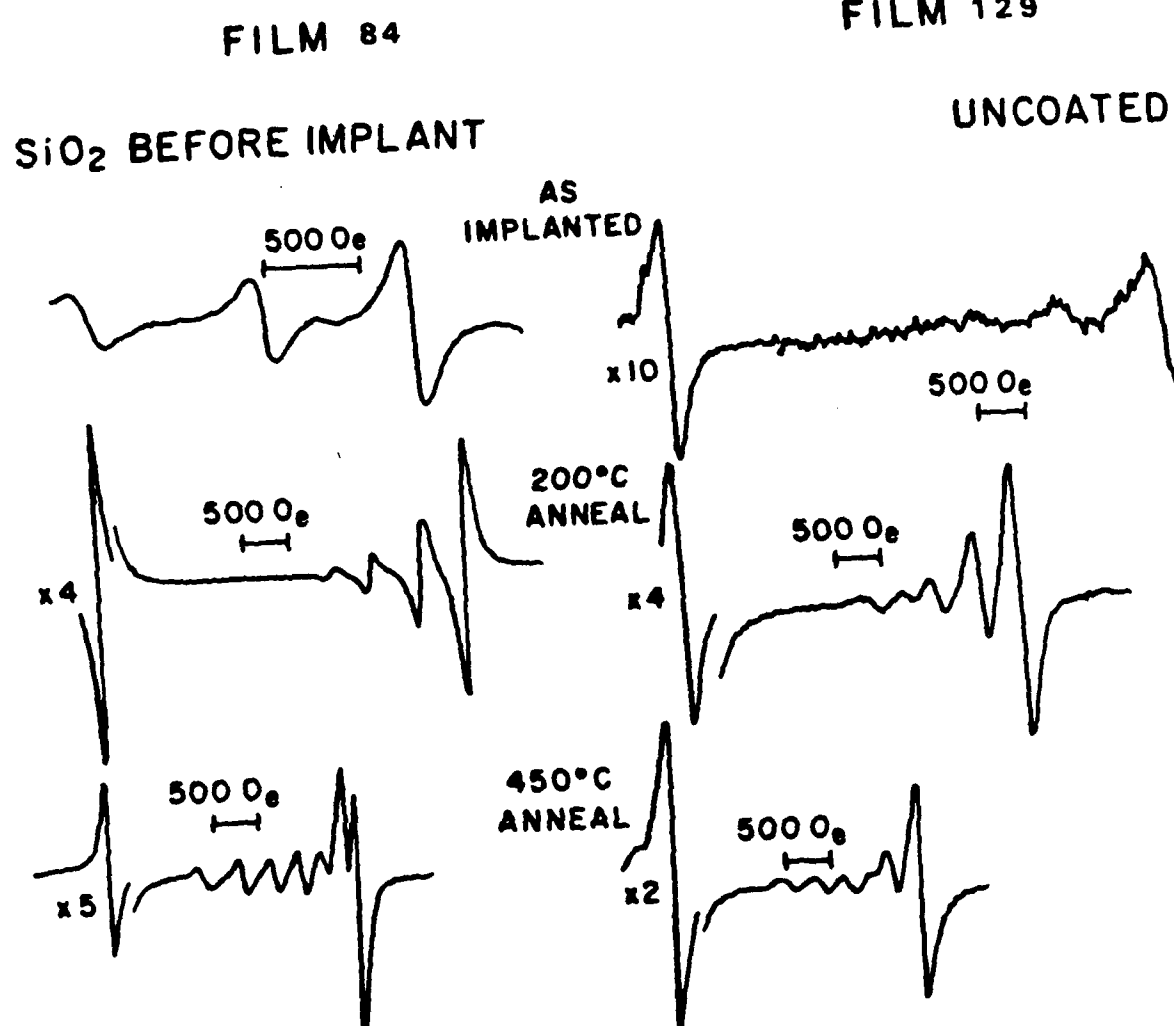
UNCOATED

Fig. 3-52:   Resonance Spectra for Films 84 and 129 – As Implanted,
250 °C Anneal, 450°C Anneal f = 4.5 GHz

Table 3-25:   Deuterium Implant Conditions for Films 77, 84, and 129

Dose	Energy
1.2×10^{16} D_2^+/cm^2	80 keV
5×10^{15} D_2^+/cm^2	50 keV
3×10^{15} D_2^+/cm^2	25 keV

Film 77 coated with 500 Å of SiO₂ after implantation

Film 84 coated with 500 Å of SiO₂ before implantation

Film 129 uncoated

implanted layer. However the weaker resonance signal and broader linewidth, and the

decrease in the gyromagnetic ratio in the uncoated film suggest that there is a fundamental difference in the implant damage mechanism.

The $\gamma(I)$ in film 129 was completely restored to the bulk value after annealing at 250°C. Thus, previous investigators who reported a drastic decrease in the change in the effective field in hydrogen implanted samples after annealing at 250°C [12, 13, 14], calculated from the difference in the field between the bulk and main surface mode, may have observed a combination of hydrogen desorption and an increase in the gyromagnetic ratio.

The results for film 77 indicate that the SiO_2 deposition after implantation caused annealing effects which were similar, but not identical, to a 250°C anneal in films 84 and 129. Before annealing, the surface mode linewidth was 1.4 times the bulk in film 77, compared to 1.1 times the bulk in films 84 and 129 after a 250°C anneal. The implant strain was 1.1% in film 77, compared to 1.16% in film 84 and 1.10% in film 129 after a 250°C anneal.

The SiO_2 layer on film 84 was removed in a hydrofluoric acid etch before the first of two anneals at 800°C. The ΔH_E in film 84 measured after the first 800°C anneal is 1240 Oe, compared to 1490 Oe after the second 800°C anneal. The lower value of ΔH_E was accompanied by a 12% reduction in $\gamma(I)$, compared to $\gamma(I)$ after the 700°C anneal. However, after the second 800°C anneal, $\gamma(I)$ increased from 1.38 to 1.58 ($\times$ 10^7 $(Oe\text{-}sec)^{-1}$). The latter value is consistent with $\gamma(B)$, and is similar to $\gamma(I)$ measured after most of the other anneals. While the acid may have etched some of the implanted garnet, this is not expected to affect the gyromagnetic ratio. Furthermore, the increase in ΔH_E after the second anneal suggests that the region where the maximum anisotropy field change occurs was not removed. Thus even after high temperature anneals, we found that the implanted layer properties are extremely sensitive to the surface treatments.

Since there was a dramatic difference in the properties of films 84 and 129, an additional experiment was performed to determine if the SiO_2 layer affected the film properties at lower doses. Films 113 and 114 were implanted at the same time with an identical double dose of deuterium. Implant conditions are given in Table 3-15, and the results from the implanted film are given in Table 3-26. Film 113 was coated with 500 Å of SiO_2 prior to the implantation, while film 114 was left uncoated. The absorption derivative linewidth at 4.5 GHz in the bulk and implanted layer are given by

Table 3-26: Results for Film 113 and 114

Film	$4\pi M_s$	$H_E(B)$	ΔK ergs/cm^3	ϵ_{max}	ϵ_{min}	ΔH_B	ΔH_1
113	1247 G	620 Oe	$174 \cdot 10^3$	1.11%	0.96%	116 Oe	127 Oe
114	1234	583	167	1.09	0.95	115	133

ΔH_B and ΔH_1 respectively. There is no significant difference in ΔH_1 in the uncoated film compared to the coated film, such as was observed in films 129 and 84.

In summary, a dramatic difference in the FMR signal was observed in films which received moderately high deuterium implant doses, depending on whether or not they were coated with SiO_2 before implantation. The degradation of the FMR signal in the uncoated films was observed on several films which received high dose deuterium implants. A possible explanation for the SiO_2 effect is that there is local heating in the coated film during implantation which partially annealed some of the implant damage by repairing broken bonds, but did not relieve the implant strain. However, further experiments must be done to identify the source of the differences. For high dose deuterium implants, we recommend implanting through an SiO_2 overlayer.

3.8. SUMMARY

The results for the deuterium implanted garnet films which are reported in this chapter were made possible, in part, by the unique set of characterization techniques which were developed as part of this project. The analysis of the FMR spectra, using the numerical spin wave analysis technique developed by Wilts [40] provides a basis for interpreting the FMR spectra. Measurements of the spectra as a function of temperature provide additional information about the magnetic anisotropy uniformity through the implanted layer. In films with low to moderate implant doses, the uniformity does not change with temperature, but in heavily implanted films, there is a change in the relative amplitudes of the resonance modes, indicating that the anisotropy profile changes with temperature. This is attributed to a significant reduction in the Curie temperature in the region of maximum implant damage. The temperature dependence of the FMR modes also provide information about the localization of particular modes in separate regions of the film.

The SiO_2 overlayers have beneficial effects, which include moderating the desorption of deuterium and preventing the severe degradation of the implanted film properties.

notably the FMR signal and the gyromagnetic ratio, in heavily implanted films. Annealing the uncoated films restores the implant-induced damage, but the deuterium desorbs from the garnet at relatively low temperatures. In uncoated films, there is a significant decrease in ΔH_E after a 250°C anneal which is attributed to the desorption of deuterium. The deuterium desorption occurs above 450°C in the coated films. The SiO_2 has the same effect on preventing the desorption of deuterium irregardless of whether it is deposited before or after implantation, indicating that the implant does not degrade the SiO_2 layer. However based on the degradation of the magnetic properties in the uncoated garnet films, we recommend implanting through an SiO_2 layer.

The effects of multiple implants on the film properties were also investigated. While the implant conditions which were used here did not result in ideally uniform anisotropy profiles, modifications to the implant conditions reported here are suggested which will create more uniform profiles. However, due to the mobile nature of the deuterium, it is not clear how the implant conditions should be adjusted if the deuterium is not annealed out of the film. In the SiO_2 coated films, the anisotropy field change becomes peaked near the film surface, due to a build-up of deuterium there.

In the annealing studies we found that ΔH_σ was only 1/3 of ΔH_E on deuterium implanted films, even after annealing at 800°C. Thus approximately 2/3 of the change in anisotropy is due to non-magnetostrictive effects. The positive ΔH_E intercept at zero strain provides additional evidence that non-magnetostrictive mechanisms are operative, even after high temperature annealing. The positive zero-strain intercept for ΔH_E in each of the films may be due to the suppression of the growth-induced anisotropy or to some other mechanism. While this effect has been observed in neon implanted films [72], it has not been reported previously for hydrogen (deuterium) implanted films.

To explain the large non-magnetostrictive portion of the anisotropy field change after the deuterium is annealed out of the film, we postulate that there is some permanent damage to the lattice due to dislocation of the rare-earth ions. This has been observed by previous investigators in neon implanted films [72]. Studies of the linewidth broadening, especially in the films with relatively high samarium content, indicate that the linewidth in the implanted layer is less than that of the bulk [15]. This decrease is attributed to the decoupling of the samarium. In the heavily implanted films, there

was significant linewidth broadening, which may be attributed to disorder. In addition to the suppression of the growth-induced anisotropy, there appears to be yet another mechanism. If we extrapolate the ΔH_E versus implant strain as a function of annealing to zero-strain, we can estimate the suppression of the growth-induced anisotropy. While it was not possible to determine if the growth-induced anisotropy was being restored by the annealing, which would confuse the interpretation, we presume that it was not significantly affected below 700°C. Thus there is an additional mechanism for which we have not been able to identify a source. The characteristics of this mechanism are that it is a linear function with strain, but does not appear to be attributed to it, and the temperature dependence is larger than that of the magnetostrictive effect.

Chapter 4
OXYGEN AND HYDROGEN IMPLANTS

Oxygen and hydrogen implants were investigated using the techniques developed here. Oxygen is of interest as it has a substantially larger mass than deuterium. Films implanted with oxygen are expected to have different properties than those implanted with deuterium due to a difference in the implant mechanisms. In addition, oxygen implants were compared to neon implants reported by previous investigators. Hydrogen is of interest, as there have been no comparisons of the properties of hydrogen to deuterium implanted films. Since hydrogen is less massive than deuterium, it is expected to have a slightly different effect on the film properties. Furthermore, since hydrogen implants have been reported by several other investigators, the results obtained here can be compared to previously published results.

4.1. OXYGEN IMPLANTS

Implants with ion species which are more massive than hydrogen or deuterium, such as neon and helium, have been widely studied by other investigators. Here, an investigation of the effects of oxygen implants, done individually and in combination with deuterium were studied. Since the characterization techniques used here are unique, it is important to compare results of oxygen implants to those for other implant species reported by previous investigators.

Oxygen implants were studied for several reasons. Since oxygen implanted films do not exhibit the large non-magnetostrictive anisotropy field change that deuterium implanted films do, it is instructive to compare the results for the two implant species. Although much has been reported on the effects of neon, oxygen, which presumably has similar effects, has received relatively little attention. In this project, the initial interest in oxygen was to use it in combination with deuterium to achieve a uniform damage profile through the depth of the implanted layer [68]. However, it was found in this study that the anisotropy profile may not be uniform even when the damage profile is

because the anisotropy field change for deuterium implants is typically twice that of an oxygen implant with a comparable amount of strain. Furthermore, since the anisotropy field change with oxygen saturates at strain levels which are typically used in submicron diameter bubble devices, the oxygen implant required to achieve a uniform strain and damage profile will degrade the magnetic properties of the implanted layer. Finally, oxygen implants are used for hard bubble suppression. In order to establish the optimal implant dose, films with a range of implant doses were measured. The dose level where the magnetic properties in the implanted layer are seriously degraded was determined.

4.1.1. Results for Oxygen Implants

A series of films with similar compositions were implanted with different oxygen doses. The bulk film parameters and oxygen implant conditions are given in Table 4-1. The films are nominal one micron diameter bubble material and have a nominal composition $(YSmTmGd)_3(FeGaAl)_5O_{12}$. The implant current density was approximately $0.11 \mu A/cm^2$.

The maximum strain is plotted versus oxygen implant dose in Fig. 4-1. The strain increases nearly linearly with dose, except for the two lowest doses, both of which lie above the linear fit. The change in the uniaxial anisotropy energy ΔK ($= \Delta H_E \times M_s/2$) is plotted versus implant strain in Fig. 4-2. The ΔK saturates between 1% and 1.4% strain, and decreases at higher strains. This effect has been widely observed with other heavy ion species, such as neon and helium, and has been attributed to the implant-induced damage [10, 8]. The maximum anisotropy field change is limited to that achievable with 1% strain. Using higher implants doses causes a degradation in the film properties, and a reduction in ΔH_E. This saturation effect has also been observed in neon implanted films and is the primary reason that hydrogen and deuterium implants were initially investigated [10].

The change in anisotropy field ΔH_E corresponding to the energy density ΔK plotted in Fig. 4-2, ΔH_σ, and the ratio $\Delta H_\sigma/\Delta H_E$ are given in Table 4-2. Results for $\lambda_{111}/M_s(B)$ and $\lambda_{111}/M_s(I)$, where (B) and (I) refer to the bulk and implanted layers respectively, and ϵ_{max} are also given in Table 4-2. For the films with low oxygen implant doses the $\lambda_{111}/M_s(I)$ was approximately equal to $\lambda_{111}/M_s(B)$. However, on film 39, the quantity $\lambda_{111}/M_s(I)$ was 25% less than $\lambda_{111}/M_s(B)$. This indicates that the implant on film 39 reduced λ_{111} more than $4\pi M_s$ compared to their bulk values. On

Table 4-1:   Bulk Parameters and Oxygen Implant Conditions

Film	Thickness	$4\pi M_s$	$H_E(B)$	λ_{111}
141	0.30 μm	750 G	1020 Oe	-2.1×10^{-6}
30	1.1	623	685	-2.1
34	0.9	654	568	-2.3
38	0.85	612	648	-2.6
39	0.90	633	686	-2.0
40	0.80	725	457	$-$

Film	Dose	Energy
	$(\times 10^{14}/cm^2)\ O^+/cm^2$	
141	0.95	110 keV
30 *	1.2	135
34	1.2	110
38	2.4	110
39	3.6	110
40	4.8	110

* Coated with 500Å SiO_2
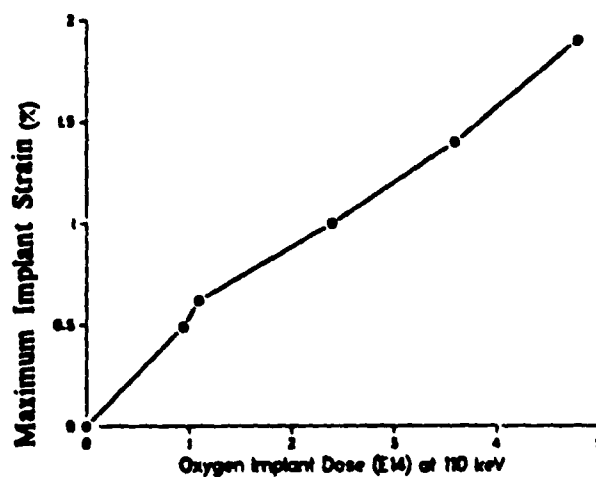
Fig. 4-1:   Maximum Implant Strain versus Dose for Oxygen Implanted Films

film 40, a similar reduction in $\lambda_{111}/M_s(I)$ is expected since the x-ray rocking curve indicates that there is more damage, however the sample broke during measurement, so no magnetostriction results were obtained.
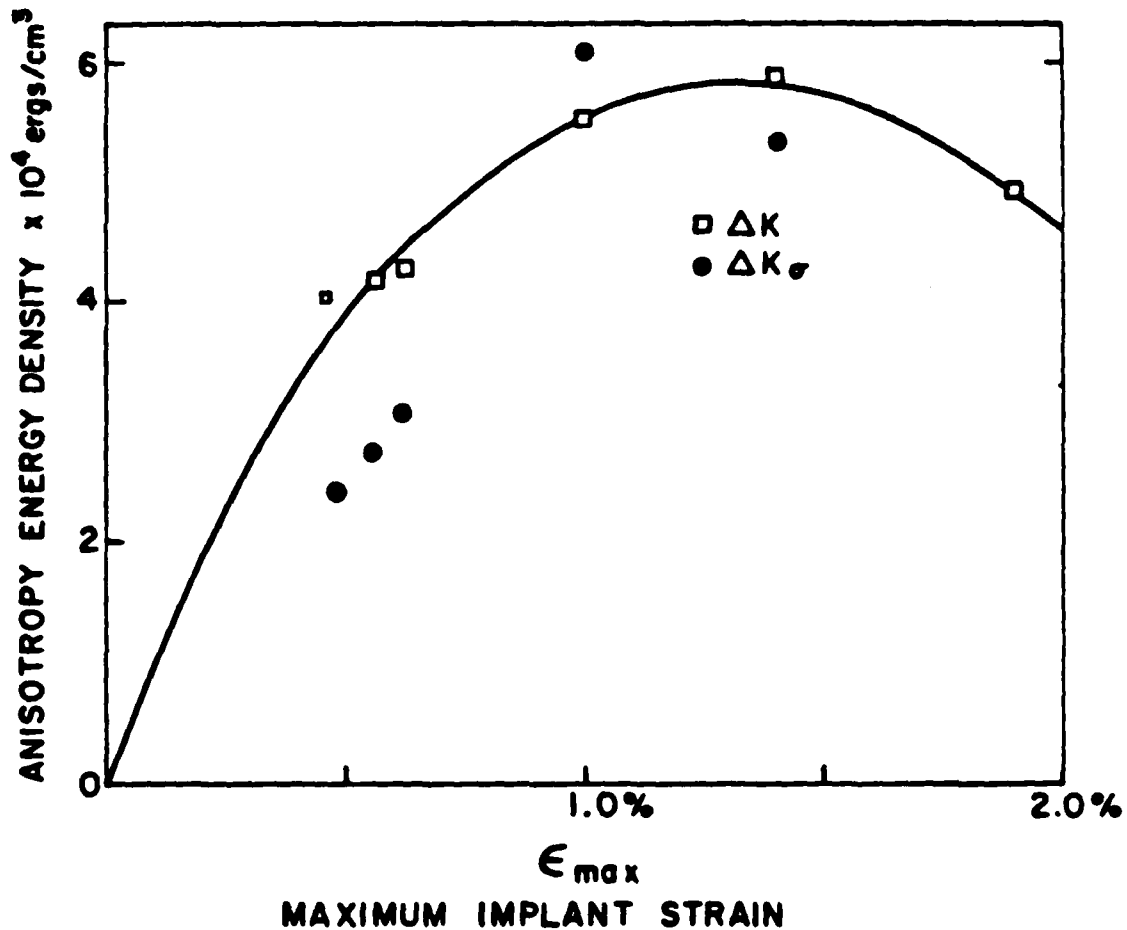
The gyromagnetic ratio in the bulk and implanted layers are also given in Table 4-2. There was no significant difference in $\gamma(B)$ and $\gamma(I)$ in the oxygen implanted films which were studied here. In Table 4-2, the cubic crystalline anisotropy field in the bulk and implanted layers, $H_1(B)$ and $H_1(I)$, for films 38, 39, and 40 are given. The $H_1(I)$ is decreased by implantation. On film 40, which had the highest dose, $H_1(I)$ could not be determined due to overlap of the surface modes. For comparison, on a neon implanted film with 1.3% strain, H_1 in the implanted layer was found to decrease by 70% [14].

A comparison of an oxygen and a deuterium implanted film which had the same strain was made. Two films with similar values of λ_{111} and $4\pi M_s$ were implanted: film 38 with oxygen, and film 165 with deuterium (8×10^{15} D_2^+/cm^2 at 48 keV). The

Table 4-2: Results for Single Energy Oxygen Implants

Film	$\lambda_{111}/M_s(B)$ G^{-1}	$\lambda_{111}/M_s(I)$ G^{-1}	ϵ_{max}	$\gamma(B)$	$\gamma(I)$
141	-3.5×10^{-8}	-3.6×10^{-8}	0.49%	2.56 MHz/Oe	2.46 MHz/Oe
30	-4.2	-4.2	0.56	2.35	2.33
34	-4.4	-4.1	0.62	2.35	2.33
38	-5.4	-5.4	1.0	2.34	2.27
39	-3.9	-2.9	1.4	2.40	2.37
40	$-$	$-$	1.9	2.42	2.37

Film	ΔH_E	ΔH_σ	$\Delta H_\sigma/\Delta H_E$
141	1366 Oe	934 Oe	0.68
30	1695	1102	0.65
34	1645	1181	0.72
38	2261	2488	1.10
39	2324	1875	0.80
40	1703	$-$	$-$

Film	$H_1(B)$	$H_1(I)$
38	-150 Oe	-90 Oe
39	-160	-20
40	-160	$-$

maximum implant strain in both films was 1.0%. The ΔK in film 38 was 55.1×10^3 ergs/cm^3 compared to 103.3×10^3 ergs/cm^3 in film 165. This shows clearly that the effects of oxygen and deuterium implants are quite different. Whereas the deuterium produces a large ΔH_E due to magnetostrictive and non-magnetostrictive effects, the ΔH_E for oxygen implants is largely attributed to magnetostrictive effects.

In the oxygen implanted films studied here, the ratio $\Delta H_\sigma/\Delta H_E$ is approximately 0.7 for the films with the low implant doses, such as 30, 34, and 141. This compares with a ratio of 0.3 to 0.5 in deuterium implanted films with similar amounts of strain. For higher doses, the maximum strain used in the calculation of the magnetostrictive field may not correspond to the region of maximum ΔH_E (ΔK). On films 38 and 39, ΔH_σ apparently accounts for most of ΔH_E. However the calculation of ΔH_σ is complicated since films 38 and 39 are in the region where ΔK saturates.

There is a further complication with the magnetostriction measurement on the singly implanted films which is related to the variation of the strain and anisotropy profiles through the film thickness. In a singly implanted film there may be a considerable exchange shift due to the curvature in the anisotropy profile. This will shift the location of the principal surface mode. Furthermore since the strain is not uniform. and is not uniquely related to the anisotropy profile, it is difficult to relate the measured magnetostrictive effect to the strain which causes it. Thus to precisely determine the magnetostrictive field in these films it may be necessary to determine the anisotropy and the strain profiles.

4.1.2. Temperature Dependence of Anisotropy Fields in Oxygen Implanted Films

Analysis of the temperature dependence of the anisotropy fields in the oxygen implanted films provides insight into the effects of overdamage on the film properties. In Figs. 4-3 and 4-4 the temperature dependence of the effective anisotropy fields in the bulk and implanted layers of film 141 and 39 are plotted.
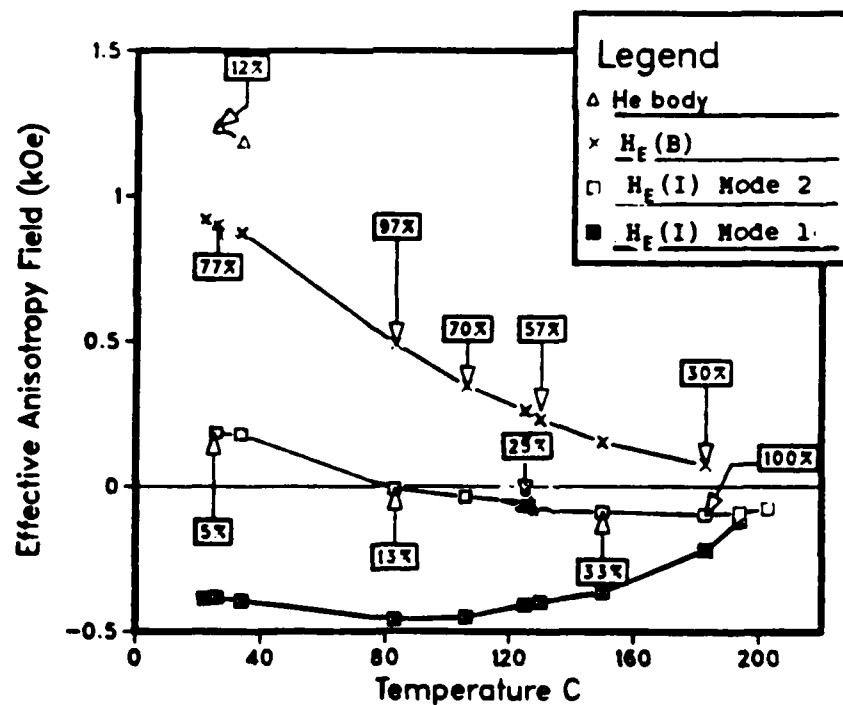
Fig. 4-3: Effective Anisotropy Field Versus Temperature For Film 141:
Mode Amplitudes Relative to Principal Surface Mode

The results for film 141 are typical of a film with a low dose oxygen implant, while those for film 39 are typical of a moderate dose implant. The amplitudes of the
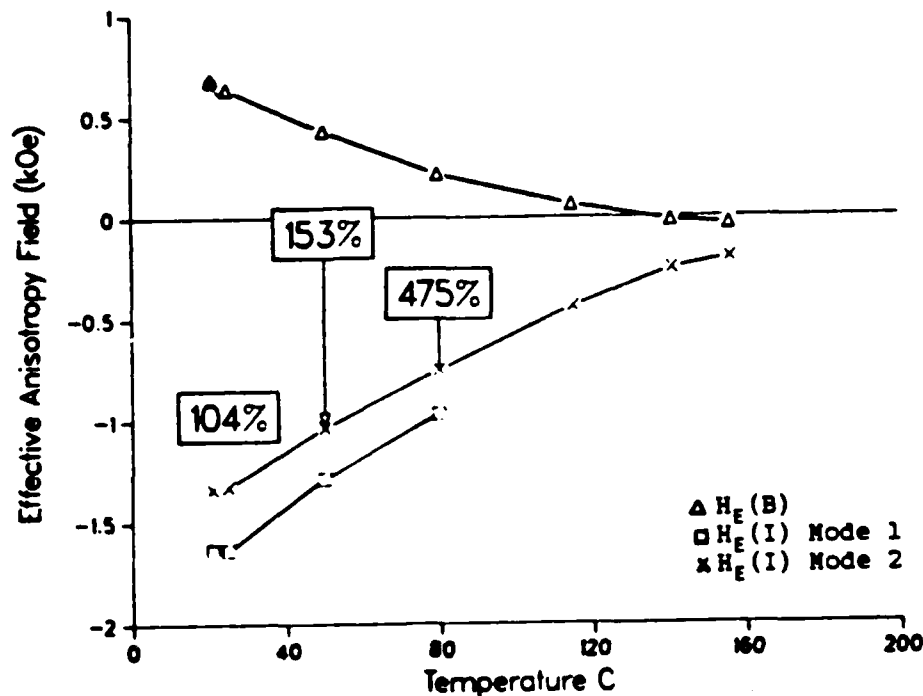
Fig. 4-4: Effective Anisotropy Field Versus Temperature For Film 39:
Mode Amplitudes Relative to Principal Surface Mode

modes, relative to that of the highest field surface mode, are indicated. For film 141, at 25°C, four modes were observed. The uppermost mode is presumed to be a spin wave mode in the thin bulk layer. This mode was not observed above 35°C. The principal bulk mode amplitude, relative to the first surface mode, increased up to approximately 85°C, and then decreased up to 180°C. Above 180°C, the principal bulk mode disappeared. The disappearance was expected, as there was a gradual reduction of the bulk mode amplitude above 85°C. The disappearance of the principal bulk mode at 180°C may be related to fact that the bulk layer is only 0.10 μm thick. The second surface mode amplitude was only 5% of the first at 25°C, but increased with temperature. At 180°C, the amplitudes of the two surface modes are equal. It appears that the (I_2) mode is the only mode observed at 193 °C, as determined from a smooth fit through the data points. The increase of the second mode amplitude, relative to the first will be compared to results for film 39.

The temperature dependence of the uniaxial anisotropy energy K_U and the anisotropy energy in the implanted layer $K_1 = ((H_E(I) + 4\pi M_s) \times (M_s/2))$ are plotted in Fig. 4-5. The K_1 was calculated assuming that the magnetization in the surface layer was the

same as that in the bulk, and the cubic crystalline anisotropy energy was negligible, which are reasonable assumptions for the purposes of the discussion here. The temperature dependence of the magnetization, determined from the bubble collapse field measurements on film 140, which had the same composition as film 141, is plotted in Fig. 4-6.
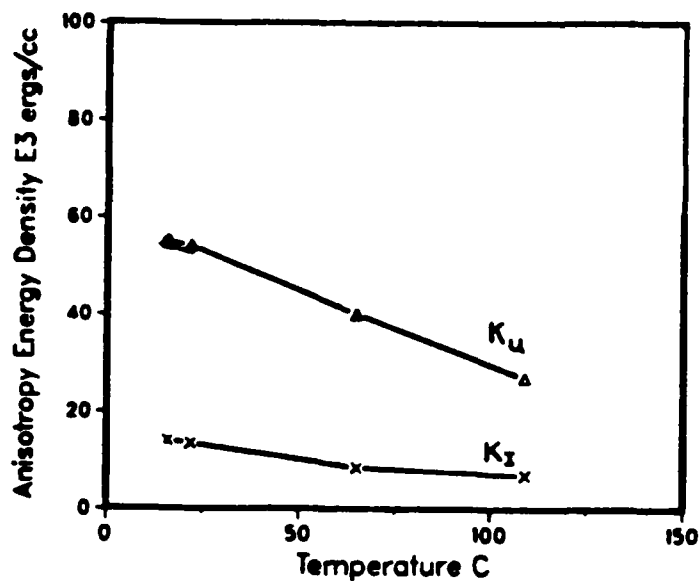
Fig. 4-5: Anisotropy Energy Density Versus Temperature
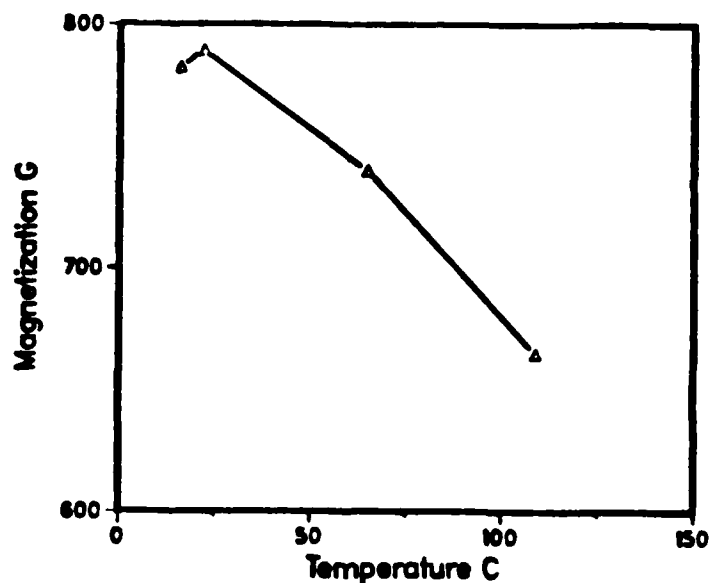
Fig. 4-6: Magnetization Versus Temperature

The temperature behavior of $H_E(I_1)$, in Fig. 4-3, is attributed to a positive K_1. Since

K_1 is small, and it, as well as K_U and $4\pi M_s$, decrease towards zero at higher temperatures. $H_E(I_1)$ is more equally influenced by the anisotropy and the magnetization. By comparison, the temperature dependence of $H_E(B)$, and $H_E(I)$ in films with higher implant doses, is dominated by the temperature dependence of the anisotropy energy K_1.

In contrast to film 141, which had a low dose implant that was not sufficient to orient the magnetization in the plane of the film, film 39 had a large in-plane anisotropy. The effective fields in the bulk $H_E(B)$, and surface layer $H_E(I_1)$ and $H_E(I_2)$ of film 39 are plotted versus temperature in Fig. 4-4. The temperature dependence of the effective fields in the surface layer is dominated by the large, negative anisotropy energy. The relative amplitude of the two surface modes are indicated in Fig. 4-4. While both surface modes have nearly identical mode amplitudes at 26°C, the amplitude of the second mode increases to 475% of the first mode amplitude at 80°C. At 115°C, only the second mode was observed. At higher temperatures, the $H_E(B)$ and $H_E(I_2)$ converge. The negative $H_E(B)$ above 140°C, only implies that the H_K is less than the $4\pi M_s$. The unusual behavior of the two implanted modes may be related to the damage. The first surface mode, which measures the maximum anisotropy field change, is presumably located in the region of maximum damage, as determined by the disappearance of the first surface mode above 80°C. The mode disappearance above 80°C is related to the reduction of the Curie temperature in the region of maximum damage. The second mode is not a higher order spin wave mode, but measures the anisotropy field in a separate region. If the second mode were simply a higher order mode, which was localized in the same region as the first, than one would expect it to disappear at the same temperature as the first mode. In fact, the second mode does not disappear; rather the amplitude increases with respect to the first mode as the temperature increases, as shown in Fig. 4-7.

The plots of the effective fields in the bulk and surface layers of film 141 and 39, shown in Fig. 4-3 and 4-4 provide an example of one of the problems with high dose oxygen implants. The ΔH_E (= $H_E(B) - H_E(I)$) in film 39 at 25°C is approximately 1000 Oe larger than ΔH_E in film 141. However, at 150°C, ΔH_E on film 141 is approximately 3 times larger than ΔH_E in film 39. Comparing the FMR spectra, two surface modes are observed at 25°C on both films. However the amplitude of the second mode is 5% of the first mode in film 141, compared to 100% in film 39. At higher temperatures, the second mode amplitude on both films increases, with respect to the first. The disappearance of the first mode in film 39 indicates that this mode is localized in the region of maximum implant damage, whereas the second mode is
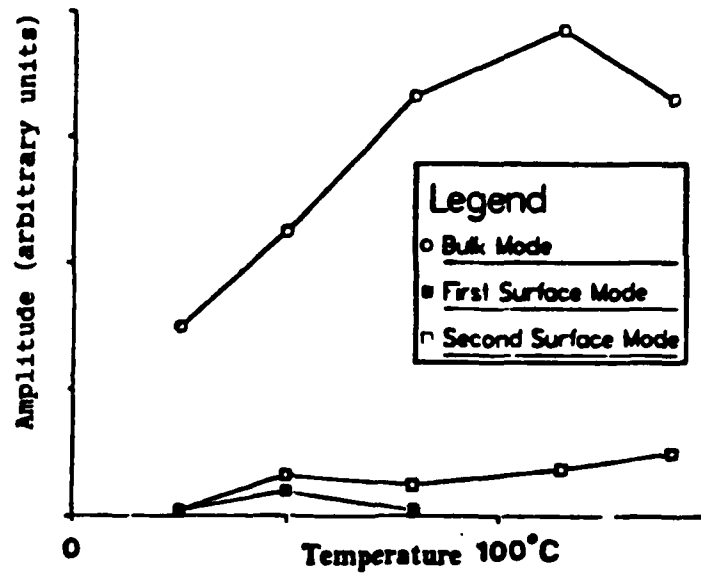
Fig. 4-7: Resonance Mode Peak Amplitude at 5.0 GHz Versus Temperature: Film 39 localized in a region with lower damage. Due to the extensive damage on film 39, the Curie temperature is reduced and the temperature dependence of ΔH_E is less favorable for device use.

4.1.3. X-ray Rocking Curves and Strain Profiles

The X-ray rocking curves for oxygen implanted films 38, 39, and 40 are shown in Fig. 4-8. These are similar to those published by Speriosu and Wilts for single energy neon implants, which are shown in Fig. 4-9. In Fig. 4-9, the dashed curves correspond to the calculated rocking curves and the solid curves represent the experimental results. The perpendicular strain for the neon implants are plotted in Fig. 4-10. Speriosu used the (444) reflection, whereas the (888) reflection was used here. As noted in Chapter 2, both rocking curves contain the same essential information. Speriosu found that the strain increased linearly with dose, but the strain profile was nearly independent of the dose. The implant damage also increased linearly with the strain. The rocking curve for film 38 is similar to that for a neon implanted film which received 2×10^{14} Ne^+/cm^2 at 190 keV.

The strain profile for a single energy neon implant in Fig. 4-9 is non-zero at the surface, is a maximum at the projected ion range, and has a Gaussian-shaped tail which extends to the unimplanted region. One of the characteristics of the neon (or oxygen) implants is that the strain profile has a less abrupt transition from the region of maximum strain to the unimplanted region than it does with hydrogen implants.
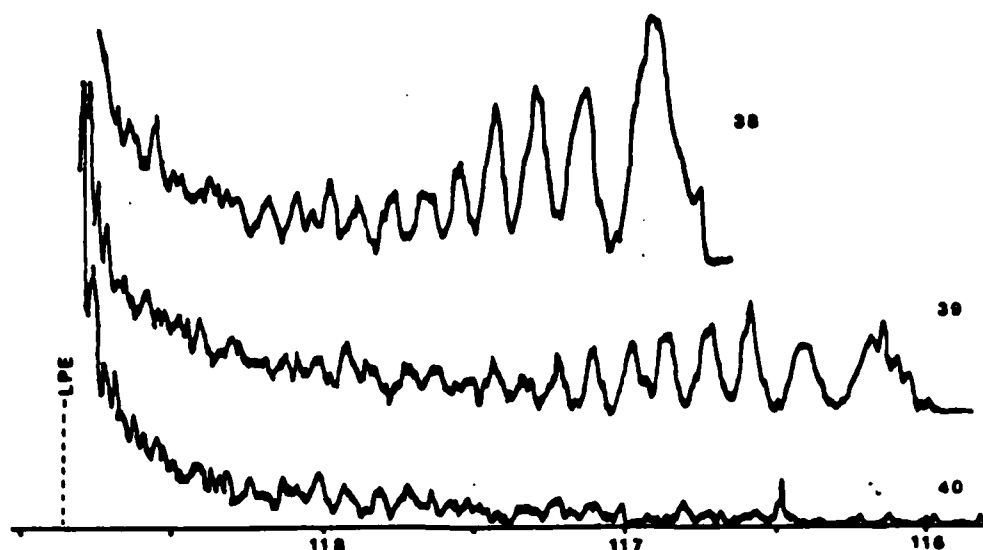
Fig. 4-8: X-ray Rocking Curves for Oxygen Implanted Films

The rocking curve for film 39 is similar to that for film 38, although the amplitudes of the low angle peaks are reduced. On film 40, it was difficult to determine the maximum implant strain from the diffraction peaks in the (888) reflection. While there were periodic peaks which could be resolved down to approximately 117° (2θ), and the maximum strain appeared to correspond to 116.5°, this could not be accurately determined due to signal to noise problems. The maximum implant strain was determined from the (444) reflection, as the diffracted signal is considerably stronger. The dramatic change in the rocking curve from film 39 to film 40 indicates that the crystal is becoming highly damaged, which is in agreement with the magnetic measurement results.

In the neon implanted samples, the strain profile was peaked near the projected range of the neon ions, but the anisotropy change was less in this region due to overdamage [14]. The two observed resonance modes were localized in the regions closer to the bulk and to the surface from the region of maximum damage.

In summary, the rocking curves from the oxygen implanted films are similar to those reported for neon with comparable strains. Thus, we conclude that the strain profiles of the oxygen implanted films are similar to those in neon implanted films.
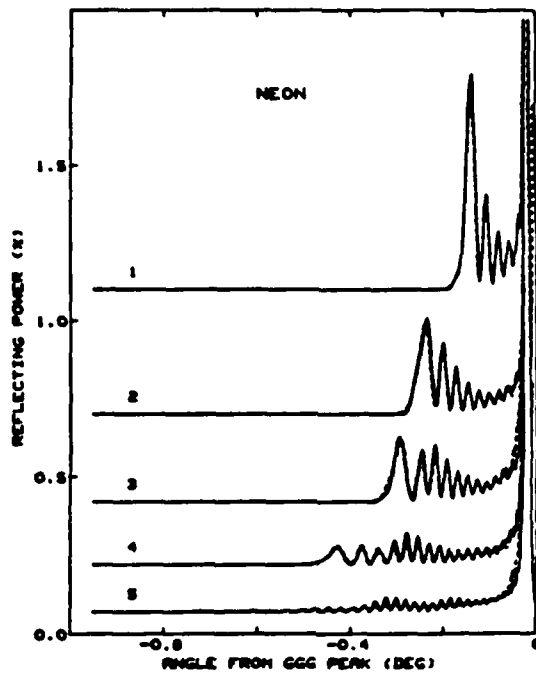
Fig. 4-9: Experimental and Calculated Rocking Curve for Neon
Implanted Films [14]
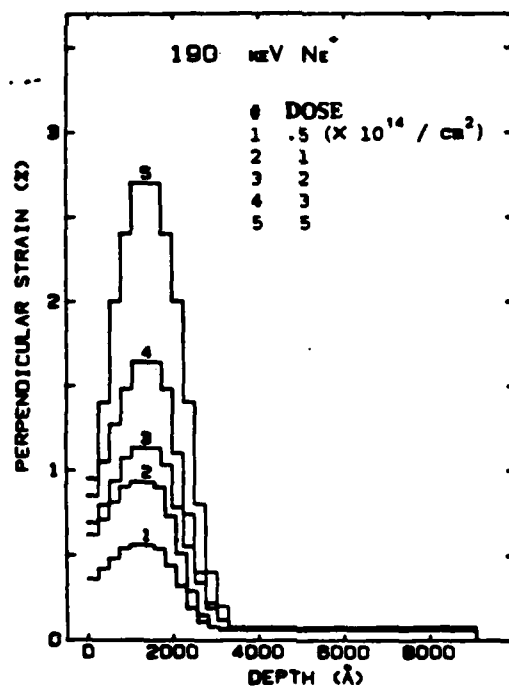
Fig. 4-10: Strain Profile for Neon Implanted Films [14]

4.1.4. SiO_2 Coatings on Oxygen Implanted Films

Since the SiO_2 overlayers had a dramatic effect on the properties of deuterium implanted films, the effects were also studied on two oxygen implanted films. Films 30 and 34 were implanted with identical doses of oxygen, given in Table 4-1, but the energy on film 30 was increased to account for a 500 $\overset{o}{A}$ thick layer of SiO_2 which was sputter deposited on the film prior to implantation. The higher strain measured on film 34 is apparently due to the lower penetration depth of the implanted ions. Thus the additional implant energy for film 30 was not completely dissipated in the SiO_2 layer. The X-ray diffraction peak at the lowest angle for the (888) reflection was slightly broader for film 30, which is attributed to the same dose being implanted at a higher energy, and to a straggling effect in the SiO_2 layer [73], both of which will increase the width of the region with the maximum strain.

There were no discernable differences in the amplitudes or linewidths of the surface modes in the FMR spectra for films 30 and 34. Thus the presence of the SiO_2 layer during implantation does not appear to have the effect on the magnetic properties of these films that it did in higher dose deuterium implanted films.

4.1.5. Combined Deuterium and Oxygen Implants

Implantations with multiple ion species have been used to achieve a uniform damage profile [68]. In films implanted with both oxygen and deuterium, the deuterium is used for the deep implant, and the oxygen for the shallow implant. Oxygen and deuterium are used, instead of a multiple energy deuterium implant, as the oxygen dose is significantly lower, which reduces the total implant time. A double dose of oxygen is not used, as the implant range is only 0.30 μm at 180 keV, which is the limit of the implanter used here. If implants are done through SiO_2 or metal layers, the range will be further reduced. Furthermore, the strain profile for the deuterium implant has a more abrupt transition to the bulk layer than that for oxygen, which makes the deuterium more desirable for the deep implant species. While oxygen can be used to obtain a uniform strain profile, due to the differences in implant mechanisms in deuterium and oxygen implanted films, it does not necessarily give a uniform anisotropy profile. First, in the region where ΔK (ΔH_E) increases with strain, the ΔK for oxygen is approximately 1/2 that of a deuterium implant which causes the same strain. Secondly, the ΔK saturates at approximately 1% strain on oxygen implanted films, so the desired ΔK will not be achieved if 1% strain does not provide an adequate

magnetostrictive energy. Thus, even though a uniform strain profile can be achieved with a combined deuterium and oxygen implant, the anisotropy profile will not be uniform.

Material parameters for the films which received combined deuterium and oxygen implants are given in Table 4-3. Implant conditions are given in Table 4-4.

Table 4-3: Material Parameters for Films Implanted with Deuterium and Oxygen

Film	Thickness	$4\pi M_s$	$H_E(B)$	λ_{111}
89	1.03 μm	703 G	872 Oe	–
112	0.85	1266	558	–
141	0.30	750	1020	-2.1×10^{-6}
142	0.30	750	1020	-2.1
143	0.30	750	1020	-2.1
96	0.70	800	747	–
152	0.24	1292	947	–

Table 4-4: Implant Conditions for Combined Deuterium and Oxygen Implants

Film	Deuterium	Oxygen
89	5×10^{15} D_2^+/cm^2 @ 60 keV	0.95×10^{15} O^+/cm^2 @ 110 keV
112	5×10^{15} D_2^+/cm^2 @ 60 keV	0.95×10^{15} O^+/cm^2 @ 110 keV
141		0.95×10^{15} O^+/cm^2 @ 110 keV
142	5×10^{15} D_2^+/cm^2 @ 60 keV	
143	5×10^{15} D_2^+/cm^2 @ 60 keV	0.95×10^{15} O^+/cm^2 @ 110 keV
96-2	8×10^{15} D_2^+/cm^2 @ 48 keV	1.2×10^{15} O^+/cm^2 @ 70 keV
152-3	8×10^{15} D_2^+/cm^2 @ 48 keV	1.2×10^{15} O^+/cm^2 @ 50 keV

To separate the effects of each ion species in the combined implant, film 89 was implanted with oxygen in one part of the film, deuterium in another part, and both ions in the overlapping region. Results for three films with similar properties, which were implanted with oxygen (141), deuterium (142), and both deuterium and oxygen (143) are also compared.

Results for the bubble collapse field, measured in each region of film 89, are given in

Table 4-5. The collapse field increased by 14% in the oxygen implanted region, but decreased by 3% in the deuterium implanted region. In the region with the combined implant, the results are similar to those in the deuterium implanted region. The increased collapse field is associated with flux closure due to in-plane magnetization in the oxygen implanted film. The decreased collapse field is indicative of an overdose, which suggests that the deuterium implant dose is too high for use in a bubble device.

Table 4-5: Collapse Field for Film 89: Combined Deuterium and Oxygen Implants

Before Implant	Oxygen	Deuterium	Combined
352 Oe	400 Oe	342 Oe	345 Oe

The X-ray rocking curves for some of the films were analyzed by V. Speriosu. Results are summarized in Table 4-6. Speriosu's analyses of these films were used as the basis for analyzing the results from the other films.

Table 4-6: X-ray Results for Combined Species Implants:
Provided Courtesy of V.S. Speriosu

Sample	Max. Strain (%)	Average $\langle \epsilon \rangle$	Surface ϵ_{surf}	Thickness
141	$0.49 \leq \epsilon_{max} < 0.59$	–	–	2400 ± 250 Å
142	$0.65 \leq \epsilon_{max} < 0.72$	0.55	0.34	3500 ± 350
143	$0.77 \leq \epsilon_{max} < 0.83$	0.71	0.66	3900 ± 400
112	$0.78 \leq \epsilon_{max} < 0.85$	0.70	0.63	3500 ± 350

The X-ray rocking curves for films with the oxygen implant (film 89), deuterium implant (film 142), and the combined implant (film 112) are given in Figs. 4-11, 4-12, and 4-13. The range of values of the maximum implant strain, given in Table 4-6, are calculated from the angle where the amplitude is 10% of the first surface peak (at the lowest angle), and the lowest angle peak. Similarly, the surface strain is determined from the first maximum on the other side of the envelope of surface peaks (on the side closer to the LPE film peak).

The rocking curve for the oxygen implant has periodic oscillations with amplitudes which increase progressively at lower angles. No average strain is given for film 141, as the profile is sharply peaked and $\langle \epsilon \rangle$ is not well defined. Similar rocking curves have been published for neon implanted films. The rocking curves for the single deuterium implant have a different shape. There are oscillations with increasing

amplitude, from 118.3 to 118.1°. Below these, there are relatively large amplitude oscillations. The strain profile for the deuterium implanted films has a lower surface strain, but a higher maximum strain and the maximum strain is located deeper in the film as determined from the ion range statistics [11], compared to the oxygen implant.

To compare the magnetic anisotropy of the individual implants, with those of the combined implants, FMR measurements were done on these films. Results are summarized in Table 4-7. Films 141, 142, and 143 were all grown from the same melt, under identical conditions. The $H_E(B)$ values, which were measured before implantation, are within 5% on all three films, indicating that the films have nearly identical material properties.

The results for film 143, in Table 4-7, indicate the oxygen implant does not increase ΔH_E beyond the level attributed to the deuterium implant, as measured on film 142, even though the oxygen implant increased the maximum strain. The results from film 112 were compared to those of film 143 by calculating the implantation-induced change in anisotropy energy ΔK. The ΔK on films 112 and 143 are in reasonable agreement, considering that the film properties are not identical and bulk magnetization on film 143 which was used to calculate ΔK was estimated. Thus, to achieve a more uniform strain profile, the oxygen implant dose should be decreased. However, since the ΔH_E is the same, irregardless of whether the oxygen implant is used, we believe the anisotropy and strain profiles cannot be made uniform simultaneously, due to the difference in the implant mechanisms for deuterium and oxygen.

4.1.6. Summary of Results for Oxygen Implants

The results from oxygen implanted films indicate that the film properties are similar to those reported by other investigators for neon implanted films. The ΔH_E saturates at about 1% strain, and decreases with higher strains. This decrease is associated with a degradation in the magnetostriction. The change in the temperature dependence of the FMR modes indicates that the Curie temperature is reduced in the region of maximum damage. There is a distinct difference in the anisotropy field change for oxygen implants, compared to deuterium, which is attributable to the non-magnetostrictive effects in deuterium implanted films. Results for films with combined deuterium and oxygen implants indicate that the anisotropy profile will not be uniform, even if the strain profile is, due to the difference in the implant mechanisms producing the change in anisotropy for oxygen and deuterium.
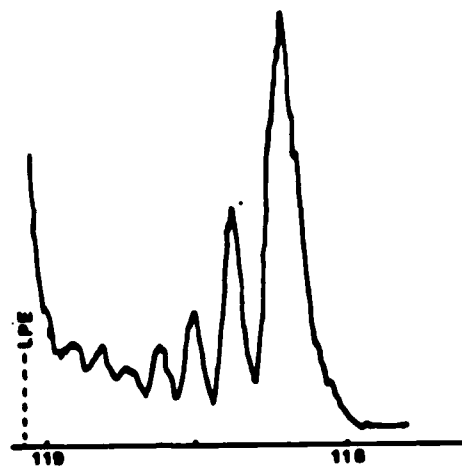
Fig. 4-11: X-ray Rocking Curve for Oxygen Implants
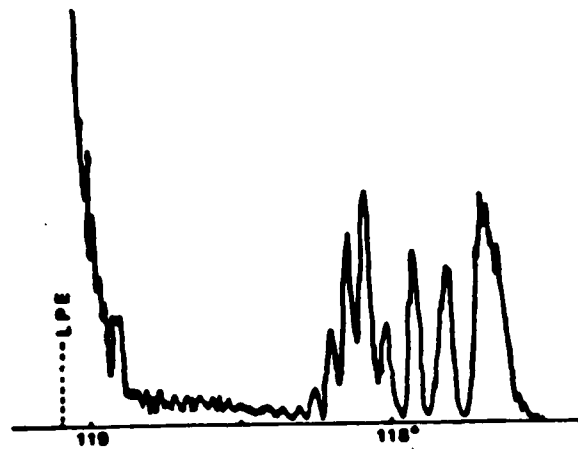
Fig. 4-12: X-ray Rocking Curve for Deuterium Implants
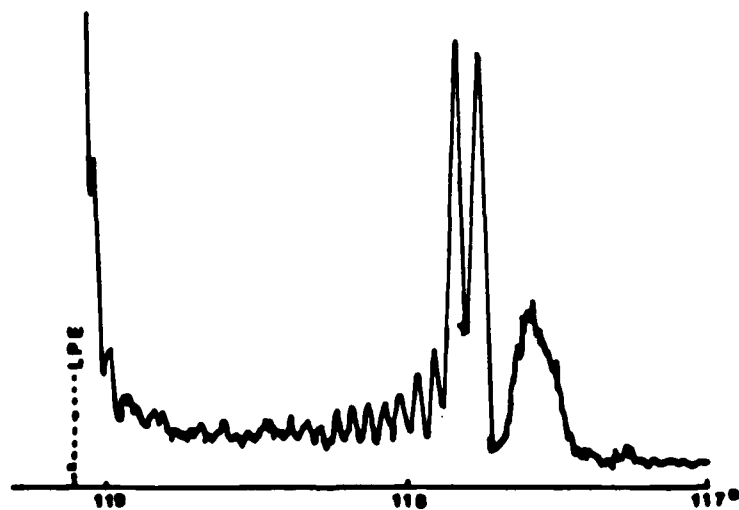
Fig. 4-13: X-ray Rocking Curve for Combined Implants

Film	Ions	$H_E(B)$	ΔH_E	ϵ_{max}	ΔK ergs/cm^3
141	O	1050 Oe	1396 Oe	0.49%	41.6($\times 10^3$)
142	D_2	1060	3210	0.65	95.5
143	$O + D_2$	1009	3200	0.77	95.5
112	$O + D_2$	558	1760	0.78	88.6

Table 4-7: FMR Results for Combined Species Implants

4.2. HYDROGEN IMPLANTS

Hydrogen implanted films exhibit a large non-magnetostrictive anisotropy field change which was previously presumed to be dependent on the presence of the implanted species [13, 14]. Here, investigations were performed to determine if the effects of hydrogen were similar to those observed in deuterium implanted films. Since previous investigators have focused on the effects of hydrogen implantation, it is worthwhile to compare their results with those obtained with the characterization techniques which were unique to this project. Two films which received identical hydrogen implants were studied here. The results are compared to deuterium implants which received a similar dose, although there was a factor of four difference in the ion mass; H^+ with mass 1 compared to D_2^+ with mass 4. Comparison of hydrogen to deuterium implants which caused the same implant strain were also made. The effects of an SiO_2 overcoating on the as-implanted and annealed film properties were studied and compared to results for deuterium implanted films.

4.2.1. Experiment

Implant conditions are given in Table 4-8. Film 130 was coated with 500 Å of SiO_2 prior to implantation, while film 134 was not coated. The anisotropy field and implant strain were measured after each of the annealings listed in Table 4-10. Garnet film parameters are given in Table 4-9. Both films 130 and 134 have similar bulk properties and are nominal half micron diameter bubble materials. The films were annealed simultaneously, so that the differences in the film properties could be related to the surface treatment.

Table 4-8: Implant Conditions

Ion	dose	energy	dose	energy	dose	energy
H^+	1.2×10^{16}	80 keV	4×10^{15}	50 keV	1.5×10^{15}	25 keV
D_2^+	1.2×10^{16}	80 keV	5×10^{15}	50 keV	3×10^{15}	25 keV

Dose H^+/cm^2 in Films 130 and 134

$\quad\quad D_2^+/cm^2$ in Films 77, 84, and 129

Table 4-9: Hydrogen Implanted Film Parameters

Film	t	$4\pi M_s$	H_E	λ_{111}/M_s
130	0.75 μm	1400 G	649 Oe	-3.4×10^{-8} G^{-1}
134	0.82	1522	750	-3.2
151*	0.62	1382	624	-2.9

* deuterium implant

Table 4-10: Annealing Conditions for Hydrogen Implanted Films

Temperature	Time	Temp.	Time
170°C	30 min	495°C	50 min
206	80	580	100
265	30	680	100
363	60	760	100
		830 (134 only)	75

4.2.2. Discussion of Annealing Behavior

The annealing behavior of ϵ_{max} in films 130 and 134 was found to be similar, as shown in Fig. 4-14. However, since the strain was relatively low, it was not possible to attach any significance to the slight differences in ϵ_{max} which were observed in the two films.

The ΔH_E and ΔH_σ are plotted versus ϵ_{max} in Figs. 4-15 and 4-16. From these plots it is difficult to ascertain any significant difference in the threshold temperature for hydrogen desorption on the coated and uncoated films. Note however that the ΔH_E zero strain intercept for film 130, as well as film 134, is positive. The ΔH_σ in both films, which is also plotted in Fig. 4-15, decreases linearly with decreasing implant strain.
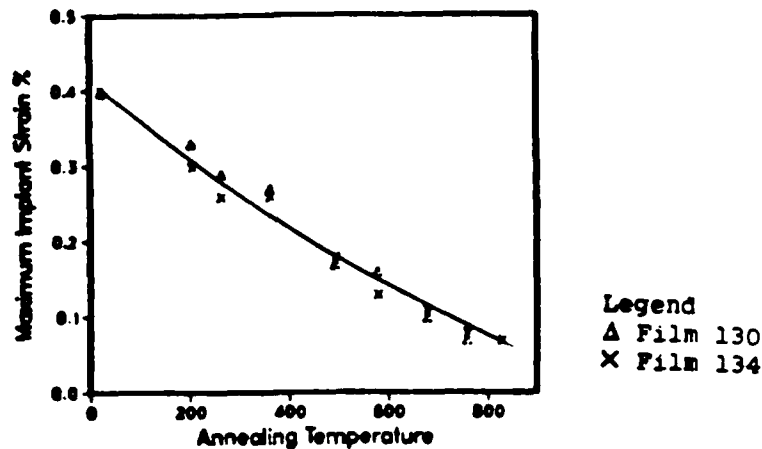
Fig. 4-14: ϵ_{max} versus Annealing Temperature for Hydrogen Implants

4.2.3. Comparison to Deuterium

The results for the hydrogen implants are compared here to those for deuterium implants. The implant conditions for both the hydrogen and deuterium implanted films are given in Table 4-8. The change in anisotropy energy density and the maximum implant strain are given in Table 4-11. The ratio of the maximum implant strain in the deuterium and hydrogen films, 3.3, is equal to the ratio of the nuclear energy loss, rather than the mass ratio. The ratio of ΔK to ϵ_{max} is about 18% higher for the hydrogen ions. Thus the non-magnetostrictive effect is slightly larger for hydrogen than deuterium.

The gyromagnetic ratio in the bulk layer and surface layers of the hydrogen implanted films are nearly the same. The $\gamma(B)$ for film 130 was 1.60 ($\pm$.03) $\times$ 10^7 (Oe-sec)$^{-1}$, compared to $\gamma(I)$ of 1.63 ($\pm$.05). On film 134 $\gamma(B)$ was 1.59 ($\pm$.03) and $\gamma(I)$ was 1.63 ($\pm$.02). The low implant dose is not expected to cause the degradation in the gyromagnetic ratio that was observed in films with high deuterium implant doses. Neither $\gamma(B)$ nor $\gamma(I)$ were significantly affected by annealing.

To determine if there are any significant differences in the annealing behavior of deuterium and hydrogen implanted films, the relative change in ΔH_E was compared on deuterium and hydrogen implanted films, both with and without SiO_2 overlayers. In Figs. 4-17 and 4-18 the ratio of ΔH_E after each anneal to ΔH_E in the as-implanted sample is plotted versus annealing temperature. Although ΔK is nearly three times larger in the deuterium implanted films, and the implant depth for the hydrogen is
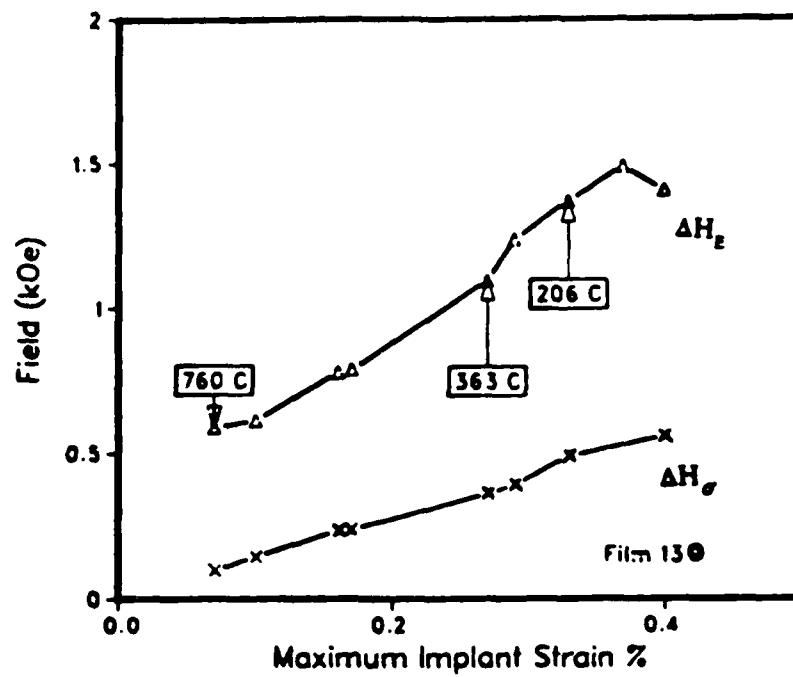
Fig. 4-15: ΔH_E and ΔH_σ versus Implant Strain for Film 130
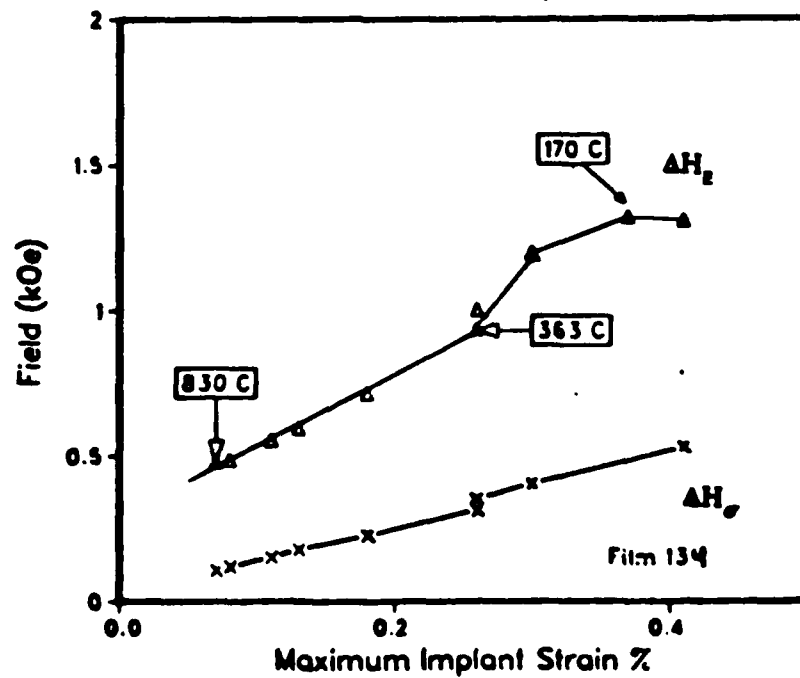
Fig. 4-16: ΔH_E and ΔH_σ versus Implant Strain for Film 134
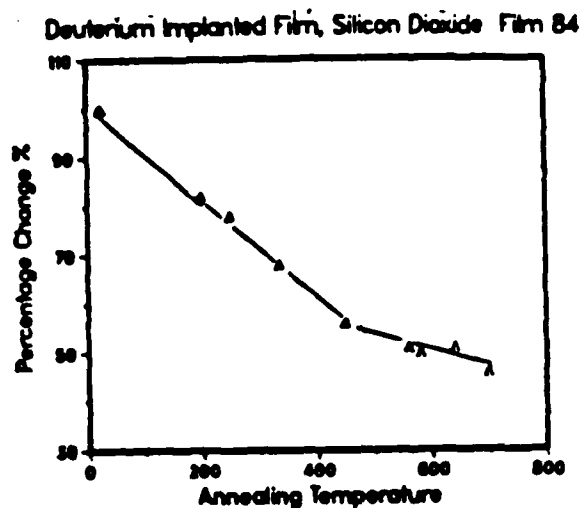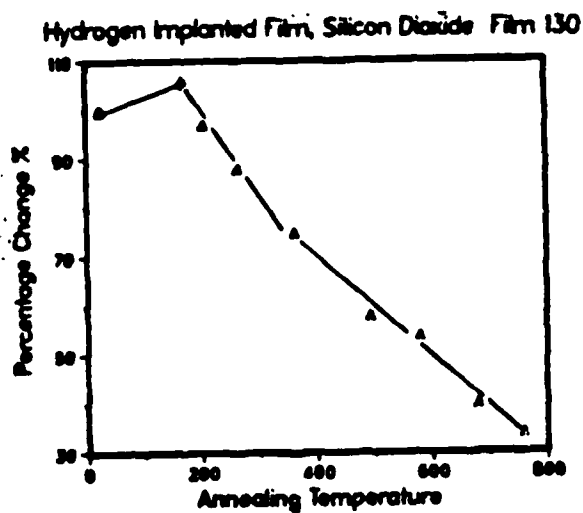
Fig. 4-17: Relative Change in ΔH_E Versus Annealing Temperature for SiO$_2$ Coated Films
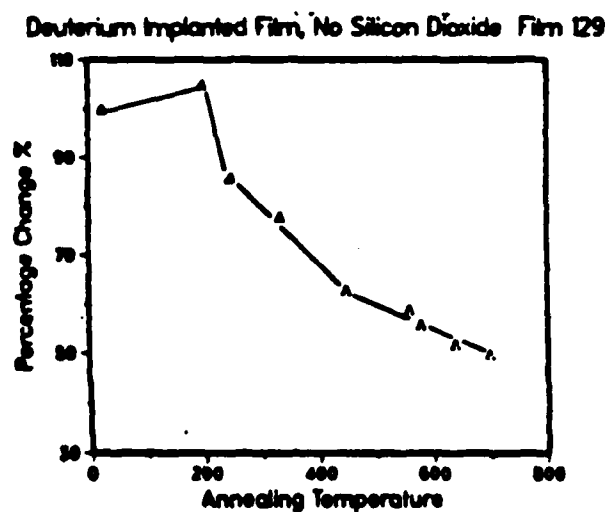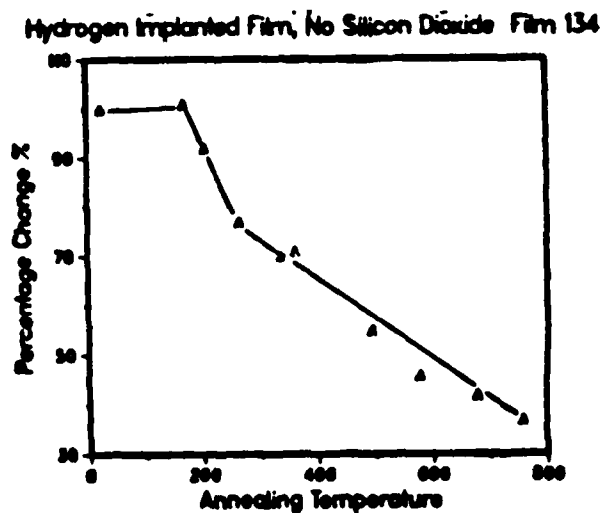
Fig. 4-18: Relative Change in ΔH_E Versus Annealing Temperature for Uncoated Films

Table 4-11: Comparison of Hydrogen to Deuterium Implants

Film	Implant Ion	ΔK ergs/cm^3	ϵ_{max}
130	H$^+$	78.5	0.40%
134	H$^+$	79.1	0.40
84	D$_2^+$	245	1.51
129	D$_2^+$	243	1.53

slightly greater (0.47 μm for hydrogen, 0.36 μm for deuterium), the implant doses were similar. The relative change in ΔH_E for hydrogen is similar to that for deuterium. For example, after a 400°C anneal, which has been used by previous investigators to stabilize film properties [12, 13], ΔH_E is between 50 and 60% of its as-implanted value. The slight increase in ΔH_E in the plot of ΔH_E versus maximum implant strain obtained by annealing the sample was observed on all of the films except 84. While the increase in ΔH_E in film 129 is attributed to the restoration of $\gamma(I)$, there was no degradation in $\gamma(I)$ in the hydrogen implanted films. The slight increase in ΔH_E in the hydrogen implanted films is attributed to a shift in the anisotropy profile due to relocation of the mobile hydrogen ions.

To select an annealing temperature for device fabrication, the plots in Figs. 4-17 and 4-18 are useful to determine the expected decrease in ΔH_E at any annealing temperature. Since the annealing-induced changes depend on the annealing time as well as the temperature, this must be taken into consideration. In heavily implanted films, where there is a significant amount of damage, increasing the annealing time will have a larger effect than in films which do not have as much damage. There is no clear threshold level above which the film should be annealed to stabilize the device performance. Note that the relative change in the properties are similar in the coated and uncoated films.

Thus, hydrogen has nearly the same threshold temperature for desorption that deuterium does. Furthermore, the magnetostrictive portion of the anisotropy field has a similar behavior to that in the deuterium implanted films, indicating that the implant mechanisms for hydrogen and deuterium are similar.

4.2.4. Comparison to Deuterium Implant with the same Strain

Results for a hydrogen and a deuterium implanted film which have the same maximum implant strain are compared here. Film 151 was implanted with a deuterium dose that produced the same value of strain as that on film 134 after a $170°C$ anneal. The film parameters for films 134 and 151 are given in Table 4-9. The implanted films results are given in Table 4-12.

Table 4-12:   Comparison of Hydrogen and Deuterium Implants

Film	ϵ_{max}	λ_{111} $\times 10^{+6}$	ΔK ($\times 10^{-3}$) ergs/cm^3	ΔK_σ($\times 10^{-3}$) ergs/cm^3	$\Delta K_\sigma/\Delta K$
134 H$^+$	0.40 %	-3.9	80	38	0.48
151 D$_2^+$	0.40	-3.2	63	32	0.51

The results in Table 4-12 indicate that the ratio $\Delta K_\sigma/\Delta K$ is nearly the same in both films. The implant dose was relatively low so λ_{111} in the implanted layer was not degraded. Thus the larger ΔK in the hydrogen implanted film is attributed to the higher magnetostriction. In spite of uncertainties in determining the magnetization, due to narrow stripwidth and small bubble size, the ratio $\Delta K_\sigma/\Delta K$ will not be affected by these uncertainties. From the results here, we can conclude that the effects of deuterium and hydrogen implants are similar for low implant doses. It remains to be shown what the differences are for higher dose implants.

4.2.5. Summary of Hydrogen Implant Results

The effects of hydrogen implantation are quite similar to those for deuterium implants. However, since the hydrogen implanted films investigated here received a relatively light dose which caused relatively little damage, extensive comparisons of the difference in the implant mechanisms cannot be made. Furthermore, no degradation in $\gamma(I)$ and $\lambda_{111}/M_s(I)$ were observed, although this may be attributable to the low implant dose, rather than a difference in the implant mechanisms for hydrogen and deuterium.

The annealing behavior of the hydrogen implanted films was similar to that of the deuterium implanted films, even though the deuterium implant caused significantly more damage. The threshold temperatures for hydrogen desorption were found to be similar to those for deuterium. We found that with hydrogen, as with deuterium, there was a

significant non-magnetostrictive portion to the anisotropy field change even after the film had been annealed well above the hydrogen desorption threshold. Thus, the results of previous investigators are called into question here. We suggest that there is an additional mechanism, besides magnetostriction, which is acting even after the hydrogen is annealed out of the film.

Chapter 5
CONCLUSIONS

5.1. SUMMARY

In this thesis, the implant mechanisms responsible for the anisotropy field change in deuterium implanted magnetic garnet films were investigated using a unique combination of characterization techniques. Ferromagnetic resonance measurements were done using a wideband microwave spectrometer, to determine the magnetic anisotropy and gyromagnetic ratio. A vacuum attachment was used to measure the magnetostriction in the virgin and implanted layers. The anisotropy fields and the magnetostriction were measured from 0°C to 200°C. The implant-induced strain was determined from the double crystal X-ray diffraction rocking curves.

While the results which are presented here agree with some of the results of previous investigations, including the large anisotropy field change and the annealing behavior of hydrogen (deuterium) implants, the explanation for the hydrogen implant mechanisms which was previously given does not satisfactorily explain the results presented here. The notable differences are the significant contribution from the non-magnetostrictive effect to the total implantation-induced anisotropy field change, even after the deuterium (hydrogen) has been annealed out of the film. Changes in the gyromagnetic ratio in the implanted layer, and the magnetostriction which are reported here have also not been previously reported.

Previous investigators have suggested that the excess anisotropy field change observed in hydrogen implanted films, which cannot be attributed to magnetostrictive effects, is only found in films in which the hydrogen has not been annealed out [13, 14]. Results are presented here which indicate that there is a substantial non-magnetostrictive effect, even in films which were annealed at temperatures which are substantially higher than the hydrogen (deuterium) desorption threshold. It was shown that the magnetostrictive field ΔH_σ only accounts for between 1/3 to 1/2 of the total

implantation induced uniaxial anisotropy field change ΔH_E in deuterium (and hydrogen) implanted films. The ratio $\Delta H_\sigma / \Delta H_E$ is approximately 1/2 for low to medium doses (up to 1×10^{16} D_2^+/cm^2), but decreases for high implant doses, due to a reduction in λ_{111}/M_s in the ion implanted layer.

The deuterium implants exhibit a substantial "non-magnetostrictive" effect which is attributed to at least two sources. The first mechanism is related to the presence of the implanted ions. This is most clearly detected by measuring the change in the anisotropy field as a function of annealing. The rapid decrease in the anisotropy field in the uncoated films near 250°C, and the increase in the anisotropy field near the film surface in the coated films after the 450°C anneal are attributed to this effect, which has been termed a chemical effect. In contrast to reports of previous investigators, who stated that there was only a magnetostrictive effect and a chemical effect, we have clearly shown that there is at least one and probably two other mechanisms. There is some permanent damage to the lattice which suppresses some of the growth-induced anisotropy by displacing some of the rare-earths from their original sites. The contribution of the suppression of the growth-induced anisotropy can be estimated from the plot of ΔH_E versus maximum implant strain, obtained by annealing the film. At zero strain, by definition, there is no magnetostrictive effect so a positive intercept at zero strain indicates a contribution from non-magnetostrictive effects. However, there is still a portion of the anisotropy field change which is unaccounted for and is presumed to be attributed to yet another mechanism which exhibits a linear dependence with strain. While this mechanism appears to be unique to deuterium and hydrogen implanted films, its source has not been identified.

The temperature dependence of ΔH_E was found to depend on the deuterium implant dose. In films with a sufficient dose to create a negative anisotropy energy in the surface layer, ΔH_E decreased nearly linearly with temperature. No saturation in ΔH_E was observed for the highest implant strain measured, up to 2.2%, although degradation of the resonance signal, the Curie temperature, and an increase in the linewidth were observed in the heavily implanted films. The ΔH_σ was found to decrease smoothly with temperature. The relative change in the temperature dependence of ΔH_σ compared to ΔH_E was dependent on the implant conditions. The high temperature measurements of ΔH_σ in films where the anisotropy decreases uniformly with temperature through the implanted layer thickness indicates that ΔH_σ and ΔH_E both decrease smoothly to zero at the Curie temperature.

In heavily implanted films, the non-magnetostrictive portion of the anisotropy field decreases more rapidly with temperature than the magnetostrictive portion. As a result, the value of ΔH_σ at high temperatures, calculated from the vacuum-induced shift in the principal surface mode and the maximum implant strain, overestimated the magnetostrictive contribution, as evidenced by the fact that the calculated value of ΔH_σ was larger than ΔH_E. However, this is an artifact and does not represent the actual situation, since the maximum ΔH_E shifts away from the region of maximum strain at high temperatures.

The annealing results from the SiO_2 coated films indicate that the threshold temperatures for desorption of the deuterium correspond with those for hydrogen. In the uncoated films, a significant amount of the deuterium has desorbed after a 250°C anneal. In the coated films, the desorption is moderated by the SiO_2 overlayer. The trapped deuterium increases the anisotropy field near the film surface after a 450°C anneal. At higher annealing temperatures, the deuterium diffuses out of the film.

In addition to the effects of the SiO_2 layer on the annealing behavior, there was a significant difference in the film properties of the as-implanted films which were coated before implantation, compared to uncoated films. In heavily implanted films with an SiO_2 overlayer, there was a significantly stronger resonance signal in the implanted layer than in films with identical implants which were not coated with SiO_2. In addition, the gyromagnetic ratio was drastically reduced and the resonance linewidth was considerably broader in the the uncoated, as-implanted film. The nature of the mechanism is not understood, but the difference in the properties of the SiO_2 coated film may be attributed to a thermal effect or to a surface effect. The annealing studies indicate that the γ is retored after a relatively low temperature anneal (250°C). The change in γ suggests that there is a fundamental difference in the properties of the garnet, such as a change in the valence of the iron atoms, or formation of metastable compounds of hydrogen (deuterium) and the garnet atoms. We should also note that the change in the iron valency, from Fe^{3+} to Fe^{2+}, increases λ_{111} (less negative) [74]. This may be the mechanism for the reduction in γ as well as the observed decrease in $|\lambda_{111}/M_s|$, since M_s is also decreased.

The temperature dependence of $\lambda_{111}/M_s(B)$ and $\lambda_{111}/M_s(I)$ were measured. At low doses, $4\pi M_s(I)$ is decreased more than $\lambda_{111}(I)$, so $\lambda_{111}/M_s(I)$ is increased slightly compared to $\lambda_{111}/M_s(B)$. However $\lambda_{111}/M_s(I)$ decreases more rapidly with temperature. At higher doses, $\lambda_{111}/M_s(I)$ less than $\lambda_{111}/M_s(B)$ at room temperature, indicating that

$|\lambda_{111}|$ is decreased more than $4\pi M_s$ by the implant. In these films, the temperature dependence of $\lambda_{111}/M_s(I)$ is less than $\lambda_{111}/M_s(B)$, so that $|\lambda_{111}/M_s(I)|$ is larger than $|\lambda_{111}/M_s(B)|$ above a certain temperature which depends on the implant dose.

Results from the hydrogen implanted films are in agreement with those published by other investigators, with regards to the large non-magnetostrictive portion of ΔH_E, and the observed annealing behavior. We found that the annealing behavior was similar to that for the deuterium implanted films. However, in both hydrogen and deuterium implanted films, we found that even after annealing the non-magnetostrictive change in the anisotropy field played an important role. Thus, the conclusions of previous investigators [13, 14], who attributed the non-magnetostrictive portion of ΔH_E to the presence of the hydrogen ions, are called into question. We propose here that the non-magnetostrictive effects of the hydrogen (deuterium) implants are not solely attributed to the presence of the implanted ions.

The results from the oxygen implants indicate that above 1.0% strain the film properties are degraded. This includes a significant reduction in the Curie temperature in the region of maximum implant damage, and the formation of a bimodal anisotropy profile due to overdamage in the region of maximum strain. In films which were implanted with both oxygen and deuterium, to achieve a uniform strain profile, the maximum ΔH_E was attributed to the deuterium implant. The anisotropy profile and strain profiles cannot be made uniform simultaneously, due to the difference in the implant mechanisms of deuterium and oxygen implants. To obtain uniform strain and anisotropy profiles, multiple energy implants, with the same ion species, are recommended over combined implant species.

5.2. SUGGESTIONS FOR FUTURE RESEARCH

To probe further into the mechanisms for the deuterium implantation, several experiments are proposed. While the deuterium effects have been shown to be similar to those for hydrogen, there is a significant degradation in the film properties, notably λ_{111}/M_s and γ for high dose deuterium implants, as well as the reduction in the Curie temperature. It would be instructive to compare the results for high dose hydrogen implants with those for high dose deuterium implants using the techniques developed here, to establish if the degradation also occurs to the same extent in hydrogen implanted films. Although we assumed that the effects of molecular deuterium ions are twice that of atomic deuterium ions, it would be interesting to see if the non-

magnetostrictive portion of the anisotropy field change was different for the two species. If the experiments were done on coated and uncoated films, the effect of the surface layer on the film properties could also be investigated.

One of the limiting factors in the measurement of the magnetostrictive field was the uncertainty in the effect of a non-uniform strain profile on the measurement results. That problem was avoided here by doing the analysis on multiply implanted films which were expected to have uniform strain profiles. For the detailed study of single energy implants, and to profile the magnetostriction through the depth of the implanted layer it will be necessary to relate the strain profile to the magnetostrictive field profile. Another limiting factor, which prevented identification of the implant-induced anisotropy change mechanisms, was the difference in the film properties. We would suggest using identical films for comparative experiments to remove uncertainty that interpreting results from films with different parameters introduces. Other factors to keep in mind are that the temperature dependence of the film properties are relatively large. Indeed, by carefully keeping track of the sample temperature, we were able to determine that there were significant changes in the bulk film properties. As the changes in the bulk film properties are relatively small, it is important that the measurements be made at the same temperature.

Another experiment which would be instructive to perform to look at the effects of implantation on the rare-earth ions, is to implant films which have different amounts of ions which contribute to the magnetostriction and to the damping. In particular, the linewidth broadening mechanism and the changes in the magnetostriction could be more thoroughly investigated.

The magnetization in hydrogen implanted films reportedly decreases with implantation, although there are conflicting reports about the magnitude of the decrease [14, 58]. It would be useful to establish how the magnetization varies with implant dose, and what effect annealing has on it. If the magnetization were known, then the magnetostriction coefficient could be calculated and the results compared to recent results which suggest that the excess anisotropy field change is attributable to an increase in $|\lambda_{111}|$ [42].

The results presented here indicate that the gyromagnetic ratio is affected by deuterium implantations. However there are unexplained variations in the gyromagnetic ratio in the implanted layer. As was shown for heavily implanted films, a significant decrease in γ was observed. By comparing results for different implant conditions, and annealing treatments, the reason for the peculiar behavior may be found.

As the surface treatments were shown to have a large effect on the implanted film properties, it would be quite useful to those interested in device fabrication to determine the effects of the different processing steps on the film properties. In particular, the effects of high temperature processes, such as sputtering and evaporation, and chemical treatments which are used in processing, should be evaluated. It would also be quite interesting to investigate films with higher implant doses, which are implanted through SiO_2 overlayers, to determine the dose where serious degradation in the film properties is observed. As the deuterium is highly mobile, conditions which will result in stable implanted film properties need to be established. As was shown here, the build-up of deuterium at the film surface increases the anisotropy field there. The effects of this on device operation should be established.

As was shown recently, neon implanted films which are subjected to a plasma containing trace amounts of hydrogen exhibit a dramatic increase in the anisotropy field change, presumably due to the incorporation of hydrogen in the films [22]. This effect should be investigated further, as it has important implications for device fabrication. There are a number of experiments which could be done. The ion species could be varied to determine if it occurs with other ions, and if it is more efficient for a particular implant species.

Another experiment which would be useful to perform to help establish the relative contribution of the different implant mechanisms would be to implant a YIG film and a typical bubble film with an identical dose. Since the YIG film has a negligible uniaxial anisotropy, the contribution of the suppression of the growth-induced anisotropy could be calculated, by comparing results from a film which had a considerable amount of uniaxial anisotropy. Also, since the magnetostriction of the YIG film is known, it would be useful to measure λ_{111}/M_s and the magnetostrictive contribution to ΔH_E as a function of annealing temperature. This might provide further insight into the nature of the non-magnetostrictive mechanism which contributes to ΔH_E.

An unusual phenomenon, which may be related to a shift in the location of the deuterium, was observed during high temperature measurements of the vacuum stress-induced shift in the implanted mode resonance. In films 63 and 140 a time dependent drift in $\delta H_{111}(I)$ was observed during high temperature measurements. Implant conditions are 5×10^{15} at 80 keV and 5×10^{15} at 40 keV for film 63. Results for film 63, which were measured after a 2 hr. 200°C anneal, are plotted in Fig. 5-1. The
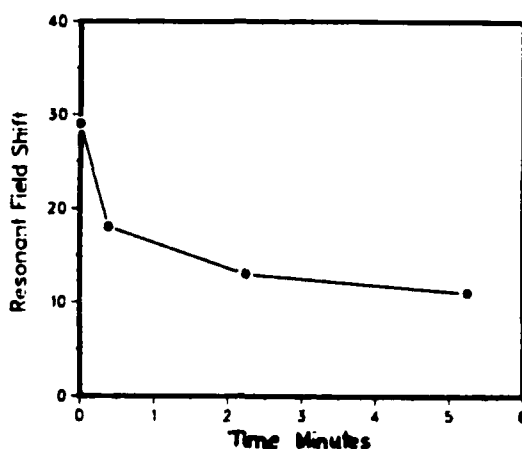
Fig. 5-1:   Drift in Resonant Field Shift Versus Time for Film 63

results given in Fig. 5-1 were obtained at 148°C and at 6.0 GHz, although results measured at 5.0 GHz were virtually identical. Before the vacuum pressure was applied, the resonant field was constant, indicating that there was no drift in the temperature. The resonant field measured immediately after the vacuum pressure was applied (+22 seconds) increased by 29 Oe ($=\delta H_{111}$) due to the stress-induced magnetostrictive field. However δH_{111} decreased by 11 Oe only 21 seconds later. Subsequent measurements, at later times (up to 5 minutes), were consistent with the initial decrease measured after the vacuum pressure was switched on. This phenomenon was also observed on film 140. Results for the δH_{111} measurement, given in Table 5-1, indicate that a decrease in δH_{111} occurs approximately 30 seconds after the vacuum pressure is applied, but the resonance field is relatively constant afterwards. Measurements on the bulk film indicate that δH_{111} was constant for longer than 2 minutes. Measurements were also done on an oxygen implanted film, but no drift was observed. Thus it appears that this effect is peculiar to the deuterium (hydrogen) implanted films.

To establish that the drift in $\delta H_{111}(I)$ was related to the film properties and not to an artifact in the measurement technique, the sources of potential errors were evaluated. The temperature dependence of the resonant field in the implanted layer is approximately 14 Oe/°C for both films, compared to an estimated temperature dependence in bulk film of approximately 3 Oe/°C near 145°C. Thus the observed drift in the resonant field corresponds to less than a 1°C change in the film temperature. Since measurement accuracy of the temperature was only 1°C, and the temperature was measured inside the minibox but not at the film surface, the possibility of an immeasurably small change in temperature cannot be ruled out. Note that the observed drift in δH_{111} would correspond to an increase in temperature. The response

Table 5-1: Temperature Dependent Drift In δH_{111}

Temperature 160°C, Freqency 3 GHz

Main Surface Mode

Time	H_{res}	$\delta H_{111}(I)$
0 sec	2012 Oe	–
60	2010	–
120	2010	–
128	2042	32 Oe (pressure applied)
158	2034	24
200	2033	23
248	2030	20

Bulk Mode

Time	H_{res}	δH_{111}
0 sec	1166 Oe	–
180	1164	–
(pressure applied)		$\delta H_{111}(B)$
196	1200	36 Oe
245	1201	37
316	1201	37

of the temperature measurement was estimated to be on the order of a few seconds, as determined by the decrease in temperature which was observed when the vacuum pressure was released. The amount of the decrease depended on the temperature, and how quickly the vacuum was released.

The observed drift in δH_{111} was repeatable, suggesting that the deuterium is displaced from its equilibrium position when the vacuum pressure is applied, but returns after the pressure is released. This effect was only observed in these two films. The measurements were repeated on film 140 approximately 3 months after the initial measurements were made. Although the values of $H_E(I)$ and $H_E(B)$ were virtually unchanged, the time dependent drift was not observed. While the reason for this is not clear, it may be related to some sort of aging effect.

In summary, an anomalous drift in the location of the principal surface mode was observed in two deuterium implanted films. While it appears that the effect is related to the presence of mobile deuterium ions, further experiments are required to verify this. These experiments should be done on freshly implanted samples as well as on annealed films. The major difficulty with this experiment is to establish that the

temperature change in the sample can be minimized so that the drift in the resonance field can be directly correlated to the implanted species. It would be informative to investigate films with a range of implants to see if the deuterium distribution has an effect on the observed drift. One might expect the drift to be larger in a film with a deuterium distribution which is sharply peaked, compared to one which is uniform, if the drift is due to the relocation of the deuterium in the stressed film.

The suggestions mentioned above can all be done with the techniques which were used in this project. We should point out that there are other techniques which were not used here, but would provide additional insight into the mechanisms of deuterium(hydrogen) implantation. The bubble collapse field under the implanted region could be measured. Since there appears to be a slight change in the bulk properties due to diffusion of hydrogen into the bulk, it would be useful to see if this has a detectable effect on the bubble properties. Chemical analysis to detect the presence of, and to profile the hydrogen concentration through the depth of the film, in conjunction with an analysis of the anisotropy, strain, and damage profiles would provide important information which would enable us to isolate the contribution of the different mechanisms. While this was done for hydrogen [14], the hydrogen concentration was deduced from the nuclear range statistics and the magnetostrictive contribution was assumed to correspond to the slope of the anisotropy field change versus implant strain for strains up to 1%. Thus, we suggest that the magnetostrictive contribution was significantly overestimated in the referenced experiment.

One final note. The effects which provide the telltale signs for differences in the implant mechanisms can be easily overlooked, or buried in systematic measurement errors, of which there are potentially a large number. To extract the full amount of information it is essential to minimize all possible sources for error. While we have been diligent about that here, circumstances were not always ideal, so some of the measurement results could not be fully utilized.

Appendix A
LIQUID PHASE EPITAXIAL GARNET FILMS

The development of material compositions which were used in this thesis is highlighted here. Results for one micron and submicron diameter bubble materials are given.

Material design of magnetic garnet films is simplified by the fact that the garnet system will accept a large range of substituent ions into the basic $\{RE_3\}$ $[Fe_2]$ (Fe_3) O_{12} formula, where $\{\}$ stand for the dodecahedral, $[]$ octahedral, and $()$ the tetrahedral lattice sites. To design submicron material, we first choose the minimum quality factor, $Q = H_K/4\pi M_s$, and select the desired value of characteristic length, l. For device applications, a bubble height of $9 \times l$ is typically chosen [5]. From Q and l, the values of $4\pi M_s$ and K_U are calculated. The composition is designed to meet these requirements with the further stipulation that the lattice constant of the film be reasonably well matched to that of the GGG substrate. The amount of iron and iron substitutes, such as aluminum and gallium, in octahedral and tetrahedral positions control the magnetization, exchange constant, and Curie temperature.

The versatility of the garnet system is in the wide range of rare earth or other substituent ions which may be incorporated into the dodecahedral sites. Adjustment of these ions is used to achieve desired anisotropy energy, lattice match, and magnetostriction constant. A typical film grown for use in an ion implanted bubble device contains a combination of Y, Sm, Tm, Gd, and Lu ions in the dodecahedral positions. Yttrium is in the basic end member garnet, $Y_3Fe_5O_{12}$ (YIG), into which the other ions are substituted. Yttrium has low spin damping and a lattice parameter close to that of the GGG substrate. Samarium provides uniaxial anisotropy, ostensibly because of preferential ordering with smaller ions such as Tm or Lu [75]. Sm also has a high $|\lambda_{111}|$ which makes it a good choice for ion implantable material. The amount of Sm must be restricted as it increases FMR linewidth, which results in decreased domain wall mobility. Thulium is used because of its high $|\lambda_{111}|$ and small ionic radius. Gadolinium is used to improve temperature coefficient of magnetization because

of its flat temperature versus magnetization profile near room temperature. Lutetium, with its small ionic radius, is helpful in reducing film lattice parameter. Thus, a wide range of film properties can be achieved by tailoring the rare-earth concentrations in the garnet film.

Garnet films are grown by liquid phase epitaxy from a lead fluxed melt containing the oxides of the rare earths, iron, and iron substituents [3]. The growth conditions strongly influence composition and thus are carefully chosen and controlled.

A.1. ONE MICRON DIAMETER BUBBLE MATERIAL

The one micron film development was based on material composition which had been reported [68]. which we believed would have reasonable properties and be relatively easy to grow. Here, the material development process will be highlighted. Estimated compositions based on unity segregation coefficients of the rare earths are listed in Table A-1. We should note that our assumption of unity segregation coefficients does not represent the actual situation. However, determining the segregation coefficients in this multi-component flux is difficult without accurate composition analysis. However, the rare-earth concentration in the melt is the most relevant piece of information for anyone who is interested in growing films with similar compositions. Material parameters are listed in Table A-2. Note that the film numbers correspond to those mentioned in the main part of this thesis.

Table A-1: One Micron Material: Expected Composition

Melt	Film	Sm	Gd	Tm	Y	Fe	Ga	Al
1	20	0.2	0.6	1.3	0.9	4.6	0.4	0
2	37	0.2	0.6	1.3	0.9	4.64	0.36	0
3	50	0.2	0.6	1.3	0.9	4.68	0.32	0
4	49	0.29	0.59	1.25	0.87	4.68	.032	0
5	59	0.3	0.6	1.3	0.80	4.68	0.16	0.16
6	87	0.3	0.6	1.3	0.80	4.72	0.14	0.14
7	34	0.35	0.55	1.2	0.9	4.72	0.14	0.14
8	135	0.35	0.55	1.2	0.9	4.70	0.16	0.14
9	165	0.35	0.55	1.2	0.9	4.66	0.20	0.14
10	167	0.35	0.55	1.2	0.9	4.61	0.25	0.14

The material parameters given in Table A-2 include the film thickness t, characteristic

length l, magnetization $4\pi M_s$, effective anisotropy field H_E (= $H_K - 4\pi M_s - 2/3\ H_l$), lattice mismatch $\Delta a = a_{substrate} - a_{film}$, quality factor Q uniaxial anisotropy energy density K_U, growth temperature, and growth rate.

Table A-2: One Micron Material: Results

Melt (Film)	t μm	l μm	$4\pi M_s$ G	H_E Oe	Δa $\overset{o}{A}$	Q	K_U ergs/cm^3 $\times$ 10^3	T_G °C	rate μm/min
1-?0	0.99	.141	610		-.005			840	.28
2-24	0.95	.114	638	763	-.004	2.2	36.9	848	.30
2-42	0.95	.095	617	465	-.006	1.75	26.6	835	.36
3-50	0.84	.102	711	600	-.006	1.84	37.1	842	.34
4-55	0.96	.097	704	577	-.010	1.82	35.9	840	.32
5-64	1.30	.116	668	899	.000	2.35	41.6	841	.31
5-69	1.26	.136	636	1060	.002	2.67	42.9	858	.25
5-71	1.11	.130	637	986	.002	2.55	41.1	859	.25
6-87	1.38	.125	680	1002	.002	2.47	45.5	857	.22
6-88	1.38	.125	703	793	.000	2.13	41.8	842	.25
7-94	0.85	.111	774	960	-.003	2.24	53.4	849	.13
8-135	1.26	.111	761					844	.18
8-136	1.36	.107	755	865	-.006	2.15	48.7	841	.19
9-165	0.94	.145	590	1273	+.001			846	.09
10-167	1.47	.196	498	1645	0.000	4.3	42.4	847	.10

rotation rate 90 rpm melts 1-4

90 rpm film 69

120 rpm film 71

100 rpm melts 6-10

The first films which were grown had an l of 0.141 μm (film 20). However, we were interested in growing films with l = 0.11 μm. To realize this we added ten percent more iron to the melt. This addition reduced l to 0.124 μm (film 24). We repeated the iron addition · and obtained l = 0.10 μm for films 42 and 50. The problem with simply adding iron to the melt, is that as $4\pi M_s$ increases, if H_K remains constant, as it will if the rare earth concentration is not changed, Q will decrease. Q for film 42 is 1.75. For one micron material, a nominal Q of 2.5 is desired.

To boost Q, samarium was added to the melt. The amount of samarium was equal to

half the original amount in the melt. In film 64 the Q was 2.35. The increase in Q
is attributed to a 300 Oe increase in H_K. Film 64 contains both aluminum and gallium
as iron substitutes. The aluminum was added in order to improve the lattice match
between the film and the substrate. The result was a perfect lattice match for films
grown melt 5 at 840°C. The increase in K_U was accompanied bu an increase in l. To
decrease l we added iron (melt 6). Comparing results for 87 and 88, shown in Table
A-2, we note that l increases at higher growth temperatures. At 842 °C, we obtained
an l = 0.11 μm. The Q for the films is also growth temperature dependent. Film 88,
grown at 842°C, has a Q of 2.13, while film 87, which was grown at 857°C, has a Q of
2.47.

To achieve a higher Q at a lower growth temperature we added gallium to the melt.
Results for films 136 and 137 grown from melt 8, indicate that this melt is suitable for
1 μm material. To increase Q, we can grow films at higher temperatures, but l also
increases. From this melt, optimal one micron material was obtained at a growth
temperature of 845 °C.

In summary, the development process for the one micron material involved fine
tuning the melt composition to optimize the material parameters. We did not have to
adjust the rare earth distribution, with the exception of samarium addition to achieve
the desired result. The use of both aluminum and gallium instead of gallium alone
helped us achieve a better lattice match. The aluminum did not seriously degrade the
temperature coefficient of magnetization.

A.2. HALF MICRON MATERIAL DEVELOPMENT

The compositions for the submicron diameter bubble films, based on unity segregation
coefficients for the rare-earths in the melt are given in Table A-3, and the film
parameters are listed in Table A-4.

The initial half micron melts were designed using the same rare earths which were
used for the one micron material. However, only aluminum was used as an iron
substitute, in order to partially compensate for increased concentration of large rare
earth ions. From the first melt, we grew material suitable for 0.75 μm bubbles. Films
78 and 81, whose properties are listed in Table A-4, were grown from this melt under
identical conditions except a 9°C difference in growth temperature. The saturation
temperature for this melt was 870°C. In general, we wanted to grow films with more

Table A-3: 0.5 Micron Material Compositions

Melt	Films	Sm	Tm	Gd	Y	Lu	Fe	Al
1	77–81	0.35	1.3	0.45	0.9	0	4.7	0.3
2	82–108	0.35	1.3	0.30	_1.05_	0	_4.8_	0.2
3	110–114	_0.45_	1.25	0.29	1.01	0	4.8	0.2
4	115–117	_0.54_	1.21	0.28	0.97	0	4.8	0.2
5	118–121	_0.63_	1.16	0.27	0.94	0	4.8	0.2
6	122–126	_0.71_	1.12	0.26	0.91	0	4.8	0.2
7	127–130	0.69	1.09	0.25	0.88	_0.09_	4.8	0.2
8	131–134	0.65	1.02	0.24	0.82	_0.27_	4.8	0.2
9	150–162	0.63	1.00	0.24	0.80	0.33	4.8	0.2

__ Indicates oxide addition to melt

Table A-4: 0.5 Micron Film Results

Melt Film	t μm	l μm	$4\pi M$ G	H_E Oe	Δa $\overset{o}{A}$	Q	K_U ergs/cm^3 $\times$ 10^3	T_G °C	rate μm/min
1–78	1.09	0.081	973	992	.008	2.02	76.1	849	.23
1–81	0.89	0.078	1005	904	.006	1.9	76.3	840	.27
2–84	1.00	0.063	1257	496	.006	1.39	87.7	841	.26
2–102	1.00	0.063	1258	530	.008	1.42	89.5	849	.21
2–106	0.69	0.065	1348	498	.006	1.37	99.0	840	.22
3–113	0.85	0.063	1286	596	0.000	1.46	96.3	840	.28
3–114	0.85	0.057	1234	596	.000	1.48	89.8	840	.28
4–116	0.83	0.066	1356	632	-.004	1.47	107.3	840	.27
4–117	0.82	0.069	1360	619		1.46	107.1	840	.27
5–120	0.85	.062	1382	632		1.46	110.7	840	.34
5–121	0.75	.065	1413	621	-.012	1.44	114.4	840	.32
6–125	0.73	0.060	1389	566	-.016	1.41	108.0	840	.36
7–127	0.64	0.057	1345	661	-.013	1.49	107.4	840	.29
8–150	0.70	.057	1292	790	-.004	1.61	107.0	850	.35
8–151	0.75	.062	1382	718	-.007	1.52	115.5	840	.43
9–163	0.69	.055	1284	831	-.004	1.65	108.1	836	.34

than 10°C but less than 40°C of undercooling to ensure adequate growth rates but to prevent unwanted nucleation of garnet crystallites in the melt. Within these constraints

we can determine the useful range of a given melt. For the first melt, we observe that l is too large. To obtain a lower l, we needed to add more iron to the melt.

In the first melt modification, we added iron and increased the amount of yttrium at the expense of gadolinium. Increasing iron and yttrium will boost the magnetization. The temperature response of the material was not seriously affected, due in part to the high iron content in the films.

The problem with the first modification is that it decreased Q. In order to increase the uniaxial anisotropy energy and thus raise Q, we added samarium to the melt. However, samarium increases the resonance linewidth and the damping factor. To quantify the effect of adding samarium, we added it to the melt in equal increments of 0.1 out of 3 stoichiometric dodecahedral positions. As expected, K_U increased with samarium addition, up to 0.63 (out of 3 dodecahedral positions), but then began to decrease. At larger values of samarium substitution the lattice mismatch problem became increasingly unfavorable due to the large size of the samarium ion. Resonance linewidth increased from 125 Oe at 0.3 Sm content to 200 Oe for 0.6 Sm content.

The stress–induced anisotropy energy density due to the lattice mismatch becomes increasingly unfavorable as the lattice mismatch increased. For melts 5, and 6 the effects of the samarium addition were offset by the magnetostrictive anisotropy induced by the unfavorable lattice mismatch. Thus, no further samarium additions were made. The problem with the material from melt 6 is that Q is too low. The next melt modification involved the addition of lutetium. This was intended to raise K_U by providing a small ion for the larger samarium ion to pair order with, and also to reduce the unfavorable lattice mismatch. A disadvantage with melt 7 is the increased complexity. With five rare earth ions reproducibility problems may arise. Another disadvantage with lutetium is that a small fraction substitutes for octahedral iron, increasing the magnetization and the lattice parameter.

Film 127 was grown from the melt after lutetium was added. The H_E increased by 100 Oe compared to film 125 which had no lutetium. The lattice parameter for film 127 decreased by 0.003 Å. The l and the $4\pi M_s$ both decreased. To further increase Q, we added more lutetium to the melt. Results for films 150 and 151 are listed in Table A-4. H_E increased over the previous composition, as did $4\pi M_s$ and l. We expect $4\pi M_s$ to increase because of the higher magnetic moment of lutetium iron garnet compared to all the other rare earth iron garnets, and because of the substitution of a

small amount of lutetium on the octahedral iron site. Note however that these are second order effects compared to magnetization adjustment achieved by aluminum substitution.

In summary, the results for typical films of each composition are given in Table A-4. The tailoring process, while inexact in terms of predictability, provided satisfactory results. The additions were made one at a time and in small increments so that the effect of each could be studied. While no attempt has been made to determine film composition, by careful control of the melt composition and feedback from measurement of the film parameters, we were able to tune the melt so that films with the desired properties were achieved.

A.3. TEMPERATURE COEFFICIENT OF COLLAPSE FIELD

The temperature coefficient of collapse field was measured for several films. Results are listed in Table A-5. The effect of Al addition is most probable explanation for increase in temperature coefficient between melts 4 and 6. The range of temperature response for the different one micron compositions was both small and considerably less than that for the standard barium ferrite bias field magnets. Temperature coefficient for 0.5 μm material, film 151, is $-0.20\%/^\circ$C. The increase over 1 μm material is attributed primarily to lower Gd content. Note that this matches that of the barium ferrite bias magnets. Temperature coefficients were obtained by taking difference between maximum collapse field and the collapse field at 90°C normalized to H_o at 30°C.

We conclude that the temperature response for the half micron material is adequate for practical device us

Table A-5: Temperature Coefficient of Collapse Field

One Micron Material		Half Micron Material	
Melt-Film	Temp. Coeff.	Melt-Film	Temp. Coeff.
2-24	-0.044 %/$^\circ$C	1-81	-0.16 %/$^\circ$C
2-42	-0.039		
4-55	-0.059		
6-87	-0.101		
6-88	-0.090		
7-94	-0.092	8-151	-0.20

Appendix B
CRYSTALLINE ANISOTROPY FIELD

The cubic crystalline anisotropy field in magnetic garnets is obtained by measuring the resonance field at several selected angles. The film is aligned so that the field is applied in the (110) plane (ϕ = 0). The sample is rotated about the [$\bar{1}\bar{1}2$] direction. The effect of the crystalline anisotropy field is essentially a perturbation in the $\sin^2$ dependence of the uniaxial anisotropy field. The value of H_1 is obtained by comparing resonance fields at the measured angles with those calculated based on an assumed H_1 value. A program was written to solve for H_1 given the measured resonance fields and the applied field angles. The equations used in the solution, a listing of the program, and a sample program execution are given.

B.1. EQUATIONS

The free energy equation for the garnet film is given by

$$E = -M_sH(\sin\theta\cos\phi\sin\beta + \cos\theta\cos\beta) + 2\pi M_s^2\cos^2\theta \tag{B.1}$$

$$+ K_U\sin^2\theta + K_1(\frac{1}{4}\sin^4\theta + \frac{1}{3}\cos^4\theta + (2^{\frac{1}{2}}/3)\sin^3\theta + \cos\theta\cos3\phi)$$

The coordinate system for Eqs. (B.1) and (B.2) is shown in Fig. B-1.
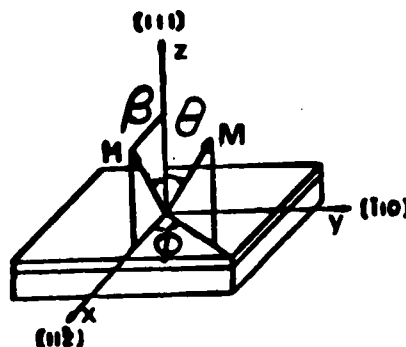
Fig. B-1: Coordinate System for H_1 Measurement

The resonance condition is given by

$$(\omega/\gamma)^2 = \frac{1}{M_s \sin^2\theta} \left[\frac{\partial^2 E}{\partial\theta^2} \frac{\partial^2 E}{\partial\phi^2} - \left(\frac{\partial^2 E}{\partial\theta\partial\phi}\right)^2 \right] \tag{B.2}$$

The resonance is measured with the applied field in the (110) plane ($\phi = 0$). For the applied field in this direction, M_s will also lie in the (110) plane. In this case, the angle between the magnetization and the applied field can be calculated by evaluating

$$\tag{B.3}$$

$$\frac{\partial E}{\partial\theta} = -H\, M_s \sin\,(\beta - \theta) + (K_U - 2\pi M_s^2) \sin\,2\theta$$

$$+ K_1\{-\tfrac{7}{24} \sin\,4\theta - \tfrac{1}{12} \sin\,2\theta + \tfrac{2^{1/2}}{3}(3\,\sin^2\theta - 4\,\sin^4\theta)\}$$

For the applied field in the (110) plane ($\phi = 0$), the resonance condition is given by

$$(\omega/\gamma)^2 = \{H\,\cos(\beta - \theta) + H_{KE}\,\cos\,2\theta + H_1\,(2^{1/2}/6\ \sin\,2\theta \tag{B.4}$$

$$(3 - 8\sin^2\theta) - \tfrac{7}{12}\cos4\theta - \tfrac{1}{12}\,\cos\,2\theta)\}$$

$$\times (H\,\frac{\sin\,\beta}{\sin\,\theta} - \tfrac{3}{4}\,(2)^{1/2}\,H_1\,\sin\,2\theta)$$

where $H_{KE} = H_K - 4\pi M_s$. Note that Eq. (B.4) is given by Eq. (B.5) when the applied field is perpendicular to the film plane (H_N), along the [111] direction, and by Eq. (B.6) for the applied field parallel to the in-plane [112] direction (H_P).

$$\omega/\gamma = H_N + H_{KE} - \tfrac{2}{3}\,H_1 \tag{B.5}$$

$$(\omega/\gamma)^2 = H_P[H_P - H_{KE} - \tfrac{1}{2}\,H_1] \tag{B.6}$$

B.2. PROGRAM

The program assumes a trial value for H_1 and calculates ω/γ and H_{KE} from H_P and H_N and the trial H_1. For each measurement angle, the equilibrium direction for the magnetization is calculated from Eq. (B.3). The bisection method is used to solve for the magnetization angle. If the sign of $\partial E/\partial\theta(x)$ changes over the x range from a to $a+\Delta$ then there must be a solution between a and $a+\Delta$. A starting angle is chosen by the subroutine setsta to be $\beta/40$ if $\beta < 35°$ and $\beta - 32$ if $\beta \geq 35$. The starting angle is increased by setinc = 2.0° until the sign of Eq. (B.3) evaluated at angle a and angle a + Δ changes. Once the solution has been passed, the angle increment is halfed and the process is repeated until the solution lies with the error limit seterr. Once the

magnetization angle θ is found, then Eq. (B.4) is evaluated to determine (ω/γ). This is repeated for each measurement angle. The average and mean square deviation of (ω/γ) are calculated. The H_1 value is incremented by a small amount (5 Oe), and the calculation is repeated. This process continues for a number of iterations (MM). After this is done, the minimum of the mean square deviation in (ω/γ) is found. If no minimum is found, the starting value for H_1 is shifted and the process is repeated.

The program listing and a copy of a program execution is attached. The user responses are underlined. After typing execute temp.for, the program prompts the user for the film number, which is used for reference only. The number of measurements, is the number of resonance field measu .nents that were made at angles other than perpendicular ($\theta = 0$). The $\theta = 0$ data are not used to compute magnetization angle, as Eq. (B.4) will blow up due to a zero in the denominator. The program then asks for the perpendicular ($\theta=0$) and parallel ($\theta=90°$) resonance fields. Next, the program asks for the resonance field and the measurement angle for each of the other measurements. Note that the parallel resonance data has already been accounted for. Once the data have been correctly entered, the program will perform the computation. When the solution is found, the program will prompt the user for the name of an output file. This feature enables the user to selectively choose which data he/she wants to print, and speeds up the program execution time.

In the output file, the film number and input data are listed. The calculated value for H_1 and H_{KE} ($= H_K - 4\pi M_s$) are also given. The H1(N) represents the trial values of H_1, Hke(N) is the calculated H_{KE} for the trial H_1, and Err(N) is the mean square deviation for the calculated (ω/γ) values. Note that the minimum error corresponds to the calculated H_1 value. The applied field angle Beta(I), the magnetization angle Theta(I), and the (ω/γ) Fre(I), for each measured angle are listed. The mean square error is given for several H_1 iterations to indicate the accuracy of the fit. This also permits extrapolation between the H_1 iterations.

If the user has data for more than one film, the program will accept new input data if the last statement is answered affirmatively. There are several features built into the program which are designed to minimize the chance of entering incorrect data. The number of measured data must be between 2 and 20. If more measurements are taken, then several of the matrices must be redimensioned. However, taking more than 20 measurements is considered to be unnecessary to obtain an accurate value of H_1. The measurement angle must be between $5°$ and $175°$. The resonance field at measurement

angles other than perpendicular and parallel resonance must be greater than 200 Oe. This is done to avoid an error due to inadvertently typing the angle instead of the field, or vice versa. If measurement angles are between 185 and 355°, then they must be converted to the equivalent angle between 5 and 175°. If any of the input data are entered incorrectly, the user has the option of retyping input data.

The program listing is attached. Documentation regarding the purpose of each of the subroutines, and definitions of the program variables are contained in the program listing.

```
[PHOTO:  Recording initiated  Mon 14-May-84 10:33AM]


 CMU Tops-20 Command Processor 5.1(1502)-2
@execute (from) temp.for
LINK:   Loading
[LNKXCT TEMP execution]
Enter sample number> 155
The number of measured data is the number of
measurements at angles other than 0 degrees (perpen.)
Enter number of measured data> 7
Enter : Hperpendicular:Oe 1527
Enter : Hparallel:Oe 2670
Enter data for other measurement angles
Input field for  2 measurement (thenreturn)> 2565
Input msnt angle              2> 80
Input field for  3 measurement (thenreturn)> 2687
Input msnt angle              3> 100
Input field for  4 measurement (thenreturn)> 2603
Input msnt angle              4> 110
Input field for  5 measurement (thenreturn)> 2425
Input msnt angle              5> 70
Input field for  6 measurement (thenreturn)> 2236
Input msnt angle              6> 60
Input field for  7 measurement (thenreturn)> 2414
Input msnt angle              7> 120
Input data for film number        155
H resonance,  Angle
1527.          0.0  Perpendicular
2670.         90.0
2565.         80.0
2687.        100.0
2603.        110.0
2425.         70.0
2236.         60.0
2414.        120.0
Is input data correct?  If no type 0, if yes type 1: 1

Output file name? fil.dat
more calculations on new data?, type 1 0

CPU time 4.97   Elapsed time 1:07.45
@pop

[PHOTO:  Recording terminated  Mon 14-May-84 10:34AM]
```

```
Input data for film number        155
H resonance,  Angle
1527.         0.0
2670.        90.0
2565.        80.0
2687.       100.0
2603.       110.0
2425.      . 70.0
2236.        60.0
2414.       120.0
```

H1 is   -120.0 (Oe) ; The Hke = (Hk - 4piM) is   713.4 (Oe).

```
H1( 3) :   -130.0 (Oe);    Hke( 3) :     711.0 (Oe) ;    Err( 3) :     100.6 .
H1( 4) :   -125.0 (Oe);    Hke( 4) :     712.2 (Oe) ;    Err( 4) :      56.2 .
H1( 5) :   -120.0 (Oe);    Hke( 5) :     713.4 (Oe) ;    Err( 5) :      30.7 .
H1( 6) :   -115.0 (Oe);    Hke( 6) :     714.6 (Oe) ;    Err( 6) :      34.8 .
H1( 7) :   -110.0 (Oe);    Hke( 7) :     715.8 (Oe) ;    Err( 7) :      53.5 .
```

Applied Field Angle, Magnetization Angle and Omega/Gamma

```
Beta( 1) :    90.00;    Theta( 1) :   89.20;    Fre( 1) :    2309.8 .
Beta( 2) :    80.00;    Theta( 2) :   76.08;    Fre( 2) :    2295.0 .
Beta( 3) :   100.00;    Theta( 3) :  102.52;    Fre( 3) :    2322.0 .
Beta( 4) :   110.00;    Theta( 4) :  115.70;    Fre( 4) :    2339.6 .
Beta( 5) :    70.00;    Theta( 5) :   63.45;    Fre( 5) :    2302.5 .
Beta( 6) :    60.00;    Theta( 6) :   51.33;    Fre( 6) :    2297.0 .
Beta( 7) :   120.00;    Theta( 7) :  128.39;    Fre( 7) :    2346.2 .
```

```
c      This program determines the effective uniaxial anisotropy field
c      Hke and the cubic anisotropy field Hkc of the film by the angular
c      dependence of the resonance field when the [111] oriented film is
c      rotated about [-110] the  microwave field frequency constant.

c      ......................................................................
c      For N measured data,
c        Hr(I) represents the resonance field in the I th set of data.
c        Beta(I) denotes the angle between the applied field and the film normal
c        Theta(I) signifies the angle between the magnetization and the
c        film normal.
c        Setsta(I) stands for the starting value of Theta(I).
c        Frequc(I) is the calculated value of the angular frequency of
c        the microwave field divided by the gyromagnetic ratio of the
c        film.
c        Stheta(I) is to store the Theta(I) if I is in middle of search range
c        Results are calculated for a trial value of Hkctry(J)
c        which is the J th  the cubic anisotropy field.
c        Hketry(J) is the J th calculated value of the effective anisotropy
c        field using the measured parallel resonance field,
c        the measured resonance field,and the assumed Hkctry(J).
c        Square(J) is the average square of the deviations of the Frequc(I)s
c        from their average.
c      .............................
c      Results are typed to an output file which the user specifies,e.g. fil.dat
c      File is appended to, so more than one set of data may be written to a
c      given file.
         Real Beta(20),Theta(20),Frequc(20),Setsta(20)
         Real Hkctry(42),Hketry(42),Square(42),Stheta(20)
         Double Precision Filout
         Real Hr(20),Avgfrq,Hktry,Frquc,abprod,ab
         Integer N,jkl, sample! sample is run number
c      jkl is counter to check for more data(i.e. re-execute program)
c      Initialize array with starting angles to zero
         Data Setsta/20*0.0/
c      Initialize parameters with subroutine Setpar
100      Call Setpar(Hkcsta,Hkcinc,Setinc,Seterr,MM,Setsta)

c      Get input data from program user
         Call Getdat(Hr,Beta,N,Sample,Hp,Hn)
c      Subroutine setsub computes starting angles  for theta setsta(I)
         Call Setsub(N,Beta,Setsta)
c      Subroutine to do calculations
         Call Crunch(MM,Hkcsta,Hkcinc,Hp,Hn,Hkctry,N,Setinc,Theta,
        +Seterr,Hr,Stheta,Beta,Setsta,Frequc,Square,Hketry)

c      Output subroutine writes results to a user specified file
490      Call Output(N,Hr,Beta,Hkctry,Hketry,MM,Square,Stheta,Frequc,
        +sample,Hn)
         write(5,500)
500      format(' ','more calculations on new data?, type 1 ',$)
         read(5,510)jkl
510      format(1)
         If(jkl.eq.1) go to 100
         End
c....................................END OF MAIN PROGRAM .........................
c..............................................................................
c...............................Subroutine Getdat............................


         subroutine Getdat(Hr,Beta,N,Sample,Hp,Hn)
```

```fortran
        Real Hr(N), Beta(N)
        Integer N,sample

        Write (5,100)
100     Format (x,'Enter sample number> ',$)
        Read (5,200)sample
200     Format(A)
220     write(5,240)
240     format(x,'The number of measured data is the number of ')
        write(5,241)
241     format(x,'measurements at angles other than 0 degrees (perpen.)')
250     Write(5,300)
300     Format(x,'Enter number of measured data> '$)
        Read(5,400)N
400     Format(I)
        If((N.lt.20).and.(N.gt.1)) go to 501
        write(5,450)
450     Format(' ','Please input number greater than 1, and less than 21')
        go to 250


c       Hp is the resonace field when the applied field is in the plane of
c       the film.
c       Hn is the resonance field when the applied field is normal to
c       the film.
501     write(5,62)
62      Format(x, 'Enter : Hperpendicular:Oe '$)
        Read(5,61)Hn

        Write(5,51)
51        Format(' Enter : Hparallel:Oe '$)
60        read(5, 61) Hp
61        Format(F)
c       parallel field
        Hr(1)=Hp
        Beta(1)=90.0


c       Loop to get resonant field measurement data
        write(5,401)
401     format(x,'Enter data for other measurement angles')
        Do 900 I=2,N
499     Write(5,500)I
500     Format(x,'Input field for 'I2' measurement ,then
       +return)> '$)
        Read(5,600)Hr(I)
600     Format(F)
c       test to make sure angle not accidently typed in, instead of field
        If(Hr(I).gt.200) go to 650
        write(5,630)
630     format(x,'Field Has to be greater than 200 Oe ')
        go to 499
650     Write(5,700)I
700     Format(x,'Input msnt angle' I'> '$)
        Read(5,600)Beta(I)
c       test input angle data, if out of bounds, then ask for valid inpu
c       Zero is not a valid angle- sin in numerator
        If((Beta(I).lt.175).and.(Beta(I).gt.5.0)) go to 900
        write(5,750)I
750     format(' ','Input angle ' I' between 5 and 175')
        go to 650
900     Continue
```
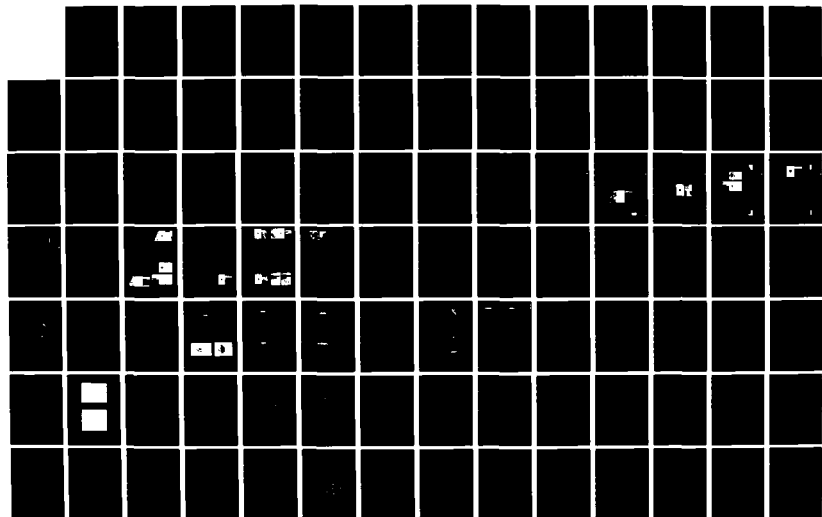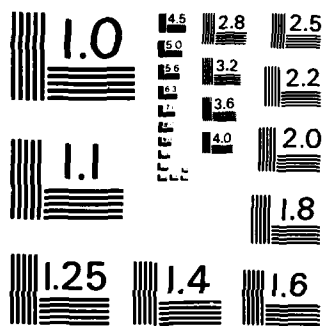
MICROCOPY RESOLUTION TEST CHART

```fortran
c     check input data

      Write(5,1900)sample
1900  Format(' ','Input data for film number  ',A10)
      write(5,1905)
1905  Format(' ','H resonance,  Angle')
      write(5,1908)Hn
1908  Format(F6.0,xxxxxxx,' 0.0  Perpendicular')
      Do 1920 I= 1, N
      Write(5,1910)Hr(I),Beta(I)
1910  Format(F6.0,xxxxxx,F5.1)
1920  Continue
      write(5,1930)
1930  format(x,'Is input data correct?  If no type 0, if yes type 1: '$)
      read(5,1940)ndc
1940  format(I)
      If (ndc.ne.0) go to 1950
      write(5,1945)
1945  format(x,'Please Re-enter all of the input data')
      If (ndc.eq.0) go to 220
1950  Return
      End
c     end of get data subroutine
c     ***********************************************************
c     ***************Subroutine Output***************************
c     Subroutine Output to report results
      Subroutine  Output(N,Hr,Beta,Hkctry,Hketry,M,Square,Stheta,
     +Frequc,sample,Hn)
      Real Hkctry(M),Hketry(M),Square(M),Hr(N),Beta(N),Stheta(M)
      real frequc(M)
      Integer N,M,sample
      Double precision filout
c     Report results
c     try to write results to a file
490    write(5,1000)
1000   format('0','Output file name? '$)

      read(5,2400) filout
2400   format(a10)
       open (unit=21, file=filout,access='append')
c     access='append' allows more than one set of data to be written to file
c     List input data
      Write(21,4900)sample
4900  Format(' ','Input data for film number  ',A10)
      write(21,4905)
4905  Format(' ','H resonance,  Angle')
      write(21,4908)Hn
4908  Format(F6.0,xxxxxxx,' 0.0')
      Do 4920 I= 1, N
      Write(21,4910)Hr(I),Beta(I)
4910  Format(F6.0,xxxxxx,F5.1)
4920  Continue

      Write(21, 491) Hkctry(M/2),Hketry(M/2)
491       Format(x,'H1 is ',F8.1,' (Oe) ; The
     1 Hke = (Hk - 4piM) is ',F8.1,' (Oe).')
c        2 In the following table ,H1(I) represents the I th assumed
c        3 value of H1,and Hke(I) denotes the I th calculated value of
c        4 Hke.Error means the average square of the deviations of the
c        5 calculated values of the angular frequency of the microwave
```

```
c        6 field divided by the gyromagnetic ratio from the average of
c        7 these values.')

495      Do 510 I=(N/2-2),(N/2+2)
c     print out results near correct result, not all values
500      Write(21,501)I,Hkctry(I),I,Hketry(I),I,Square(I)
c500     Write(5,501)I,Hkctry(I),I,Hketry(I),I,Square(I)
501      Format(' Hl(',I2,') : ',F8.1,' (Oe);    Hke(',I2,') : ',
         1F8.1,' (Oe) ;    Err(',I2,') : ',F9.1,' .')
510      Continue
c     The following table shows the relation between the
c      Beta(I) and the Theta(I),and the scatter of Fre(I).
c     Beta(I) signifies the angle between the applied field and the
c     normal of the film. Theta(I) stands for the angle between
c     the magnetization and the normal. Fre(I) is the calculated
c     value of the angular frequency of the microwave field
c     divided by the gyromagnetic ratio.')
         write(21,520)
520      Format(' ','Applied Field Angle, Magnetization Angle
        +and Omega/Gamma')
525      Do 540 K=1,N
530      Write(21, 531)K,Beta(K),K,Stheta(K),K,Frequc(K)
531      Format(' Beta(',I2,') : ',F7.2,';    Theta(',I2,') : ',
         1F7.2,';    Fre(',I2,') : ',F9.1,' .')
540      Continue
         close(unit=21)
      Return
      End
c              ****************************************
c              *********Subroutine Setsub*************
c     This subroutine sets the starting angles for theta - magnetization
c     direction, depending on beta - applied field direction
c
      Subroutine Setsub(N,Beta,Setsta)
      Real Beta(N),Setsta(N)
      integer I

      Do 200 I = 1, N
      If (Beta(I).LE.35.0)go to 150
      Setsta(I) = Beta(I) - 32.0
      Go to 200
150      Setsta(I) = Beta(I)/40.0
200      Continue
      Return
      End
c     ********************
c     Function to compute average frequency
      Function Avgfrq(N, Frequc)
      Dimension Frequc(N)
      Integer K,L
      Real Sum,Avefre
2800     Sum=0.0
2900     Do 3100 K=1,N
3000     Sum=Sum+Frequc(K)
3100     Continue
3200     Avefre=Sum/Float(N)
3300     Sum=0.0
3400     Do 3600 L=1,N
3500     Sum=(Frequc(L)-Avefre)*(Frequc(L)-Avefre)+Sum
3600     Continue
```

```fortran
      Avgfrq = Sum/Float(N)
3700  Return
      end
c     ....................................
c     ...........Subroutine Setpar..............
c     Subroutine to initialize parameters
      Subroutine Setpar(Hkcsta,Hkcinc,Setinc,Seterr,MM)
      Real Hkcsta, Hkcinc, Setinc, Seterr
      integer   MM
c       Hkcsta is the starting value of the crystal field H1 in the calculation
c       Hkcinc is the increment of H1 in the calculation.
c       Setinc is the increment of Theta(I).
c       Seterr is the allowable error in the theta calculation.
c       MM is the number of iterations in the H1 calculation
c     If MM is set larger than 42, than dimension statements for
c     Hkctry() Hketry() and Square() must be changed to accomodate
c     larger array
        Hkcsta=-200.0
        Hkcinc=5.0
        Setinc=2.0
        Seterr=0.050        ! initially set to .005
        MM=11
      Return
      End


c     ...................
c     function to compute Hketry
      function Hketry(Hp,Hn,Hkctry,JJ)
      real Hp,Hn,Hkctry
      Dimension Hkctry(42)
      YY=(Hp*0.5+Hn-Hkctry(JJ)*0.6666667)*(Hp*0.5+Hn-Hkctry(JJ)*0.66667)
      XX=Hp*(Hp-Hkctry(JJ)*0.5)
      AA=YY+XX
      BB =(Hn-Hkctry(JJ)*0.6666667)*(Hn-Hkctry(JJ)*0.6666667)
      DD=(AA-BB)**0.5
      CC=Hkctry(JJ)*0.6666667-Hn-Hp*0.5
      Hketry=DD+CC
      return
      end
c     ..................................................
c     .................Subroutine Crunch..............
c     Subroutine to calculate H1
c       There will be four Do Loops in total. Three independent Do Loops are
c       nested in an outer Do Loop.The first inner one calculates Hketry(J)
c       via the measured Hp,the measured Hn,and the assumed Hkctry(J).Then it
c       will evaluate Theta(I) for the measured Hr(I) and Beta(I) along with
c       the Setsta(I),Setinc,Seterr,the assumed Hkctry(J),and the calculated
c       Hketry(J).Finally,it calculates the Frequc(I) via Hr(I),Beta(I),Theta(
c       I),Hkctry(J),Hketry(J).The second inner one evaluates the average of
c       all the Frequc(I)s.The third inner one calculates the average square
c       of the deviations of Frequc(I)s from their average.Subsequently,the
c       data are printed out in two tables.The outer DO Loop repeats those
c       procedures for another assumed Hkctry(J+1) MM times.
      Subroutine Crunch(MM,Hkcsta,Hkcinc,Hp,Hn,Hkctry,N,Setinc,
     +Theta,Seterr,Hr,Stheta,Beta,Setsta,Frequc,Square,Hketry)

      real Hkcsta,Hkcinc,Hp,Hn,Hkctry(MM),Setinc
      real Theta(N),Seterr,Hr(N),Stheta(MM),Beta(N),Setsta(N)
      real Frequc(MM),Square(MM)
      real Hketry(42),Hktry,Freten,fretel,frete2
```

```
110      DO 380 J=1,MM
c        Solve for the Hketry(J)


120      Hkctry(J)=Hkcsta+Hkcinc*(Float(J)-1.0)
c     Assign dummy variable so loop index is not modified in function
c     Hktry
         JJJ=J
130      Hketry(J)=Hktry(Hp,Hn,Hkctry,JJJ)


c        Solve for the Theta(I)
c      Call Comfre(N,Setinc,Theta,Seterr,Hketry,Hr,Hkctry,Stheta
c     +,Beta,MM,Setsta,Frequc)
140      Do 270 I=1,N
150      Theta(I)=Setsta(I)
c     setdel is theta difference, initially same as theta increment setinc
160      Setdel=Setinc
170      Settes=Theta(I)+Setdel
180      If((Setdel-Seterr).le.0.0) go to 250
         IIT=I
         JJT=J
         ab=abprod(Settes,Hketry,Hkctry,Beta,Theta,Hr,IIT,JJT)
210      If(ab)230,240,220
220      Theta(I)=Settes
         Go to 170
230      Setdel=Setdel*0.5
         Go to 170
240      Theta(I)=Settes
         Go to 255
250      Theta(I)=Theta(I)+Setdel*0.5
c        Store the Theta(I) in the Stheta(I) if J=(MM/2).
c        Solve for the Frequc(I)
         KK=MM/2


c     find integer equivalent of midpoint of search loop
255      If(J.EQ.(KK)) Stheta(I)=Theta(I)

         fret=Hr(I)*Cosd(Beta(I)-Theta(I))
         frep=Hketry(J)*Cosd(Theta(I)*2.0)
         fretq=fret+frep
         fret3=Hkctry(J)*(2.828427*Sind(Theta(I)*2.0)*(3.0-8.0*Sind(
         2Theta(I))**2)-7.0*Cosd(Theta(I)*4.0)-Cosd(Theta(I)*2.0))/12.0
         fretl=fretq+fret3
c        12 only divides part of fretl
         fret2=(Hr(I)*Sind(Beta(I))/Sind(Theta(I))
         +-1.06066*Sind(Theta(I)*2.0)*Hkctry(J))

         fretem=fretl*fret2
260      Frequc(I)=sqrt(fretem)
270      Continue

c        Calculate the average of the Frequc(I).
c ***  function avgfrq to compute average frequency
370      Square(J)=Avgfrq(N,Frequc)
380      Continue
c        Center the minimum of the Frequc(J)s.
390      N=1
400      Nt=N+1
410      If(Square(Nt)-Square(N))420,460,450
420      If((N-(MM-1)).ge.0) go to 440
430      N=N+1
```

```fortran
         Go to 400
c440      Hkcsta=Hkcsta+Hkcinc*39.0
440      Hkcsta=Hkcsta+Hkcinc*Float(MM-1)
         Go to 110
450      If(M.EQ.KK) go to 490
452      If(M.GT.1) go to 470
         Hkcsta=Hkcsta-Hkcinc*Float(MM-1)
         Go to 110
460      If(M.EQ.KK) go to 490
470      Hkcsta=Hkcsta+Hkcinc*(Float(M)-Float(KK))
480      Go to 110
490      Return
         end
c**************************************************
c        Function to compute A*B lines 190,200
         function abprod(Settes,Hketry,Hkctry,Beta,Theta,Hr,I,J)
c         ab=abprod(Settes,Hketry,Hkctry,Beta,Theta,Hr,I)
         real Theta(20),Beta(20),Hketry(40),Hkctry(40),Hr(20)
         real set1,set2,set4,the1,the2,the4
         real A,AA1,AA2,AA3,AA4,AA5,AA6,AA7
         real B,BB1,BB2,BB3,BB4,BB5,BB6,BB7
         real Settes
         set1=Sind(Settes)
         set2=set1*set1
         set4=set2*set2
         BB1=Hketry(J)*Sind(Settes*2.0)
         BB2=-2.0*Hr(I)*Sind(Beta(I)-Settes)
         BB3=1.414214*set2
         BB4=-0.2916667*Sind(Settes*4.0)
         BB5=-0.0833333*Sind(Settes*2.0)
         BB6=-1.885618*set4
         BB7=Hkctry(J)*(BB3+BB4+BB5+BB6)
200      B=BB1+BB2+BB7
         the1=Sind(Theta(I))
         the2=the1*the1
         the4=the2*the2
         AA1=Hketry(J)*Sind(Theta(I)*2.0)
         AA2=-2.0*Hr(I)*Sind(Beta(I)-Theta(I))
         AA3=Hkctry(J)*(1.414214*the2)
         AA4=-0.2916667*Sind(Theta(I)*4.0)
         AA5=-0.0833333*Sind(Theta(I)*2.0)
         AA6=-1.885618*the4
190      A=AA1+AA2+AA3+AA4+AA5+AA6
         abprod=A*B
         return
         end
c        function abprod replaced these
c190     A=Hketry(J)*Sind(Theta(I)*2.0)-2.0*Hr(I)*Sind(Beta(I)-Theta(I))+
c        1Hkctry(J)*(1.414214*Sind(Theta(I))**2-0.2916667*Sind(Theta(I)
c        2*4.0)-0.0833333*Sind(Theta(I)*2.0)-1.885618*Sind(Theta(I))**4)

c200     B=Hketry(J)*Sind(Settes*2.0)-2.0*Hr(I)*Sind(Beta(I)-Settes)+
c        1Hkctry(J)*(1.414214*Sind(Settes)**2-0.2916667*Sind(Settes
c        2*4.0)-0.0833333*Sind(Settes*2.0)-1.885618*Sind(Settes)**4)
c        Assign dummy indices to I and J for use in function abprod
c210     If(A*B)230,240,220
```

Appendix C
EXPERIMENTAL APPARATUS

C.1. FERROMAGNETIC RESONANCE APPARATUS

The following is a listing of the components in the ferromagnetic resonance system.

- Magnet: Varian V-3603 12 inch electromagnet with V-FR2501 Fieldial regulator

- Microwave source: HP Model 8350B Frequency Generator with Model 83525A RF Plug-in. Frequency range 0.01 to 8.4 GHz.

- Lock-In Amplifier: PAR Model HR-8, with Type A preamp.

- Circulator: Trak Model 50A3001 SN 452, frequency range 2-4 GHz, Model 50A6001 SN 435, frequency range 4-8 Ghz.

- Detector: Omni Spectra Model 20760, PN 2086-6000-00, 1 - 15 GHz

- DC Block: Omni Spectra Model 2044-6010-00

- Modulating Frequency Source: HP Model 3300A Function Generator

- Modulating Frequency Amplifier: Crown DC300 Audio Amplifier

- X-Y Recorder: HP Model 7035B

- Gaussmeter: Bell Model 620 with Model HTB4-0608 Probe

Resonance measurements were made using a minibox which had a serpentine-shaped conductor. The serpentine-shaped conductor pattern was photolithographically defined on the alumina substrate. Typical operation involved shorting one end of the microstrip and using a circulator to send the reflected microwave signal to a diode detector. A DC block was used to reduce pick-up from the modulating field. An audio amplifier was used to amplify the 88 Hz sinusoidal signal which excited the modulating field coils. The modulating field amplitude was typically 25 Oe.

The Varian magnet has 12 inch diameter pole pieces with a 3 inch gap. The field

was controlled by a Fieldial regulator, which was capable of sweeping over any range from 1 G to 10 kG, at sweep times ranging from 1 to 50 minutes. Typical operating conditions were 1 kG field sweep in 1 minute. For field measurement, a gaussmeter with a Hall probe was used. The resonance fields were measured by manually setting the field to the zero-cross field of the absorption derivative resonance, and reading the field directly from the gaussmeter. The Fieldial had an output which was proportional to the field sweep range which was used to drive the x-axis of the recorder. The modulating field coils were wound around the pole pieces of the Varian magnet. The microwave generator was used in the continuous wave (CW) mode.

The minibox was connected to the microwave generator with low-loss coaxial cables. For operation in transmission, a second low-loss coaxial cable was connected between one end of the stripline and the diode detector. A dc block was placed in front of the detector to reduce the modulating field pickup. The signal from the detector was fed into the phase-lock amplifier. In reflection, a circulator was placed at the output of the microwave generator. Port 2 of the circulator was connected to the coaxial cable which went to the minibox and port 3 was directly connected to the dc block and diode detector. The other end of the microstrip was terminated in a short. The reflection mode provided a slightly stronger signal and had the additional advantage of requiring one less connecting cable. As the cables provided an easy path for heat conduction away from the minibox, using only one resulted in improved thermal stability at high temperatures.

C.2. ION IMPLANTATION

The implants were done by J. Tabacchi in a Veeco Accelerators Inc. AIM 210 Ion Implanter, which was located at Mellon Institute under the auspices of Dr. A. M. Guzman. The samples were tilted so that the film normal was 7° from the direction of the incident beam to avoid channelling effects. The samples were taped to a 3" diameter silicon wafer. The implant current density was typically between 5 and 10 μA over the 3" diameter target area. The substrate was not cooled during implantation.

The implant species D_2^+ was used as the presence of this species is significantly larger than D^+. Thus higher implant currents can be achieved.

Appendix D
ANALYSIS OF RESONANCE SPECTRA

The anisotropy profiles for film 84, which were described in Chapter 3, were obtained from the spin wave analysis program. The details of the fitting procedure, and the sensitivity of the fit to minor profile variations are discussed here. In addition, the problem of fitting the spectra from samples which do not have unimodal anisotropy profiles is discussed.

D.1. FIT FOR FILM 84, AFTER 700 C ANNEAL

To determine the relative uncertainty in the anisotropy profile shown in Fig. 3-3 and to evaluate the sensitivity of the calculated resonance spectra to small changes in the anisotropy profile, the effects of small variations in the anisotropy profile were studied. In Table D-1 the anisotropy fields in the nine 500 angstrom thick surface layers are listed for fit A. In the adjacent columns, if the profile was varied in a layer, the signed magnitude of the variation is given. For example, in Fit B, H_K in layer #1 was decreased by 200 Oe, to 1150 Oe. If no variation is indicated, the profile is identical to that listed in column A. In Table D-2 the experimental perpendicular resonance mode locations and amplitudes are given. Also listed are the modes for Fit A, and the difference between the calculated and measured modes. The parallel resonance spectra will not be discussed here. Since most of the parallel modes are localized in the bulk film, the surface profile variations all had a relatively small effect on the parallel spectra. The significant changes in the mode spectra for each profile variation are listed in Tables D-2 and D-3. For clarity, changes in mode location which are less than 10 Oe, and mode amplitudes which are less than 4% are not included.

Fit A corresponds to the profile which is shown in Fig. 3-3 for the 700°C anneal. The changes in the calculated spectra for fit A through I are listed in Tables D-2 and D-3. In the fourth column, Δ is the difference between the calculated and measured spectra. Under each of the letters B through I, changes in the spectra relative to fit A

Table D-1: Anisotropy Field Profile in Surface Layer of Film 84

L#	A	B	C	D	E	F	G	H	I
1	1350	-200							
2	-200		-200						
3	-400						-240	-200	-200
4	-500						-140	-100	-100
5	-570						-70	+70	+70
6	-580					-60		+80	+80
7	-580					-60			
8	-640						+60		-30
9	-525			-115	+100				-195

Table D-2: Experimental and Calculated Perpendicular Resonance
Spectra for Film 84 after 700°C Anneal

Mode	Exp.	A	Δ	B	C	D	E
1	3473	3473	0	-	-	+37	-20
	100%	100%	0				
2	3317	3332	+15	-	-	+23	-21
	20%	17%	+3%	-	-	+21%	-9%
3	3109	3119	-10	-	+17	+17	-19
	17%	14%	+3%	-	-	-	-
4	2853	2853	0	-	+36	+13	-16
	4%	6%	-2%	-	-	-	
5	2530	2512	+18	-	+43	+12	-11
	9%	5%	+4%	-	-	-	
6	2157	2100	+57	+12	+35	-	-10
	7%	4%	+3%	-	-	-	-
7	1665	1621	+44	+27	+23-	-	-
	16%	8%	+8%	-	-	-	-
Bulk	1341	1339	-2	-	-	-	
	170%	170%	0	+5%	-	+31%	-11%

are given. Thus the change in any particular mode for each profile variation can be compared to the desired change to achieve a perfect fit.

In fits B, C, D, and E, H_K is varied in a single layer. In fit B, H_K is decreased by

Table D-3:   700°C Profile Variations: Continued

Mode	F	G	H	I
1	+24	+12	−10	+78(Ampl. = 100%)
2	+9	+60	+29	+47
	−6%	−17%	+8%	+70%
3	+17	+72	+37	+73
	+5%	−9%	−11%	−13%
4	+12	+58	+23	+50
	−	−	−3%	−
5	+14	+17	+13	+37
6	−	+34	−	+29
7	+14	+45	+25	+43
Bulk	−42%	−8%	+77%	

200 Oe in layer 1.   This only affects the locations of modes 6 and 7, and the bulk mode amplitude.   The increase in the bulk mode amplitude in fit B is attributed to a stronger coupling of the bulk mode to the surface layer due to the decrease in ΔH_K in that region.   A sharper transition in H_K between the bulk and the surface will decrease the coupling and thus decrease the bulk mode amplitude.   In fit C, the anisotropy field in layer 2 was decreased by 200 Oe.   This resulted in a decrease in the locations of modes 3 through 6.   The mode amplitudes did not change significantly.   In fits D and E, the anisotropy field at the film surface was varied.   In fit D, the maximum anisotropy field change occurs at the film surface, in layers 8 and 9.   This increased the location of all of the surface modes slightly and also increased the second and bulk mode amplitudes.   In fit E, ΔH_K at the surface was decreased, so there was a sharper transition between the maximum anisotropy change in layer 8, and the film surface (layer 9).   This lowered all of the resonance modes, and decreased the amplitude of mode 2 and the bulk mode.   In fit F, the region with the maximum anisotropy change was extended to include layers 6 and 7, as well as layer 8.   This resulted in a slight increase in all of the mode locations, and an increase in the amplitude of the third mode.

The variation in fit G involved shifting the location of the region of the maximum ΔH_K closer to the bulk film.   This was accomplished by increasing H_K in layer 8, and decreasing it in layers 3, 4, and 5.   The locations of the surface modes increased, with the largest increases in modes 2, 3, 4, and 7.   The amplitudes of modes 2 and 3 both decreased.

In fit H, the profile is bimodal. There are local maxima in ΔH_K in layers 3-4 and 8. The first mode location decreased slightly, while the location of the higher order modes all increased. Note that through fit G, all of the variations in the profile caused either no change, or changes of the same sign in the mode location. To get a better fit to experimental data, which requires both increases and decreases in mode locations, use of a bimodal profile may be required. However, there are problems with uniqueness with bimodal anisotropy profiles, which complicate their use.

In fit I, the profile was identical to fit H, except for an increase in ΔH_K at the film surface. The profile was still bimodal, but now the maximum ΔH_K was at the film surface. This caused an increase in the locations of all the surface modes, due to an increase in ΔH_K. However, the most dramatic difference was in the amplitude of the second mode, which increased from 24% in fit H to 87% in fit I. The third mode amplitude was significantly lower than that in fit A, but was comparable to that in fit H. The increase in the second mode amplitude, corresponding to the peak in the anisotropy field at the film surface has been observed experimentally in films which were overcoated with SiO_2 and then annealed. Also note in fit I that the increase in ΔH_K at the film surface increased the location of the first surface mode, thus increasing ΔH_E, although the average anisotropy field through the film thickness does not change significantly.

The depth dependence of the spin wave solutions are plotted in Fig. D-1. The lefthand column represents solutions of the first ten perpendicular spin wave modes; the righthand column represents the solutions for the parallel modes. The mode amplitudes are normalized to that of the first mode. For the higher order modes, the amplitude is the net difference in the area above and below the horizontal axis. The modes have a sinusoidal oscillation in the s... e layer with an exponential decay into the bulk. Note that the bulk mode is given by the eighth perpendicular mode. This corresponds to the first mode that extends into the bulk region. In parallel resonance, the first 6 modes are localized in the bulk layer. The seventh mode is overlapped between the two regions and the eighth is realted to the anisotropy at the film surface.

The first (highest field) surface mode in the perpendicular resonance is localized in the region with the maximum ΔH_E, which is close to the film surface. Note that the program can profile H_K and $4\pi M_x$ independently, whereas the results from the frequency dependence of the highest field mode can only be used to determine $H_E(I)$ and ΔH_E, and cannot be used to determine relative changes in H_K and $4\pi M_x$. The

strong amplitude of the second mode can be seen as asymmetry in the spin wave solution, due to the localization of the first mode at the film surface. The amplitude of the third mode is strongly affected by the H_K profile close to, but not at the bulk surface interface. To get a significant amplitude for the third mode, a lower value of ΔH_K near the bulk was required. No way was found to independently adjust modes 4 through 6, however their locations could be adjusted relative to the other modes by profiling $4\pi M_s$ and A through the film thickness. The seventh mode amplitude is strongly dependent on the H_K transition between the bulk and the implanted regions. A sharp transition gives a very small seventh mode amplitude, whereas a gradual transition results in significant exchange shift in the bulk resonance, and a larger third and seventh mode amplitude.
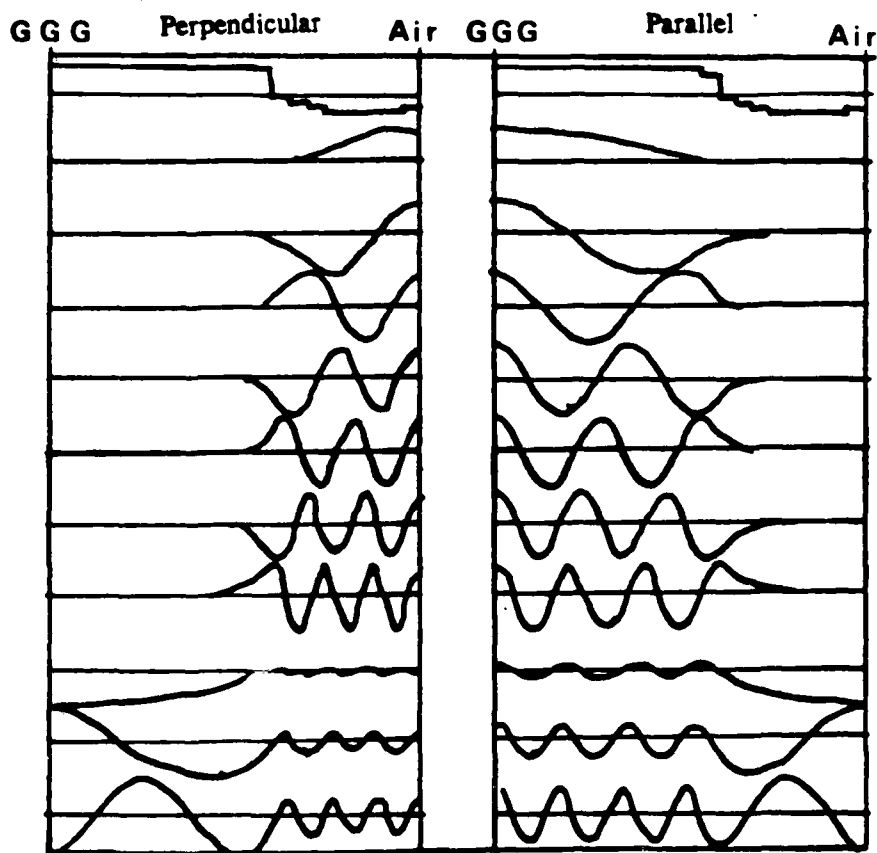

Fig. D-1: Depth Dependence of Spin Wave Solutions for 700°C Fit Perpendicular and Parallel Modes

In summary, variations of 100 Oe to 200 Oe in H_K in any given layer have a significant effect on the spectra, which make discrepancies of this magnitude unlikely. Furthermore, while H_K in any given layer may not be accurately known to better than

100 Oe, the shape of the anisotropy profile, including the location of the maximum change, the transition to the bulk layer, and the value at the film surface are quite sensitive to relatively small variations in the profile. Large discrepancies in the anisotropy profile, due either to incorrect numbering of the modes due to presence of undetected intermediate modes, or drastic differences in the film parameters, compared to those used in the program, are highly unlikely.

D.2. FIT FOR FILM 84 AFTER THE 250 C ANNEAL

The fit for the resonance spectra measured after the 250°C anneal was much more difficult to obtain. This may be attributed to a significant variation in $4\pi M_s$ and A through the film thickness. In the fit which was obtained, no variations were used. Trial fits with profiles of $4\pi M_s$ and A, which were scaled proportionately with the H_K profile, were done, although they did not result in a significantly better match.

The depth dependence of the spin wave solution is plotted in Fig. D-2. In perpendicular resonance, the first mode is localized in the center of the implanted layer. The amplitude of the second mode is nearly zero, as can be seen by the symmetric spin wave solution. This was achieved by locating the maximum ΔH_K near the center of the surface region. The amplitude and location of the odd numbered modes depends on the H_K profile at the film surface. The wider the region with a lower change in H_K, the stronger the higher order odd mode amplitudes will be. Note that this agrees with the experimental result observed for film 55, which had a high energy, single dose implant which created a large region with a lower ΔH_E than the region with the maximum ΔH_E.

In the parallel resonance, the first mode is localized predominantly in the bulk, but has small contribution from the film surface. The eighth parallel mode is strongly localized in the surface region.

The accuracy of the anisotropy profile obtained after the 200°C anneal is estimated to be between 100 to 200 Oe at any given depth in the film. This uncertainty is partially attributed to the uncertainty in determining the changes in $4\pi M_s$ and A. However the relative shape of the profile has a large effect on the surface modes and therefore is presumed to be correct.
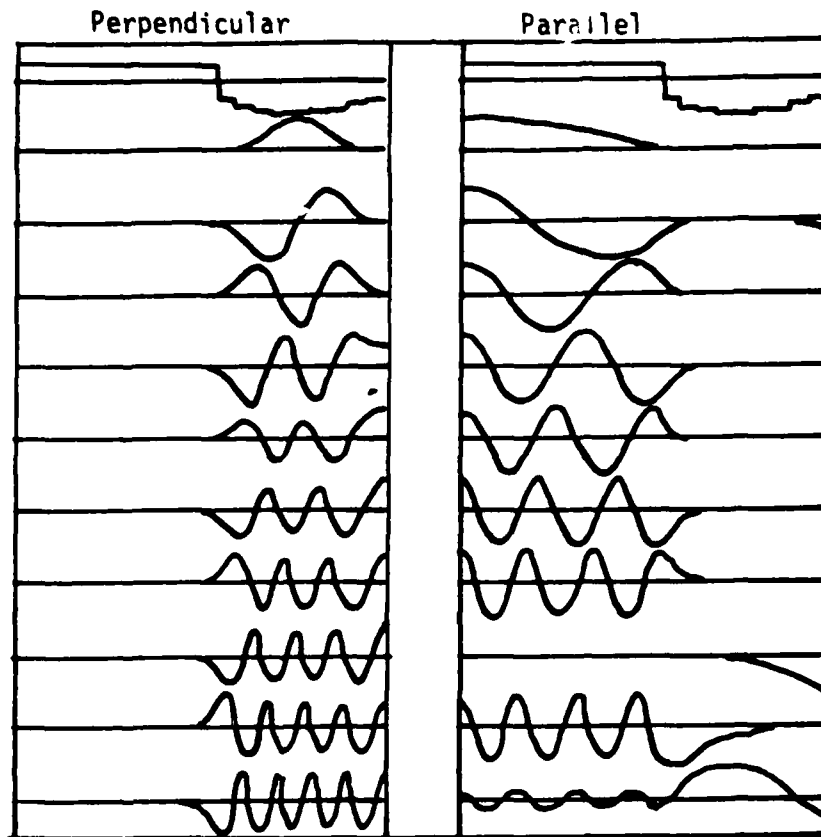
182

Perpendicular   Parallel

**Fig. D-2:   Depth Dependence of Spin Wave Solutions for 250°C Fit
Perpendicular and Parallel Modes**

D.3. BIMODAL ANISOTROPY PROFILES

Multiple implants are required to achieve uniform properties through the implanted layer. However, incorrect selection of the implant conditions may create bimodal or polymodal anisotropy profiles. Bimodal anisotropy profiles have two distinct regions which have a local maximum in the anisotropy field change. In films with polymodal anisotropy profiles, there are more than two local maxima. These profiles are typically created by multiple energy implants. It is important to recognize telltale signs of bimodal profiles in the FMR spectra. In the case where the multiple implants create a bimodal anisotropy profile, it is important to know how the implant conditions should be adjusted. The analysis of these spectra is complicated, and results may not be unique. However, by analyzing a set of hypothetical bimodal anisotropy profiles, some insight into the characteristics of the spectra can be gained. Characteristics of bimodal profiles include irregular mode spacing and overlapped modes. Examples of these, both from calculated profiles, and from experimental measurements will be given.

The bimodal profile shown in Fig. D-3 was obtained during the fitting procedure for film 84 after the 250°C anneal. While this particular distribution does not match the spectra, it is possible that such a profile would be obtained from a film implanted with a combination of high and low energy ions. The calculated mode spectra are plotted in Fig. D-4. The characteristic features of the spectra are the pairs of modes; 1 and 2, 3 and 4, and 5 and 6. The plot of the solution to the spin waves versus the film depth shown in Fig. D-5 provides insight into the reason for this particular mode distribution. The first surface mode is localized in the region near the film surface, as this region has the highest ΔH_K. The second mode is localized in the region closer to the bulk. The second mode amplitude is slightly greater, since this region is slightly wider than the region near the surface. The third and fourth modes are also isolated in separate regions. This partially explains the pairing of the mode spectra. The spin waves do not extend through the entire film thickness until the fifth mode, and are significantly perturbed from the sinusoidal solution up to the eighth mode. Since the mode amplitude is the net difference in the positive and negative halves of the spin wave solution in Fig. D-5, large mode amplitudes generally result from these asymmetric spin wave solutions. In parallel resonance, the first 7 modes are strongly localized in the bulk layer. The eighth mode is localized in the surface region closer to the bulk, and the ninth mode is the first to reach the film surface-air interface.
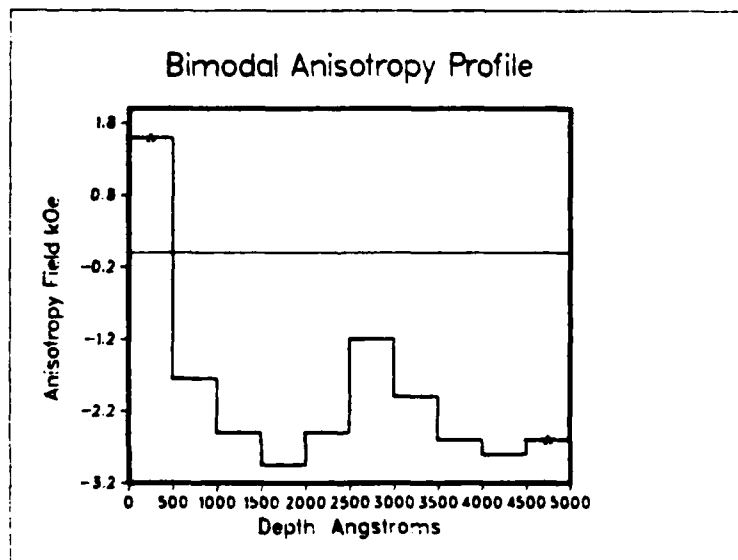

Fig. D-3:   Bimodal Anisotropy Profile

In summary, bimodal profiles cause unusual resonance spectra, which are characterized by irregular mode spacings, and large amplitudes for higher order modes. One set of
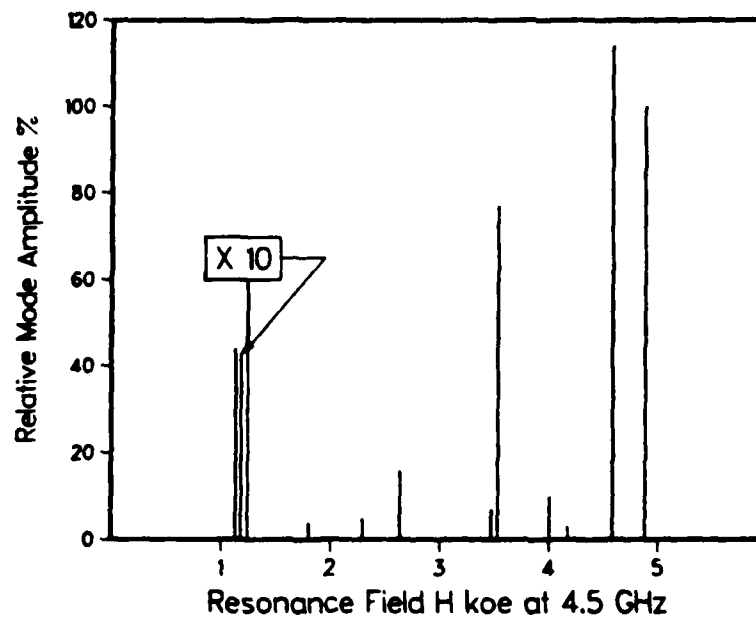
184

Fig. D-4: Calculated Resonance Spectra for Bimodal Anisotropy
Profile in Fig. D-3

resonance spectra does not provide enough information to accurately determine the anisotropy profile, since the number of fitting parameters is typically greater than the number of observed modes. Thus the number of degrees of freedom is not sufficient to obtain a reliable fit [66]. Previous investigators have suggested that it is impossible to guess the anisotropy profile if it is bimodal [14] due to ambiguity in identification of the mode localization. The analysis must be done by etching the film and reconstructing the profile from the spectra measured after each etching step, in the reverse order from which they were obtained.
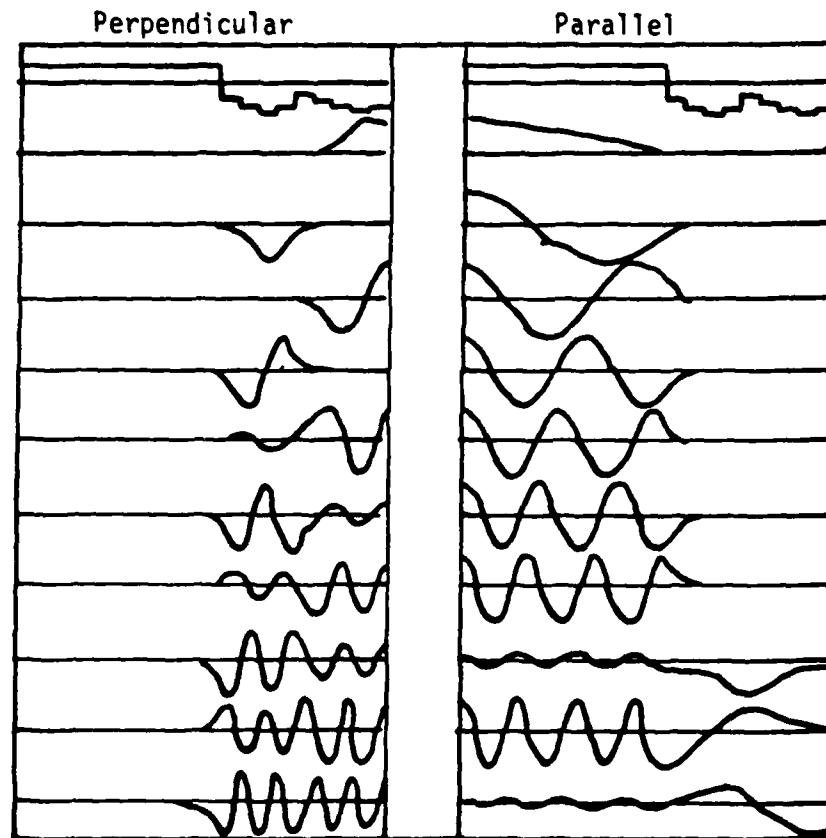
Perpendicular   Parallel

Fig. D-5:   Depth Dependence of Solution to Spin Wave Equations
for Bimodal Anisotropy Profile

References

1. A. H. Bobeck and H. E. D. Scovil, Scien. Amer. **224**, 78 (1971).
2. A. A. Thiele, Bell Syst. Tech. J. **48**, 3287 (1969).
3. H.J. Levinstein, R.W. Landorf, S.J. Licht, S.L.Blank, Appl. Phys. Lett. **19**, 486 (1971).
4. M. H. Kryder and D. A. Saunders, IEEE Trans. Magn. MAG **15**, 1817 (1983).
5. A. H. Eschenfelder, *Magnetic Bubble Technology*, (Springer–Verlag, New York, 1980) .
6. R. Wolfe, and J.C. North, Bell Syst. Tech. J. **51**, 1436 (1972).
7. S. Chikazumi and S. H. Charap, *Physics of Magnetization*, (Robert E. Krieger Publishing Co., New York, 1978) .
8. K. Komenou, I. Hirai, K. Asami, and M. Sakai, J. Appl. Phys. **49**, 5816 (1978).
9. H. Matsutera, S. Esho, and Y. Hidaka, J. Appl. Phys. **53**, 2504 (1982).
10. R. Hirko, and K. Ju, IEEE Trans. Magn. MAG-**16**, 958 (1980).
11. J. Lindhard, M. Scharff, and H. E. Schiott, Mat. Fys. Medd. K. Dan. Vidensk. Selsk. 33 , 1 (1963).
12. H. Makino, Y. Hidaka, H. Matsutera, J. Magn. Magn. Mater. **35**, 311 (1983).
13. Y. Sugita, T. Takeuchi, and N. Ohta, Paper CA-5, Magnetism and Magnetic Materials Conference, Atlanta, 1981.
14. V.S. Speriosu and C.H. Wilts, J. Appl. Phys. **54**, 3325 (1983).
15. G. Suran, H. Jouve, and P. Gerard, J. Appl. Phys. **54**, 2006 (1983).
16. G. Marest, F. Ravel, J. L. Ponthenier, P. Gerard, J. M. Robertson, J. Appl. Phys. **55**, (1984).
17. P. Gerard and T. M. Duc, unpublished results
18. V.S. Speriosu and C.H. Wilts, J. Appl. Phys. **54**, 3325 (1983).
19. P. Gerard, Thin Solid Films **114**, - (1984), In press
20. M.H. Kryder, X. Wang, C.S. Krafft, and A.M. Guzman, J. Magn. Magn. Mater. **35**, 307 (1983).
21. R. Hirko and T. Gallagher, private communication, Deuterium Range Statistics Calculated from LSS Theory.
22. K. Komenou, T. Miyashita, K. Betsui, M. Ohashi, Y. Satoh, K.Yamagishi, to be published in J. Appl. Phys.,.
23. G. F. Dionne, J. Appl. Phys. **41**, 2264 (1970).
24. A.B. Smith, Rev. Sci. Instrum. **39**, 378 (1968).
25. R. Wolfe, J. C. North, and Y. P. Lai, Appl. Phys. Lett. **22**, 683 (1973).
26. H.A. Washburn, G. Galli, J. Appl. Phys. **50**, 2267 (1979).
27. I. Maartense and C. W. Searle, Appl. Phys. Lett. **34**, 115 (1979).
28. J. P. Omaggio and P. E. Wigen, J. Appl. Phys. **50**, 2264 (1979).
29. Y. Satoh, M. Ohashi, T. Miyashita, K. Komenou, J. Appl. Phys. **53**, 3740 (1982).
30. P. J. Picone and A. H. Morrish, J. Appl. Phys. **53**, 2471 (1982).
31. J. Fernandez, , (Master's thesis, Electrical Engineering, Carnegie-Mellon University, 1980), unpublished
32. J.C. North, R. Wolfe, in *Ion Implantation in Semiconductors and Other Materials*, B.L. Crowder, ed., (Plenum, New York, 1973), p. 505.
33. W.H. deRoode, H.A. Algra, J. Appl. Phys. **53**, 2507 (1982).
34. H. Jouve, J. Appl. Phys. **50**, 2246 (1979).
35. B. M. Paine, V. S. Speriosu, L. S. Wielunski, H. L. Glass, and M. Nicolet, Nucl. Instrum. Methods **191**, 80 (1981).
36. T. Omi, C. L. Bauer, and M. H. Kryder, J. Appl. Phys. **53**, 2528 (1982).
37. J. A. Seman, S. H. Wemple, and J. C. North, J. Appl. Phys. **45**, 2700 (1974).
38. P. Gerard, M. Madore, and G. Suran, IEEE Trans. Magn. MAG **18**, 1274 (1982).

39. P. Gerard, P. Martin, and R. Danielou, J. Magn. Magn. Mater. 35, 303 (1983).

40. C.H. Wilts and S. Prasad, IEEE Trans. Magn. MAG-17, 2405 (1981).

41. V.S. Speriosu, J. Appl. Phys. 52, 6094 (1981).

42. T. Takeuchi, N. Ohta, Y. Sugita, and A. Fukuhara, J. Appl. Phys. 54, 715 (1983).

43. C. S. Krafft, *Characterization of Magnetic Garnet Materials*, (Master's thesis, Electrical Engineering, Carnegie-Mellon University, 1981), unpublished

44. D.C. Fowlis and J.A. Copeland, AIP Conf. Proc. 5, 240 (1972).

45. A. H. Morrish, *The Physical Principles of Magnetism*, (Robert E. Krieger, New York, 1980) .

46. D. C. Cronemeyer, T. S. Plaskett, and E. Klokholm, AIP Conf. Proc. 24, 586 (1975).

47. A. Gangulee and R. J. Kobliska, J. Appl. Phys. 51, 3333 (1980).

48. H. Makino, Y. Hidaka, Mat. Res. Bull. 16, 957 (1981).

49. X. Wang, C.S. Krafft, and M.H. Kryder, IEEE Trans. Magn. MAG-18, 1295 (1982).

50. C. H. Wilts, private communication.

51. B. Hoekstra, F. van Doveren, and J. M. Robertson, Appl. Phys. 12, 261 (1977).

52. G.P. Vella-Coleiro, Rev. Sci. Instrum. 50, 1130 (1979).

53. P. Hansen, J. Appl. Phys. 45, 3638 (1974).

54. LPE YIG sample provided by H. Glass of Rockwell International Anaheim, California courtesy of their contract F19628-83-C-0132 with the Electronics Systems Division, AFSC, United States Air Force

55. S. Timoshenko, S. Woinowsky-Krieger, *Theory of Plates and Shells*, (McGraw-Hill, New York, 1959) .

56. R. Wolfe, private communication.

57. C. S. Krafft, and M. H. Kryder, J. Appl. Phys. 55, 2557 (1984).

58. T. Takeuchi, N. Ohta, and Y. Sugita, IEEE Trans. Magn. MAG-20, 1108 (1984).

59. S. Geschwind and A. M. Clogston, Phys. Rev. 108, 49 (1957).

60. White, R.L., IEEE Trans. on Magn. MAG-9, 606-609 (1973).

61. W.T. Stacy, M.M. Janssen, J. Cryst. Growth 27, 282 (1974).

62. G. Winkler, *Magnetic Garnets*, (Friedr. Vieweg & Sohn, Braunschweig Germany, 1981) , Vol. 5, .

63. B. Hoekstra, R.P. van Stapele, and J.M. Robertson, J. Appl. Phys. 48, 382 (1977).

64. R. G. De Cesaris, Tech. report, (Carnegie-Mellon University, 1983).

65. J. O. Artman, private communication.

66. P. I. Bonyhard, F. B. Hagedorn, et al, Tech. report AFWAL-TR-83-1121, (Bell Laboratories, August 1983).

67. E.C. Meyers, S.-Y. Bi, S.H. Charap, and J.O. Artman, J. Appl. Phys. 53, 2099 (1982).

68. K. Ju, H. L. Hu, R. G. Hirko, E. B. Moore, D. Y. Saiki, R. D. Schwenker, IBM J. Res. Develop. 25, 295 (1981).

69. J.F. Gibbons, W.S. Johnson, and S.W. Mylroie, *Projected Range Statistics in Semiconductors*, (Halstead, New York, 1975) .

70. I.L. Sanders and W.J. Kabelac, IEEE Trans. Magn. MAG-20, 118 (1984).

71. S. Chikazumi and S. H. Charap, *Physics of Magnetization*, (Robert E. Krieger Publishing Co., New York, 1978) , pp. 41 .

72. G.P. Vella-Coleiro, R. Wolfe, S.L. Blank, R. Caruso, T.J. Nelson, and V.V.S. Rana, J. Appl. Phys. 52, 2355 (1981).

73. K.Y. Ahn, D.E. Cox, A. Gangulee, S.M. Kane, R.J. Kobliska, and R.P. McGouey, Tech. report 33239, (IBM T.J. Watson Research Center, 1979).

74. P. Hansen, J. Appl. Phys. **48**, 801 (1977).
75. E. M. Gyorgy, M. D. Sturge, L. D. Van Uitert, E. J. Heilner, W. H. Grodkiewicz, J. Appl. Phys. **44**, 438 (1973).

Liquid Phase Epitaxial Growth of Garnets
Progress Report - October 1984

R. O. Campbell and M. H. Kryder

Introduction

Creation of a computer modelling system has greatly eased film design and provided new film compositions for sub-micron bubble diameter films and isotropic magnetostrictive films. Materials suitable for half-micron bubble diameter ion-implanted contiguous disk (CD) use have been improved. Two film compositions were developed to provide half-micron to one-micron diameter bubble films. A difficulty of measuring the magnetization of these films also has been solved.

Isotropic Magnetostrictive film compositions have been calculated by the computer model. Several possible film compositions were shown to have suitable properties. The incorporation of dysprosium or bismuth seems to be a requirement for isotropic magnetostriction. Several bismuth based and dysprosium doped films have been grown; but all have been unsuitable for bubble work.

Several other film compositions have been developed for use in microwave applications and bubble logic devices. The films for microwave use are of a low Q and low $4\pi Ms$ character, unsuitable for bubble applications, while all of the bubble logic films are standard $2\mu m$ diameter bubble films, as have been grown in past years.

Computer Aided Film/Melt Design Program

The computer aided film design system (CAFE) has been developed to quickly produce film compositions that will satisfy many criteria concurrently. By using the properties of the film constituents such as rare-earths, iron, and iron dilutants, CAFE can extrapolate the hypothetical film properties. Lattice mismatch, magnetostriction coefficients, magnetization, damping, and growth induced and stress induced anisotropies are calculated for any film composition from standard published data.

The magnetostriction coefficients (λ_{111} and λ_{100}),the magnetization, and the damping are calculated using the proportion of each of the rare earths and adjusting for the exchange (A) due to the tetrahedral-octahedral ion pairs. Each rare-earth has associated with it magnetization, damping, and magnetostriction coefficients, so that the net value is the sum of the proportion of each constant. This net value is then decreased due to the exchange which is calculated from the iron dilution.

The lattice mismatch is similiarly calculated, however the dilution of the iron sites must be carefully considered. Typical iron substituents such as gallium and germanuim have been installed in CAFE by using a quadratic equation describing the lattice reaction to the dilutant incorporation. The quadratic describes the probability of the ions residing at a tetrahedral site [a smaller site resulting in expansive

strain] or an octahedral site [a larger site resulting in compressive stress]. The equations are derived from fitting published data to a curve and approximating the curve numerically.

The growth induced anisotropy is calculated using the pair ordering model of large ion-small ion interaction. A constant K_{ij} is assigned to each pair of rare-earths so that the net growth induced anisotropy is the sum of each K_{ij}-rare-earth product (ie. $K_G = K_{ij} x_Y x_{Lu}$). Anisotropy results from the pair ordering of samarium and europium with other rare-earths have correctly estimated published results. Using the lattice mismatch previously calculated, the stress induced anisotropy is calculated and added to the growth induced anisotropy to find the total uniaxial anisotropy (K_u).

Choosing a Q and a bubble diameter, the values of A, K_u, and 4πMs can be determined from two standard bubble equations. First, the ratio of K_u to $2\pi M_s^2$ is equal to Q

$$Q = K_u / 2\pi M_s^2$$

The characteristic length (l) is directly related to the bubble diameter, the exchange constant (A), the anisotropy constant (K_u), and the magnetization (4πMs) by:

$$l = 16\pi (A K_u)^{1/2} / (4\pi Ms)^2 = (\text{bubble diameter})/9$$

It should be noted that both A and 4πMs are closely coupled to the amount and type of iron dilutant. Both A and 4πMs vary linearly with the iron dilutant, thus they are related in a third, but seldom used, expression. CAFE finds suitable film compositions given any Q, bubble diameter, and choice of film constituents by scanning all possible film compositions and retaining only those that satisfy all requirements. Calculated results agree well with published data as can be seen in Table 1.

Recently a bismuth anisotropy model has been implemented with mixed results. Bismuth appears to not behave as the pair-ordering model would suggest, but it does have a great effect on anisotropy. Results of heavily bismuth doped films (Bi_x with $x > 0.7$) do not correlate with published data. The bismuth implementations should be completed within the year.

Film Growth Technique

All garnet film growth is by the standard vertical dipping method. Non-bismuth films are grown from a platinum crucible that contain a solution of the film's constituents dissolved in a $PbO\text{-}B_2O_3$ flux (the melt). This solution is super heated to above the saturation temperature (T_{sat}) and allowed to homogenize for a minumum of 24 hours.

The films are grown by decreasing the temperature below T_{sat} (typically 880°C) and lowering a $Gd_3Ga_5O_{12}$ (GGG) substrate rotating at 100 RPM into the melt. The substrate is allowed to reach the

melt temperature before being inserted into the melt. The film will grow as long as the melt temperature is below T_{sat} and the mismatch between the film and the substrate is not too great: typically less than 0.03A. The film is grown approximately $0.1\mu m$ thicker than the bubble diameter; thus for a $1\mu m$ diameter bubble film, the thickness would be $1.1\mu m$. Typical growth rates (dependent upon super-cooling) are $0.2\mu m/min$ to $0.5\mu m/min$, so that growth times vary from 2 minutes to 10 minutes. After the film is grown, the substrate must be dismounted from the platinum holder and any remaining PbO flux drops must be dissolved.

A 40% acetic acid, 10% nitric acid, 50% water solution proved effective for removing $PbO-B_2O_3$ flux from the substrate and substrate holder. This flux removing solution was found to be insufficient when removing the $PbO-Bi_2O_3$ flux used for growing bismuth doped films. The flux removing solution was systematically altered to 40% acetic acid, 40% nitric acid, 20% water which proved to remove all of the remaining flux. During the flux removal procedure, the substrate, while mounted on the substrate holder is alternately placed on heat ($90^{\circ}C$) and submerged in an ultrasonic bath.

Characterization Techniques

The grown films are characterized for possible melt alteration as well as to provide data for device work. Every film grown has its thickness measured, while most have the characteristic length and magnetization measured. Sample films are further characterized for lattice mismatch, damping, gyromagnetic ratio, magnetostriction coefficients, and H_{eff}.

The thickness measurements are made optically from a reflectance trace of the film. Using the interference of the light reflected from the bottom surface and the top surface of the film, a reflectance trace of the film is made by varying the wavelength of the incident light. This trace can then be used with a curve of the index of refraction as a function of the light's wavelength to determine the thickness. This results in a fast nondestructive measurement of the thickness that relies on one destructive measurement which determines the index of refraction curve.

The refractance curve is found by using a standard measuring system, such as a Dectak surface profilometer. The film is first prepared by etching stripes on the film and running the profiler perpendicular to the stripes. Once the thickness is known, one may work backwards using the refractive trace and calculate the refractive index versus wavelength curve. It has been found that the inaccuracy of this method is less than 5% for a given melt system.

Both the characteristic length (l) and the magnetization ($4\pi Ms$) are found optically by domain observation. l is found by measuring the strip width of a demagnetized sample. $4\pi Ms$ is found by determining the perpendicular field that causes the bubbles to collapse and by calculating the ratio of stripe width to film thickness. Published tables relate the ratios of strip width and film thickness to the collapse field and $4\pi Ms$.

Using ferromagnetic resonance (FMR) we can calculate the gyromagnetic ratio, gilbert damping parameter, effective field, and magnetostriction coefficients. By finding the resonance of the sample at various microwave frequencies, a curve of resonant frequency versus applied field is constructed. The slope of the curve is the gyromagnetic ratio, and the Gilbert damping parameter is related to the linewidth of the resonance. The effective field is similiarly found. Furthermore, by stressing the sample mehanically, the magnetostriction coefficients can be determined. The stress is produced mechanically by a vacuum applied to one side of the substrate. The shift in the resonant field can be related to the magnetostriction constants. This method will be used to verify that films are isotropic magnetostrictively.

The lattice mismatch is measured using a double crystal X-ray diffractometer. The X-rays penetrate approximately $4\mu m$ into the garnet, thus going through the film to the substrate. Peaks are observed at the two angles corresponding to the substrate's lattice spacing and the film's lattice spacing. The difference of the angles is measured and used to determine the lattice mismatch, and from the relative intensities of the peaks, the thickness is approximated.

Current Materials Development

Two submicron film compositions have been developed. The first melt produced films of $(Sm_{0.65}Gd_{2.40}Tm_{1.0}Y_{0.8}Lu_{0.27}Fe_{4.8}Ga_{0.2})$. A typical film (AA02) had an l value of $0.056\mu m$ for a bubble diameter of $0.504\mu m$. Difficulties of being unable to produce large enough perpendicular fields prevented the measurement of $4\pi Ms$; however, a larger magnet has been purchased to solve this problem.

A second melt producing films of $(Sm_{1.2}Lu_{1.7}Tm_{0.1}(FeGa)_5O_{12})$ was developed for sub-micron bubbles. Data from films typical of the melt, AC21, AC22, AC32 are shown in Table 2. This melt required significant alterations including an addition of gallium and iron to adjust the strip width (l) from $0.08\mu m$ to $0.06\mu m$. The films were grown with a super cooling of $20^{\circ}C$ and a T_{sat} of $880^{\circ}C$. Again difficulties arose in measuring the collapse field, although we found that it was above 775 Oe resulting in $4\pi Ms$ exceeding 1.2KG. These films have been shown to successfully demonstrate propagation of $0.5\mu m$ bubbles in $2\mu m$ period contiguous disk devices.

Present work is centered on developing a bubble material with isotropic magnetostriction suitable for ion-implanted contiguous disk (CD) devices . For CD devices the magnetostriction coefficients must be negative, and as large as possible. Most rare-earth ions have λ_{111} less than λ_{100}, so that a balancing ion with λ_{111} greater than λ_{100} must be used. Two such balancing ions are being investigated for use; dysprosium, with $\lambda_{111} = -5.90$ and $\lambda_{100} = -12.60$, and bismuth with $\lambda_{111} = +15.5$ and $\lambda_{100} = +8.20$. Thus dysprosium may be used without making the coefficients positive; however, dysprosium has a damping that is about forty times greater than the standard rare-earths. By using both dysprosium and bismuth together in a film, we will be able to satisfy the isotropic magnetostriction requirements and have

large negative magnetostrictive coefficients <u>and</u> maintain a reasonable damping. Table 3 lists the film elements and properties for easy comparison. Two sets of films have been grown from two different flux based melts: the first melt was a dysprosium doped standard $PbO-B_2O_3$ flux melt and the second melt was a bismuth $PbO-Bi_2O_3$ flux melt.

The Dysprosium film composition was to be $(Sm_{0.3}Dy_{1.6}Gd_{0.4}Lu_{0.7}(FeGa)_5O_{12})$ which would have magnetostriction coefficients of -2.8×10^{-6} and a mismatch of less that 0.005 A. Films were grown from this melt and the lattice was adjusted. The first films were grown with a -0.11A mismatch; this was reduced to a +0.012A mismatch by varying the growth temperature. This method of lattice correction succeeded due to the temperature dependence of the segregation coefficients, which control how much of a given element will be incorporated into the film from the melt. It is believed that reducing the temperature increased the amounts of samarium and dysprosium deposited into the film. No magnetic properties of the films were measurable. The reason for this is uncertain; however chemical analysis should enable us to discover the problem.

The second isotropic magnetostrictive melt was based on the bismuth system. The incorportation of bismuth into the film has several advantages including an increase of optical contrast due to an increase of the Faraday rotation, a secondary source of anisotropy, and a correction of magnetostriction. Due to bismuth's positive magnetostriction coefficients, $(\lambda_{111} = +15.50$ and $\lambda_{100} = +8.20)$, bismuth is used in small quantities as a correction to the magnetostricton. The greatest difficulty with using bismuth is that a new flux system must be developed employing $PbO-Bi_2O_3$ instead of $PbO-B_2O_3$. We have previously had little experience and no success with this system.

We have designed a melt and grown films of a bismuth doped nature $(Y_{0.8}Sm_{0.3}Lu_{1.5}Bi_{0.4}(FeGa_5)O_{12})$. The first films grown were unsuitable for any measurements due to severe cracking. The cracking occurs when the film's lattice is greatly different ($a_s-a_f > 0.05A$) from the substrate's lattice spacing. Successive additions of 15% Lu; a smaller ion than the other rare-earths, resulted in films with a lattice mismatch less than 0.02A. As with the dysprosium films, no magnetic measurements were possible with these films. We are now working to understand the reasons for these initial difficulties. We believe that gallium incorporation into the octahedral sites may be reducing $4\pi M_s$ to a small value. We expect to solve this problem in the near future.

Another difficulty with the bismuth films is the non-uniformity of the surface. This is due to the flux adhering to the film while being being withdrawn from the melt letting the film continue to grow until the flux drops solidify. These flux drops result in a thicker film where the flux drops remain after withdrawl. Solving this problem was accomplished by adding Vanadium to the melt so that the surface tension of the melt was increased while the melt viscosity was decreased.

Standard bubble materials for bubble logic devices and micro-wave use have also been grown. The bubble logic materials are standard $2\mu m$ bubble diameter films. Several $2\mu m$ bubble systems have been developed in the past by Charles Krafft. The microwave material was developed for research of microwave generated ring domains. The required material was of composition $(Y_{3-x}La_xFe_{5-y}Ga_yO_{12})$ where x is approximately 0.2 and y approximately 1.2. These films had an extremely small magnetization of less than 250 Oe. This resulted in a small Faraday rotation and poor optical contrast due to the relation between $4\pi Ms$ and Faraday rotation. Typical film properties are listed in Table 2.

Conclusion

The development of CAFE for modeling film compositions is very successful and has enabled a greater variety of compositions to be studied. Agreement with published results is good for the standard garnet constituents. Development of sub-micron materials is proceeding well and films have been used for ion-implanted contiguous disk devices. Film designs with isotropic magnetostriction have been created by CAFE and work has begun to develop relevent melt/flux systems. We have had limited success with bismuth based films and dysprosium doped films. A working isotropic magnetostrictive melt should be developed in the near future.
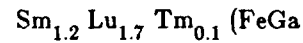
Tables

Table 1: Comparison of CAFE Results to Published Experimental Data

| Film composition	CAFE Results				Published Data				Source
	Lattice	λ_{111}	λ_{100}	K_g	Lattice	λ_{111}	λ_{100}	K_g	
$Sm_{1.2}Lu_{1.8}Fe_{5.0}O_{12}$									
	12.382	-4.84	7.56	30.2	12.38	-	-	30	1
$Eu_{1.0}Tm_{2.0}Fe_{5.0}O_{12}$									
	12.381	-2.9	7.9	12.0	12.38	-	-	12	2
$Eu_{1.0}Tm_{2.0}Fe_{4.4}Ga_{0.6}O_{12}$									
	12.372	-1.97	5.46	7.7	12.38	-	-	7	3
$Sm_{0.2}Tm_{0.2}Y_{1.7}(CaGe)_{0.9}Fe_{4.1}O_{12}$									
	12.379	-1.33	0.41	0.9	12.38	-	-	1.3	4
$Y_{1.2}Lu_{0.5}Sm_{0.4}Ca_{0.9}Fe_{4.1}Ge_{0.9}O_{12}$									
	12.378	-1.46	1.18	2.42	12.383	-1.9	-	2.30	5
$Dy_{0.35}Sm_{0.15}Lu_{1.50}Bi_{0.30}Ca_{0.70}Fe_{4.30}Ge_{0.70}$									
	12.365	-2.3	-0.9	1.20	12.383	-2.3	-0.9	-	6
$Y_{1.0}Lu_{0.7}Sm_{0.5}Ca_{0.8}Fe_{4.2}Ge_{0.8}O_{12}$									
	12.378	-1.8	1.7	3.9	12.383	-2.2	-	3.6	7

[1] Eschenfelder, *Magnetic Bubble Technology*, Springer-Verlag, New York, 1981, p185

[2] Eschenfelder, *Magnetic Bubble Technology*, Springer-Verlag, New York, 1981, p185

[3] Eschenfelder, *Magnetic Bubble Technology*, Springer-Verlag, New York, 1981, p185

[4] Eschenfelder, *Magnetic Bubble Technology*, Springer-Verlag, New York, 1981, p185

[5] S. L. Blank, Wolfe, et al, J. Appl. Phys., 50, 2155, (1979).

[6] H. Makino, O.Okada, and Y. Hidaka, J. Appl. Phys., 55, 2551, (1984).

[7] S. L. Blank, Wolfe, et al, J. Appl. Phys., 50, 2155, (1979).

Table 2: Typical Film Properties

$$Sm_{0.3}\ Gd_{0.4}\ Tm_{0.73}\ Y_{1.57}\ Fe_{4.4}\ Ga_{0.6}\ O_{12}$$

film number	h (μm)	l (μm)	$4\pi Ms$ (G)	Δa (A)	Rate (μm/min)	Temp ($^{\circ}$C)
194	2.00	0.10	765	-.----	0.40	835
205	1.46	0.120	753	-.----	0.42	836
206	1.45	0.099	610	-.----	0.41	838
melt alteration: addition of Gallium						
207	1.98	0.159	586	-.----	0.33	854
208	1.64	0.146	593	-.----	0.33	838

$$Sm_{1.2}\ Lu_{1.7}\ Tm_{0.1}\ (FeGa_{5.0}\ O_{12}\ )$$

film number	h (μm)	l (μm)	$4\pi Ms$ (G)	Δa (A)	Rate (μm/min)	Temp ($^{\circ}$C)
AC03	0.70	0.070	>1275	-.----	0.23	838
melt alteration: addition of Gallium						
AC04	1.53	0.080	—	0.0144	0.26	856
melt alteration: addit.on of Iron						
AC21	1.21	0.064	1230	-.----	0.24	860
AC22	1.29	0.059	1134	0.0155	0.26	868
melt alteration: addition of Lutetium						
AC32	1.20	0.077	---	0.0103	0.30	872
AC41	1.11	0.062	—	-.----	0.37	878

$$Y_{2.8}\ La_{0.2}\ Fe_{3.7}\ Ga_{1.3}\ O_{12}$$
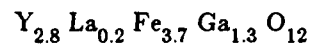
film number	h (μm)	l (μm)	$4\pi Ms$ (G)	Δa (A)	Rate (μm/min)	Temp ($^{\circ}$C)
AD03	1.20	-.---	---	-0.0093	0.20	860
AD41	3.20	0.144	220	-.----	0.32	880

Table 3: Physical Properties of Rare-Earth Elements

Element	$4\pi M_s$	Curie(T)	A_o	λ_{111}	λ_{100}	damping	$K_{ij}(Eu)$	$K_{ij}(Sm)$
Sm	1675	578	12.529	-8.50	20.99	12.00	-.--	-.--
Eu	1172	566	12.497	1.79	20.99	2.09	-.--	-.--
Gd	56	564	12.470	-3.09	0.00	0.52	0.00	0.00
Y	1767	533	12.375	-2.40	-1.40	0.52	1.00	3.30
Lu	1815	549	12.283	-2.40	-1.40	0.52	10.49	14.00
Tm	1397	549	12.322	-5.19	1.40	1.20	6.00	10.00
Dy	376	563	12.405	-5.89	-12.60	25.99	0.00	0.00
Bi	-	-	12.621	15.50	8.20	1.00	0.00	0.00
La	-	-	12.725	-	-	0.00	0.00	0.00
Tb	-	-	12.436	-	-	0.00	0.00	0.00
Yb	-	-	12.302	-	-	0.00	0.00	0.00
Er	-	-	12.346	-	-	0.00	0.00	0.00
Ho	-	-	12.374	-	-	0.00	0.00	0.00

Temperature dependence of anisotropy fields in deuterium implanted garnet films

C. S. Krafft and M. H. Kryder

Carnegie-Mellon University, Pittsburgh, Pennsylvania 15213

The total implantation-induced uniaxial anisotropy field change ΔH_E, and that portion attributed to the magnetostriction ΔH_σ, have been measured in deuterium implanted garnet films from 20 to 180 °C. No saturation in ΔH_E was observed for the highest strain measured, 2.2%. ΔH_E and ΔH_σ were found to decrease nearly linearly with increasing temperature. The ratio $\Delta H_\sigma / \Delta H_E$ was approximately 0.4. In films which were implanted with doses up to 1×10^{16} D_2^+/cm^2, $4\pi M_s(I)$ decreased more than $\lambda_{111}(I)$ relative to their nonimplanted values, although $\lambda_{111}(I)$ decreased faster than $4\pi M_s(I)$. The quantity $\lambda_{111}/M_s(B)$ in the bulk and $\lambda_{111}/M_s(I)$ in the implanted layer had different temperature dependences, which depended on the amount of implant-induced damage.

PACS numbers: 76.50. + g, 61.70.Tm, 75.80. + q, 61.10. − i

INTRODUCTION

Recently investigators have reported that the reduction in the uniaxial anisotropy due to magnetostriction ΔH_σ, does not, by itself, account for the total implantation-induced change in the uniaxial anisotropy field ΔH_E, in magnetic garnet epitaxial films.[1-4] That part of ΔH_E not attributed to ΔH_σ, given here by ΔH_0, is attributed to the suppression of growth-induced anisotropy in neon implanted films,[1] and to chemical effects in hydrogen implanted films.[2,3] The chemical effects are related to large doses of hydrogen ions used to obtain the desired ΔH_E.

Although there has been a great deal of interest recently in both extending the temperature range of operation for bubble memories,[5] and using materials which have isotropic magnetostriction,[6] there have been no reported measurements of the temperature dependence of magnetostriction on ion implanted garnet films. Here, the temperature dependence of the magnetostriction divided by the magnetization in the bulk $\lambda_{111}/M_s(B)$, and in the implanted layer $\lambda_{111}/M_s(I)$, are reported for deuterium implanted films. The change in uniaxial anisotropy field ΔH_E was measured from 20 to 200 °C, and compared to ΔH_σ.

EXPERIMENTAL DETAILS

Investigations were carried out on 1-in.-diam garnet films which were grown by the standard liquid phase epitaxy (LPE) method on ⟨111⟩ oriented GGG substrates,[7] and etched prior to implantation to remove the back film. LPE film compositions are SmTmGdLuAl:YIG for film 2, and SmTmGdAlGa:YIG for films 1 and 3. Film thickness t, characteristic length 1, $4\pi M_s$, $H_E(B)$, and $\lambda_{111}(B)$ are given in Table I. The effective field in the bulk is given by

$$H_E(B) = H_E - 4\pi M_s - (2/3)H_1, \qquad (1)$$

where H_E is the uniaxial anisotropy field, $4\pi M_s$ the magnetization, and H_1 the crystalline anisotropy field. H_1 measured on similar films is approximately − 150 Oe for films 1 and 3, and − 110 Oe for film 2 at 24 °C.[8] $4\pi M_s$ and 1 were determined from bubble collapse field and zero field stripwidth measurements.[9]

Implantation with molecular deuterium D_2^+, was done at current densities less than $0.2 \mu A/cm^2$. Implant doses and energies are given in Table II. Films were annealed at 200 °C after each implant. At 200 °C a 30-min anneal was sufficient to stabilize the implanted film properties. The ferromagnetic resonance (FMR) apparatus consisted of a wideband microwave spectrometer with a shorted microstrip conductor. Details of the serpentine-shaped microstrip conductor and minibox structure with the vacuum attachment used to stress the wafer were previously reported.[10] The wafer temperature could be varied from 0 to 200 °C and held to ± 1 °C.

$H_E(B)$, $H_E(I)$ and the gyromagnetic ratio in the bulk $\gamma(B)$ and implanted $\gamma(I)$ layer were determined from the frequency dependence of perpendicular resonance. The change in uniaxial anisotropy field is given by

$$\Delta H_E = H_E(B) - H_E(I).$$

Since the implanted films had several resonance modes associated with the surface layer, the highest field resonance was used to determine $H_E(I)$. On multiply implanted samples, uniformity of the magnetic profile through the film thickness was judged by amplitude and spacing of the surface modes. On a uniformly implanted film, there was a large resonance mode at the highest field, with progressively decreasing mode amplitudes with decreasing field. No attempt was made to obtain the anisotropy profile through the film thickness.[11] Likewise, there was a simplified analysis performed on the x-ray rocking curve to judge the uniformity of the strain profile.[12] A single implanted layer peak in the rocking curve was assumed to represent a uniformly strained

TABLE I. Garnet film parameters.

Sample	Thickness (μm)	1 (μm)	$4\pi M_s$ 4(G)	$H_E(B)$ (Oe)	$\lambda_{111}(B)$ ($\times 10^{-6}$)
1	0.94	0.14	990	1273	− 2.0
2	0.70	0.06	1292	810	− 2.5
3	0.85	0.11	774	960	− 2.6

Film	Implant	Dose ($\times 10^{16}$ D_2^+/cm^2)	Energy (keV)
1:	1	0.8	48
	2	1.25	55
		0.3	25
2:	1	3	88
	2	1.25	55
		0.3	25
3:	1	0.5	44
	2	0.5	55
		0.5	25
	3	0.5	50

implanted layer. The uniformity of the multiple implanted films is not expected to cause significant differences in the implanted film properties $H_E(I)$ and the maximum implant strain ϵ_{max}, even though the particular implant doses, especially on film 3, were not optimized.

The magnetostrictive field is given by

$$\Delta H_\sigma = 3\sigma\lambda_{111}/M_s, \qquad (2)$$

where the stress σ, which is calculated from the strain as determined from double crystal x-ray diffraction, is given by

$$\sigma = \delta\theta /\tan\theta \times E /(1 + \nu), \qquad (3)$$

where $\delta\theta$ is the maximum angular spread of the x-ray diffraction rocking curve, θ the Bragg angle, E Young's modulus (2.08×10^{12} dyn/cm^2 at 25 °C), and ν Poisson's ratio (0.29). The quantities $\lambda_{111}/M_s(B)$ and $\lambda_{111}/M_s(I)$ were determined from the vacuum stress-induced shift in the resonant field δH_{111} of the bulk and highest field surface mode[10,13] where

$$\lambda_{111}/\dot{M}_s = (2/3)\delta H_{111}/\sigma_v. \qquad (4)$$

To account for variation of the stress over the serpentine microstrip pattern, the average vacuum-induced stress σ_v was determined from measurements on an LPE YIG film. Using published values of λ_{111} and $4\pi M$, for YIG,[14] σ_v was calculated from Eq. (4), and found to be 85% of the stress at the center of the wafer,[15] from 20 to 160 °C. The deflection at the center of a GGG substrate was found to increase linearly with temperature from 33 μm at 25 °C to 42 μm at 175 °C. This increase is apparently due to a decrease in the elastic constants. To account for this change in elastic constants in the calculation of $\Delta H\sigma$, we assumed that the implant induced stress decreases in proportion to the variation in wafer deflection as the temperature is changed.
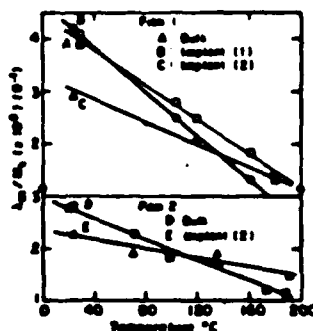
FIG. 1. Temperature dependence of implantation-induced uniaxial anisotropy field change ΔH_E, stress-magnetostrictive field ΔH_σ, and effective anisotropy field in the bulk layer $H_E(B)$ for film 1. Annealed at 200 °C for 2 h.
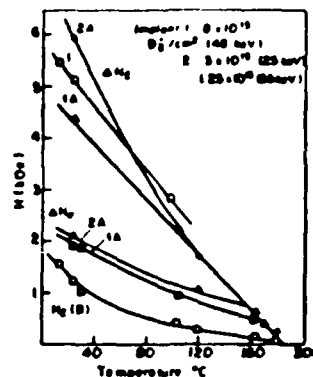
FIG. 2. Temperature dependence of λ_{111}/M, in bulk and implanted layers of films 1 and 2

The accuracy of H_E is approximately ± 25 Oe. The error in determining δH_{111} was ± 5 Oe. At a given frequency, from 2 to 7 GHz, δH_{111} was reproducible within 2 Oe. The uncertainty in ΔH_σ is $\pm 10\%$. Error in determining implant strain, calculated from double crystal x-ray rocking curve, is less than 2%.

RESULTS AND DISCUSSION

ΔH_E decreased smoothly and rapidly with increasing temperature on all of the films studied here. A typical result is given in Fig. 1 for film 1. ΔH_E is shown for this film after a single implant (curve 1), after a single implant and anneal (curve 1A), and after an additional double implant and anneal (curve 2A). The first anneal reduced ΔH_E and x-ray analysis shows that the maximum implant-induced strain decreased from 0.98% to 0.90%. The second implant, at 55 and 25 keV, increased ΔH_E at 24 °C, although above 120 °C, ΔH_E was the same for both implants. The Curie temperature in the implanted layer was estimated to be 180 °C by extrapolating to the temperature where ΔH_E goes to zero.

The temperature dependence of ΔH_σ is also plotted in Fig. 1 for film 1. The curves 1A and 2A represent ΔH_σ after first implant and anneal and after the additional second implant and anneal. Curve 1A indicates that ΔH_σ is only about 40% of ΔH_E. After the second implant, which was designed to increase the maximum strain as well as improve the strain and magnetic uniformity, ΔH_σ remained nearly constant, even though ΔH_E increased, and ϵ_{max} increased to 1.43%. This is attributed to a reduction in $\lambda_{111}/M_s(I)$, which will be discussed later.

The effects of increasing implant dose on $\lambda_{111}/M_s(I)$ were also measured. In Fig. 2, $\lambda_{111}/M_s(B)$ and $\lambda_{111}/M_s(I)$ are plotted as a function of temperature for films 1 and 2. In the implanted layer of all of the films investigated, at doses up to 1×10^{16} D_2^+/cm^2 there was a slight increase in $\lambda_{111}/M_s(I)$ at 24 °C but $\lambda_{111}/M_s(I)$ decreased more rapidly than $\lambda_{111}/M_s(B)$ as temperature was increased. At higher implant doses, $\lambda_{111}/M_s(I)$ became less than $\lambda_{111}/M_s(B)$ even at 24 °C. If we assume that $4\pi M_s$ decreases with deuterium implantation, as it reportedly does in hydrogen implanted films,[3,16] then on film 1, the initial implant reduced $4\pi M_s$ more than λ_{111} but the temperature dependence of $\lambda_{111}(I)$ was higher than that for $4\pi M_s(I)$. After the second implant $\lambda_{111}(I)$ was reduced more than $4\pi M_s(I)$. On film 2, $\lambda_{111}/M_s(I)$ was 75% of $\lambda_{111}/M_s(B)$ at 24 °C, but decreased more slowly with temperature so that it exceeded $\lambda_{111}/M_s(B)$ by 18% at 173 °C.

Thus, the temperature dependence of $\lambda_{111}/M_s(I)$ is dependent on the implantation-induced damage.

In order to compare the relation between ΔH_E, ΔH_σ, and ϵ_{max} a film which received several implants was studied. In Fig. 3, ΔH_E and ΔH_σ are plotted versus ϵ_{max} for film 3. ΔH_σ is given after first and third implants on the as-implanted films by points 1 and 3, and after a 200 °C anneal for all three implants, shown by points 1A, 2A, and 3A. The two data points for ΔH_σ after the second implant were measured after two successive anneals. The second anneal caused additional changes in the film properties, increasing both ΔH_E and ΔH_σ. After annealing heavily implanted films, ΔH_E decreased, but ΔH_σ remained constant or increased slightly, even though the implant strain decreased. This is attributed to an increase in $\lambda_{111}/M_s(I)$ with annealing.

No saturation in ΔH_E was observed here or on any of the other films investigated. ΔH_σ increases with strain, but not as rapidly as ΔH_E. The reduction in $\lambda_{111}/M_s(I)$ at 24 °C is believed to cause the apparent saturation in ΔH_σ. The remainder of ΔH_E is attributed to other mechanisms besides magnetostriction, such as chemical effects or suppression of growth-induced anisotropy.[1,2] It should be noted that since the magnetostriction alone does not account for all of ΔH_E in deuterium implanted films, one can obtain an erroneous value of λ_{111}/M_s if one calculates it from the slope of ΔH_E vs ϵ_{max}, as investigators have done in the past for other ion species.[3,17]

The gyromagnetic ratio in the bulk and implanted layers of film 3 are given in Table III. $\gamma(I)$ was found to decrease after high dose implantations, but was increased after annealing. Measurements made after each of two annealing steps after the second implant indicate that the $\gamma(I)$ is gradually restored by annealing. This increase in $\gamma(I)$ was accompanied by the increase in ΔH_E and ΔH_σ shown by points 2A(1) and 2A(2) in Fig. 3. Measured values of $\gamma(I)$ and $\gamma(B)$ were the same at 180 °C.

CONCLUSION

The total implantation induced uniaxial anisotropy field change ΔH_E was measured and found to decrease nearly linearly with temperature. At low doses $4\pi M_s(I)$ is decreased, so $\lambda_{111}/M_s(I)$ is increased slightly compared to the bulk value, although $\lambda_{111}/M_s(I)$ decreases faster with temperature than $\lambda_{111}/M_s(B)$. As dose was increased, $\lambda_{111}/M_s(I)$ became less than $\lambda_{111}/M_s(B)$, indicating that λ_{111} is decreased more than $4\pi M_s$. Here, the temperature dependence
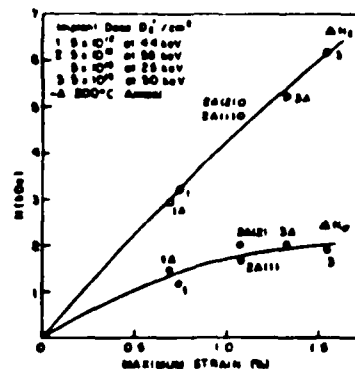
FIG. 3. ΔH_E and ΔH_σ vs maximum implant strain ϵ_{max} for film 3.

of $\lambda_{111}/M_s(I)$ is less than $\lambda_{111}/M_s(B)$. The magnetostrictive field ΔH_σ was found to constitute only 40% of ΔH_E. The remaining 60% must be attributed to mechanisms other than magnetostriction. In heavily implanted films there was a marked reduction in the gyromagnetic ratio and the quantity λ_{111}/M_s. Finally, researchers are cautioned not to use plots of ΔH_E versus maximum implant strain in the determination of λ_{111}/M_s. Nonstress related contributions to ΔH_E are accompanied by changes in strain, but are not caused by magnetostriction.

TABLE III. Gyromagnetic ratio in the bulk $\gamma(B)$ and implanted layer $\gamma(I)$ of film 3.

Implant No.	$\gamma(B)$	$\gamma(I)$
1	1.49×10^7 (sec Oe)$^{-1}$	1.48×10^7 (sec Oe)$^{-1}$
2	1.51	1.04
2A(1)	1.53	1.44
2A(2)	1.52	1.67
2A at 180 °C	1.60	1.60
3A	1.55	1.27
A: 200 °C anneal		

[1]G. P. Vella-Coleiro, R. Wolfe, S. L. Blank, R. Caruso, T. J. Nelson, and V. V. S. Rana, J. Appl. Phys. 52, 2355 (1981).

[2]G. Suran, H . Jouve, and P. Gerard, J. Appl. Phys. 54, 2006 (1983).

[3]V. S. Speriosu and C. H. Wilts, J. Appl. Phys. 54, 3325 (1983).

[4]M. H. Kryder, X. Wang, C. S. Kraft, and A. M. Guzman, J. Magn. Magn. Mater. 35, 307 (1983).

[5]V. V. S. Rana, T. J. Nelson, R. C. LeCraw, and S. L. Blank, J. Appl. Phys. 53, 9093 (1982).

[6]A. Hubert, J. Magn. Magn. Mater. 31-34, 976 (1983).

[7]H. J. Levinstein, R. W. Landorf, S. J. Licht, and S. L. Blank, Appl. Phys. Lett. 19, 486 (1971).

[8]C. S. Kraft, X. Wang, and M. H. Kryder, IEEE Trans. Magn. MAG-18, 1295 (1982).

[9]D. C. Fowlis and J. A. Copeland, AIP Conf. Proc. 5, 240 (1972).

[10]X. Wang, C. S. Kraft, and M. H. Kryder, IEEE Trans. Magn. MAG-18, 1295 (1982).

[11]C. H. Wilts and S. Prasad, IEEE Trans. Magn. MAG-17, 2405 (1981).

[12]V. S. Speriosu, J. Appl. Phys. 52, 6094 (1981).

[13]G. P. Vella-Coleiro, Rev. Sci. Instrum. 50, 1130 (1979).

[14]P. Hansen, J. Appl. Phys. 45, 3638 (1974).

[15]S. Timoshenko and S. Woinowsky-Krieger, Theory of Plates and Shells (McGraw-Hill, New York, 1959).

[16]Y. Satoh, M. Ohashi, T. Miyashita, K. Komenou, J. Appl. Phys. 53, 3740 (1982).

[17]T. J. Nelson, J. E. Ballintine, L. A. Reith, B. J. Roman, S. E. G. Slusky, and R. Wolfe, IEEE Trans. Magn. MAG-18, 1358 (1982).

Annealing Behavior of Deuterium Implanted Garnet Films

C. S. Krafft, M. H. Kryder, and J. O. Artman

Abstract

The total implantation-induced anisotropy field change and the portion of it which is attributable to magnetostriction were measured on deuterium implanted films which were annealed up to 800°C. Results for three films, the first of which was coated with SiO_2 before implantation, the second of which was coated afterwards, and the third of which was left uncoated are compared. On the uncoated film, there is a rapid decrease in the anisotropy field change at low annealing temperatures, which is presumably caused by the desorption of deuterium. Overcoating with SiO_2 prevents desorption up to 450°C. Even after the deuterium desorbs from the garnet as a result of anneals up to 800°C, magnetostrictive effects account for only 1/3 of the total anisotropy field change. By comparison, it was found that more than 2/3 of the anisotropy field change in oxygen implanted films can be attributed to magnetostrictive effects. Finally, the resonance signal from the uncoated film was considerably weaker than that in the film coated before implantation, even though the strain profiles on both films are similar, suggesting that implantation through an overcoat has a beneficial effect on the magnetic properties of the implanted layer.

Introduction

Since a large change in anisotropy is required for submicron contiguous disk bubble devices, hydrogen implantation is of substantial interest since there is a significantly larger change in the anisotropy compared to heavier ions such as neon or oxygen [1]. Although the change in anisotropy produced by implantation with heavier ions is predominantly attributable to magnetostriction, the magnetostrictive effect alone is not adequate to explain the change in anisotropy produced by hydrogen implants [2]. Some researchers have suggested that the non-magnetostrictive change in anisotropy is dependent upon the presence of the implanted hydrogen ions and that a sudden reduction in anisotropy is observed when the hydrogen escapes as a result of annealing at elevated temperatures [3]. It was observed that SiO_2 overcoated films did not suffer a sudden change in anisotropy when thermally annealed at moderate temperatures, and it was suggested that the overcoat inhibited the escape of hydrogen [4]. While deuterium has twice the mass of hydrogen, thus requiring half the implant time to achieve the same damage level, and its observed effects are similar to those of hydrogen, it has not been studied as widely as hydrogen implantation [1, 5].

Previously, we reported that the magnetostrictive portion ΔH_σ was 40% of the total implantation-induced uniaxial anisotropy field change ΔH_E in deuterium implanted films [5]. In this paper, we report on the effects of annealing on both ΔH_E and ΔH_σ for deuterium implanted films. Even after an 800°C anneal, only 1/3 of ΔH_E was attributable to ΔH_σ. By comparison, more than 2/3 of ΔH_E in oxygen implanted films was attributable to ΔH_σ. Comparisons of the FMR spectra on annealed films both with and without SiO_2 coatings, deposited both before and after implantation, were made. In addition to preventing the desorption of deuterium at annealing temperatures up to 450°C, the films with SiO_2 deposited prior to implantation exhibited better magnetic properties than the uncoated films.

Experimental Techniques

Investigations were carried out on 2.54 cm diameter garnet films which were grown by the standard LPE method on $\langle 111 \rangle$ oriented GGG substrates. The back films were removed in a 160°C phosphoric acid etch prior to implantation. Details of the wideband ferromagnetic resonance (FMR) spectrometer and the vacuum attachment used to stress the wafer for the magnetostriction measurement were previously reported [5, 6]. The effective uniaxial anisotropy field H_E is given by

$$H_E = H_K - 4\pi M_s - (2/3)H_1 \qquad (1)$$

where H_K is the uniaxial anisotropy field, $4\pi M_s$ is the magnetization, and H_1 is the cubic crystalline anisotropy field. ΔH_E is determined from $(H_E(B) - H_E(I))$, where (B) and (I) refer to the bulk and implanted layer, respectively. ΔH_σ was calculated from λ_{111}/M_s and implant stress σ using the following relations

$$\Delta H_\sigma = 3\sigma \, \lambda_{111}/M_s(I) \text{ and } \sigma = \epsilon_{max}. E/(1+\nu) \qquad (2)$$

where ϵ_{max} is the maximum perpendicular implant strain, E is the Young modulus and ν is the Poisson ratio. The ϵ_{max} is determined from the angular separation of the LPE film peak and the lowest angle surface peak in the $\langle 888 \rangle$ reflection of the double crystal X-ray diffraction rocking curve. The $\lambda_{111}/M_s(I)$ is determined from the vacuum pressure-induced shift in resonance field of the highest field surface mode in perpendicular resonance [5, 7].

Garnet film parameters including film thickness t, characteristic length l, $4\pi M_s$, H_E, and λ_{111} are given in Table I. The LPE garnet compositions are $(YSmTmGd)_3(FeAl)_5O_{12}$ for films 1 and 2, $(YSmTmGdLu)_3(FeAl)_5O_{12}$ for film 3, and $(YSmTmGd)_3(FeGaAl)_5O_{12}$ for films 4 through 8. The absorption derivative peak-to-peak linewidth at 4.5 GHz was 90 Oe for Film 1, 100 Oe for film 2, and 140 Oe for film 3.

Table I: Material Parameters

Film	t	l	$4\pi M_s$	H_E	λ_{111}
1	1.0 μm	.06 μm	1257 G	534 Oe	-3.0×10^{-6}
2	1.1	.08	950	1060	-2.6
3	1.2	.06	1400	644	-3.5
4	1.1	.11	623	685	+2.1
5	0.9	.10	654	568	-2.3
6	0.8	.10	612	648	-2.6
7	0.9	.11	633	686	-2.1
8	0.8	.10	725	457	--

Deuterium and oxygen implant conditions are given in Table II. The multiple deuterium implants were designed to create a relatively uniform magnetic anisotropy and strain profile through the implanted layer thickness. The maximum current density for deuterium implants was 0.13 μA/cm^2, with no sample cooling. Surface treatments and annealing conditions are listed in Table II. All of the SiO_2 layers were sputter deposited at 500 W RF power. The films were annealed simultaneously in air. The deuterium implant depth is approximately 0.48 μm, based on the projected range, 0.39 μm, and the standard deviation, 0.09 μm for molecular deuterium ions (mass 4) at 88 keV [8, 9]. The SiO_2 layer decreases the implant depth by approximately 0.02 μm.

Table II: Implant Conditions and Sample Treatment

Deuterium $(\times 10^{14})$ D_2^+/cm^2 in films 1, 2, 3

Dose	Dose	Dose
12 @ 80 keV	5 @ 50 keV	3 @ 25 keV

Film	Oxygen $(\times 10^{14})$ O^+/cm^2
4	1.2 @ 135 keV
5	1.2 @ 110
6	2.4 @ 110
7	3.6 @ 110
8	4.8 @ 110

Film	Sample Treatment
1	500 Å SiO_2, Before Implant
2	500 Å SiO_2, After Implant
3	Uncoated

Annealing Conditions for Films 1, 2, and 3

206°C	90 (min)	640°C	40 (min)
254	80	700	50
335	30	670	120
450	60	800	70 (1&3 only)
560	30	800	120
560	50		

Experimental Results

In Fig. 1 ΔH_E and ΔH_σ for films 1, 2, and 3 are plotted versus ϵ_{max}, where ϵ_{max} is the maximum implant-induced strain after annealing. The annealing temperatures are listed next to selected data points. On all three films, ΔH_E and ΔH_σ decrease nearly linearly with decreasing strain, except in film 3 between 1.5% and 1.3% strain, where both ΔH_E and ΔH_σ increase. The zero-strain intercept of ΔH_E for film 3 is approximately 800 Oe, and the zero-strain intercepts for films 1 and 2 are also positive, if linear fits through the data points over the entire measurement range are assumed.
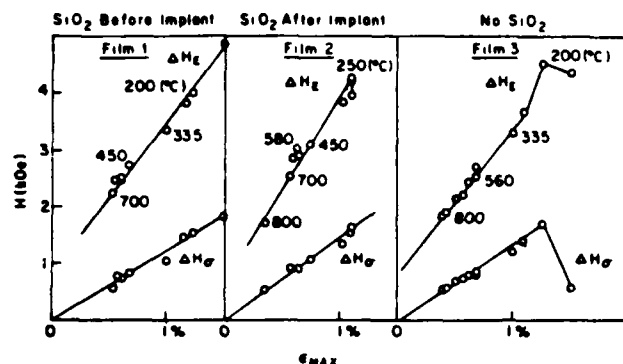
Figure 1: Implant-Induced Change in Uniaxial Anisotropy Field ΔH_k and Magnetostrictive Field ΔH_σ Versus Strain ϵ_{max}

The FMR spectra measured after selected anneals were analyzed, using the spin wave program developed by Wilts and Prasad [10], to determine the depth profiles of the anisotropy field. The H_k profiles in film 1, after 250°C and 700°C anneals, are plotted in Fig. 2. The film parameters used in the two fits and listed in Table III include H_k, $4\pi M$, exchange energy A, H_i, damping parameter c, and the gyromagnetic ratio γ. The calculated and experimental spectra for both of the profiles shown in Fig. 2 are given in Fig. 3. The locations for coincident modes are given by the boundary between adjacent rectangles. The calculated mode locations are indicated by arrows where the amplitudes are less than 4% of the principal surface (main implanted) mode. These modes are not observed experimentally either because they were too weak to detect, or the applied field was not sufficient to align the magnetization in the region of the maximum anisotropy field change [11].
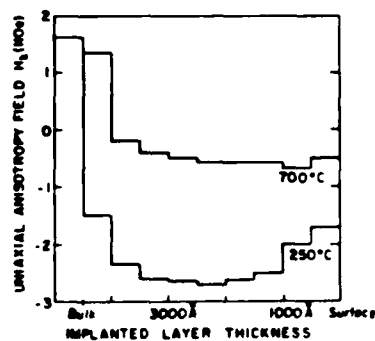
Figure 2. H_k Profile For Film 1
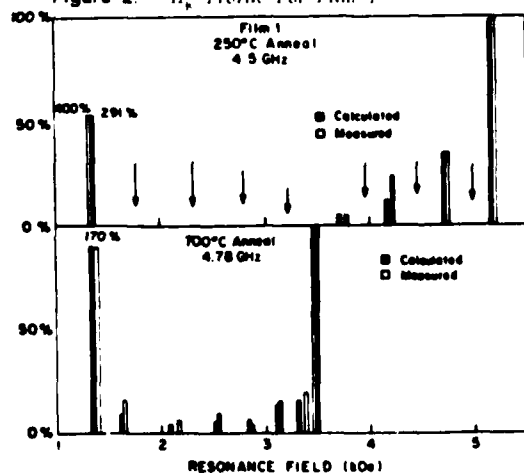
Figure 3: Experimental and Calculated FMR Spectra for film 1 after 250°C and 700°C anneals

Perpendicular FMR spectra after some of the annealing steps are shown in Fig. 4. All of these spectra were measured at 24°C and at 4.5 GHz. The position of the bulk mode and its amplitude relative to the highest field surface mode are indicated in each spectrum.

Table III: Parameters for Film 1 Used in Spin Wave Analysis

Layer	H_k	$4\pi M$	A	H_i	c	γ
250°C Anneal			ergs/cm			(Oe-sec)⁻¹
Bulk	1620 Oe	1257 G	3.5×10⁻⁷	-200 Oe	.05	1.58×10⁷
Implant •		900	2.2	-100	.06	1.60
700°C Anneal						
Bulk	1620	1160	3.5	-200	.043	1.55
Implant •		1100	3.4	-200	.04	1.54
• Profiled through thickness						

Absence of the SiO_2 overcoat led to a significant degradation of the magnetic properties in the implanted layer, as determined by increased linewidths and decreased amplitudes of the surface modes relative to the bulk modes, and a decreased gyromagnetic ratio. In the as-implanted state, films 1 and 3 have a similar sequence of FMR mode amplitudes, as shown in Fig. 4. However the gyromagnetic ratio in the implanted layer of film 3 was 70% of that in the bulk. Furthermore, the main implanted mode linewidth in film 3 was twice the bulk linewidth, compared to 1.4 times the bulk in film 1. The bulk mode amplitude in film 3 was 20 times the main surface mode, whereas in film 1 the bulk mode was 12 times the main surface mode, even though film 3 was slightly thinner. Evaluating the relative change in $4\pi M$ from the area under the absorption resonance curve, we find that $4\pi M$ in films 1 and 3 is reduced by a comparable amount. The X-ray rocking curves for films 1 and 3 were nearly identical, indicating that the strain profiles were similar as they should have been since they were implanted at the same time.

The degradation of the magnetic properties on the uncoated films was only observed in films which received moderately high implant doses. The FMR spectra for coated and uncoated films which received a combined implant dose of 8×10^{15} D_2^+/cm^2 at 60 keV and 4×10^{15} D_2^+/cm^2 at 25 keV, were virtually identical.
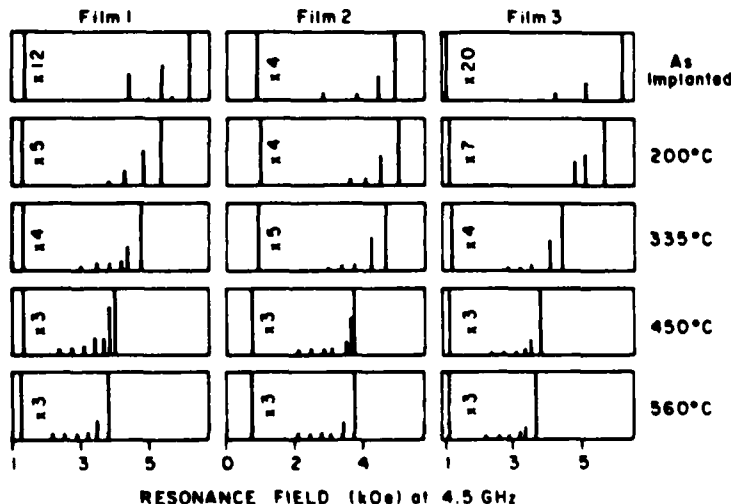
Figure 4: Perpendicular FMR Spectra for Different Annealings

The results from film 2 indicate that the SiO_2 deposition after implantation caused annealing effects which were similar, but not identical, to a 250°C anneal on films 1 and 3. Before annealing, the surface mode linewidth was 1.4 times the bulk in film 2, compared to 1.1 times the bulk in films 1 and 3 after a 250°C anneal, and the implant strain was 1.1% in film 2, which is nearly equivalent to that in films 1 and 3 after a 250°C anneal.

The implant-induced change in uniaxial anisotropy energy density $\Delta K = (\Delta H_k \times M/2)$ is plotted versus the maximum implant strain for the oxygen implanted films in Fig. 5. The numbers next to the ΔK data points refer to the films listed in Table 1. Also plotted are the values of the magnetostrictive energy density $\Delta K_\sigma = (\Delta H_\sigma \times M/2)$. The energy density rather than the anisotropy field change is plotted in Fig. 5, as the films had slightly different $4\pi M$ values.
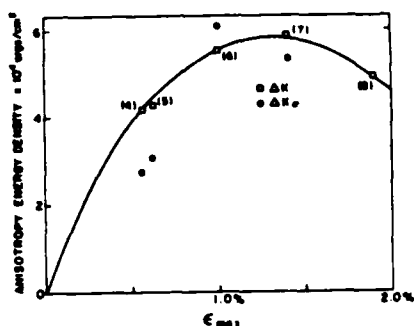
Figure 5: Anisotropy Energy Change Versus Implant Strain ϵ_{max} for Oxygen Implanted Films

Discussion

It has been found that in deuterium implanted films, approximately 2/3 of the change in anisotropy is caused by non-magnetostrictive effects. As shown in Fig. 1, ΔH_σ is only 1/3 of ΔH_E on deuterium implanted films, even after annealing at 800°C. Furthermore, the positive ΔH_E intercept at zero strain in Fig. 1 provides evidence that non-magnetostrictive mechanisms are operative, even after high temperature annealing. Previous investigators have observed the same behavior on neon implanted samples which were annealed to high temperatures [12]. They attributed the positive intercept to the suppression of the growth-induced anisotropy. This effect has not been observed on hydrogen implanted films, presumably because the hydrogen does not do as much damage to the lattice. Here, the positive intercept may be due to the suppression of the growth-induced anisotropy or to some other mechanism.

The anisotropy profiles for film 1 in Fig. 2 indicate that the region with the maximum anisotropy field change shifts towards the surface as a result of high temperature annealing. The accuracy of H_k at any given depth is approximately ±150 Oe for the 250°C fit and ±50 Oe for the 700°C fit. Furthermore, certain characteristics of the H_k profile, including the location of the peak in ΔH_k, and the ratio of the peak ΔH_k to that at the film surface, were required to obtain the fit. Although $4\pi M_s$ and A were not profiled, it was necessary to decrease both A and $4\pi M_s$ as indicated in Table III, to obtain the fit for the 250°C spectra. While A and $4\pi M_s$ were not determined independently, the mode spacing is proportional to $A/(M_s t^2)$, where t is the implant thickness. Thus relative values of these parameters are determined by the fit to the experimental spectra.

Evidence for the desorption of deuterium from the garnet was obtained by analyzing the FMR spectra on films 1, 2, and 3. Although the anisotropy profiles after every anneal were not determined using the program of Wilts and Prasad [10], certain characteristics of the spectra shown in Fig. 4 allow us to draw conclusions about the anisotropy profiles and the changes produced by annealing. On film 1, there is an alternating strong-weak mode amplitude sequence up to 335°C. Furthermore, the second mode amplitude increased dramatically after a 450°C anneal on films 1 and 2. The alternating strong-weak mode amplitude sequence is typical of films which have a maximum ΔH_k in the interior of the film; whereas the strong second mode amplitude after the 450°C anneal is typical of films in which the maximum ΔH_k is near the surface. Thus we suggest that the profiles in Fig. 2 and the characteristics of the spectra in Fig. 4 indicate that in films 1 and 2, prior to annealing at 335°C, the anisotropy profile shows a peak well within the film. After the 335°C anneal, however, the peak (presumably corresponding to the presence of deuterium) moves towards the film surface. This correlates with reported annealing behavior of hydrogen implanted films, where hydrogen was found to accumulate at the film surface after a 450°C anneal, but was prevented from escaping by the SiO_2 layer [4]. By comparison, on film 3, at 450°C the strong second mode is not observed. Results for film 3 agree with previous studies on hydrogen implanted films, where the desorption is found to occur between 200°C and 250°C [3, 13]; however the proportional change in ΔH_E on the deuterium implanted film is significantly smaller. The spectra for film 2 at higher annealing temperatures are similar to those for film 1 although they are not identical. The differences are believed to be related to the desorption of some of the deuterium during the SiO_2 deposition.

The scatter in the data points in Fig. 1, especially between 450°C and 580°C anneals on film 2, are presumably caused by a shift in the anisotropy profile. Since the highest field resonance mode is a measure of the maximum change in anisotropy field, if this occurs near the surface it will not represent the average in the implanted layer. Furthermore, if the location of the maximum shifts, then the measured ΔH_E may exhibit peculiar, non-linear behavior with respect to strain, such as that indicated by the scatter in the data for film 2 in Fig. 1.

Whereas non-magnetostrictive effects account for a major portion of the anisotropy change in deuterium implanted films, in oxygen implanted films magnetostrictive effects are dominant. As shown in Fig. 5, ΔK_σ accounts for at least 70% of ΔK in the region where ΔK increases with increasing strain. In the high strain region (above 1%) where ΔK saturates, $\Delta K = \Delta K_\sigma$; although, it should be pointed out that films with such high strain may have such severe damage that the maximum ΔK no longer occurs at the location of ϵ_{max}, causing ΔK and ΔK_σ to be poorly defined in that region.

The SiO_2 layer has a beneficial effect on the change in the magnetic properties of the deuterium implanted layer. Comparison of the as-implanted FMR spectra from films 1 and 3 indicates that the increase in the linewidth and the decrease in the surface mode amplitude of film 3 are accompanied by a reduction in the gyromagnetic ratio. The implant strain, ΔK (assuming bulk value for $4\pi M_s$), and the FMR mode amplitude sequence for films 1 and 3 are similar. Thus, while the SiO_2 layer apparently does not alter the strain and anisotropy profiles, it does prevent a degradation of the FMR signal. However after a 250°C anneal the FMR signal in the uncoated film was similar to that in the coated films.

Conclusions

In deuterium implanted garnets, it was found that the deuterium desorbs from the film at temperatures near 250°C. Overcoating with SiO_2 prevents desorption until about 450°C. However, even after the deuterium desorbs, the magnetostrictive anisotropy ΔH_σ, is only 1/3 of the total implantation-induced anisotropy field change ΔH_E. Thus ΔH_σ cannot account for all of ΔH_E, even after annealing at 800°C. By comparison, on oxygen implanted films, ΔH_σ was 70% of ΔH_E over the region where ΔK increases linearly with strain. Finally, a degradation in the FMR signal and the gyromagnetic ratio on the as-implanted uncoated films suggests that SiO_2 has an anomolous, but beneficial effect on the surface properties of the film.

References

1. R. Hirko, and K. Ju, IEEE Trans. Magn. **MAG-16**, 958 (1980).

2. Y. Satoh, M. Ohashi, T. Miyashita, K. Komenou, J. Appl. Phys. **53**, 3740 (1982).

3. H. Makino, Y. Hidaka, H. Matsutera, J. Magn. Magn. Mater. **35**, 311 (1983).

4. Y. Sugita, T. Takeuchi, and N. Ohta, Paper CA-5, Magnetism and Magnetic Materials Conference, Atlanta, 1981.

5. C. S. Krafft, and M. H. Kryder, J. Appl. Phys. **55**, 2557 (1964).

6. X. Wang, C.S. Krafft, and M.H. Kryder, IEEE Trans. Magn. **MAG-18**, 1295 (1982).

7. G.P. Vella-Coleiro, Rev. Sci. Instrum. **50**, 1130 (1979).

8. R. Hirko and T. Gallagher, private communication. Deuterium Range Statistics Calculated from LSS Theory.

9. J.F. Gibbons, W.S. Johnson, and S.W. Mylroie, *Projected Range Statistics in Semiconductors*, (Halstead. New York, 1975) .

10. C.H. Wilts and S. Prasad, IEEE Trans. Magn. **MAG-17**, 2405 (1981).

11. C. H. Wilts, private communication.

12. G.P. Vella-Coleiro, R. Wolfe, S.L. Blank, R. Caruso, T.J. Nelson, and V.V.S. Rana, J. Appl. Phys. **52**, 2355 (1981).

13. G. Suran, H. Jouve, and P. Gerard, J. Appl. Phys. **54**, 2006 (1983).

AMORPHIZATION OF GARNET BY ION IMPLANTATION*

A. M. GUZMAN, T. YOSHIIE**, C. L. BAUER and M. H. KRYDER,
Carnegie-Mellon University, Pittsburgh, PA 15213, USA.

ABSTRACT

Amorphization by ion implantation has been investigated in films of $(SmYGdTm)_3Ga_{0.4}Fe_{4.6}O_{12}$ garnet by transmission electron microscopy, incorporating a special cross-sectioning technique. These films were produced by liquid phase epitaxy on (111) garnet substrates and subsequently implanted with ions of deuterium at 60 keV and doses ranging from 0.50 to 4.5×10^{16} D_2^+/cm^2 and ions of oxygen at 110 keV and doses ranging from 0.95 to 8.6×10^{14} O^+/cm^2. The amorphization process proceeds in separate stages involving the formation of isolated amorphous regions, merging of these regions into a continuous band and subsequent propagation of the amorphous band toward the implanted surface. Details of these processes are interpreted in terms of various atomic displacement mechanisms.

INTRODUCTION

Ion implantation in magnetic garnet epitaxial thin films is of special interest because of its role in altering the magnetic anisotropy of garnet crystals. The effects of ion implantation have recently been reported in various technical papers [1-3]. From the viewpoint of the garnet crystal structure, the effect of ion implantation is to generate isolated vacancies and interstitials as well as displacements of the garnet ions from their regular lattice sites. As the implantation doses increase, however, the corresponding increase in lattice defects may be sufficient to induce a crystalline to amorphous transformation, thus rendering the implanted layer magnetically inactive since amorphous garnet is believed to be paramagnetic [4].

Komenou et al.[4] have investigated the amorphization of garnet films implanted with neon ions at 100 keV using a double-crystal diffraction technique. Their results indicate that the process evolves in three distinct stages involving the formation and propagation of an amorphous band. More recently, amorphization of garnet by ion implantation with deuterium and oxygen ions has been studied by Yoshiie et al. [5] using transmission electron microscopy (TEM). Their results show that the amorphization process evolves in three slightly different stages involving the initial formation of isolated amorphous particles at low implantation dose and the subsequent merging of these particles into an amorphous band at higher doses.

We report on the investigation of the amorphization process of thin film garnets implanted with deuterium and oxygen ions by TEM, incorporating a special cross-sectioning technique. Direct observations of the structural changes and phase morphology are presented and discussed.

EXPERIMENTAL TECHNIQUES

Magnetic garnet films of $(SmYGdTm)_3Ga_{0.4}Fe_{4.6}O_{12}$, ranging from 0.6 to 1.1 μm in thickness, were grown by liquid phase epitaxy (LPE) on (111) oriented $Gd_3Ga_5O_{12}$ (GGG) substrates. These films were subsequently uniformly implanted at room temperature with deuterium ions at 60 keV and doses ranging from 0.5 to 4.5×10^{16} D_2^+/cm^2 and oxygen ions at 110 keV and doses ranging from 0.95 to 8.6×10^{14} O^+/cm^2. The ion beam was aimed at an angle about 7° off the normal to the implanted surface to avoid channeling effects. The choice of deuterium and oxygen as implant species in our investigation has been discussed elsewhere (3). Specimens were extracted from the implanted samples for examination by TEM in the direction parallel and perpendicular to the garnet film surface. Thin foils were made by thinning the specimens by mechanical grinding to approximately 50 μm followed by ion milling with a collimated beam of argon ions accelerated by 6 kV. The thinned regions were then examined in a JEOL JEM 120CX electron microscope.

RESULTS

The experimental results are presented in a series of photomicrographs depicting bright-field images parallel (in the (111) plane) and perpendicular (in the (110) plane) to the implanted surface, the corresponding electron diffraction patterns and selected dark-field images. The perpendicular bright-field images contain information related to the implantation profiles and the LPE/GGG interface, as well as morphological features of the implanted area. The electron diffraction patterns reveal details of changes in the crystalline structure resulting from an increased implantation dose.

Figure 1 shows typical results for a specimen implanted with 0.5×10^{16} D_2^+/cm^2 and then 0.95×10^{14} O^+/cm^2. The diffraction pattern of Fig. 1(b) verifies that the implanted
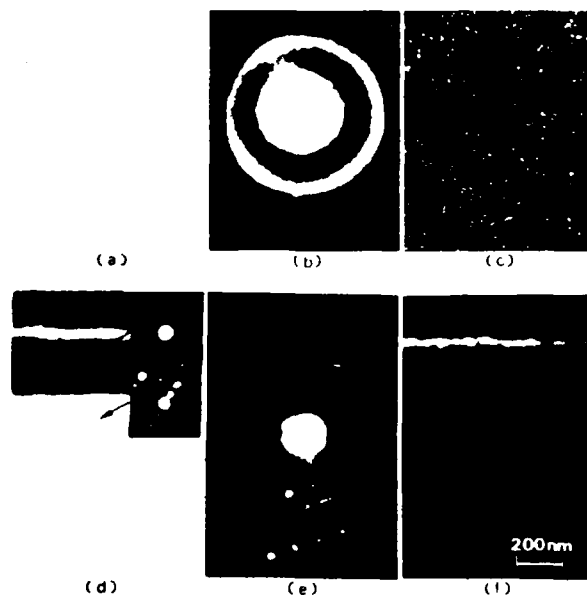
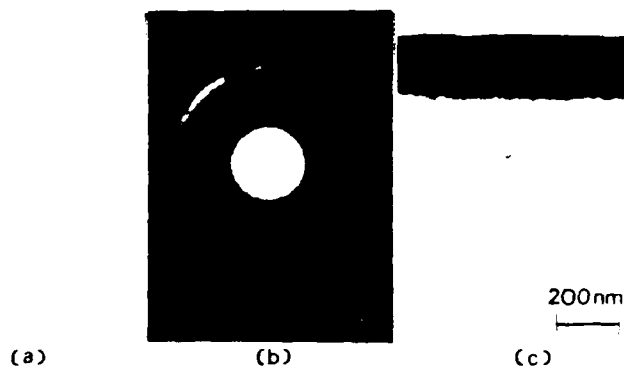**Implanted Surface**

(a)　　　　(b)　　　　(c)

LPE
GGG
200 nm
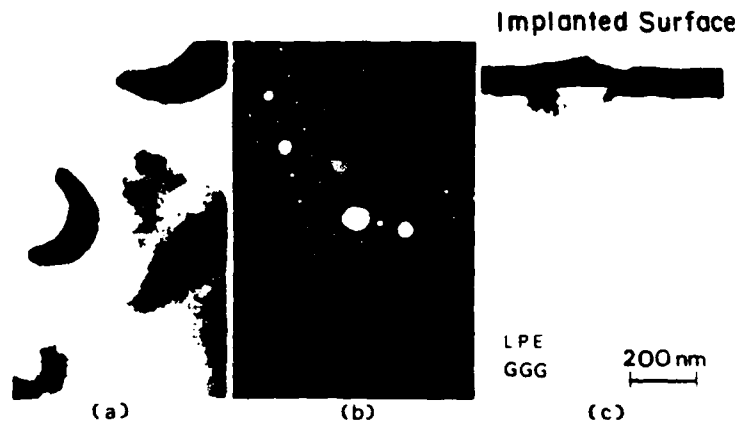
Fig. 1. Bright-field image parallel to the implanted surface (a), (b) corresponding electron diffraction pattern, and (c) bright-field image perpendicular to the implanted surface following implantation with 0.50×10^{16} D_2^+/cm^2 and then 0.95×10^{14} O^+/cm^2.

area is entirely monocrystalline with no evidence of observable lattice defects. In addition to the LPE/GGG interface visible in the cross-sectional view in Fig. 1(c), a faint band at approximately 450 nm below the implanted surface is also visible. This band corresponds to the deuterium implantation depth profile. The oxygen implantation profile, estimated to extend about 150 nm below the surface, is too faint to be easily detected.

Results for a specimen implanted with 1.5×10^{16} D_2^+/cm^2 and then 2.85×10^{14} O^+/cm^2 are shown in Figure 2. The slight graininess visible in Fig. 2(a), and the appearance of halo rings in the corresponding electron diffraction pattern in Fig. 2(b) suggest the formation of localized amorphous regions in the monocrystalline matrix. Moreover, the cross-sectional view shown in Fig. 2(c) and the inserted micro-microdiffraction patterns clearly indicate this morphology, whereas a mixture of amorphous particles, about 10 nm in diameter, in a crystalline matrix is observed in the deuterium plus oxygen implanted region extending about 150 nm below the implanted surface. The diffraction pattern of the deuterium implanted region also shows that this region is fully monocrystalline. These micro-microdiffraction patterns, each originating from an area less than 10 nm in diameter, clearly reveal the presence of amorphous particles rather than randomly oriented crystallites.

(a)   (b)   (c)
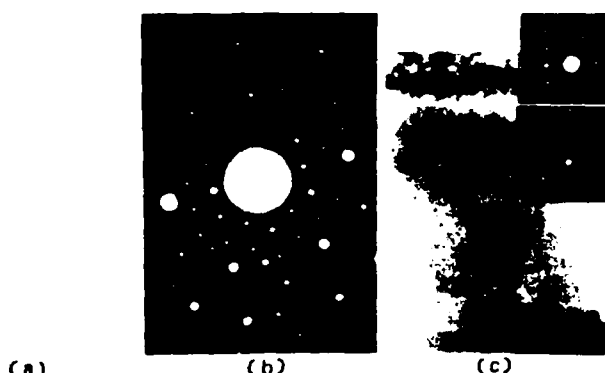
Fig. 2. Bright-field image parallel to the implanted surface (a), (b) corresponding electron diffraction pattern, and (c) bright-field image perpendicular to the implanted surface (with inserted micro-microdiffraction patterns) following implantation with 1.5×10^{16} D_2^+/cm^2 and then 2.9×10^{14} O^+/cm^2.

Figure 3 shows typical results for a specimen implanted with 3.0×10^{16} D_2^+/cm^2 and 5.7×10^{14} O^+/cm^2. Figures 3 (a), (b) and (c) indicate that although the implanted layer is predominantly amorphous, numerous crystallites are present. This is particularly evident in Fig. 3(b) where a fine Debye ring is superposed on a more diffuse halo ring. Moreover, the dark-field image produced from part of the Debye ring, picture in Fig. 3(c), verifies the existance of small crystallites. The cross-sectional view depicted in Fig. 3(d) and the corresponding micro-microdiffraction patterns reveal that the deuterium plus oxygen implanted region is transformed into an amorphous band, as verified by the sole presence of halo rings. The deuterium

implanted region remains monocrystalline. The corresponding
selected-area diffraction pattern in Fig. 3(e) shows a mixture
of halo rings, sharp monocrystalline diffraction spots and weak
randomly oriented diffraction spots. The halo rings and the
sharp diffraction spots originate from the amorphous and
monocrystalline regions. The randomly oriented diffraction spots
are produced by crystallites at the implanted surface as it is
revealed by the dark field image obtained from one of such spots
in Fig. 3(f).

(a)   (b)   (c)

(d)   (e)   (f)

200nm

Fig. 3. Bright-field image parallel to the implanted surface
(a), (b) corresponding electron diffraction pattern and (c)
dark-field image, (d) bright-field image perpendicular to the
implanted surface (with inserted micro-microdiffraction
patterns) and (e) electron diffraction pattern and (f) dark-
field image following implantation with 3.0×10^{16} D_2^+/cm^2 and then
5.7×10^{14} O^+/cm^2.

Figure 4 shows typical results for a specimen implanted
with 4.5×10^{16} D_2^+/cm^2 and 8.6×10^{14} O^+/cm^2. At this implantation
dose all features have disappeared from the bright-field image
and the corresponding electron diffraction pattern of the
deuterium plus oxygen implanted region shows only halo rings
(Fig. 4a and b respectively), thus indicative of a totally
amorphous state. Fig. 4(c) depicts the amorphous D_2^+ plus O^+, and
the crystalline D_2^+ implanted regions.

| | | 200 nm |
| (a) | (b) | (c) |

Fig. 4. Bright-field image parallel to the implanted surface (a), (b) corresponding electron diffraction pattern, and (c) bright-field image perpendicular to the implanted surface following implantation with 4.5×10^{16} D_2^+/cm^2 and then 8.6×10^{14} O^+/cm^2.

DISCUSSION OF RESULTS

The combination of bright and dark field images and the corresponding electron diffraction patterns have shown the transformation of the implanted garnet from the crystalline to the amorphous state. These experimental results indicate that amorphization is caused by implantation with oxygen, but prior implantation with deuterium may sensitize the lattice by increasing the stress.

Table I. Parameters for deuterium and oxygen ions in garnet.[6]

Ion	Energy (keV)	Proj. range	Std. dev.	Nucl. stopp. (keV/μm)	Elect. stopp. (kev/μm)
Deuterium	60	0.492	0.102	1.09	137.1
Oxygen	110	0.136	0.081	194.4	440.1

During ion implantation the incident ions collide with the target garnet ions establishing cascades of recoil atoms. The resulting strain and damage are directly related to the energy deposited in the garnet lattice through nuclear collisions. Table I shows the values for mean projected range, projected standard deviation, and nuclear and electronic energy loss for deuterium at 60 keV and oxygen at 110 keV in garnet [6]. Implanted molecular deuterium ions, with mass 4, predominantly lose energy by electronic interactions. Their effect is to increase the stress in the implanted layer, but their contribution to damage is negligible. Thus, implantation with deuterium at a dose as high as 4.5×10^{16} ions/cm^2 does not result in amorphization. Oxygen ions lose a substantial portion of their energy by nuclear stopping as is indicated by the nuclear energy loss factor in Table I. Their relatively large momentum transfer occurring during atomic collisions results in large cascades. For typical implantation doses and energies used

144

in this work the number of atomic collisions per incident oxygen
ion is several hundred [7]. At an intermediate oxygen dose the
lattice ions are sufficiently displaced by these collisions to
promote amorphization of isolated areas. With increasing
implantation doses, the amorphization propagates toward the free
surface of the garnet until the entire region becomes amorphous.
The last region to be amorphized is the garnet surface not only
because the damage is less at the surface but also because of
stress relaxation.

** Present address: Faculty of Engineering, Hokkaido University,
Sapporo 060, Japan.

REFERENCES

1. R. Wolfe, J. C. North, W. A. Johnson, R. R. Spiwak, L. J.
   Varnerin and R. F. Fischer, AIP Conf. Proceedings 10, 339
   (1973).
2. Y. S. Lin, G. S. Almasi and G. E. Keefe, J. Appl. Phys., 48,
   5201 (1977).
3. A. M. Guzman, C. S. Krafft, X. Wang and M. H. Kryder, Nucl.
   Instr. and Meth., 209/210, 1121 (1983).
4. K. Komenou, I. Hirai, K Asama and M. Sakai, J. Appl. Phys.,
   49, 5816 (1978).
5. T. Yoshiie, C. L. Bauer and M. H. Kryder, Proceedings of 21st
   Intermag Conf., J. IEEE (in press).
6. J. F. Gibbons, W. S. Johnson and S. W. Mylroie, Projected
   Range Statistics, 2nd ed. (Halstead, New York, 1975).
7. H. Matsutera, S. Esho and Y. Hidaka, J. Appl. Phys. 53, 2504
   (1982).

Investigation of amorphization and crystallization processes in ion-implanted garnet by transmission electron microscopy

T. Yoshiie,[a] C. L. Bauer, and M. H. Kryder

Carnegie-Mellon University, Pittsburgh, Pennsylvania 15213

Amorphization produced by ion implantation and subsequent crystallization produced by thermal processing have been investigated in films of $(SmYGdTm)_3Ga_{0.4}Fe_{4.6}O_{12}$ garnet by transmission electron microscopy, incorporating a special cross-sectioning technique. These films were produced by liquid-phase epitaxy on {111} garnet substrates and subsequently implanted with ions of deuterium at 60 keV and doses ranging from 0.50 to 4.5×10^{16} D_2^+/cm^2 and ions of oxygen at 110 keV and doses ranging from 0.95 to 8.6×10^{14} O^+/cm^2. The amorphization process evolves in four separate stages: (1) an implanted (crystalline) band, delineated by the implantion strain profile, forms at doses of about 0.50×10^{16} D_2^+/cm^2/ and 0.95 O^+/cm^2, (2) isolated amorphous regions of about 10 nm in diameter form at doses of about 1.0×10^{16} D_2^+/cm^2 and 1.9×10^{14} O^+/cm^2, (3) the amorphous regions merge to form a continuous band below the implanted surface at doses of about 3.0×10^{16} D_2^+/cm^2 and 5.7×10^{14} O^+/cm^2, and (4) this band expands to the implanted surface at larger doses. Amorphization is caused by implantation with oxygen, but prior implantation with deuterium sensitizes the lattice by increasing the strain. The crystallization process evolves in three separate stages: (1) small crystallites, about 10 nm in size, form throughout the entire amorphous band after annealing for 10 min at 350 °C, (2) larger crystallites nucleate and grow from the implanted surface and amorphous/crystalline interface after annealing for 10 min at 450 °C, and (3) these crystallites grow in size until they merge to form a continuous polycrystalline layer. Some epitaxial regrowth of the monocrystalline into the amorphous region is also observed. Details of these processes are interpreted in terms of atomic displacement mechanisms and compared with corresponding changes of certain magnetic properties.

I. INTRODUCTION

Ion implantation in magnetic garnets produced by liquid-phase epitaxy is of special interest because of its role in defining propagation patterns in bubble memory devices and suppressing hard bubbles.[1,2] The effect of ion implantation is to generate isolated vacancies and interstitials, as well as cascades of displaced atoms, which produce an expansion of the lattice and corresponding changes in magnetic anisotropy; i.e., a rotation of the direction of magnetization from perpendicular to parallel to the implanted surface, assuming a negative magnetostriction effect. As the implantation dose increases, however, the corresponding increase in lattice defects may be sufficient to promote a transformation from the crystalline to amorphous state, thus rendering the implanted layer magnetically inactive, since amorphous garnet is believed to be paramagnetic.[3]

Amorphization of garnet by implantation with ions of neon at 100 keV has been investigated by Komenou et al.[3] using a double-crystal x-ray diffraction technique. Their results indicate that the amorphization process evolves in three separate states: (1) the implanted layer retains its crystalline structure up to doses of about 7×10^{13} Ne^+/cm^2, (2) an amorphous band forms below the implanted surface, thereby isolating a crystalline surface layer of about 12 nm in thickness, at doses of about 2×10^{14} Ne^+/cm^2, and (3) the amorphous band expands to the implanted surface, thereby consuming this crystalline surface layer, at doses of about 1×10^{15} Ne^+/cm^2. More recently, amorphization of garnet

by implantation with ions of deuterium and oxygen has been investigated by Yoshiie et al.[4] using transmission electron microscopy (TEM). Their results indicate that the amorphization process evolves in three slightly different stages: (1) the implanted layer retains its crystalline structure up to doses of about 0.50×10^{16} D_2^+/cm^2 and 0.95×10^{14} O^+/cm^2, (2) isolated amorphous particles appear at doses of about 1.0×10^{16} D_2^+/cm^2 and 1.9×10^{14} O^+/cm^2, and (3) these particles merge into a continuous band at doses of about 3×10^{16} D_2^+/cm^2 and 5.7×16^{14} O^+/cm^2. These results reflect the essence of the amorphization process in garnet by ion implantation.

The purpose of this investigation is to explore the evolution of the amorphization process in greater detail and to extend results to evolution of the crystallization process during subsequent thermal processing by TEM, incorporating a special cross-sectioning technique. In this manner, not only can the structure and phase morphology be characterized at a high degree of resolution, but also the projected ranges of various ion species under a variety of experimental conditions can be determined. The remainder of this article is divided into four sections: First, experimental procedures are outlined in Sec. II; then experimental results are presented and analyzed in Secs. III and IV respectively; lastly, important results stemming from this investigation are summarized in Sec. V.

II. EXPERIMENTAL PROCEDURES

Films of $(SmYGdTm)_3Ga_{0.4}Fe_{4.6}O_{12}$ garnet, ranging from 0.6 to 1.1 μm in thickness, were produced by liquid-phase epitaxy (LPE) on gadolinium-gallium garnet (GGG)

[a] Now associated with the Faculty of Engineering, Hokkaido University, Sapporo 060 Japan.

substrates and subsequently uniformly implanted at ambient temperature with ions of deuterium at 60 keV and doses ranging from 0.50 to 4.5×10^{16} D_2^+/cm^2 and with ions of oxygen at 110 keV and doses ranging from 0.95 to 8.6×10^{14} O$^+$/cm^2. Following implantation, two types of specimen were prepared for examination by TEM: One type, for examination perpendicular to the implanted surface, was prepared by thinning from the back (unimplanted) face by mechanical grinding to approximately 50 μm, followed by further thinning with a Gatan Model 600 ion miller, utilizing a collimated beam of argon ions accelerated by 6 kV. The other type, for examination parallel to the implanted surface, was prepared by bonding two samples with implanted surfaces in contact with one another (face-to-face) by an epoxy resin and subsequent curing under moderate temperature and pressure. Thin slices were then cut perpendicular or parallel to the implanted surfaces by a diamond saw and subsequently thinned by the previously described procedure.[4] The thinned regions, either perpendicular or parallel to the implanted surface, were then examined in a JEOL JEM 120CX electron microscope.

III. EXPERIMENTAL RESULTS

The experimental results may conveniently be divided into two parts involving (1) amorphization by ion implantation and (2) crystallization by annealing. Details associated with each part are presented sequentially in the following sections.

A. Amorphization by Ion Implantation

Typical results for a specimen implanted with 0.50×10^{16} D_2^+/cm^2 and then 0.95×10^{14} O$^+$/cm^2 are presented in Fig. 1, wherein a bright-field image parallel to the implanted surface, i.e., in the {111} plane, and corresponding electron diffraction pattern are pictured in (a) and (b) respectively, and a bright-field image perpendicular to the implanted surface, i.e., in the {110} plane, is pictured in (c). The bend contours in Fig. 1(a) and (especially) the electron diffraction pattern of Fig. 1(b) verify that the LPE layer is entirely monocrystalline with no evidence of lattice defects. In addition to the LPE/GGG interface clearly visible in the cross-sectional (perpendicular) view in Fig. 1(c), a faint band, corresponding to the implantation profile for deuterium and

(a)   (b)   (c)
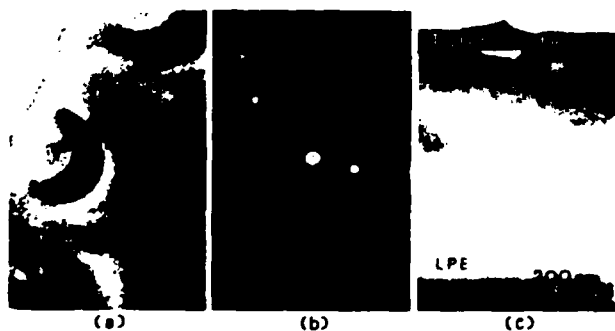
FIG. 1. (a) Bright-field image parallel to the implanted surface, (b) corresponding electron diffraction pattern, and (c) bright-field image perpendicular to the implanted surface following implantation with deuterium at 60 keV and a dose of 0.50×10^{16} D_2^+/cm^2 and then with oxygen at 110 keV and a dose of 0.95×10^{14} O$^+$/cm^2. The implanted surface, deuterium-implanted band, and the LPE/GGG interface are evident in (c).

(a)   (b)   (c)
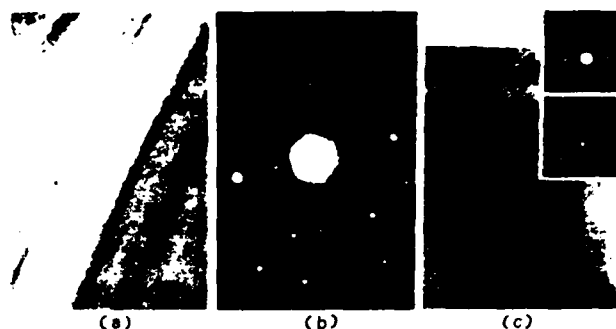
FIG. 2. (a) Bright-field image parallel to the implanted surface, (b) corresponding electron diffraction pattern, and (c) bright-field image perpendicular to the implanted surface (with inserted micro-microdiffraction patterns) following implantation with deuterium at 60 keV and a dose of 1.5×10^{16} D_2^+/cm^2 and then with oxygen at 110 keV and a dose of 2.9×10^{14} O$^+$/cm^2.

terminating at about 450 nm below the implanted surface, is visible. Detection of such bands by TEM has been previously reported by Yoshiie et al.[4] In this case, however, the oxygen profile, estimated to extend about 150 nm below the implanted surface, is too faint to be easily detected.

Typical results for a specimen implanted with 1.5×10^{16} D_2^+/cm^2 and then 2.9×10^{14} O$^+$/cm^2 are presented in Fig. 2, wherein a bright-field image parallel to the implanted surface and corresponding electron diffraction pattern are pictured in (a) and (b), respectively, and a bright-field image perpendicular to the implanted surface is pictured in (c). The slight graininess of Fig. 2(a) and especially the halo rings

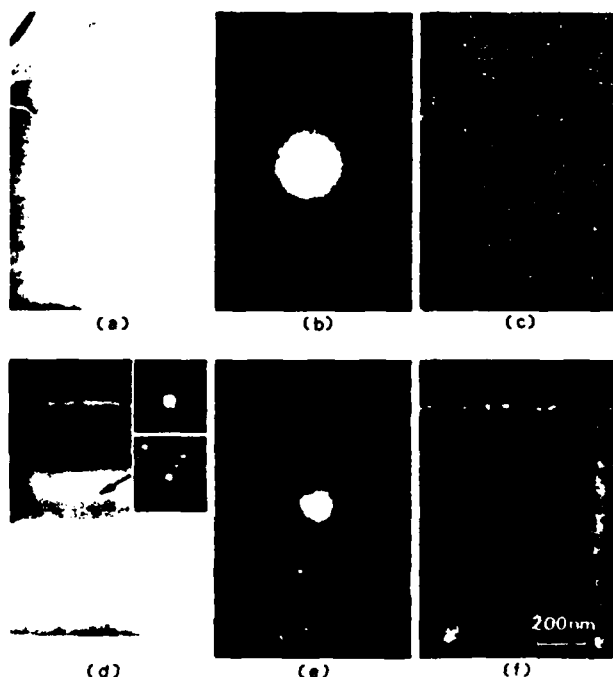(a)   (b)   (c)

(d)   (e)   (f)

FIG. 3. (a) Bright-field image parallel to the implanted surface, (b) corresponding electron diffraction pattern, and (c) dark-field image, (d) bright-field image perpendicular to the implanted surface (with inserted micro-microdiffraction patterns) and corresponding (e) electron diffraction pattern, and (f) dark-field image following implantation with ions of deuterium at 60 keV and a dose of 3.0×10^{16} D_2^+/cm^2 and then with oxygen at 110 keV and a dose of 5.7×10^{14} O$^+$/cm^2.

visible in the corresponding diffraction pattern, obtained from an area less than 100 nm in thickness, suggest that localized amorphous regions have been produced by the implantation process in an otherwise monocrystalline matrix. This morphology is especially clear in Fig. 2(c), wherein a mixture of amorphous particles, about 10 nm in diameter, in a crystalline matrix is observed in the oxygen plus deuterium implanted region, extending about 150 nm below the implanted surface, whereas a fully monocrystalline structure is observed in the deuterium implanted and unimplanted regions, as verified by the corresponding inserted micro-microdiffraction patterns, each originating from an area less than 10 nm diameter. These micro-microdiffraction patterns clearly reveal the existence of amorphous particles (rather than randomly oriented crystallites) in the oxygen plus deuterium implanted region and demonstrate the great utility of the cross-sectioning technique. In this case, however, the deuterium band and LPE/GGG interface, extending about 450 nm and 1 μm below the implanted surface, respectively, are too faint to be easily detected. Further investigation at lower doses indicates that the amorphization process commences slightly below 1.0×10^{16} D_2^+ /cm^2 and 1.9×10^{14} O^+/cm^2.

Typical results for a specimen implanted with 3.0×10^{16} D_2^+ /cm^2 and then 5.7×10^{14} O^+ /cm^2 are presented in Fig. 3, wherein a bright-field image parallel to the implanted surface and corresponding electron diffraction pattern and dark-field image are pictured in (a), (b), and (c), respectively, and a bright-field image perpendicular to the implanted surface and corresponding electron diffraction pattern and dark-field image are pictured in (d), (e), and (f), respectively. Figures 3(a), 3(b), and 3(c) indicate that, although the structure is predominantly amorphous, numerous crystallites are also present, as indicated by the appearance of small crystallites in (a) and especially a superposition of fine Debye rings on more diffuse halo rings in (b). Moreover, the dark-field image produced from part of the Debye ring, picture in Fig. 3(c), verifies the existence of small crystallites. The depth resolution of features pictured in Figs. 3(a), 3(b), and 3(c) are more clearly revealed in the corresponding cross-sectional bright-field, electron diffraction pattern and dark-field images pictured in Figs. 3(d), 3(e), and 3(f), respectively. Figure 3(d) reveals that the oxygen plus deuterium implanted region is transformed into an entirely amorphous band, as verified by the sole presence of halo rings in the inserted micro-microdiffraction pattern, whereas the deuterium-implanted region remains entirely crystalline, as verified by the monocrystalline diffraction pattern in the inserted micro-mcirodiffraction pattern. The LPE/GGG interface is also clearly visible in this figure. The corresponding selected-area diffraction pattern (obtained from an area less than 800 nm in diameter) in Fig. 3(e) displays a mixture of sharp monocrystalline diffraction spots, halo rings, and weak randomly oriented diffraction spots. The sharp diffraction spots and halo rings clearly originate from the monocrystalline and amorphous regions, respectively, whereas origin of the randomly oriented diffraction spots is revealed in the dark-field image, obtained from one such spot, in Fig. 3(f). This figure reveals that these spots are produced by randomly oriented

crystallites at the implanted surface. Therefore, it may be concluded that the amorphization process involves production of small amorphous particles below the implanted surface, a gradual merger to form a continuous band, and subsequent expansion of this band to the implanted surface where the remaining crystalline surface layer decomposes into a number of randomly oriented crystallites.

Typical results for a specimen implanted with 4.5×10^{16} D_2^+ /cm^2 and then 8.6×10^{14} O^+/cm^2 are presented in Fig. 4, wherein a bright-field image parallel to the implanted surface and corresponding electron diffraction pattern are pictured in (a) and (b), respectively, and a bright-field image perpendicular to the implanted surface is pictured in (c). At this dose, all features have disappeared from the bright-field image pictured in Fig. 4(a). Only halo rings, indicating a completely amorphous structure, appear in the corresponding electron diffraction pattern of Fig. 4(b), and the amorphous oxygen plus deuterium implanted band, extending about 200 nm below the implanted surface, and the crystalline deuterium implanted band, extending about 450 nm below the implanted surface, are the only features remaining in the bright-field image pictured in Fig. 4(c). In this case, the width of the amorphous layer has increased by 20 nm ($\sim 10\%$) compared to the layer produced by a dose of 3.0×10^{16} D_2^+ /cm^2 and 5.7×10^{14} O^+ /cm^2.

Experimental results, associated with the amorphization process induced by ion implantation, have been presented in this section. Corresponding results, associated with reversion to the crystalline state, induced by thermal processing, are presented in the following section.

B. Crystallization by annealing

Reversion of the amorphous region, produced by ion implantation, to the original crystalline state was investigated in a specimen implanted with oxygen to a dose of 8.6×10^{14} O^+/cm^2 and then with deuterium to a dose of 4.5×10^{16} D_2^+ /cm^2 as a function of *in situ* annealing. No significant structural changes were observed following annealing for 30 min at 300 °C or less. Annealing for 10 min at 350 °C, however, produces noticeable structural changes, as revealed in Fig. 5, wherein a bright-field image parallel to the
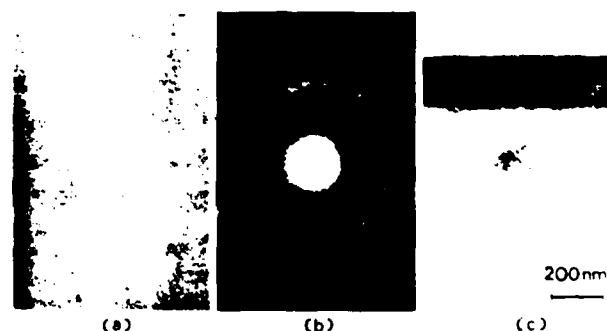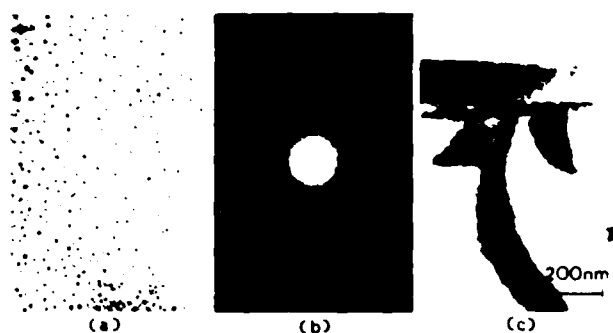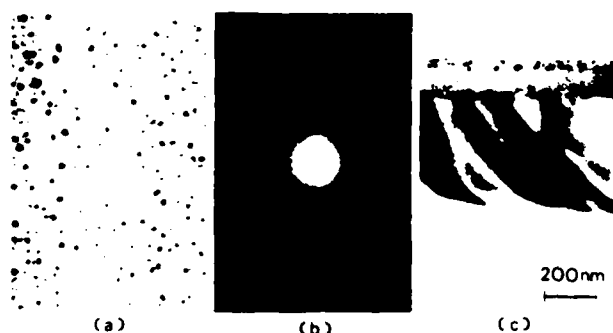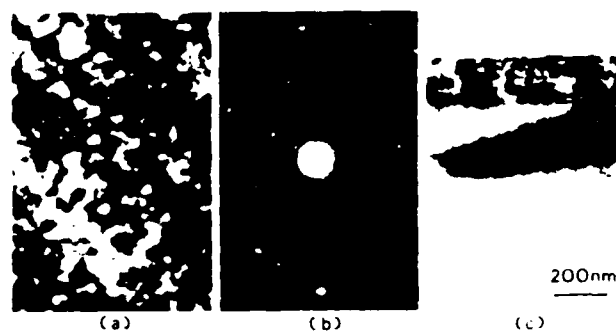

FIG. 4. (a) Bright-field image parallel to the implanted surface, (b) corresponding electron diffraction pattern, and (c) bright-field image perpendicular to the implanted surface following implantation with deuterium at 60 keV and a dose of 4.5×10^{16} D_2^+ /cm^2 and then with oxygen at 110 keV and a dose of 8.6×10^{14} O^+ /cm^2.

FIG. 5. (a) Bright-field image parallel to the implanted surface, (b) corresponding electron diffraction pattern, and (c) bright-field image perpendicular to the implanted surface following implantation with oxygen at 110 keV and a dose of 8.6×10^{14} O$^+$/cm^2 and then with deuterium at 60 keV and a dose of 4.5×10^{16} D$_2^+$/cm^2 and subsequent annealing for (a) 10 min (c) 5 min at 350 °C.

FIG. 7. (a) Bright-field image parallel to the implanted surface, (b) corresponding electron diffraction pattern, and (c) bright-field image perpendicular to the implanted surface following implantation with oxygen at 110 keV and a dose of 8.6×10^{14} O$^+$/cm^2 and then with deuterium at 60 keV and a dose of 4.5×10^{16} D$_2^+$/cm^2 and subsequent annealing for 10 min at 500 °C.

implanted surface and corresponding electron diffraction pattern are pictured in (a) and (b), respectively, and a bright-field image perpendicular to the implanted surface is pictured in (c). Figure 5(a) reveals the presence of small crystallites of about 10 nm in diameter (dark particles), Fig. 5(b) also reveals the presence of small crystallites through appearance of very fine Debye rings superposed on the halo rings, and Fig. 5(c) reveals the location of these particles at the amorphous/crystalline interface. Some of these crystallites may nucleate heterogeneously at the amorphous/crystalline interface, but the majority nucleate homogeneously in the bulk of the amorphous layer, as verified by the increasing particle density from top to bottom of Fig. 5(a), corresponding to increasing specimen thickness (due to non-uniform ion milling) from top to bottom.

Crystal growth was observed following annealing for 10 min at 450 °C, as demonstrated in Fig. 6, wherein a bright-field image parallel to the implanted surface and corresponding electron diffraction pattern are pictured in (a) and (b), respectively, and a bright-field image perpendicular to the implanted surface is pictured in (c). Figure 6(a) reveals slight growth of the crystallites (with some epitaxy) as well as appearance of smaller crystallites, to a diameter of about 20 nm, Fig. 6(b) reveals individual diffraction spots associated

with these crystallites, and Fig. 6(c) reveals that these crystallites have nucleated at both the (external) implanted surface and the amorphous/crystalline interface.

The crystallization process is nearly completed following annealing for 10 min at 500 °C, as revealed in Fig. 7, wherein a bright-field image parallel to the implanted surface and corresponding electron diffraction pattern are pictured in (a) and (b), respectively, and a bright-field image perpendicular to the implanted surface is pictured in (c). Figure 7(a) reveals a polycrystalline structure, Fig. 7(b) reveals grainy Debye rings, produced by the polycrystalline structure superposed on the monocrystalline diffraction pattern of garnet, and Fig. 7(c) reveals that the polycrystalline region is confined to the original oxygen plus deuterium implanted region. In addition, epitaxial regrowth of about 20 nm has occurred at the polycrystalline/monocrystalline interface [c.f. dashed lined in Fig. 7(c)], indicating that some "grain growth" at this interface has occurred. Following this particular anneal, existence of the prior amorphization process could no longer be detected.

When the order of the implantation sequence is reversed, so that first deuterium is implanted at a dose of
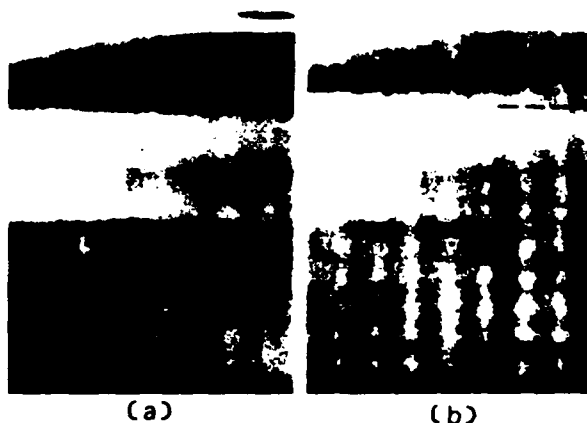

FIG. 6. (a) Bright-field image parallel to the implanted surface, (b) corresponding electron diffraction pattern, and (c) bright-field image perpendicular to the implanted surface following implantation with oxygen at 110 keV and a dose of 8.6×10^{14} O$^+$/cm^2 and then with deuterium at 60 keV and a dose of 4.5×10^{16} D$_2^+$/cm^2 and subsequent annealing for 10 min at 450 °C.

FIG. 8. Bright-field images perpendicular to the implanted surface following implantation with deuterium at 60 keV and a dose of 4.5×10^6 D$_2^+$/cm^2 and then with oxygen at 110 keV and a dose of 8.6×10^{14} O$^+$/cm^2 (a) at room temperature and (b) subsequent to annealing for 10 min at 300 °C.

FIG 9 Bright-field images perpendicular to the implanted surface following implantation with deuterium at 60 keV and a dose of 1.5×10^{16} D$_2^+$ and then with oxygen at 110 keV and a dose of 2.9×10^{14} O$^+$/cm^2 and subsequent annealing for 5 min at (a) 250, (b) 300, (c) 350 °C.

4.5×10^{16} D$_2^+$/cm^2 and then oxygen is implanted at a dose of 8.6×10^{14} O$^+$/cm^2, another type of crystallization is observed. Namely, by annealing for 10 min at 300 °C, band widths of the amorphous layer decrease from about 200 to 160 nm, as illustrated in Fig. 8, wherein bright-field images perpendicular to the implanted surface (a) before and (b) after annealing are pictured. This particular process allows epitaxial regrowth of the crystalline region without detectable change in orientation. Following this stage, crystallization proceeds in an identical manner as for the case of oxygen followed by deuterium implantation.

Dissolution of the amorphous particles, produced by implantation doses of 1.5×10^{15} D$_2^+$/cm^2 and 2.9×10^{14} O$^+$/cm^2, was also investigated during subsequent thermal processing. Typical results are presented in Fig. 9, wherein bright-field images perpendicular to the implanted surface following annealing for 5 min at (a) 250, (b) 300, and (c) 350 °C, are pictured. Figure 9(a) reveals that little or no change occurs at 250 °C, whereas Figs. 9(b) and 9(c) reveal that particle density decreases at 300 °C and disappears entirely at 350 °C, leaving no remnant trace of the preexisting amorphous regions. In this particular case, the curved amorphous/crystalline interface is mobile at about 300 °C, whereas planar amorphous/crystalline interfaces do not become mobile until about 450 °C. The significance of these results and others is discussed in the following section.

IV. DISCUSSION OF RESULTS

Results show that at low doses (0.50×10^{16} D$_2^+$/cm^2 and then 0.95×10^{14} O$^+$/cm^2) faint strain profiles for both deuterium and oxygen are observed but no structural or morphological changes can be detected. The oxygen strain profile is especially difficult to detect due to the fact that the strain gradient is partly compensated by the deeper deuterium implantation. Detection of similar strain profiles by TEM was first reported by Omi et al.[5] At intermediate doses (1.0 $\times 10^{16}$ D$_2^+$/cm^2 and then 1.9×10^{14} O$^+$/cm^2) isolated amorphous particles are formed in the deuterium plus oxygen implanted layer. With increasing implantation dose, these particles increase in size and finally merge into a continuous band below the implanted surface, which subsequently expands toward the implanted surface, eventually

causing the monocrystalline surface to decompose into a large number of individual crystallites. The implanted surface is last to amorphize not only because the damage is less at this surface but also because of stress relaxation. This result corresponds to the results of Komenou et al.,[1] who report that amorphization of the surface of garnet during implantation with neon occurred last. Finally, at large doses (4.5×10^{16} D$_2^+$/cm^2 and then 8.6×10^{14} O$^+$/cm^2) a completely amorphous layer, extending about 200 nm below the implanted surface, is produced. Although the exact correlation between the width of the amorphous band and the corresponding strain profile is not known, this width, in general, agrees well with computed projected ranges.[4] No structural or morphological changes were observed in the deuterium-only implanted layer; thus, amorphization is caused by oxygen implantation, although the structure may be sensitized by prior implantation with deuterium.

Although amorphization is caused by oxygen implantation, the resulting thickness of the amorphous layer (~ 200 nm), produced by implantation with deuterium at a dose of 4.5×10^{16} D$_2^+$/cm^2 followed by implantation with oxygen at a dose of 8.6×10^{14} O$^+$/cm^2, is greater than the resulting thickness of the amorphous layer (~ 150 nm), produced only by equivalent oxygen implantation. Therefore, it is concluded that garnet is sensitized by prior implantation with deuterium. The resulting thickness of the amorphous layer is also affected by the order of implantation. For example, at doses of 4.5×10^{16} D$_2^+$/cm^2 and then 8.6×10^{14} O$^+$/cm^2, the resulting thickness for oxygen followed by deuterium implantation is about 160 nm, whereas the resulting thickness for deuterium followed by oxygen implantation is about 200 nm. The thickness of 160 nm is in close agreement with that for only oxygen implantation at the same dose (150 nm), indicating again that implantation with deuterium does not produce appreciable amorphization.

The amorphization process is caused by the relatively large momentum transfer produced by oxygen implantation, wherein concentration of defects produced by atomic cascades is sufficient to promote transformation to the amorphous state in isolated regions below the implanted surface, which grow in both size and number with increasing implantation dose. Since the order of implantation affects the details of this process, it seems that two conditions are required: (1) accumulation of stress and (2) disordering of the lattice. Implantation with oxygen meets both conditions, whereas implantation with deuterium only meets the first condition. For this reason, implantation with deuterium sensitizes garnet by extending the edge of the amorphous layer where the oxygen concentration falls off rapidly, but, by itself, cannot promote amorphization.

Evolution of the crystallization process by thermal processing is also clearly described by a combination of bright-field images parallel and perpendicular to the implanted surface and corresponding selected-area and microelectron diffraction patterns. The crystallization process in fully amorphous layers following implantation at large doses 8.6×10^{14} O$^+$/cm^2 and then 4.5×10^{16} D$_2^+$/cm^2 evolves in three separate stages: (1) small crystallites nucleate homogeneously during annealing for about 10 min at 350 °C, (2)

other crystallites nucleate heterogeneously at the implanted surface and at the amorphous/crystalline interface during annealing for about 10 min at 450 °C, and (3) these isolated crystallites merge to form a polycrystalline structure during further annealing at 450 °C. Epitaxial regrowth of the monocrystalline garnet at the amorphous/crystalline interface is also observed.

Evolution of the crystallization process in specimens implanted first with deuterium at a dose of 4.5×10^{16} D_2^+ / cm^2 and then with oxygen at a dose of 8.6×10^{14} O^+ / cm^2 involves yet another stage; namely, epitaxial regrowth of the monocrystalline garnet of about 40 nm occurs during annealing for 5 min at 300 °C. Therefore, the amorphous region produced by prior sensitization by implantation with deuterium reverts back to its original (crystalline) state by epitaxial regrowth as a precursor to a more general crystallization process. Such behavior indicates that defects produced by implantation with oxygen are more stable than those produced by implantation with deuterium, thus requiring a greater amount of thermal energy to promote the subsequent crystallization process.

Finally, dissolution of amorphous particles occurs at a much lower temperature (300 °C) than epitaxial regrowth of a completely amorphous layer (450 °C). This is attributed to the fact that the driving force acting on the interface separating crystalline and amorphous regions is the sum of the enthalpy of crystallization (per unit volume) and $2\gamma/r$, where γ denotes the interfacial energy and r denotes the (spherical) particle radius. Since r for the observed amorphous particles is very small (~ 10 nm), the corresponding driving force is larger than that for a completely amorphous layer and, therefore, dissolution occurs at lower temperatures.

The results of this investigation are relevant to fabrication of ion-implanted contiguous disk bubble devices.[1,2] The fact that the order of implantation affects the degree of amorphization suggests that order of implantation should also affect, to some extent, operating margins of bubble devices. In particular, results of this investigation suggest that, if large implantation doses are to be used, it would be preferable to implant first with oxygen and then with deuterium rather than in the reverse order, since amorphization, which generally reduces device margins, occurs more easily in a sample first implanted with deuterium. Moreover, results suggest that a temperature of about 350 °C is required to induce reversion of the amorphous regions to the crystalline state. This temperature is in good agreement with observations that characteristics of devices implanted with modera-

tely heavy doses can be improved by annealing at temperatures near 350 °C.[2] It is likely that such annealing promotes a reversion of small amorphous regions to the crystalline state.

V. SUMMARY

Amorphization produced by ion implantation and subsequent crystallization produced by thermal processing have been investigated in films of $(SmYGdTm)_3 Ga_{0.4} Fe_{4.6} O_{12}$ garnet by transmission electron microscopy, incorporating a special cross-sectioning technique. The amorphization process evolves in four separate states: (1) an implanted (crystalline) band, delineated by the implantation strain profile, forms at low doses, (2) isolated amorphous regions of about 10 nm in diameter form at intermediate doses, (3) these amorphous regions merge to form a continuous band below the implanted surface, and (4) this band expands to the implanted surface at larger doses. Amorphization is caused by implantation with oxygen, but prior implantation with deuterium sensitizes the lattice by increasing the strain. The crystallization process evolves in three separate stages: (1) small crystallites of about 10 nm in size form homogeneously during annealing at 350 °C, (2) larger crystallites nucleate heterogeneously and grow from the implanted surface and amorphous/monocrystalline interface at 450 °C, and (3) these crystallites grow in size until they merge to form a continuous polycrystalline layer at longer annealing times. Some epitaxial regrowth of the crystalline region into the amorphous region is also observed. These results depend on details of the implantation and annealing processes, as well as on the nature of the defects created and kinetics of the amorphous/crystalline interfacial migration.

ACKNOWLEDGMENTS

[1] R. Wolfe, J. C. North, W. A. Johnson, R. R. Spiwak, L. J. Varnerin, and R. F. Fischer, AIP Conf. Proc. 10, 339 (1973)

[2] Y. S. Lin, G. S. Almasi, and G. E. Keefe, J. Appl. Phys. 48, 5201 (1977).

[3] K. Komenou, I. Hirai, K. Asama, and M. Sakai, J. Appl. Phys. 49, 5816 (1978).

[4] T. Yoshiie, C. L. Bauer, and M. H. Kryder, IEEE Trans. Magn. MAG-19, 1823 (1983).

[5] T. Omi, C. L. Bauer, and M. H. Kryder, J. Appl. Phys. 53, 2528 (1982).

CHARGED WALL FORMATION IN ION-IMPLANTED GARNETS

D. A. Saunders and M. H. Kryder

In ion-implanted, contiguous-disk devices, the bubbles are propagated by highly polarized domain walls, known as "charged walls," which move along the edges of ion-implanted patterns in response to a rotating in-plane field. These walls form as a result of magnetostrictive anisotropies caused by implantation-induced stress (Fig. 1). During this last year, we have been further developing the theory behind these magnetostrictive anisotropies and have been calculating their effect on charged wall formation and propagation. Some results of this effort will be presented at the Conference on Magnetism and Magnetic Materials (MMM) at San Diego in November, 1984[1]. This theoretical development has included the determination of the stress distribution in and around implanted patterns for various implant conditions and the computer modeling of the response of the magnetization to these stresses and to the applied fields.

Stress Calculations

In calculating the stress distribution due to ion-implantation, we treat the implanted ions as "centers of dilitation" which push outwardly in all directions from their location in the implanted crystalline lattice. This causes an expansion of the implanted lattice and, hence, results in various stresses and strains due to the incompatability of the expanded lattice with the surrounding lattice. In this regard, the expansion due to ion-implantation can be likened to thermal expansion due to spatial changes in the temperature of the lattice. For example, a rectangular area uniformly implanted to a depth D in a bubble chip causes the same stress distribution as a "hot" rectangle of depth D in a cold half-space. From this analogy, the stress distribution can be calculated according to the equations given in a paper by Ignaczak and Nowacki [2]. Due to their complexity, these equations have been programmed into a computer, allowing stress distributions to be calculated for various propagation structures and for various implantation conditions. In Fig. 2, the normalized differential stresses $S_2 = (\sigma_y - \sigma_x)/\sigma_p$ and $S_3 = (\sigma_z - \sigma_x)/\sigma_p$ and the normalized shearing stress $S_{13} = \sigma_{xz}/\sigma_p$ at the edge of an implanted region are plotted versus position, where σ_p is the planar stress in the implanted area far from the mask edge and x, y, z are the coordinate axes shown. The stresses in Fig. 2 are for an implant which is uniform throughout the implantation depth, herein refered to as a "uniform implant". The stress distribution due to

an implantation with ion density varying with depth (profiled implant) has also been calculated as has the stress distribution due to a poorly defined mask edge (beveled implant).

The models for these implants are shown in Fig. 3. The uniform implant is a region of depth t which comes to an abrupt end at the mask edge. The density of centers of dilitation--the ions--is constant throughout the depth, t. The profiled implant is intended to model a 200 KeV Neon implant. It is modeled as a ten-layer, piecewise-uniform implant with each layer having a different ion density as shown in Fig. 3. The profiled implant is scaled to have the same total ion dosage as the uniform implant. To investigate the effect of a sloped mask edge, a beveled implant was modeled as a uniform implant having a 45° stepped edge made up of ten steps.

Magnetostrictive Anisotropies

The impact of the stress on the magnetization distribution is described by the magnetostrictive energy equation given in the MMM paper [1]. This magnetostrictive anisotropy energy can be separated into five terms. The anisotropies of four of these terms are illustrated in Fig. 4. The anisotropy not illustrated is the uniaxial anisotropy perpendicular to the film with an easy plane induced by negative S_2 and S_3. Fig. 4a shows that the stress relaxation of σ_x relative to σ_y (i.e. S_2) gives rise to an easy axis of magnetization along the implanted edge. This anisotropy leads to the formation of charged walls. In Fig. 2, it is seen that this stress relaxation drops off with distance from the edge, a feature which is consistent with the observation that charged walls are stable only near to the edge. It is also seen that S_2 peaks at the surface of the film, indicating that charged walls may be more likely to form near the surface. Within the non-implanted region the sign of S_2 reverses and an easy plane of magnetization is formed perpendicular to the edge. As will be seen later, this allows the formation of domains which are perpendicular to the implantation edge within the non-implanted region.

In addition, the stress relaxation, S_2, gives rise to a unidirectional anisotropy which varies with threefold symmetry around a non-implanted disk, Fig. 4b. This causes three favorable positions for a charged wall around a disk and results in discontinuous motion of the charged

wall--a highly undesirable effect. This anisotropy is proportional to Δ, the difference in the magnetostrictive constants, $\Delta = (\lambda_{111} - \lambda_{100})/\lambda_{111}$. Therefore, as we have recommended in previous reports and publications[2], this undesirable effect can be minimized by using materials with $\lambda_{111} = \lambda_{100}$, i.e. $\Delta = 0$.

The shearing stress, S_{13}, gives rise to an anisotropy with an easy axis at $45°$ to the film normal which, under the influence of the bubble biasing field, appears to be a unidirectional anisotropy perpendicular to the implantation edge (Fig. 4c). S_{13} also causes an in-plane easy axis which varies with threefold symmetry around a non-implanted disk (Fig. 4d).

Magnetization Distributions

The magnetostrictive equation has also been programmed into a computer. Using the previously calculated stress distribution, the computer program minimizes the magnetic energies (including applied field energy, magnetostrictive energy, and other anisotropy energies; however, exchange and dipolar interactions are not included) to find the resultant magnetization distribution. The magnetization distributions have been calculated for uniform implants, profiled implants and beveled implants for varying material parameters (such as Δ)and for different mask edge orientations (varying ψ). The magnetization distribution at a mask edge for a magnetostrictively isotropic film $(\lambda_{111} = \lambda_{100}$ or $\Delta = 0)$ with a uniform implant is shown in Fig. 5. This is a cross-sectional view of the film at the implantation edge. The vectors are schematic representations of the magnetization indicating the projection of the magnetization into the cross-sectional plane (the xz-plane).

As expected, most of the magnetization in the implanted region of Fig. 5 is parallel to the edge (perpendicular to the page). However, the magnetization at the bottom of the implant at the mask[4] edge is not along the mask edge. In this region the shearing force (see Fig. 2) peaks, inducing a strong easy axis at $45°$ from the film normal. Hence, a charged wall at this edge would be shifted outward from the mask near the bottom of the implant. The peak in S_{13} is due to the abrupt transition from implanted region to non-implanted region in both the x and z directions. S_{13} can therefore be reduced by using an implant which gradually trails off with

depth, similar to the profiled implant.

Another significant feature of the distribution in Fig. 5 is the existence of an in-plane magnetization just under the mask lip in the non-implanted region. This region has planar magnetization because S_3 has a negative peak in this vicinity. In addition, S_2 has a negative peak which causes the magnetization to lie perpendicular to the mask edge. Planar domains have not been observed in these regions before now. However, we have observed these "edge domains" in a Bi-substituted garnet with a single neon implant (Fig. 6). We find that these domains have a relatively high coercivity (about 20 oe) and act as one would expect when the anisotropies of Fig. 4 are taken into account. These observations further indicate the validity of this model.

Effect of Anisotropic Magnetostriction

Most bubble garnets have anisotropic magnetostriction; that is, Δ is non-zero. Generally, Δ is greater than zero and, typically, Δ is about equal to one. This has a number of undesirable effects:

1. The uniaxial anisotropy responsible for charged wall formation is reduced.

2. The unidirectional anisotropy responsible for discontinuous charged wall movement is increased.

3. The anisotropy responsible for the "edge domains" is increased.

4. The anisotropy which causes perpendicular magnetization in the implanted region near the mask edge is increased.

Some of these effects are seen in Fig. 7. This is the distribution near a mask edge with a normal along the [112] direction ($\psi = 90°$) and for a material with $\Delta = 1$. In Fig. 7 the magnetization in the implanted region near the mask edge is more perpendicular to the film than that in Fig. 5. This means that the charged wall may be displaced outwardly from the mask edge. Attributible to the above effects 1 and 4, such "edge shifting" may effectively reduce track-to-track spacing and cause bubbles to unexpectantly jump to adjacent tracks. This edge shifting becomes increasingly evident for increasing Δ as illustrated in Fig. 8 where $\Delta = 3/2$.

Also evident in Figs. 7 and 8 is the increase in the planar magnetization under the mask

edge. This indicates that edge domains are more likely to occur in films with $\Delta > 0$. The effect of edge domains on charged walls is not well understood, but it has been observed that charged walls sometimes tend to stick to the transition between antiparallel edge domains. Subsequently, the presence of edge domains may cause irregular charged wall movement. In addition, the existence of a planar edge domain effectively reduces the thickness of the non-implanted film having perpendicular magnetization. This reduces the magnetostatic energy barrier which prevents the bubble from moving into the non-implanted area and hence may allow bubbles to slide under the mask from one side of a minor loop to the other. For these reasons, it is further apparent that isotropically magnetostrictive garnets ($\Delta = 0$) should be developed to improve device performance.

Profiled Implant

Figure 9 shows the magnetization distribution due to the 200 KeV Neon implant model for $\Delta = 0$. Because the Neon implant has a wide peak it is not a great deal different than the uniform implant. However, because the shearing stress is reduced and because ion density of the Neon implant peaks near the bottom of the implant the magnetization in the implanted area near the mask edge is slightly more planar than that in the uniform implant. Thus, by properly profiling the ion density with depth it may be possible to minimize edge shifting.

Beveled Implant

The magnetization distribution at a beveled edge for $\Delta = 0$ in Fig. 10 has, as one might expect, a beveled planar region. However, most of the bevel is provided by increased planarity of the magnetization nominally under the mask ($x < 0$) rather than by decreased planarity of the magnetization at $x > 0$. Here the transition from magnetization perpendicular to the film to planar magnetization along the mask edge (into the page) is gradual and a charged wall may not be well-defined.

Highlights and Conclusions

A model for the behavior of the magnetization at the edge of an implanted region has been formulated and implemented. The model may be used as a tool for investigating the effect of different implantation conditions and material parameters on device performance. Through the use of this model the existence and behavior of heretofore unseen "edge domains" have been correctly

predicted. Recommendations have been made regarding implant conditions and material parameters:

1. Use implant profiles which trail off with depth to decrease shearing stresses and edge shifting.

2. Implantation masks should have vertical edges to avoid poorly defined charged walls.

3. Bubble garnets used in these devices should have isotropic magnetostriction, $\lambda_{111} = \lambda_{100}$, to minimize the discontinuous motion of charged walls, to decrease edge shifting and to suppress "edge domains".

4. Use hydrogen or deuterium implants to suppress edge shifting[1].

Future Work

The model may be used to design different ion-implantation dosages or to analyze the reasons for one implantation working better than another. The model is three-dimensional and therefore is capable of calculating the effects of different mask patterns and dimensions. Consequently, actual propagation structures may be modeled and analyzed.

1. D.A. Saunders and M.H. Kryder, "Stress Gradients and Magnetoelastic Anisotropies at Implantation Edges in Ion-implanted Garnet Films," paper AD-07, Conference on Magnetism and Magnetic Materials, San Diego, November (1984).

2. M.H. Kryder and D.A.Saunders,"The Effects of Stress Relaxation and Anisotropic Magnetostriction on Charged Walls in Ion-implanted Garnets," IEEE Trans. Mag., Mag-15, No. 5, 1817 (1983).
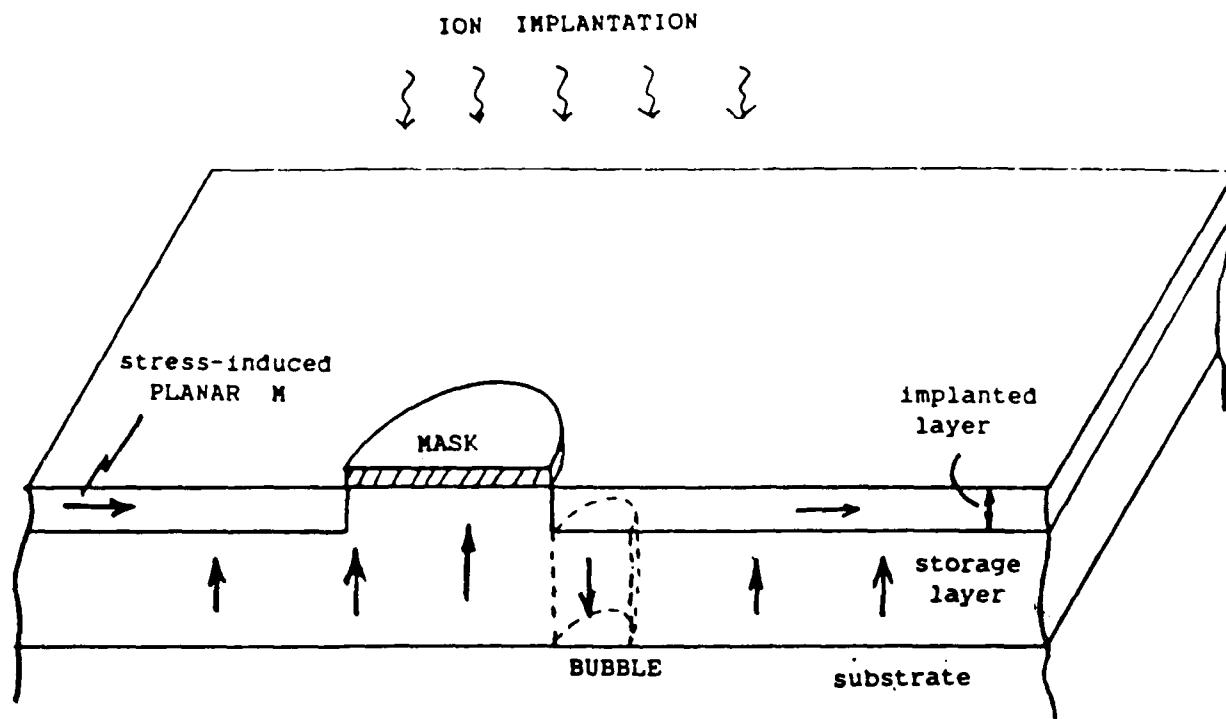
ION IMPLANTATION

Ion-Implanted Bubble Memory
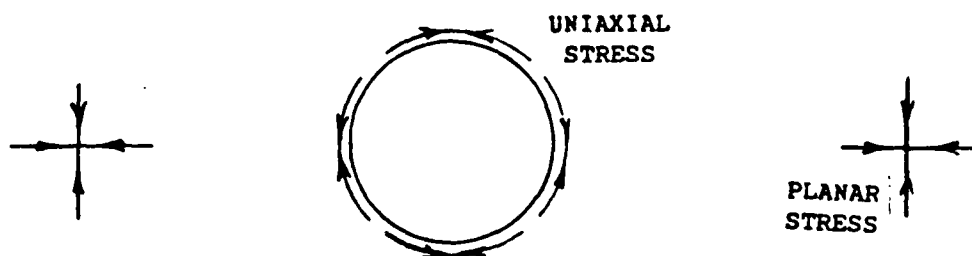
Stresses induced by ion-implantation.
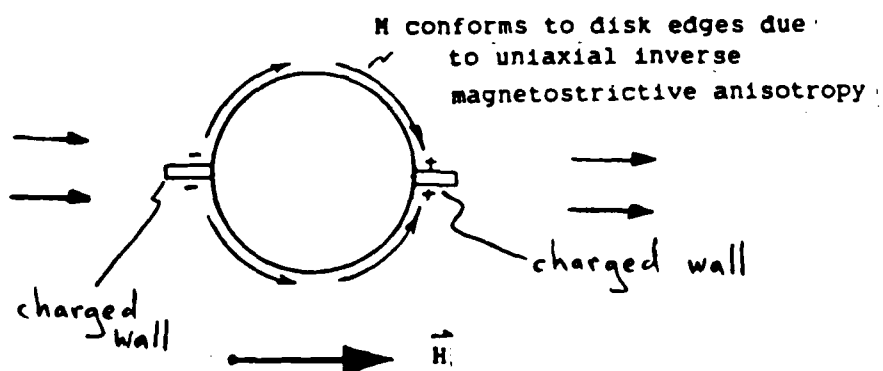
Flow of M in implanted layer.

Fig. 1. Charged walls form in ion-implanted bubble devices due to stress relief.
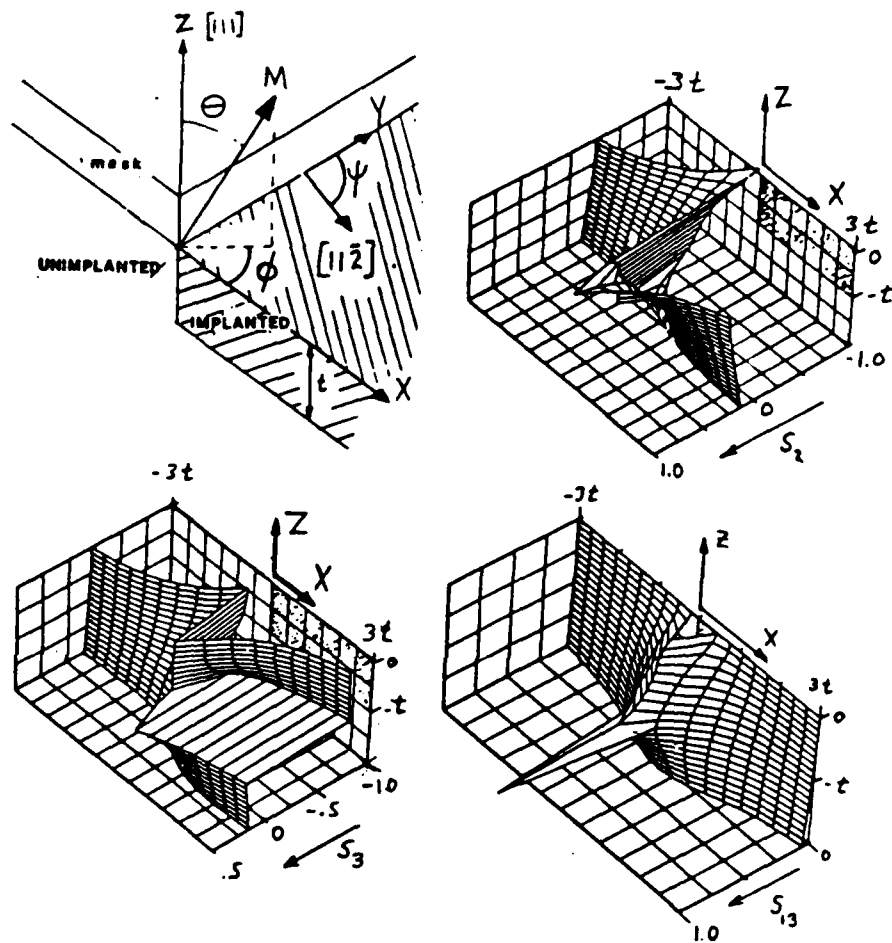
Fig. 2. Normalized differential stresses $S_2 = (\sigma_y - \sigma_x)/\sigma_p$ (the stress relief) and $S_3 = (\sigma_z - \sigma_x)/\sigma_p$ and normalized shearing stress $S_{13} = \sigma_{xz}/\sigma_p$ at the edge of an implanted region plotted versus position, where σ_p is the planar stress in the implanted area far from the mask edge and x, y, z are the coordinate axes shown.
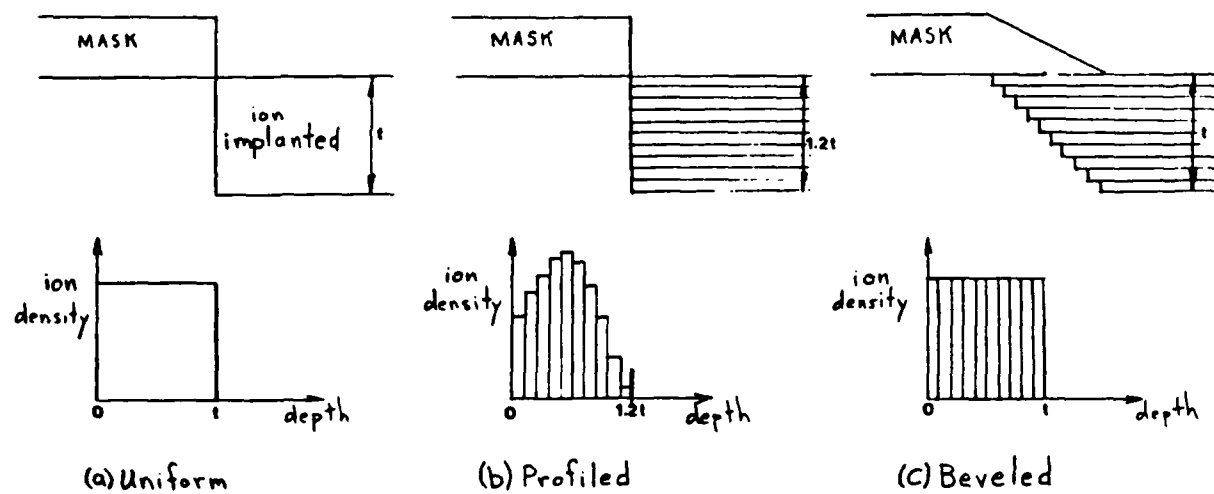
Fig. 3. Implantation models and profiles used for calculations of magnetization distributions.

$$[S_2 (1-\Delta/3)] \sin^2\theta \cos^2\phi$$

$$[S_2 (\sqrt{2}\Delta/6)] \sin 2\theta \sin(\phi+3\psi)$$

$$-[S_{13} (1-2\Delta/3)] \sin 2\theta \cos\phi$$
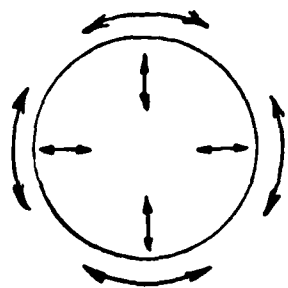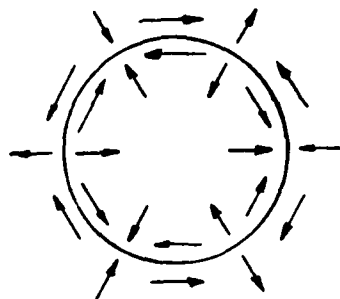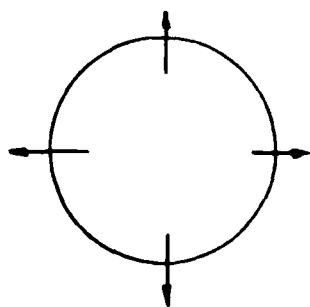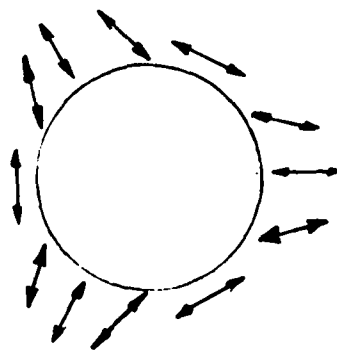
$$+[S_{13} (\sqrt{2}\Delta/3)] \sin^2\theta \sin(2\phi+3\psi)\}$$

Fig. 4. Qualitative representation of magneto-elastic anisotropies induced by stresses around a non-implanted disk. Easy magnetization directions of uniaxial anisotropies are illustrated by double-ended arrows. Easy directions of unidirectional anisotropies are shown by single-ended arrows (axial symmetry is broken by the presence of bubble biasing field perpendicular to film).

MAGNETIZATION DISTRIBUTION AT EDGE OF UNIFORM IMPLANT
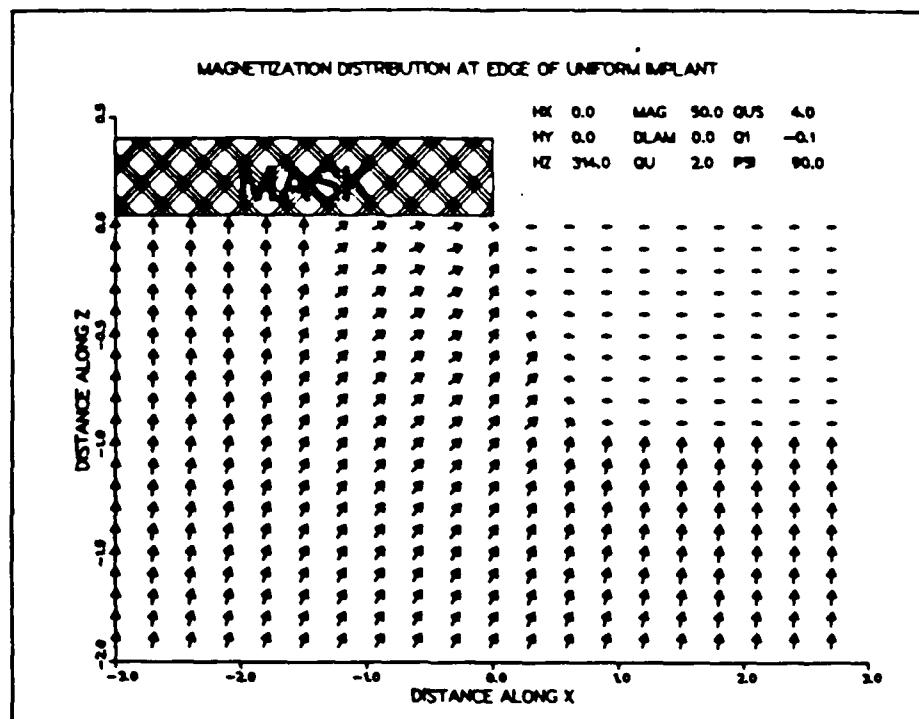
Fig. 5. Magnetization distibution for uniform implant with Δ=0. Note slight "edge shift" in implanted region and in-plane magnetization at edge of masked region.
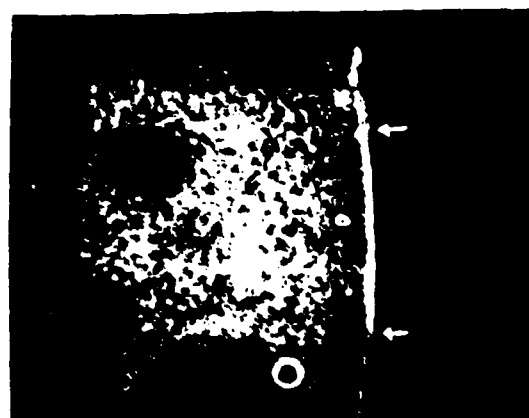
Fig. 6. In-plane "edge domains" at edge of masked region made visible via ferrofluid on the surface of the film.   (between arrows)
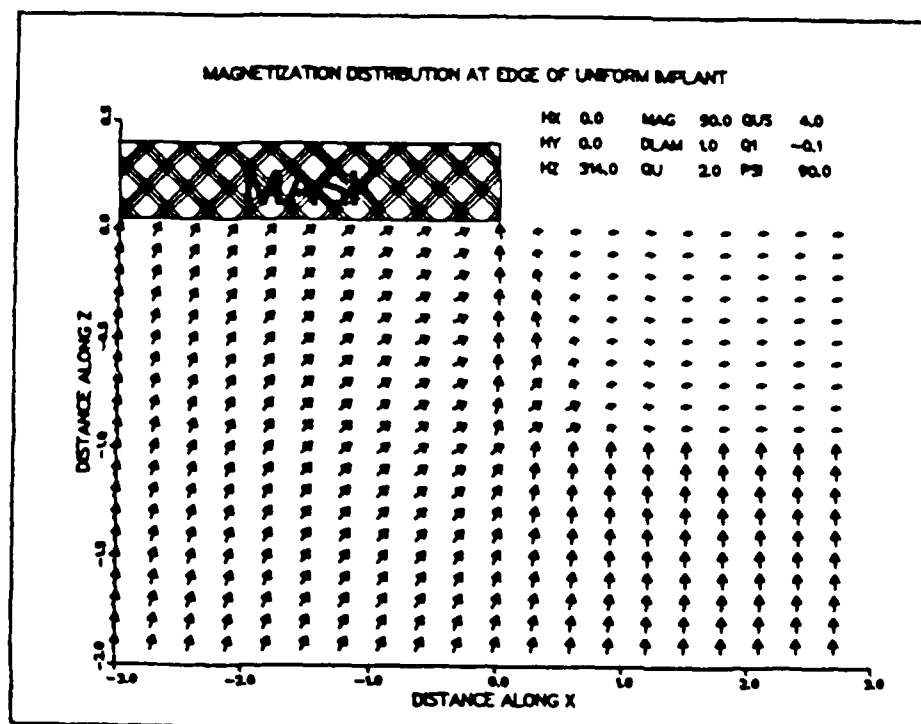
Fig. 7. Magnetization distribution for uniform implant with $\Delta = 1$. Increase in Δ causes increase in S_{13} uniaxial anistropy and results in increased "edge shifting" and expansion of "edge domain".
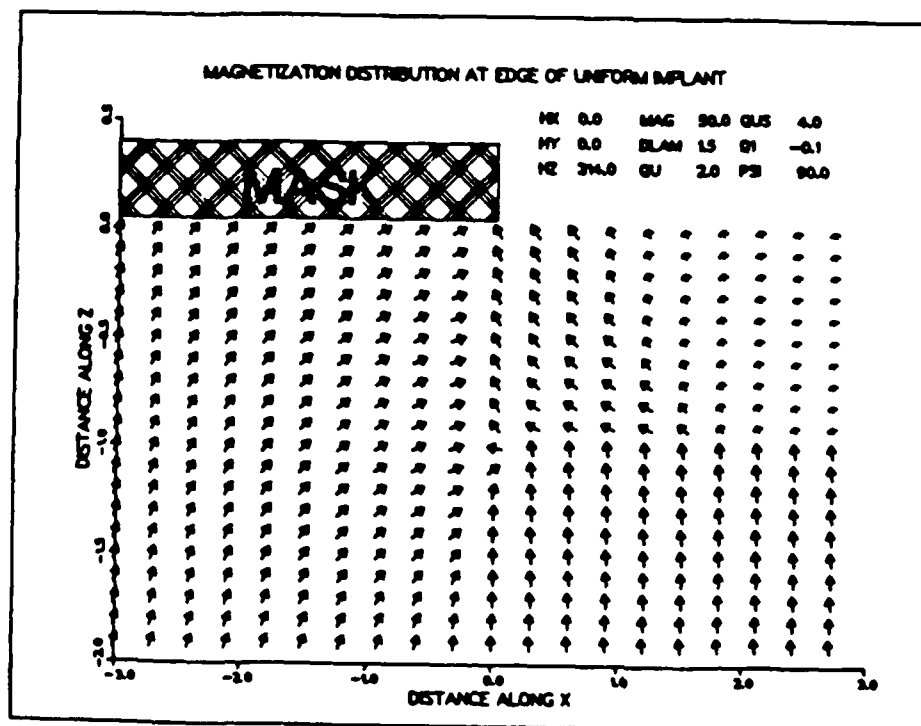
Fig. 8. Magnetization distribution for uniform implant with $\Delta = 1.5$. Edge shifting becomes very noticeable with this value of Δ.
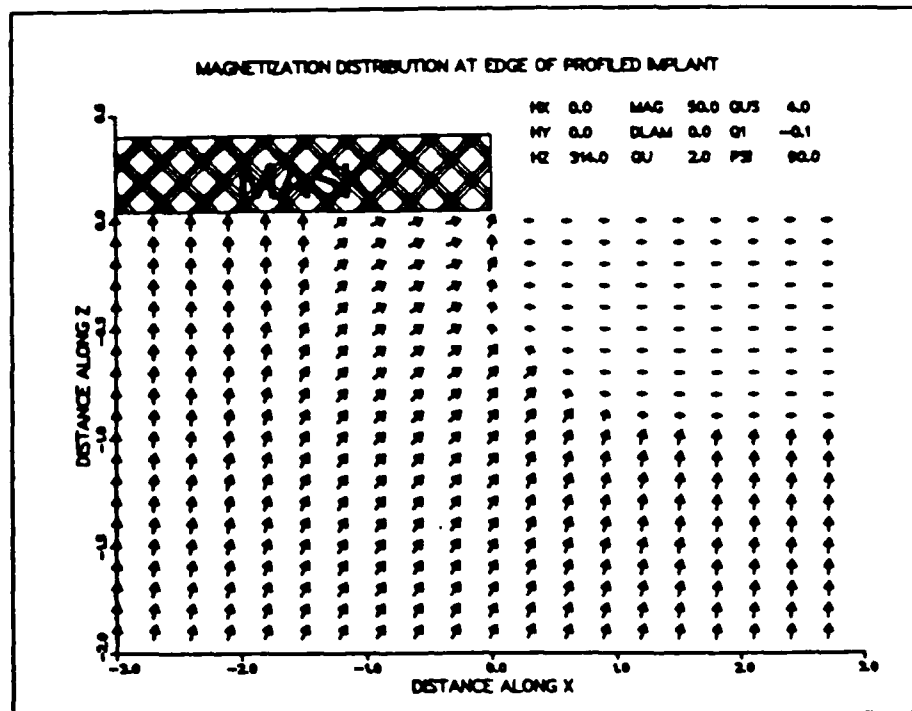
Fig. 9. Magnetization distribution due to 200 keV Neon implant for Δ=0. Edge shifting is decreased slightly compared to the uniform implant.
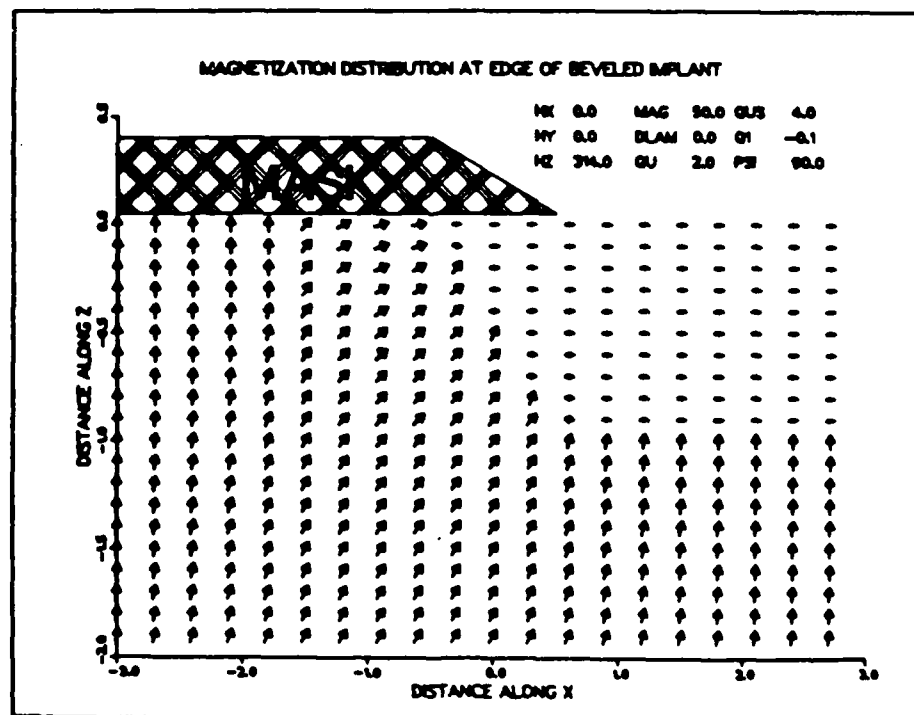
Fig. 10. Magnetization distribution at a beveled implant for Δ=0. Edge is poorly defined.

Stresses and magnetoelastic anisotropies at implantation edges in ion-implanted garnet films

D. A. Saunders and M. H. Kryder

Department of Electrical and Computer Engineering, Carnegie-Mellon University, Pittsburgh, Pennsylvania 15213

Stresses at the edge of an ion-implanted region in a magnetic garnet film have been calculated by analogy with thermal-induced stresses in an elastic half space. From these stresses, magnetoelastic anisotropies have been computed for two different implant profiles. Stress calculations show that stress relaxation near an implantation edge decreases with distance from the edge with an exponential decay length of approximately $4t$, where t is the implantation layer thickness. Stress perpendicular to the film surface and shearing stress are significant at the implantation edge, but decrease more quickly with decay lengths of approximately $0.8t$ and $0.6t$, respectively. Because of perpendicular and shearing stresses, the anisotropy under the edge of the implantation mask favors planar magnetization. For similar reasons, the anisotropy in the implanted region near the mask edge favors perpendicular magnetization, effectively causing a shift in the mask edge toward the $[11\bar{2}]$ direction. The shift is especially evident in materials with $\lambda_{111} \neq \lambda_{100}$ and is on the order of $2.5t$ for a material with $\lambda_{111} = -\lambda_{100}$.

INTRODUCTION

As first outlined by Hidaka and Matsutera,[1] relaxation of ion-implantation-induced stress at the interface between implanted and unimplanted regions in contiguous-disk bubble devices leads to the formation of charged walls. The stress relief gives rise to a large, uniaxial, magnetoelastic anisotropy parallel to the implantation edge, which stabilizes the charged walls. Other stresses present can also affect the magnetization behavior.[2] In this paper the stresses near boundaries between implanted and unimplanted regions of a garnet are calculated and used to find the variation of magnetoelastic anisotropies with position. Stable magnetization directions as a function of position are calculated by energy minimization of the various anisotropy energies at those positions.

ELASTIC MODEL

In the elastic model, the implanted ions are treated as "centers of dilitation" which push outwardly in all directions from their positions in a uniform, elastic half space, i.e., the garnet film and substrate. From this point of view, the expansion due to implantation is analogous to the thermal expansion due to a temperature rise. By this analogy the calculations of Ignaczak and Nowacki[3] are used to model the stresses around rectangular implanted patterns in a garnet film. The garnet is assumed to be elastically isotropic and completely described by Poisson's ratio ν. The strength and density of the implanted ions and the Young's modulus of the garnet are all taken into account by choosing the planar stress σ_p present in the regions far from the implant masks.

An implant with uniform ion density throughout its depth t is used as the reference implant. It is defined as causing a planar stress σ_p which leads to a planar anisotropy Q_{US}. For comparison, a 200-keV neon ion implant is modeled as a ten-layer, piecewise-uniform implant which varies with depth as determined by MacNeal and Speriosu.[4] The

neon implant is scaled to have the same total dosage as the uniform implant.

The coordinate system for the stresses near to a long, straight mask edge is shown in Fig. 1. For the purpose of calculating the magnetoelastic anisotropies [Eq. (1)], it is only necessary to deal with the normalized, differential stresses, $S_2 = (\sigma_y - \sigma_x)/\sigma_p$ and $S_3 = (\sigma_z - \sigma_x)/\sigma_p$, and the normalized shear stress, $S_{13} = \sigma_{xz}/\sigma_p$.

MAGNETIC MODEL

The orientation of the magnetization at the edge of an implanted region was found by minimization of the following energy equation:

$$
\begin{aligned}
E = {} & -(Q_U - 1)\cos^2\theta + Q_{US}\{[-S_3 + S_2(\Delta/6)]\cos^2\theta \\
& - [S_2(1 - \Delta/3)]\sin^2\theta\sin^2\phi \\
& - [S_2(\sqrt{2}\Delta/6)]\sin 2\theta\sin(\phi + 3\psi) \\
& - [S_{13}(1 - 2\Delta/3)]\sin 2\theta\cos\phi \\
& + [S_{13}(\sqrt{2}\Delta/3)]\sin^2\theta\sin(2\phi + 3\psi)\} \\
& + Q_1\{(\sin^4\theta)/4 + (\cos^3\theta)/3 \\
& + (\sqrt{2}/3)\sin^3\theta\cos\theta\cos 3(\phi + \psi)\} \\
& - \{H_X\sin\theta\cos\phi + H_Y\sin\theta\sin\phi \\
& + H_Z\cos\theta\}/2\pi M,
\end{aligned}
\tag{1}
$$

where Q_U is the perpendicular uniaxial anisotropy, $K_U/2\pi M^2$; Q_{US} is the magnetoelastic planar anisotropy due to implantation, $1.5\lambda_{111}\sigma_p/2\pi M^2$ (the change in perpendicular Q was assumed to be totally due to implantation stress); Δ is the anisotropic magnetostriction constant, $(\lambda_{111} - \lambda_{100})/\lambda_{111}$; Q_1 is the magnetocrystalline anisotropy, $K_1/2\pi M^2$; H_X, H_Y, and H_Z are the fields along the axes of Fig. 1; M is the magnetization; θ and ϕ are the angles of the magnetization as shown in Fig. 1; and ψ is the angle of the mask edge as in Fig. 1.
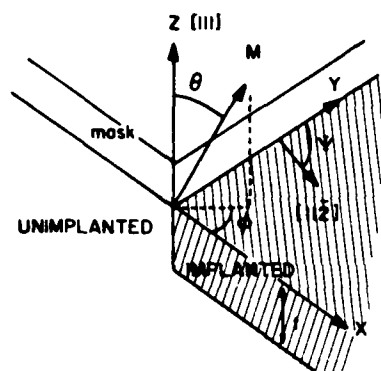
FIG. 1. Coordinate system of Eq. (1).

Using the stress distributions calculated from the elastic model, the distributions of the magnetization near to the implant mask edge were calculated for varying material parameters. Exchange interactions and demagnetizing effects were not included in the model (except for a thin-film demagnetizing term) and, therefore, the distributions are due only to the spatial variation of the stress. The spacing of the grid is such that exchange effects could cause noticeable interaction between adjacent dipoles along the z direction but little interaction along the x direction. Demagnetizing fields would also alter the distributions shown here, but the magnetoelastic anisotropies are generally large enough to resist demagnetization (as evidenced by the formation of charged walls).

UNIFORM IMPLANT

Shown in Fig. 2 are plots of S_2, the "stress relief" perpendicular to the mask edge; S_3, the differential stress perpendicular to the film plane; and S_{13}, the shear in the xz plane, for an implant uniform with depth. In Fig. 3 is shown the magnetization distribution due to this implantation in a magnetostrictively isotropic film ($\Delta = 0$). (Note that the vertical axis and horizontal axis are not equally scaled in these figures and that the distances are given in implantation depths t.) It can be seen that the magnetization is planar and is aligned parallel to the mask edge throughout the implanted region, except at the bottom corner of the implant near to the mask edge. This is due to the decrease in stress relief S_2 and the increases in perpendicular stress S_3 and shear stress S_{13} in this area. Thus, the easy axis parallel to the mask edge and the planar anisotropy are weakened, while a strong easy axis of magnetization is induced at 45° from the film normal by S_{13}. This region does not extend far from the mask edge, but it does indicate that a charged wall is more likely to reside near the surface of a film.

Another significant characteristic of Fig. 3 is the formation of a planar "edge domain" just under the lip of the mask within the unimplanted region. This is due to the negative peak in S_3 in this area. Also, S_2 is negative in this area, inducing a hard axis parallel to the mask edge so that the magnetization lies perpendicular to the mask edge. In general, these domains are not seen (if indeed they exist) in most films; however, we have observed such domains in at least one film.

For an edge at $\psi = 90°$ and $\Delta > 0$ (Fig. 4), the easy axis parallel to the edge is weakened via the S_2 term and the sec-
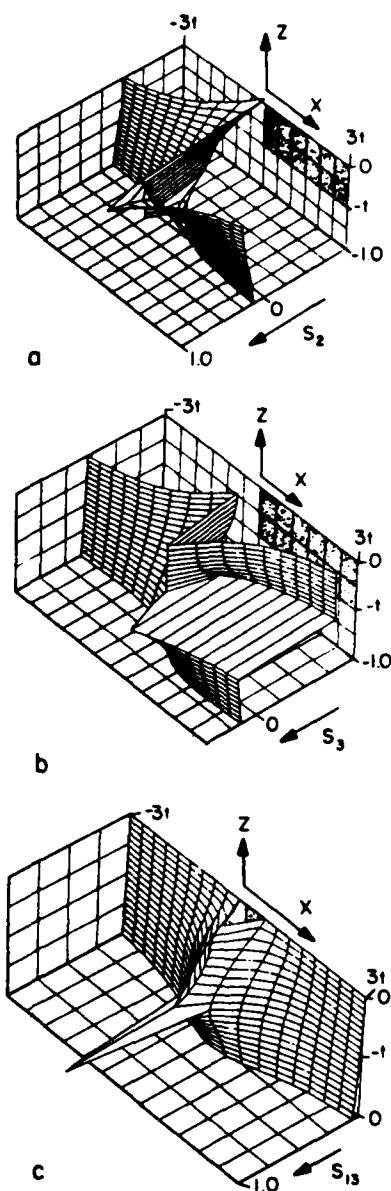
FIG. 2. (a) Stress relief S_2, (b) differential stress S_3, and (c) shearing stress S_{13} as functions of position. Shaded areas indicate implanted regions.
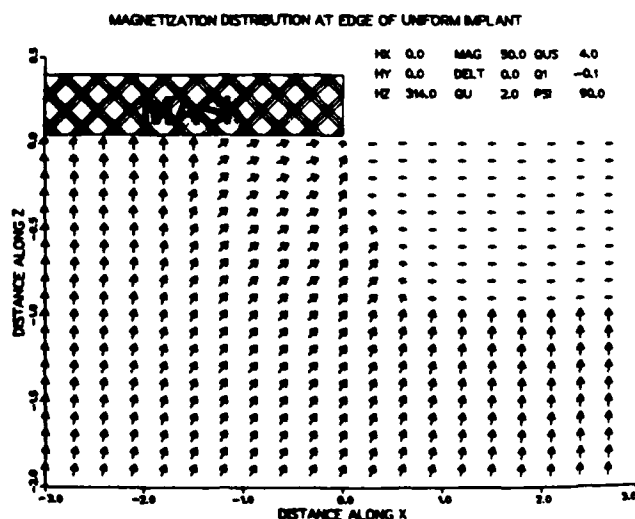

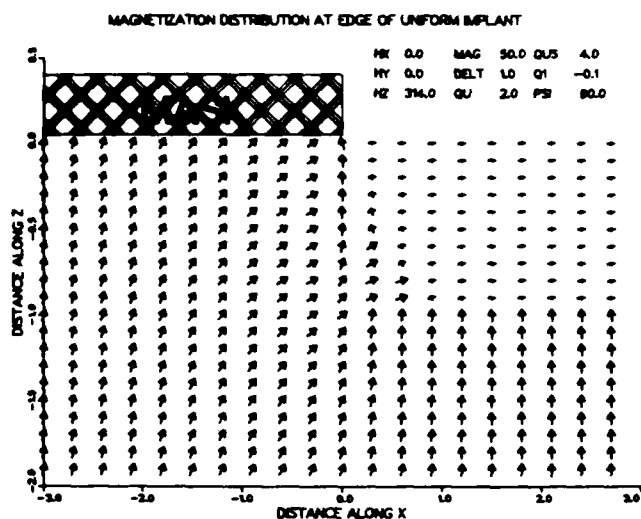FIG. 3. Magnetization at mask edge for a uniform implant, Δ (DELT) = 0.

FIG. 4. Magnetization at mask edge: uniform implant, $\Delta = 1$, $\psi = 90°$.
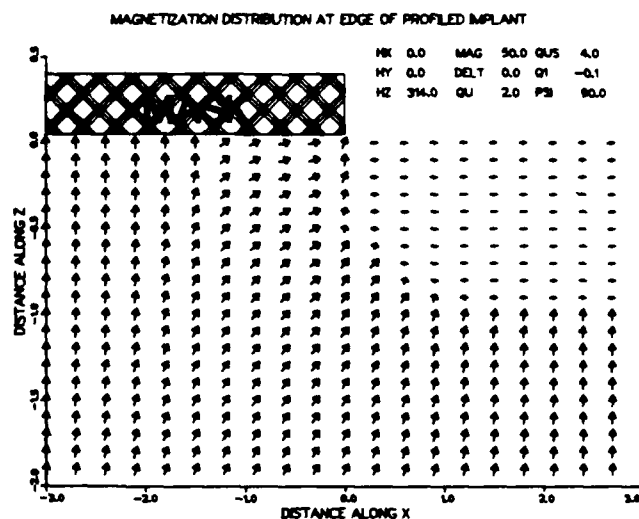
FIG. 5. Magnetization at mask edge: neon implant, $\Delta = 0$.

ond S_{13} term in Eq. (1). This causes the planar magnetization region to shift outward from the mask edge: about $0.5t$, $1.3t$, and $2.5t$ for $\Delta = 1$, 1.5, and 2, respectively. At $\psi = -90°$ and $\Delta > 0$ (no figure), the S_{13}-induced anisotropy is of the opposite sign, strengthening the easy axis parallel to the mask edge near the implantation depth where S_{13} dominates. There the planar region is shifted inward under the mask edge (though less so than the outward shift at $\psi = +90°$.)

200 keV NEON IMPLANT

Because the 200-keV implant has a wide peak, the magnetization distributions due to the neon implant (Fig. 5) are not very different from those due to the uniform implant. However, because the less well-defined implantation depth (the tail of the implant) reduces the shearing at the mask edge, the magnetization in the implanted region for $\Delta = 0$ is more planar at the edge than in Fig. 3. Distributions for $\Delta > 0$ and $\psi = 90°$ and $-90°$ are not shown here but have been generated. These indicate that a charged wall is more likely to reside near the bottom of this implant and that the planar region is less shifted from the mask edge.

CONCLUSIONS AND SUGGESTIONS

It is shown here that an implant uniform in depth does not lead to magnetization uniform in depth near to the mask edge. If uniform magnetization is desired and if $\Delta = 0$, the implant should be uniform throughout most of the depth and then taper off into the bulk (most "uniform" implants

are like this anyway). If $\Delta \neq 0$, the implant should peak slightly near the surface to increase the reduced "stress-relief anisotropy." Implants with smooth peaks deep in the drive layer may have the advantage of causing more uniform stress relief S_2 and allowing the charged wall to reside near to the bubble layer. However, peaked implants do not give uniform planarity, and a charged wall in such an implanted film may vary greatly with depth. Because the implantation of heavy ions induces planar magnetization primarily through magnetostriction,[5] heavy ion implants can produce "edge shifting": perpendicular magnetization near the mask edge due to the peak in σ_z. However, light ions such as hydrogen and deuterium produce additional planar anisotropy to suppress the edge shift. For this reasons, the use of lighter ions, such as hydrogen and deuterium, may be preferable. Some mixing of heavy and light ions could also be done to separately tune the distribution of stress and the planarity of magnetization.

ACKNOWLEDGMENT

The authors wish to thank P. Asselin for proposing the elastic model utilizing the centers of dilitation.

[1]Y. Hidaka and H. Matsutera, Appl. Phys. Lett. 39, 116 (1982).
[2]M. H. Kryder and D. A. Saunders, IEEE Trans. Magn. MAG-15, 1817 (1983).
[3]J. Ignaczak and W. Nowacki, Bull. Acad. Pol. Sci. Ser. Sci. Tech. VI, 309 (1958).
[4]B. E. MacNeal and V. S. Speriosu, J. Appl. Phys. 52, 3935 (1981).
[5]C. S. Krafft, M. H. Kryder, and J. O. Artman, IEEE Trans. Magn. MAG-20, 1111 (1984).

4063   J. Appl. Phys., Vol. 57, No. 1, 15 April 1985

D. A. Saunders and M. H. Kryder   4063

Contiguous Disk Magnetic Bubble Memory Devices

November 14, 1984
S. Jo and M. H. Kryder

Introduction

Design and fabrication of full function contiguous disk magnetic bubble memory devices was described in the last report (Nov. 30, 1983). Some of the test results were also reported. In this report, device fabrication and test results for 0.5 μm bubble propagation devices are mainly described. To test these devices, a new water-cooled bias magnet has been installed, which can produce bias magnetic field of up to 1.4 KOe. In addition, progress in testing full function bubble devices is presented. Lastly, future research plans for this next year are briefly mentioned.

The shapes of the bubble propagation devices used in the experiment are shown in Figure 1 and Figure 2. Figure 1 shows the scanning electron micrograph of gold ion implantation masks of "contiguous diamond shaped devices" and Figure 2 shows the scanning electron micrograph of gold ion implantation masks of "contiguous triangular shaped devices".

Device Fabrication

The 0.5 μm bubble propagation devices were fabricated on two garnet wafers (S103 and S116). Their LPE magnetic garnet film compositions are $(YSmTmGd)_3(FeAl)_5O_{12}$. The magnetic properties of the films are as follows: d(bubble diameter)=0.51 μm, $4\pi M$ (saturation magnetigation)=1258 Oe, Q (quality factor)= 1.37, t (film thickness)=0.79 μm for S103 and d=0.59 μm, $4\pi M$=1356 Oe, Q=1.47, t=0.83 μm for S116. Progagation tracks were formed by electroplanting gold. Detailed fabrication procedures were described in the previous report(Nov. 30, 1981).

To determine the dependence of bubble device performance on various ion implantation parameters such as ion species, dosage and energy, each wafer was divided into four regions and different ion implantation conditions were selected for each region. Ion implantation conditions for each region are described in Tables 1 and 2. The energy values cited here are the estimated values that the ions would have as they arrive at the surface of the garnet film. Since ions are implanted through variuous layers of films such as SiO_2, Au, Mo and Al on top of the garnet

film, the actual implantation energy are higher than those mentioned here. Energy levels selected here for deterium, namely 32 KeV, 48 KeV and 60 KeV, are estimated to correspond to implantation depth of 2,000 A 3,000 A and 3,500 A, respectively. After ion implantation, garnet wafers were dipped in gold etching solution for 1 minute to remove the gold ion implantation mask patterns.

The back LPE film of S116 was removed to enhance the visibility of bubbles during testing. The front LPE film was covered with silicone rubber to protect it during the removal of the back film. A mixture of phosphoric acid and sulfuric acid (75%: 25%) at boiling temperature (180 C) was used to dissolve the film. 5 minutes was more than enough to remove all of the LPE garnet film which was approximately 0.8 μm thick.

Testing of Devices

Bias margins for propagation devices were measured to determine optimum ion implantation conditions and propagation pattern shape. The new bias magnet and Leitz Orthoplan microscope equipped with a Dage T.V. camera and a 50X Leitz long working distance objective lens were used in the experiment. All the measurements were done for the propagation tracks oriented in the good propagation direction which is [112] crystal orientation of the garnet and at quasi-static in-plane rotating field frequency of 1 Hz. Testing of S103 showed that devices in region 2 and 4 did not propagate at all. These two regions were ion implanted with relatively low dosages (0.5×10^{16}/Cm^2) of deuterium and seemed to need more dose. Bubbles propagated in devices of region 3 at very high rotating in-plane field (100 Oe). Whereas, bubbles propagated very well in devices located in region 1. The main difference in ion implantation conditions between region 1 and 3 was the implantation depth. Region 1 had a deeper implantation (3,000 A) than region 3 (2,000 A), while dosages were almost the same. This shows that implantation depth required is more than 2,000 A and possibly closer to 3,000 A. Bias margins for devices in region 3 are shown in Figure 3 and Figure 4. Figure 3 is for diamond shaped 2.5 μm period propagation tracks and Figure 4 is for triangular shaped 2 μm period device. Minimum drive field was near 60 Oe for both devices. The 2.5 μm period device showed wider maggin (11%) than the 2 μm period device (9%) as expected. Drive field higher than 80 Oe was not applied for testing. Therefore, 80 Oe does not represent maximum in-plane field. This applies to all following measurements as well.

Recent studies of ion implantation done under this grant (1) suggested that

implantations which use only a single species of ion may have an advantage over multiple species implantation because it enables one to obtain an uniform anisotropy profile as well as an uniform strain profile. Following this idea, S116 was implanted with deterium only. Implantation depth was estimated to be about 0.35 μm. We chose this depth , while maintaining roughly the same dose, to see if increased driving layer thickness improved the bias margin compared with the devices in region 1 of S103 which had fairly good margin with 0.3 μm driving layer thickness. Margin plots for 2.5 μm period diamond shaped propagation patterns are shown in Figure 5 and those of 2 μm period triangular shaped patterns are shown in Figure 6. Both figures show a minimum drive field of 45-50 Oe which is a 10-15 Oe improvement over S103. As the dose is increased from $6 \times 10^{15}/Cm^2$ to $10^{16}/Cm^2$, the high bias end of the margin plot improves, which indicates insufficient dosage at lower dose levels. Maximum bias margins for 2.5 μm period device and 2 μm period device are approximately 11% and 9% respectively, which are the same as those for S103. Therefore, it seems that the increase in driving layer thickness from 0.3 μm to 0.35 μm dose not significantly widen the bias margin. It remains to be seen whether 'the improvement in the minimum drive field is due to increased implantation depth or to the use of a single ion species.

Bias margins for isolated single diamond and triangular patterns were also measured. Figure 7 shows the bias margin of an isolated diamond pattern located in region 3 of S116 and Figure 8 that of an isolated triangular pattern in the same region. Both show about 15% of bias margin with minimum drive field of approximately 20 Oe. The high end of the bias margin of the triangular pattern does not degrade as much as that of the diamond pattern at both extremes of the driving field. From this observation it seems that triangular patterns are better suited for propagation tracks than diamond patterns. This was not evident from the previous margin plots (Figures 3,4,5 and 6), because the periods of the devices were not the same (2 μm for triangular shaped pattern vs 2.5 μm for diamond shaped pattern). We plan to do the same kind of experiment using the devices with the same periods.

A few conculsions may be drawn from these preliminary experiments. Firstly, 0.5 μm bubbles can be propagated with reasonable minimum drive fields and good bias field margins. Secondly, the optimum thickness of the driving layer seems to be in the neighborhood of 3,000 A. Thirdly, the triangular shaped propagation element has slightly better bias margins than the diamond shaped element.

Conductor controlled functions of full function devices are now being measured.

Initial measurement of the generator margins of 1 μm bubble devices shows very good bias margins. Typical margins are more than 15% at 100 mA current level and minimum pulse width required is around 100 nanosecond.

Future Research

Our future research on ion-implanted contiguous-disk technology will be directed at the development of fully functional 0.5 μm bubble devices. To achieve this goal we plan futher work on optimization of 0.5 μm bubble propagation margins including more extensive studies of the dependences of margins on ion implantation conditions and pattern geometry. In parallel with the optimization of the 0.5 μm bubble propagation margins we will pursue the design and demonstration of fully functional devices using 1 μm bubbles. Once fully functional 1 μm devices are obtained, they will be scaled to 0.5 μm bubble size.

Reference

1. C.S. Krafft, *Deuterium Implantation in Magnetic Garnets*, (Ph. D. thesis, Carnegie-Mellon University, 1984).

Table 1.   Ion Implantation Conditions for S103

Region	Deuterium (D_2^+) Energy (KeV)	Dose (/Cm^2)	Oxygen (O^+) Energy (KeV)	Dose (/Cm^2)
1	48	1×10^{16}	60	1.5×10^{14}
2	48	0.5×10^{16}	60	0.75×10^{14}
3	32	1×10^{16}	35	1.2×10^{14}
4	32	0.5×10^{16}	35	0.6×10^{14}

Table 2.   Ion Implantation Conditions for S116

Region	1st Deuterium (D_1^+) Energy (KeV)	Dose (/Cm^2)	2nd Deuterium (D_2^+) Energy (KeV)	Dose (/Cm^2)
1	60	6×10^{15}	25	3×10^{15}
2	60	7×10^{17}	25	3.5×10^{15}
3	60	10×10^{15}	25	5×10^{15}
4	60	8×10^{15}	25	4×10^{15}
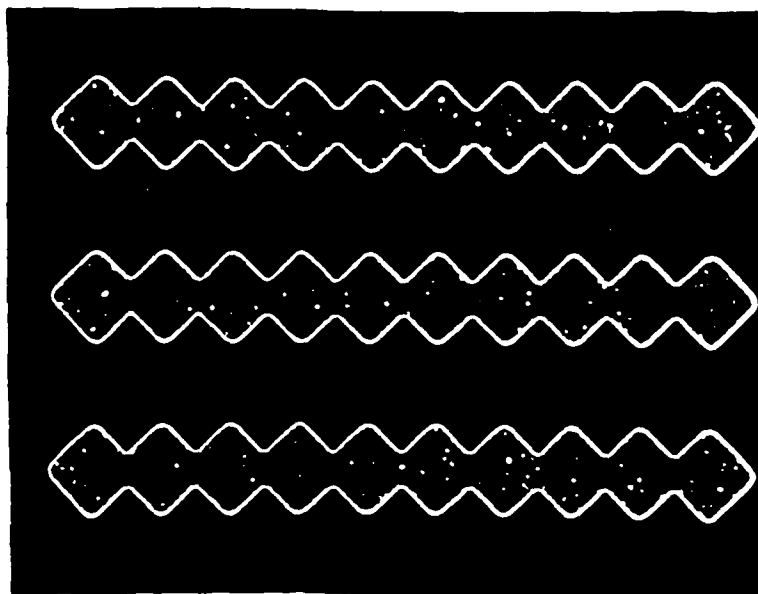
Figure 1: Scanning Electron Micrograph of Gold Ion Implantation Masks of "Contiguous Diamond Shaped Devices" for 0.5 µm Bubbles   Period: 2.5 µm
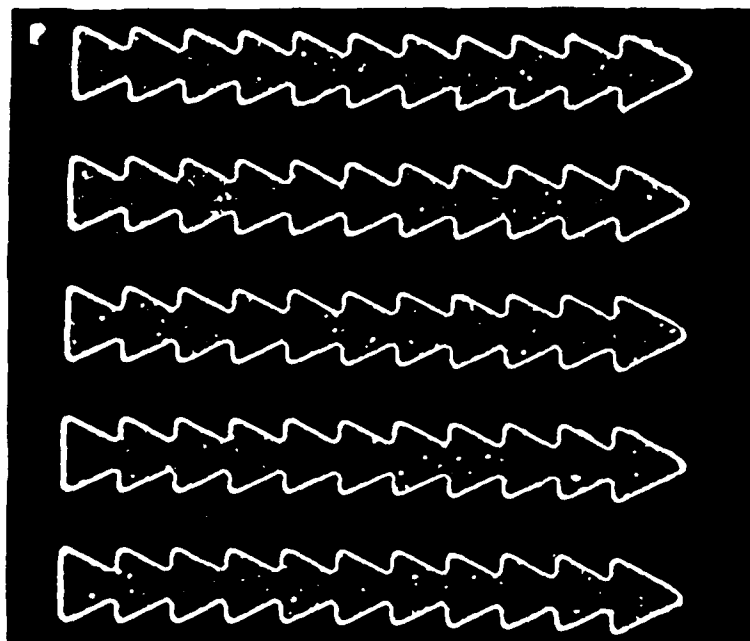
Figure 2: Scanning Electron Micrograph of Gold Ion Implantation Masks of "Contiguous Triangular Shaped Devices" for 0.5 µm Bubbles   Period: 2 µm
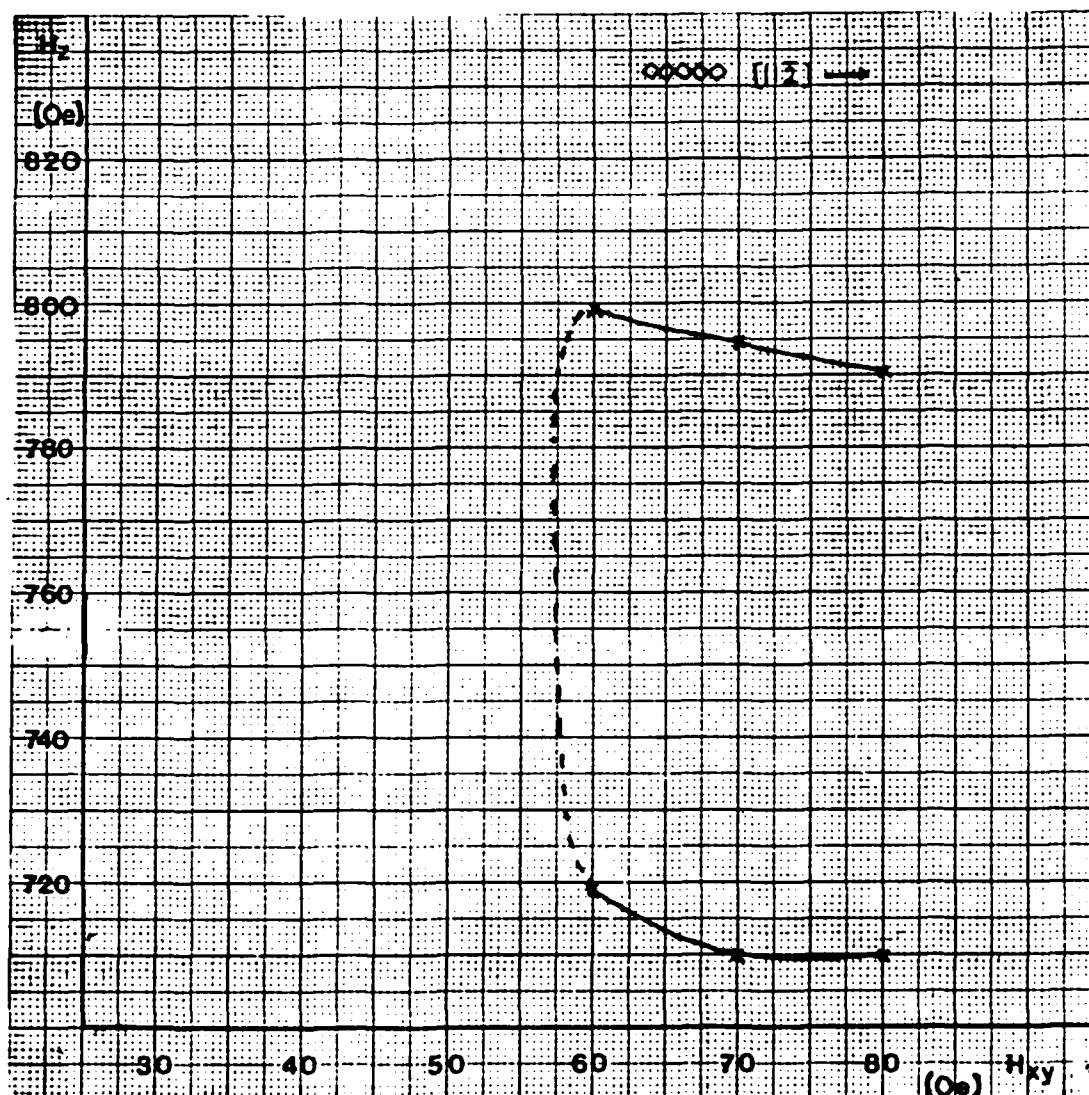
Figure 3. Bias Margin of "Contiguous Diamond Shaped Device"
for 0.5 μm Bubbles

Wafer ID: S103, Period: 2.5 μm, Good Track,
Drive Field Frequency: 1 Hz

Implantation Conditions:
48 KeV, 1 x 10^{16}/Cm^2 for Deuterium
60 KeV, 1.5x 10^4/Cm^2 for Oxygen

Figure 4. Bias Margin of "Contiguous Triangle Shaped Device"
for 0.5 μm Bubbles

Wafer ID: S103, Period: 2 μm, Good Track,
Drive Field Frequency: 1 Hz

Implantation Conditions:
48 KeV, $1 \times 10^{16}/Cm^2$ for Deuterium
60 KeV, $1.5 \times 10^{4}/Cm^2$ for Oxygen
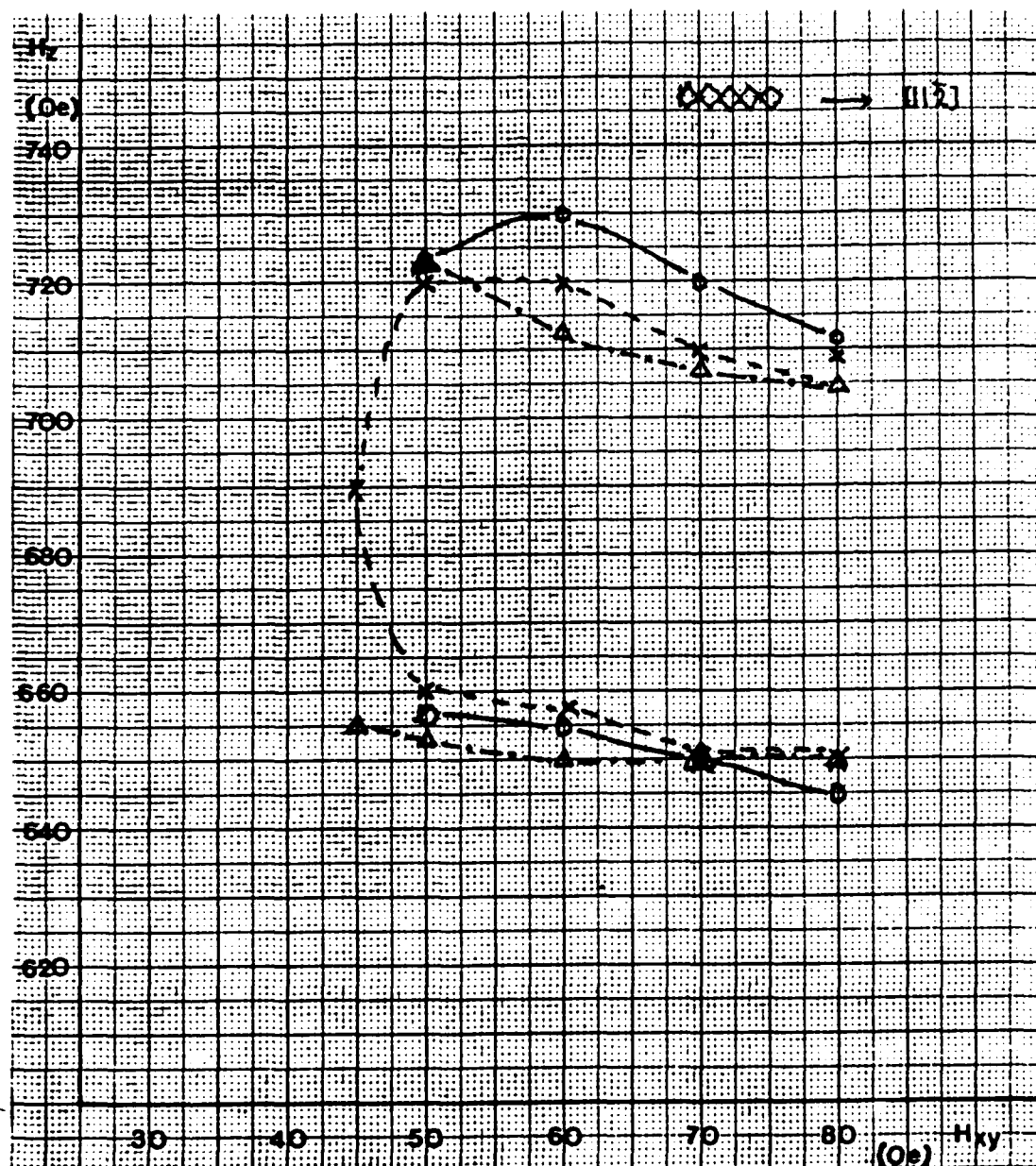
Figure 5. Bias Margins of "Contiguous Diamond Shaped Device"
for 0.5 µm Bubbles

Wafer ID: S116, Period: 2.5 µm, Good Tracks,
Drive Field Frequency: 1 Hz

Implantation Conditions:

····x···: 60 KeV, 6 x 10^{15} /Cm^2 for 1st Deuterium Implantation
         25 KeV, 3 x 10^{15} /Cm^2 for 2nd Deuterium Implantation
---Δ--: 60 KeV, 8 x 10^{15} /Cm^2 for 1st Deuterium Implantation
         25 KeV, 4 x 10^{15} /Cm^2 for 2nd Deuterium Implantation
——o—: 60 KeV, 10 x 10^{15} /Cm^2 for 1st Deuterium Implantation
         25 KeV, 5 x 10^{15} /Cm^2 for 2nd Deuterium Implantation

Figure 6ʰ **Bias Margins of "Contiguous Triangle Shaped Device"**
for 0.5 µm Bubbles

Wafer ID: S116, Period: 2 µm, Good Tracks, Drive
Field Frequency: 1 Hz

Implantation Conditions:
·····x···: 60 KeV, 6 x 10^{15}/Cm² for 1st Deuterium Implantation
          25 KeV, 3 x 10^{15}/Cm² for 2nd Deuterium Implantation
─·─·─Δ─: 60 KeV, 8 x 10^{15}/Cm² for 1st Deuterium Implantation
          25 KeV, 4 x 10^{15}/Cm² for 2nd Deuterium Implantation
──o─: 60 KeV, 10 x 10^{15}/Cm² for 1st Deuterium Implantation
          25 KeV, 5 x 10^{15}/Cm² for 2nd Deuterium Implantation

Figure 7.   Bias Margin of Single Diamond Element for 0.5 μm
            Bubbles

            Wafer ID: S116,   Drive Field Frequency: 1 Hz
            Diagonal Distance of the Element: 0.6 μm

            Implantation Conditions:
                60 KeV,   10 x 10^{15} /Cm² for 1st Deuterium Implantation
                25 KeV,   5 x 10^{15} /Cm² for 2nd Deuterium Implantation

Figure 8. Bias Margin of Single Triangle Element for 0.5 µm
Bubbles

Wafer ID: S116, Drive Field Frequency: 1 Hz
Height of the Element: 0.6 µm

Implantation Conditions
60 KeV, 10 x 10^{15} /Cm² for 1st Deuterium Implantation
25 KeV, 5 x 10^{15} /Cm² for 2nd Deuterium Implantation

Current-Access Perforated Sheet Magnetic Bubble Logic Devices

Progress Report

R. L. Smith and M. H. Kryder
Carnegie-Mellon University
4 December 1984

Abstract

Bubble logic gates have been designed, fabricated, and tested. The results are compared with a new computer simulation that contains a simple bubble model dependent on the material parameters of the actual bubble film. The model includes gyrotropic forces necessary to explain the different empirical margins obtained when the bias field direction is reversed. Work is proposed to design, fabricate and test a new chip featuring gates designed with the aid of the new computer simulation.

Introduction

The basic concept of magnetic bubble memories is to move binary information encoded in bubble domains to a detector. Many schemes for moving bubbles, called access methods, have been proposed; most are based on the phenomena that bubbles move in a perpendicular field gradient. Current-access techniques, first proposed by Walsh and Charap [1] create a perpendicular field by perturbing uniform planar current flow with perforations in a conductive sheet overlying the bubble film. Using two conductive sheets [2] improves operation by placing the bubble in a travelling potential well. Current flowing around an aperture creates a field with components, perpendicular to the sheet, that have opposite sign on opposite sides of the hole as shown in Fig. 1. Bubbles with upward-pointing magnetization are attracted to the left side of the hole. Overlapping apertures are placed, as shown in Fig. 2 in the second conductive sheet. The current in the first sheet is turned off, the second sheet current turned on and the bubble propagates from position 1 to position 2. The bubble is made to propagate to position 3 by applying a reverse current in the first sheet and turning off the current in the second. Position 4 is reached with a reversed second sheet current and the first sheet turned off. The periodic current pulses shown in Fig. 2 thus create a travelling potential well and propagate the bubble.

Bubble logic gates are capable of improving system performance and reducing system cost through the local handling of bad loop correction [3], addressing, and data flow [4]. The work in progress examines the design, fabrication, testing, and modelling of bubble logic gates. Perforated sheet current accessed bubbles are suitable for implementing logic gates because they are easily modelled and because there is no magnetic overlayer, as in permalloy devices, to interfere with bubble interactions.

One bubble logic gate which has been found to be very useful is the controlling gate wherein bubbles confined to a control path influence bubbles in the data path to take one of two alternate paths as shown in Fig. 3. The dual conductor current-access propagation technique is used to bring two bubbles together so that the bubbles experience a mutual repulsive force. With proper placement of apertures, bubbles entering the control input on the left will always exit at point A. A control bubble will repel a bubble entering the data input and force it to exit at C. If the data bubble enters alone it will take the easy path

and exit at B. Representing binary 1 with the presence of a bubble and 0 with its absence, the operation of the logic gate is defined by the truth table at the bottom of Fig. 3.

Bubbles move at a velocity proportional to the gradient of the local perpendicular field in a direction determined by the field gradient and the bubble wall structure. The structure of the bubble domain walls can take on many forms; a few examples are shown in Fig. 4. An important feature of each structure is the S-value, defined as the number of net rotations of the in-plane wall magnetization in one complete circuit of the wall perimeter. If the bubble has no net winding in the wall magnetization (S=0 see Fig. 4), the bubble travels in the direction of the gradient. If the wall structure has a net winding (S>0) the bubble will deflect from the gradient at an angle ϵ shown in Fig. 5. The deflection angle can be determined [5] from S, μ_w, γ, and d

$$\epsilon = \arctan \frac{4S\mu_w}{\gamma d} \tag{1}$$

The deflection angle can also be measured directly by propagating the bubble in a uniform gradient created by two parallel wires or "strip lines" [6]. The sign of deflection depends on bias field direction as shown in Fig. 5. In general the bubble will deflect in the direction $H_z \times v$. This report describes how this gyrotropic phenomena has an important effect on gate operation.

Current-accessed magnetic bubble devices are readily modelled using the finite element technique for calculating current flow in perforated sheet conductors, numerical integration for calculating the perpendicular fields and a simple dipole-dipole description of bubble interactions [7]. A new model has been developed which includes the effect of gyroptropic deflections as described by Eq. (1).

In the last report, an improved second chip had been designed and fabricated. The chip featured a third conductor layer patterned to form generators at the input to each gate and thus improve testability. Design time had been reduced with improved CAD tools. The fabrication procedure produced, in ascending order from the bubble film surface, a 500 angstrom silicon dioxide stress relief layer, 2500 angstroms of patterned aluminum for the first conductor, patterned and hard-baked photoresist for a 2800 angstrom insulator, 2500 angstroms of patterned aluminum for the second conductor, patterned hard-baked photoresist to form another 2800 angstrom insulator, and finally 2500 angstroms of aluminum for the third conductor to be used for generators. The chips contained 24 variations on the gate shown in Fig. 3 each connected to third level generators to repetitively test the three non-trivial input conditions at normal operating frequencies.

This report summarizes the method of testing these devices, the results and a comparison of these results with an improved version of the computer bubble simulator.

Experimental Method

The bubble material was supplied by Allied Corporation and has the characteristics shown in Table 1:

Wafer	h(μm)	w(μm)	H_o(Oe)	T_c(°C)	$4\pi M_s$(G)	l(μm)	Q	H_K(Oe)
K-14	2.53	2.32	242	214	445	.25	4.6	1918

Table 1: Material Parameters Measured by Allied Corporation

The γ, H_k and α of this material are determined using ferromagnetic resonance (FMR) using methods described by C. Krafft [8] and J. Artman [9]; the results are shown in Table 2:

Wafer	γ(OeS)$^{-1}$	H_E(Oe)	α	H_K(Oe)	μ_w	K_u(erg/cm^3)
K-14#1	1.51×10^7	1588	.127	1933	392	3.4×10^4

Table 2: Bulk Parameters Measured by FMR

FMR techniques are also used to measure the magnetic properties of the bubble film surface, uniformly ion-implanted with oxygen to suppress hard bubbles. These results along with implant conditions are shown in Table 3:

Wafer	Ion	Dose(cm^{-2})	Energy	γ(Oe^{-1}S^{-1})	H_E(Oe)	H_K(Oe)	Q
K-14#1	O	2.4×10^{14}	110(keV)	1.26×10^7	-1694	-1349	-3.0

Table 3: Implantion Conditions and Surface Parameters Measured by FMR

Two parallel conductors spaced 40 microns apart are fabricated alongside the chips and are used to measure bubble mobility, angle of deflection from the gradient and the dynamic and static coercivities as shown in Table 4:

Wafer	μ_B(cm/Oe-S)	ϵ	H_c^{dyn}(Oe)	H_c^{stat}(Oe)
K-14#1	207	14°	.66	1.18

Table 4: Strip Line Results

Device testing in this work depends upon the optical observation of magnetic domains using the Faraday effect wherein the polarization plane of linearly polarized light is rotated during transmission through a ferromagnetic material along the axis of magnetization. Domains are observed when the rotated light passes through a polarizer orthogonal to the original plane of polarization.

A sampling optical technique [10] is employed to observe brief instants or samples of periodic

phenomena analagous to the stroboscopic observation of wagon wheels. The ten nanosecond images produced by a pulsed laser source are integrated and stored by a television camera.

Appropriate current pulses applied perodically (usually at 60 Hz) to the chips produce periodic events that are sampled with laser pulses at the same frequency. With an adjustable phase delay on the laser, any 10 nanosecond portion of the events can be "frozen" as an image. Variations between the events will appear as variations in the image. By sweeping the adjustable phase delay, the unfolding of events can be examined both forward and backward in time. The sampling optical technique in conjunction with the Faraday effect has been used to study a wide variety of dynamic phenomena in magnetic materials, particularly bubble films. The technique is used in this work to observe the trajectories of bubbles as they propagate and pass through the gates with different bias fields and drive currents.

Results

Conventions for labelling the gate output and failure regions in the margins are shown in Fig. 6. Regions labelled A, B and C in the margins (Figs. 7 to 14) denote outcomes in which the bubble leaves the gate on the respective paths indicated in Fig. 6. Overlapping regions indicate that more than one outcome was observed for events with identical margin parameters. The failure outcomes include the control bubble coming out of the top of the gate (F1), the data bubble coming out of the bottom of the gate (F4), and either bubble getting off of the output paths (F2 and F3). Curves labelled "p" in the margin plots bound regions in which the bubble(s) fails to propagate to the gate input because the input path propagation margins is exceeded. "s" labels denote margin curves where stripes have been noticed anywhere in the field of vision.

Two or more different outcomes of identical experiments are often observed. For example, control bubbles entering a gate will sometimes exit at point A and sometimes at point B under identical conditions. The statistics of each outcome (that is, the relative frequency of its occurence) vary with changing margin parameters. To display margins we have used Venn diagrams wherein overlapping regions indicate that more than one outcome is observed with the same margin parameters. Qualitative description of the frequency of events in these intersecting regions and of how the frequency changes with varying margin parameters is possible but tedious. Quantitative measurement of statistical effects is not pursued here.

Margins for the controlling gate "igate17" are shown in Figs. 7 to 14 with no parallel field applied. The three non-trivial input conditions (lone control bubble, lone data bubble and dual bubbles) require four margin plots, one for each bubble to reduce confusion. Bias field and drive current density are the margin parameters. We note that the margins depend on the bias field direction with each direction

yielding a small region of correct operation. The negative bias field seems to encourage the bubbles to turn right with respect to the propagation direction whereas the positive bias field produces turns to the left. A tendency for the bubbles to turn right or left depending on the direction of the bias field has been observed on all the gates.

We have also made the following observations:

- Significant sections of the margins for the dual bubble input condition cannot be tested on the gates because either the control bubble fails to make it through the input path at zero parallel fields or the control bubble is collapsed while generating the data bubble at non-zero parallel fields.

- Subject to this limitation, margins have been taken on the gates varying the bias field and either the drive current density or the parallel field. The margins consist of regions of outcomes that overlap where two or more outcomes occur for the same margin parameters.

- The frequency of occurence of outcomes in overlapping regions can be described qualitatively (e. g. often, rarely, etc.) but a new experimental apparatus would be required for quantitative measurement which is not being pursued at this time.

- Changing the direction of the bias field changes the direction of bubble deflection in the strip line experiment as predicted by theory and changes the outcome of gate experiments.

- The bubble switches from a 20 to a zero degree deflection when the parallel field is raised above approximately 220 Oe along the gradient direction in the rocking experiment.

Discussion

We compare here the experimental margins with margins produced by a new computer simulation that includes the material parameters given above especially static and dynamic coercivity and a gyrotropic deflection of $15°$.

Figs. 7 through 14 show the simulated and experimental results for igate17 with zero parallel field. Although these plots show remarkable qualitative agreement, the computer simulator must be improved to explain the discrepancies in bias field and drive current density.

Conclusions and Proposed Work

Bubble logic gates have been designed, fabricated and tested. The operation of these gates is qualitatively described by a new computer simulator which includes the gyrotropic force and a simple bubble model dependent upon empirical material parameters. These parameters have been measured using strip line and FMR techniques and are included in the simulation.

The following work is planned for the coming year:

- A new chip will be designed, fabricated, and tested. The chip will feature improved generators and gate input paths so that entire margins of gates can be tested.

- Working gates will be designed using the improved computer simulator. These gates will be fabricated on the new chip.

- The computer simulator will be improved to obtain better agreement between simulation and experiment. Discrepancies in drive currents and bias fields will be investigated.

Table of Symbols

S	Number of net wall magnetization revolutions.
μ_w	Wall mobility.
γ	Gyromagnetic ratio.
d	Bubble diameter.
ϵ	Angle of bubble deflection from perpendicular field gradient.
H_z	Magnetic field z-component.
v	Velocity of bubble.
h	Thickness of bubble film.
w	Width of stripes in demagnetized unsaturated film.
H_o	Bubble collapse field.
T_c	Curie temperature.
$4\pi M_s$	Saturation magnetization of bubble film.
l	Characteristic length of bubble film.
Q	Quality factor of bubble film.
H_K	Anisotropy field.
H_E	Effective field.
α	Gilbert damping parameter.
K_u	Uniaxial anisotropy.
μ_b	Bubble mobility.
H_c^{dyn}	Dynamic coercivity.
H_c^{stat}	Static coercivity.
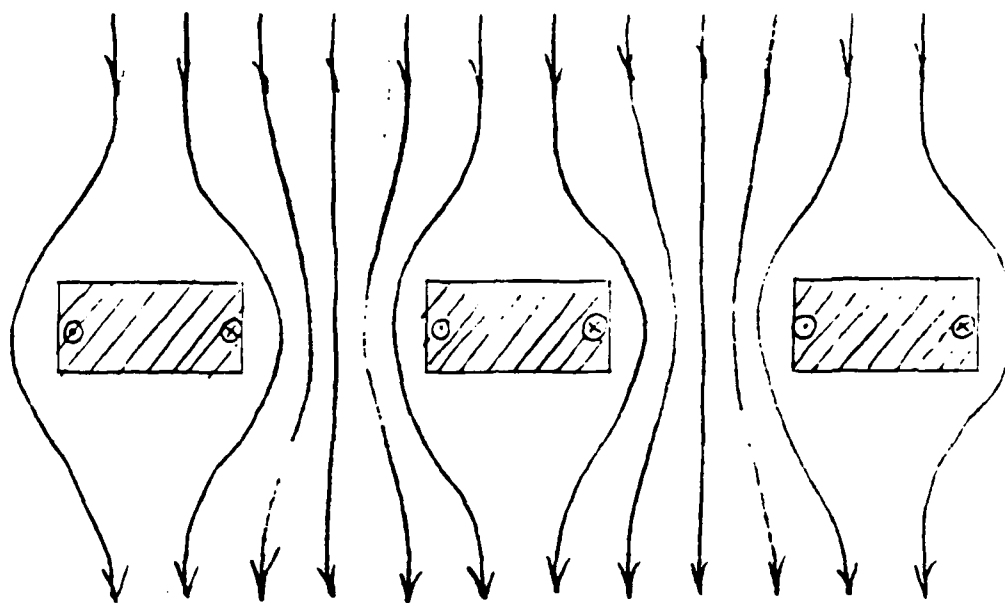
Figure 1: Fields Produced by Planar Current Flow Around Aperture
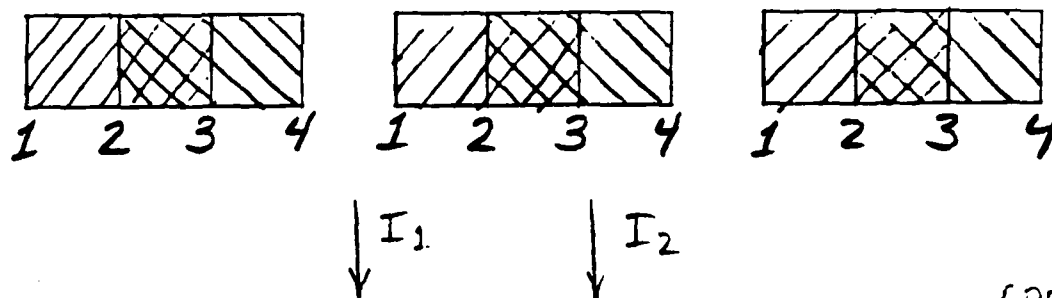
Figure 2: Overlapping Apertures in Two Conductive Sheets
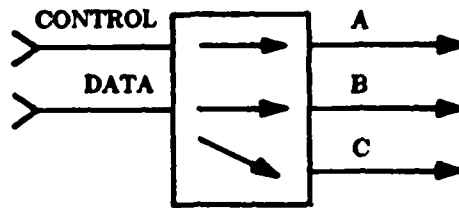
apertures in top conductor

apertures in bottom conductor

current flow
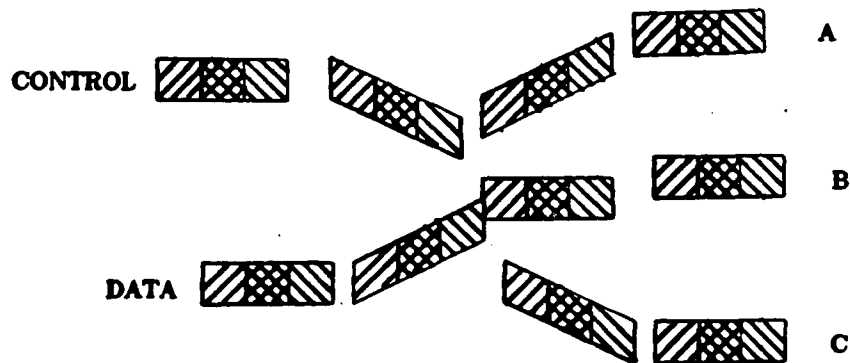
CONTROL	DATA	A	B	C
1	1	1	0	1
1	0	1	0	0
0	1	0	1	0
0	0	0	0	0

Figure 3: Control Gate #17: Schematic, Layout, and Truth Table

$S = 1$ wall structure
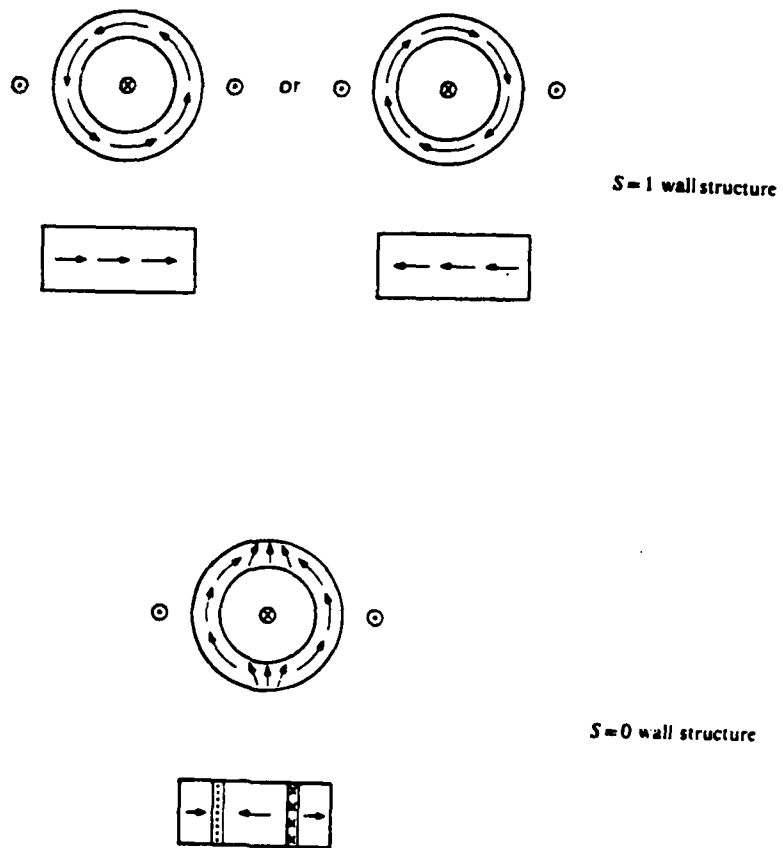
$S = 0$ wall structure

Figure 4: Domain Wall Structures
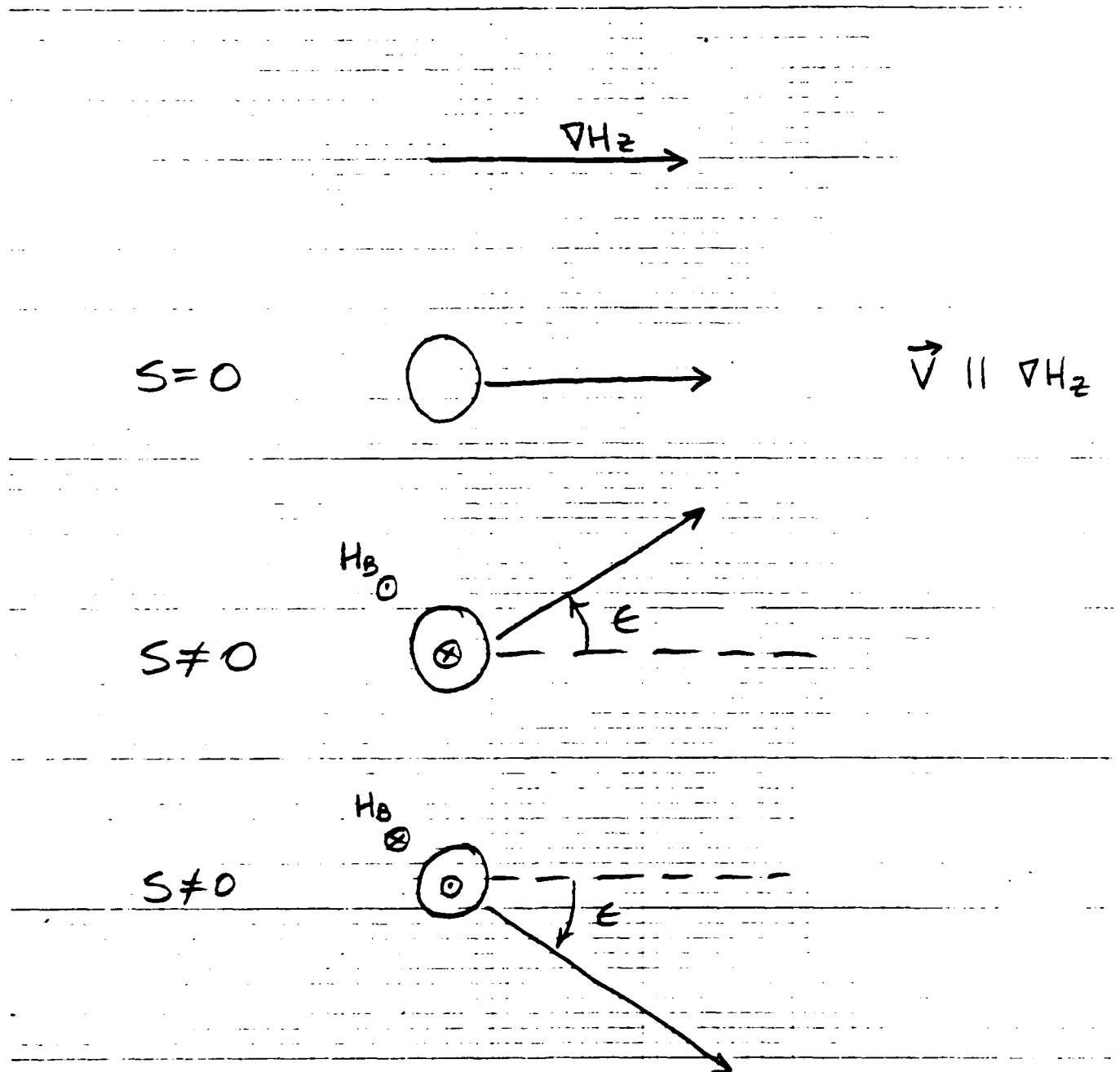
Figure 5: Bubble Deflection in Uniform Gradient
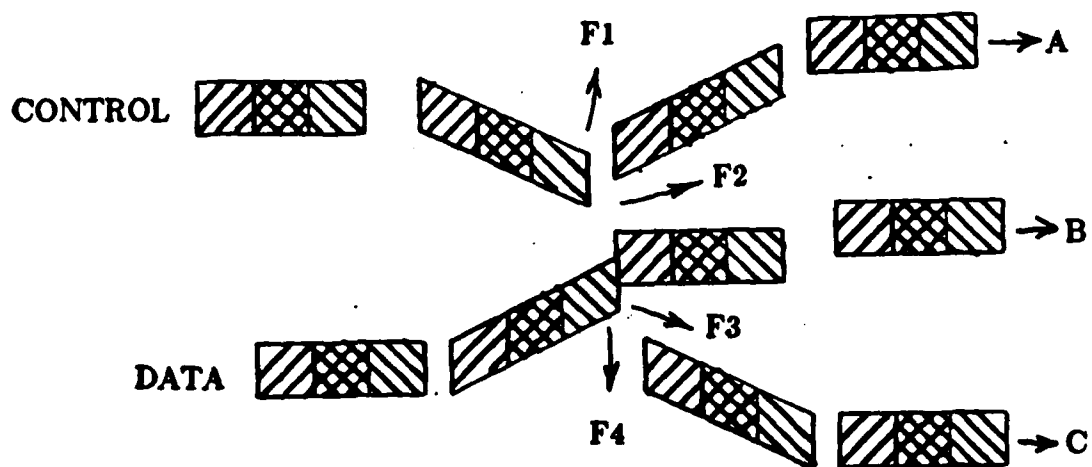
Figure 6: Typical Experimental Trajectories and Landing Sites
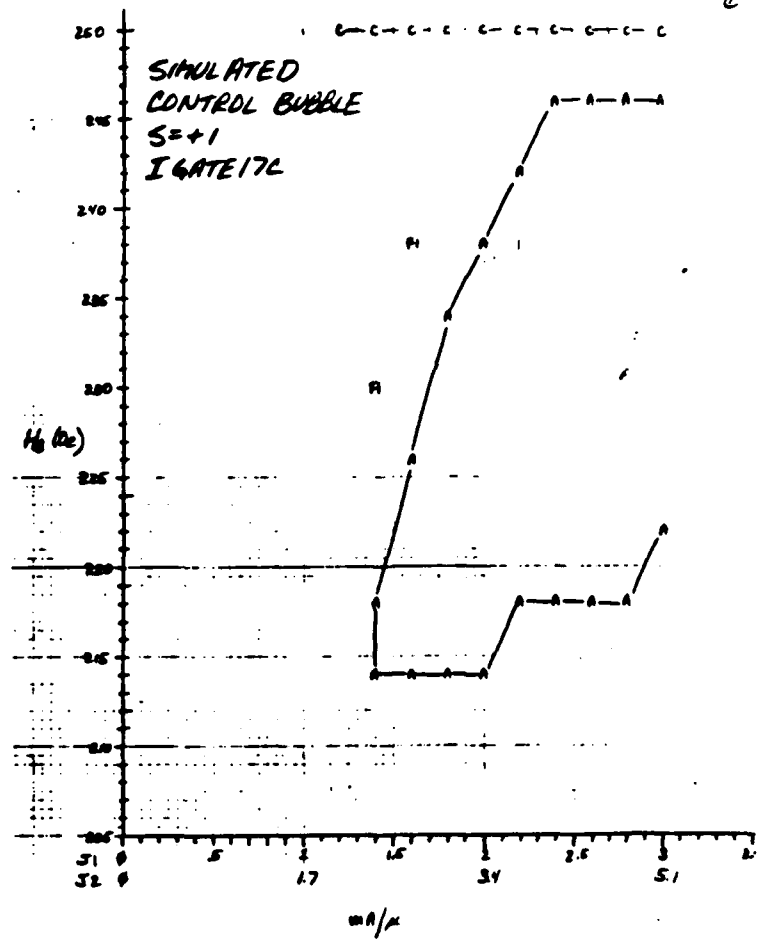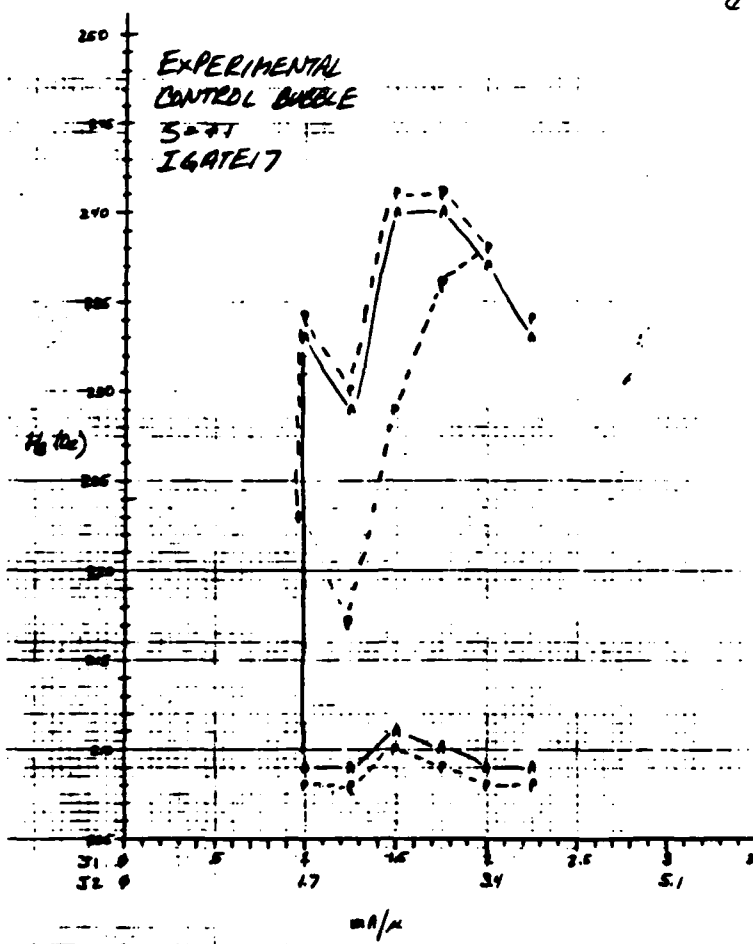
Figure 7:
Empirical and Simulated Margins: Gate #17
Lone Control Bubble, Positive Bias Field
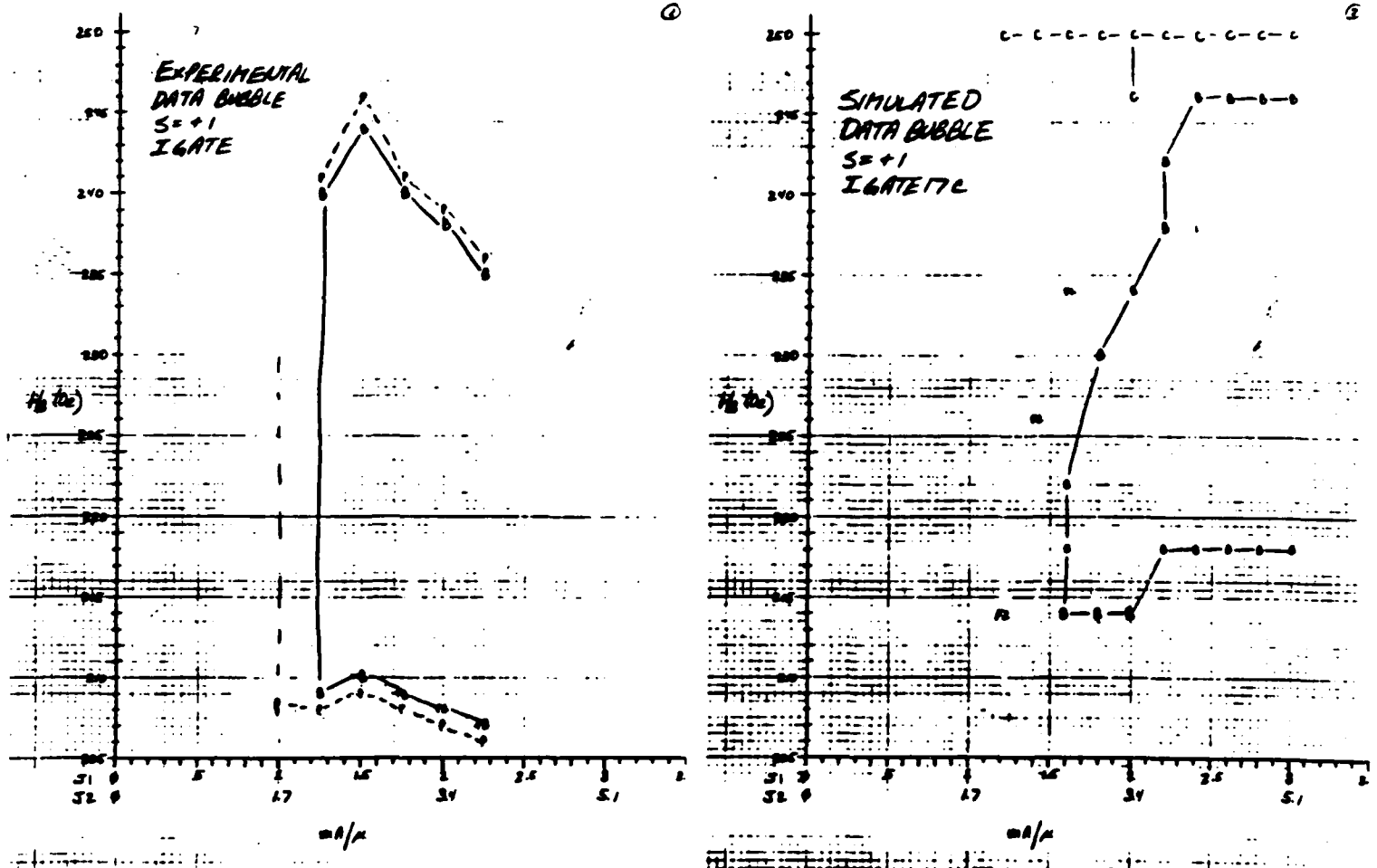
Figure 8:
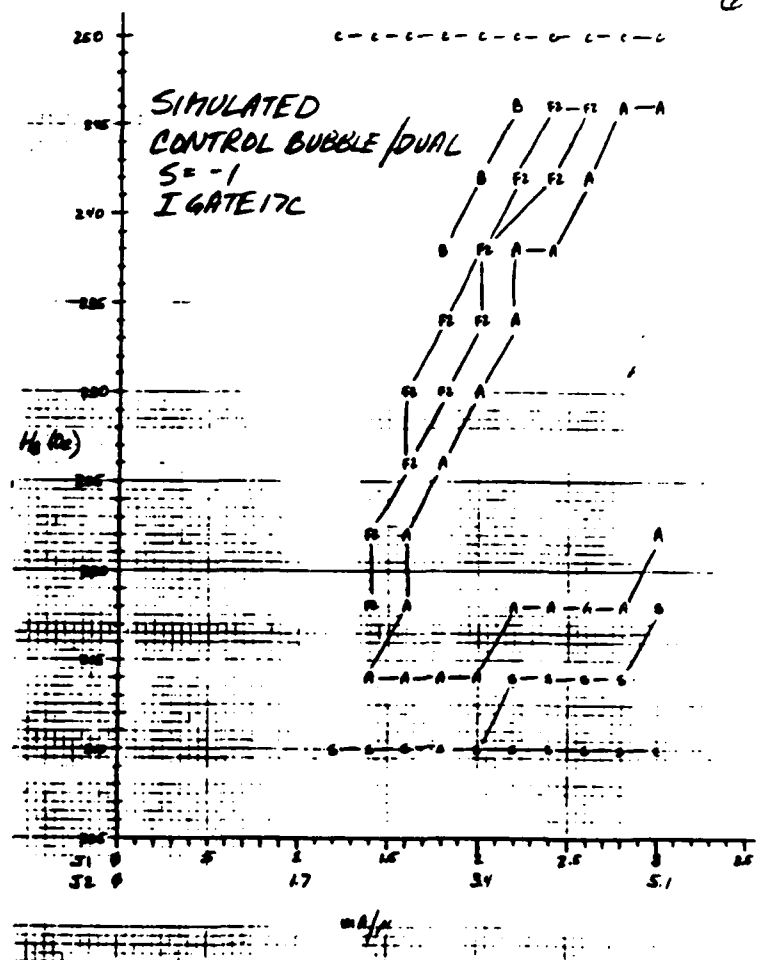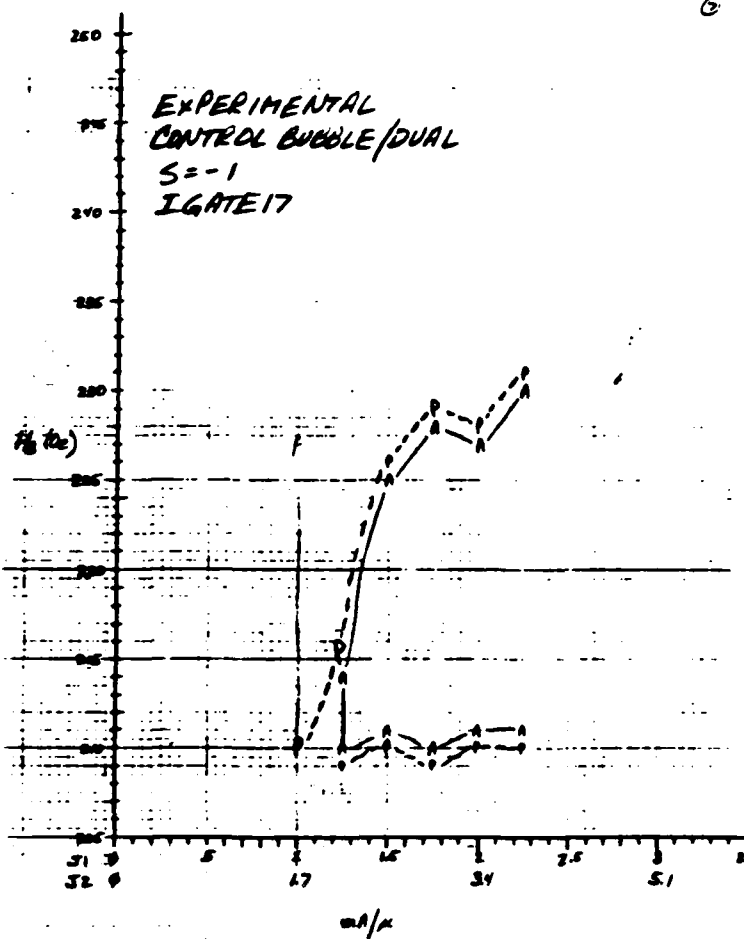Empirical and Simulated Margins: Gate #17
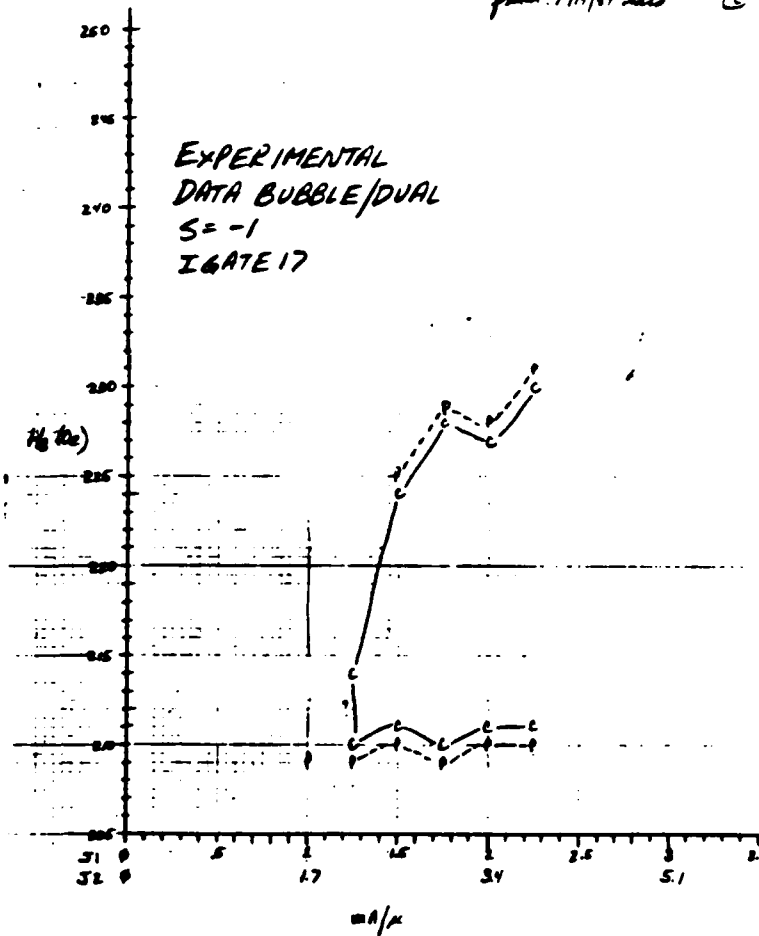Lone Data Bubble, Positive Bias Field
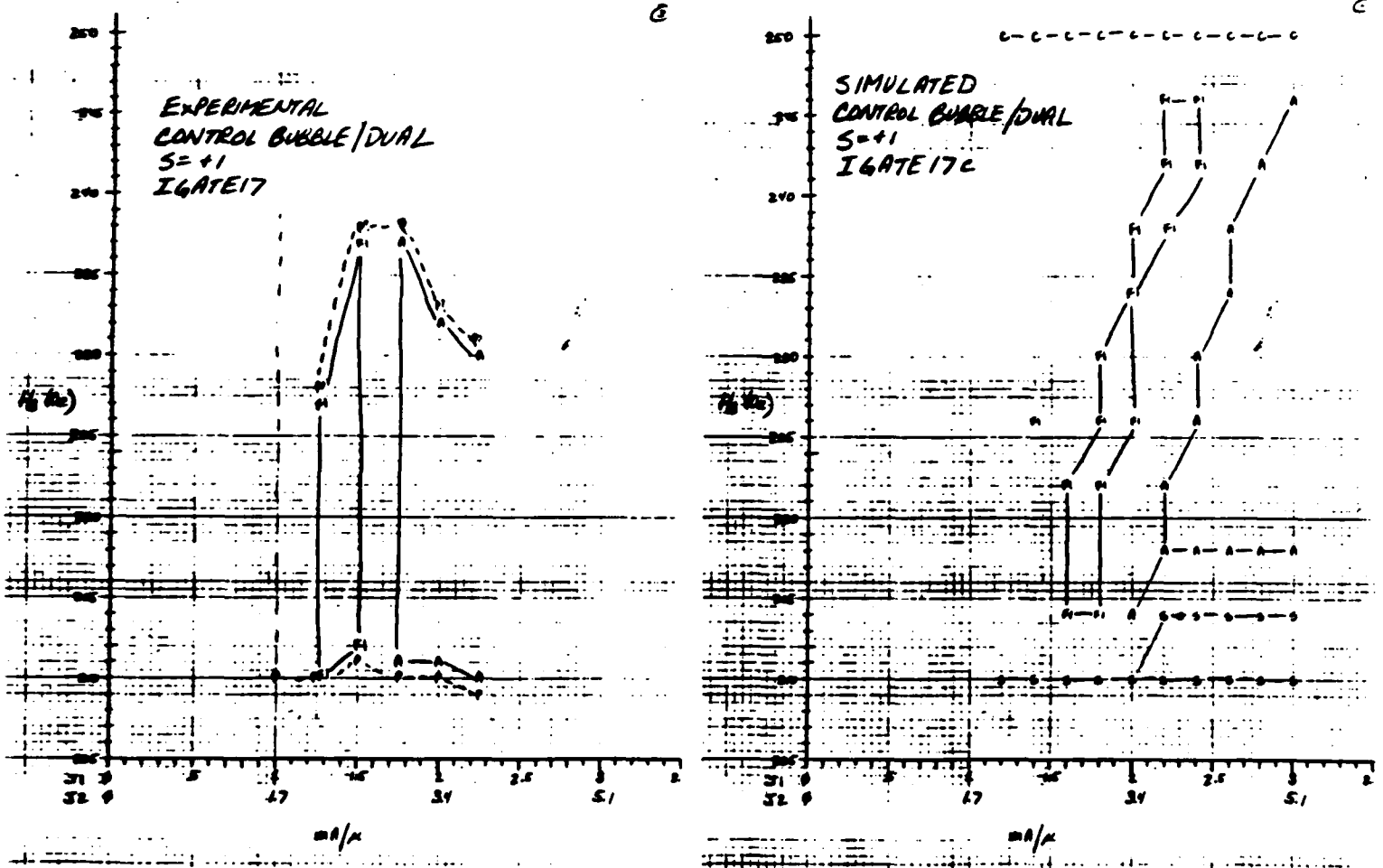
Figure 9:
Empirical and Simulated Margins: Gate #17
Control Bubble/Dual Input, Positive Bias Field
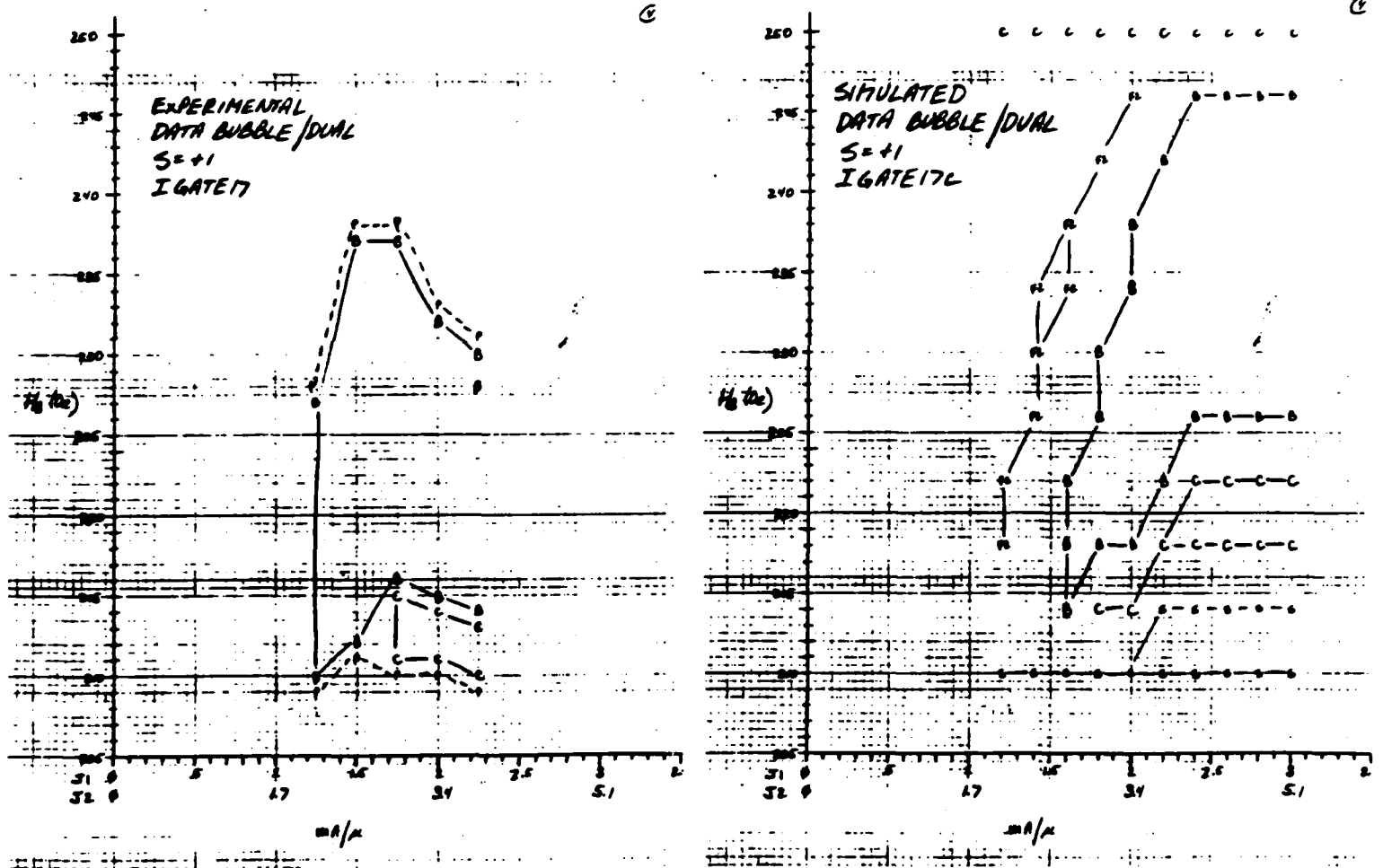
Figure 10:
Empirical and Simulated Margins: Gate #17
Data Bubble/Dual Input, Positive Bias Field

16
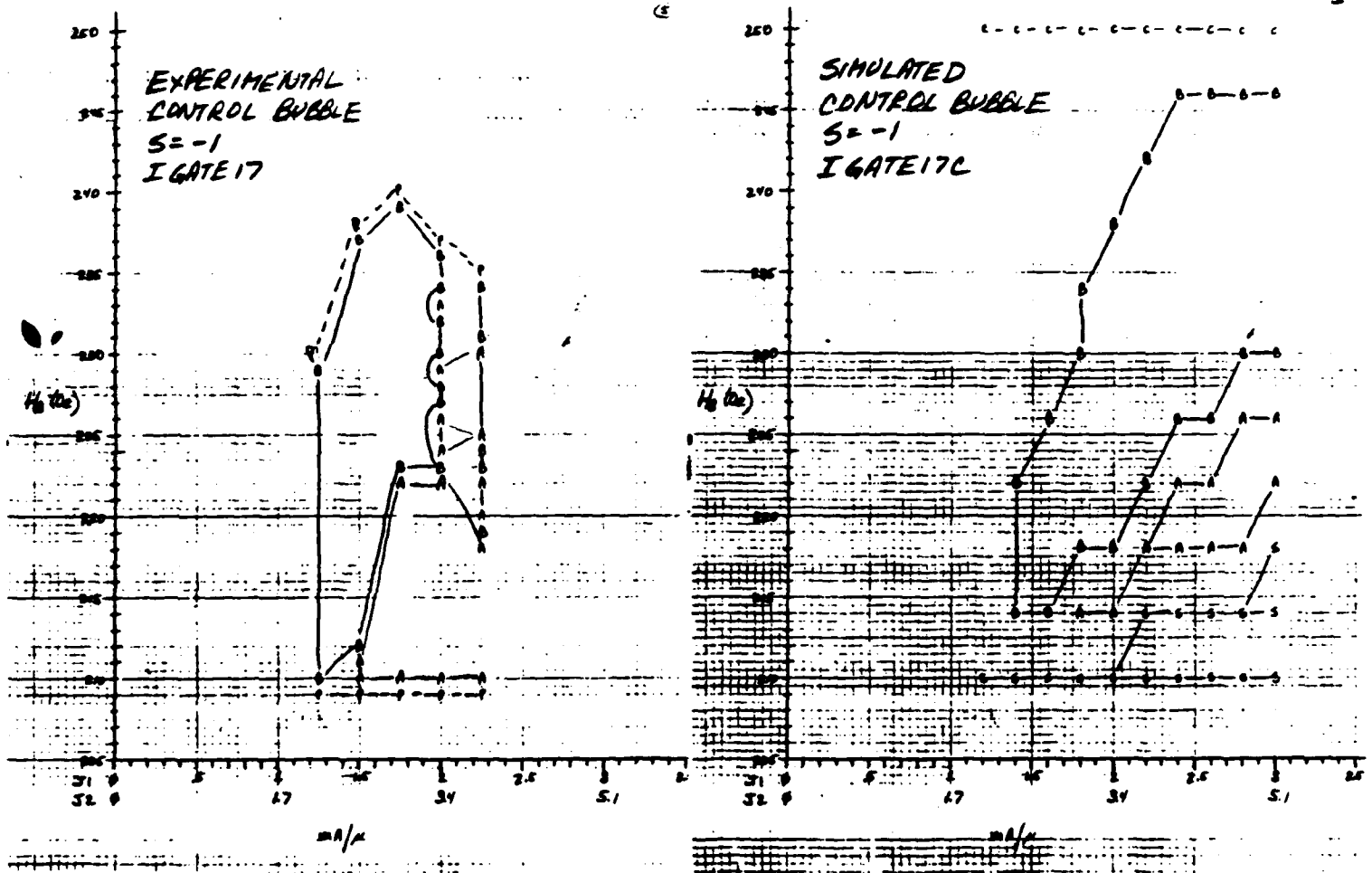
Figure 11:
Empirical and Simulated Margins: Gate #17
Lone Control Bubble, Negative Bias Field
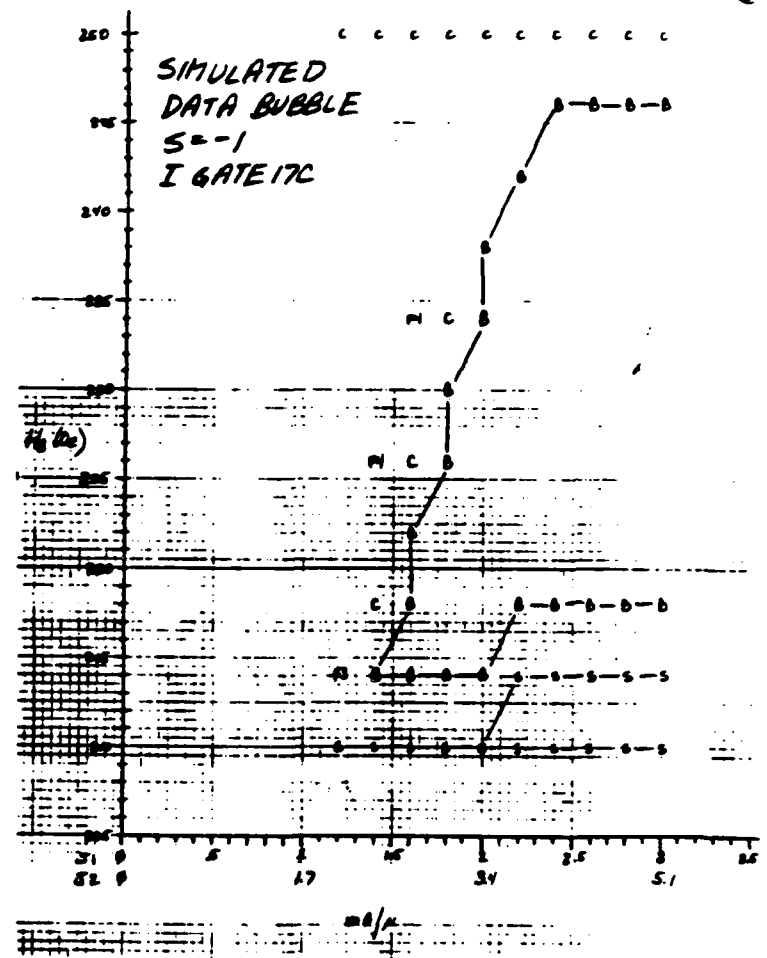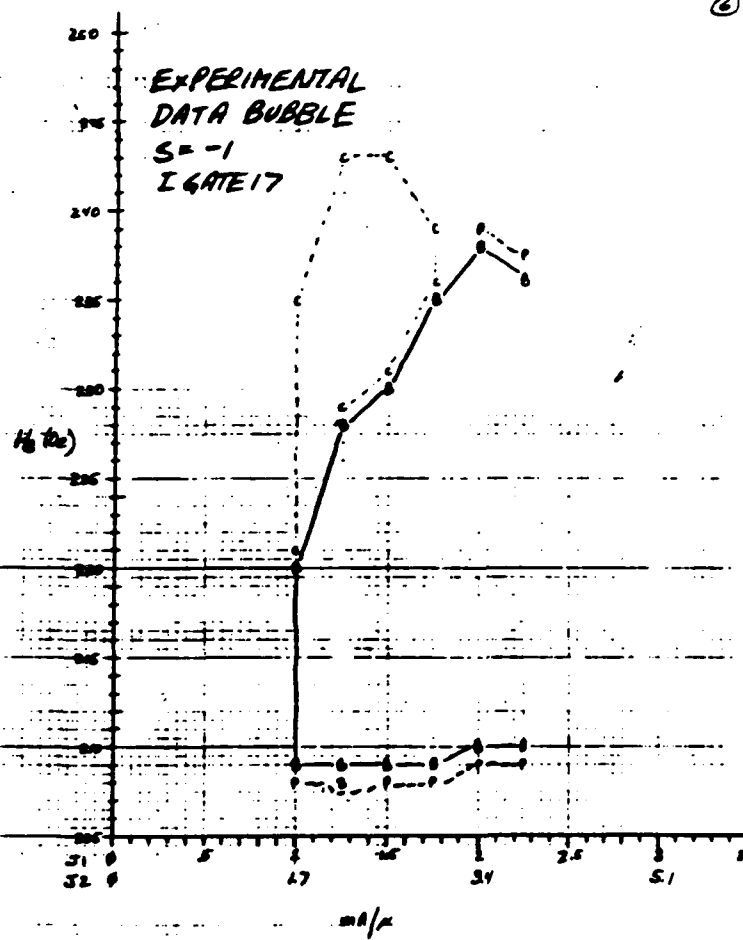
Figure 12:
Empirical and Simulated Margins: Gate #17
Lone Data Bubble, Negative Bias Field

Figure 13:
Empirical and Simulated Margins: Gate #17
Control Bubble/Dual Input, Negative Bias Field
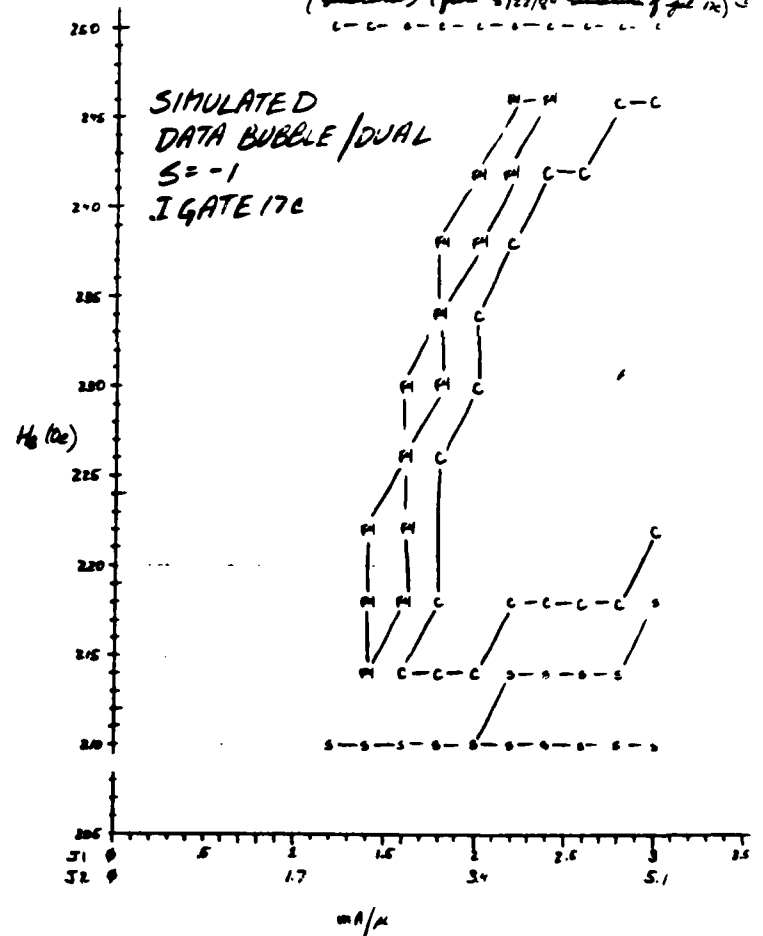
Figure 14:
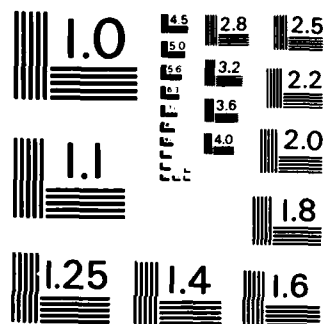Empirical and Simulated Margins: Gate #17
Data Bubble/Dual Input, Negative Bias Field

END

FILMED

DTIC

MICROCOPY RESOLUTION TEST CHART

NATIONAL BUREAU OF STANDARDS-1963-A

Current-Accessed Ion-Implanted Device Fabrication Procedure

SiO$_2$ Prespacer Deposition

Following epitaxial layer cleaning, a thin SiO$_2$ prespacer (on the order of 500 angstroms), is deposited by rf sputtering. This layer is used to protect the epitaxial bubble film during subsequent processing.

Backside Epitaxial Film Removal

In order to enhance the imaging of bubbles during device testing, the epitaxial layer on the back of the wafer is removed at this point in time. First, AZ 1350-J photoresist is spun for 30 sec. on the wafer's good side at 4000 rpm and baked for 30 minutes at 160 degrees centigrade. The wafer is then placed for several minutes in a bath of phosphoric acid heated up to 150 degrees centigrade. At this temperature, it takes only a few minutes to remove a one micron thick epitaxial layer. After cooling for several minutes, the wafer is rinsed well with water and dried. The front photoresist layer is stripped by immersion in acetone and plasma ashing. Wafer cleaning follows.

Ion-Implantation Level

To promote adhesion of the implant photoresist mask to the SiO$_2$ layer, the wafer is dehydrated in an oven for roughly one hour at a temperature of 200 degrees centigrade. After cooling to room temperature, the wafer is mounted on a spinner chuck, HMDS (an adhesion promoter) is statically dispensed and the wafer is spun at 5000 rpm for 30 seconds. AZ 1400-27 photoresist is statically dispensed and the wafer is again spun at 5000 rpm for 30 seconds, yielding a coat of resist approximately one micron thick. The resist layer is then prebaked at 90 degrees centigrade for 30 minutes.

Photoresist patterns were printed using a Karl Suss contact printer. For the implant level photoresist patterns, the exposing power density was 12 mw/cm^2. With a developer bath

consisting of Shipley AZ 351 developer and de-ionized water (a 1/3 ratio respectively) and a developing time of 60 seconds, exposure times were typically on the order of 15 seconds. A scanning-electron micrograph of an ion-implant level photoresist pattern may be seen in Fig 1.

Alignment Mark Etch

Following ion-implantation, alignment marks are etched into the epitaxial layer on the front of the wafer. This is done as follows: First, AZ 1350 J photoresist is spun onto the wafer at 4000 rpm for 30 seconds and prebaked at 90 deg. C for 30 minutes. Note that *the ion-implant photoresist mask patterns are still intact*. Once cooled, the wafer is printed with the alignment mark etch mask which opens windows in the resist on four chips on the wafer. Using a power density of 12 mw/cm^2, and no filter on the Karl Suss contact printer, an exposure time of roughly 30 seconds was required. The AZ 1350 J resist is developed for 60 sec. in a 3/1 ratio of water and AZ 351 developer respectively; the ion-implant and alignment mark resist patterns remain and the remaining 12 chips are protected beneath the thick AZ 1350 J layer. After a 30 minute, 120 deg. centigrade hardbake, the wafer is placed in a buffered hydrofluoric acid solution for five minutes which will etch away the SiO$_2$ prespacer in the exposed regions. After rinsing, the wafer is then submerged in hot (90 deg. C) phosphoric acid for three minutes. The implant and alignment mark patterns of the four unprotected chips are etched into the implanted, highly soluble substrate. To remove the implanted resist, the wafers are soaked in acetone and ultrasonically agitated for several minutes. After drying, they are then soaked in RT-2 stripping solution for a few minutes, rinsed well with DI water, and dried.

Although this method of alignment mark etching requires a few chips to be sacrificed, it has its advantages. First of all, the four chips used are extremely close to the wafer edge and would most likely be lost due to normal wafer handling, photoresist and deposited film non-uniformities at the wafer edges and defects induced by the GGG substrate holder during LPE growth of the bubble layer. More important, however, is the fact that once the implanted patterns are etched into the wafer, the first conducting sheet apertures may be

directly aligned with these implanted patterns. This allows finer and more accurate registration than if the standard, much larger fiduciary marks are used. In practice, the large "maltese cross" marks are used for coarse alignment and gross chip orientation; the etched patterns are used for more precise and final registration prior to exposure.

Conductor Deposition

The two conducting levels of this device consisted of evaporated aluminum. In the evaporation system, cleaned aluminum staples are draped over a tungsten filament; the wafer on which a film is to be deposited is suspended face down above the filament (behind an operator-controlled shutter) and the bell jar containing the filament/wafer mount assembly is evacuated. When a suitably low base pressure is reached (typically 5×10^{-7} Torr.), current is sent through the tungsten filament, heating it up and causing the aluminum to evaporate, after which the shutter is opened. A pre-calibrated deposition thickness monitor is used to track the film thickness. The shutter is closed when the desired film thickness is reached, preventing further aluminum deposition.

Conductor Sheet Level Patterning

To pattern the aluminum conductors, the following procedure is used: First, AZ 1350B photoresist is statically dispensed onto the clean aluminum film and spun for 30 sec. at 7000 rpm. Following a 90 deg. C bake for 30 minutes, the aperture level masks are printed using an exposure time of roughly 4.5 seconds at an optical power density of 10 mw/cm^2 on the Karl Suss contact printer. A UV filter is used for this exposure. Exposed wafers are developed for 60 sec. in a 3/1 ratio of water and AZ 351 developer, respectively.

Aluminum Conductor Etching

Apertures were etched into the aluminum films using a chemical etchant. It consisted of phosphoric acid, acetic acid, deionized water and nitric acid in the volume ratios of 80:5:10:1, respectively. (It is hereafter referred to as PAWN.) This etchant was used at

room temperature and mildly agitated by hand. The end-point of the etch process was determined visually and confirmed by placing the rinsed and dried wafer under a microscope and inspecting small features in the transmission mode. Good resolution was obtained, as may be seen in Figure 2. In this photograph, 0.5 μm lines and spaces are seen. Features as small as 0.75 microns were etched routinely. This etching method was able to reproduce virtually any photoresist pattern precisely.

Insulating Layer Application

In this work, hard-baked photoresist was used as an insulating layer. It was easily applied and patterned, and was found suitable for the experimental devices described in this report. It provided conformal coating of patterned aluminum structures and resulted in a planar device structure. It was applied as described below:

First, AZ 1350B was spun over the patterned aluminum sheet at 6000 rpm for 30 seconds. The resist was then baked for 30 minutes at 90 degrees centigrade. The masking level was aligned and exposed using the Karl Suss contact printer at a power density of 10 mw/cm^2. The light was filtered and exposure times were on the order of six seconds. A 60 sec. development in a 3/1 ratio of water and AZ 351 developer, respectively, followed. Hardbaking consisted of placing the wafer into a 200 degree C oven for two hours.

Pad Build Up

In order to facilitate testing and improve electrical contact to the chip via probes or wire bonds, the contact pad regions of the conducting sheets were made thicker by an aluminum evaporation and lift-off process. By making these areas thicker, contact resistance is reduced and electrical connections to the chip are more mechanically robust and reliable. The procedure is as follows:

After the top level aluminum conductor is patterned by etching, the remaining photoresist is removed in an acetone bath. Then, a thick layer of AZ-1350 J resist is applied by

spinning on at a speed of 5500 rpm (for 30 sec.), which results in a coat of roughly 1.5 microns. The wafer is then prebaked at 90 degrees C for 20 minutes and soaked in chlorobenzene for 15 minutes. After drying with nitrogen, the wafer is printed with the pad-build up mask using a relatively high exposure density (due to the thick resist layer). Typical exposure times were on the order of 30 seconds using a power density of 12 mw/cm^2 and without using a filter on the Karl Suss contact printer. Standard development follows (one part AZ-351 developer in three parts water for 60 seconds) and then the wafer is postbaked for 20 minutes at a temperature of 90 degrees centigrade.

The resulting photoresist pattern on the wafer covers the entire chip area except the contact pads. Now, aluminum (5000 angstroms) is evaporated in the same manner as the conducting sheets. Upon cooling, the wafer is soaked in acetone; the underlying resist is dissolved and the aluminum on top of it will "lift-off" (patience is the key here). The final product is a negative of the pad-build up mask; aluminum pads are left behind in the areas designated as electrical contacts. After the wafer is dried, the devices are ready for electrical testing.
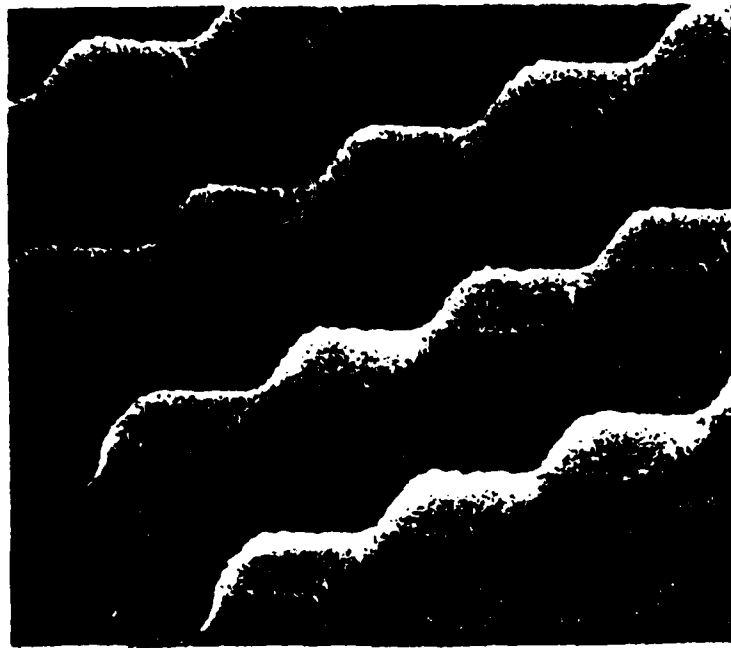
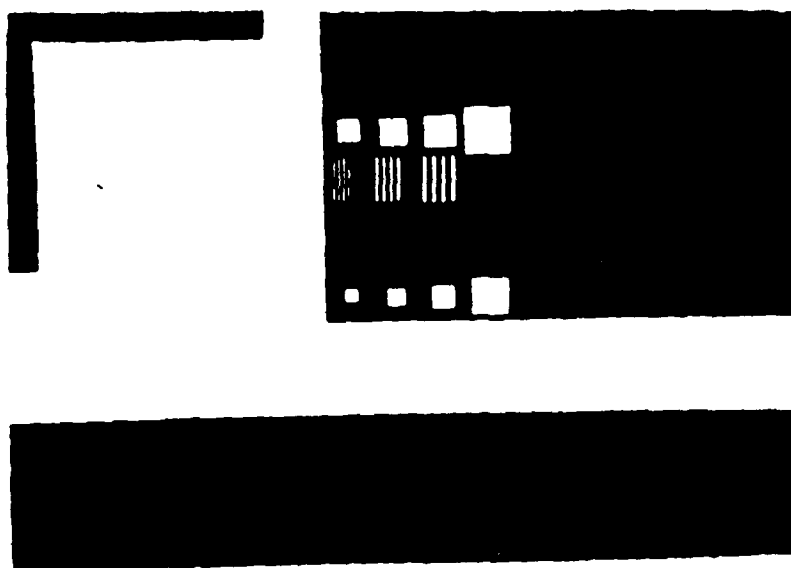Figure 1: 470X Micrograph of a 1 μm Thick Photoresist Implant Pattern

Figure 2: Micrograph of Etched Aluminum Pattern. The smallest line/space pattern has a period of 1 μm.

List of Figures

END

FILMED

1-86

DTIC